Semiconductors, Vol. 39, No. 1, 2005, pp. 1–3. Translated from Fizika i Tekhnika Poluprovodnikov, Vol. 39, No. 1, 2005, pp. 5–7.

ATOMIC STRUCTURE AND NONELECTRONIC PROPERTIES OF SEMICONDUCTORS

Effect of the Parameters of Sapphire Substrates on the Crystalline Quality of GaN Layers

Yu. N. Drozdov*^, N. V. Vostokov*, D. M. Gaponova*, V. M. Danil'tsev*, M. N. Drozdov*, O. I. Khrykin*, A. S. Filimonov, and V. I. Shashkin***

**Institute for Physics of Microstructures, Russian Academy of Sciences, Nizhni Novgorod, 603950 Russia*
^e-mail: drozdyu@ipm.sci-nnov.ru
***Monokristal Synthetic Corundum Factory, Stavropol, 355044 Russia*
Submitted June 1, 2004; accepted for publication June 14, 2004

Abstract—The effect of certain types of sapphire substrate treatment on the properties of gallium nitride layers grown by metal–organic vapor-phase epitaxy is investigated. © *2005 Pleiades Publishing, Inc.*

1. INTRODUCTION

Substrates of α-Al_2O_3 *c*-plane sapphire are widely used for growing the wurtzite phases of GaN, AlN, InN, and their solid solutions, which are important materials in modern microelectronics. Under the conditions of a large layer–substrate lattice mismatch, the region of optimal growth parameters is rather narrow and very difficult to detect. One of the parameters of a substrate is its quality. The difficulty is that we cannot change this parameter for a given substrate, and it is necessary to prepare a special experimental series of substrates for investigation. For this reason, there are few studies in this field. For example, it was shown in [1] that a misorientation angle of 0.25° between the cut and crystallographic plane is optimal if GaN is grown on an *a*-plane sapphire substrate.

The preparation of substrates is a complicated technological process, whose physics, to the best of our knowledge, has not been investigated. For example, it was recently revealed [2] that the dislocation structure of a 2-μm scratch on sapphire gradually relaxes on contact with air over the course of one month. In recent years, the technology of substrate treatment has advanced greatly due to the use of atomic-force microscopy for monitoring. As a result, substrates with a surface roughness of 1 Å have become an ordinary commercial product.

The purpose of this study is to compare substrates in relation to their parameters and their effect on the quality of GaN layers. Using the production potential of the Monokristal synthetic corundum factory, we prepared several series of substrates with the set of misorientation angles (0.1°, 0.2°, 0.3°, 0.4°, and 0.5°) between the cut and the (0001) crystallographic plane. We used three types of substrates with different concentrations of small-angle boundaries and two types of sample annealing (low- and high-temperature annealing) between the cutting and polishing operations.

The substrates and layers were investigated by atomic-force probe microscopy (Solver P4, NT MDT) and X-ray diffraction analysis (DRON-4). In addition, the depth composition of the layers was determined by secondary-ion mass spectrometry (SIMS) (Shipovnik-3 mass spectrometer). Photoluminescence spectra were excited by a He–Cd laser with a wavelength of 325 nm.

2. INVESTIGATION OF SUBSTRATES

Atomic-force microscopy (AFM) measurements of the substrate surface were performed for one wafer in each series (see table). It can be seen that the face surface roughness measured in a field of 0.5×0.5 μm^2 does not exceed 0.2 nm and, in most cases, is somewhat lower for the substrates annealed at low temperatures. Figures 1 and 2 show the AFM images for two samples. One difference is that, in the case of high-temperature

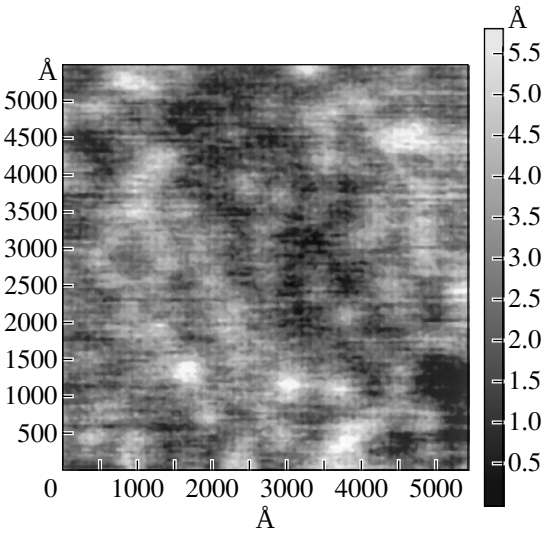

Fig. 1. AFM image of the surface of substrate BN024.

1063-7826/05/3901-0001$26.00 © 2005 Pleiades Publishing, Inc.

Comparative characteristics of sapphire substrates

Series	Substrate type				Comparison of GaN layers		
	Δ, minutes of arc	*M*	*T*	*R*, nm	⟨*F*⟩	σ	*n*
BN006	6	Absent	Low	0.10	+0.17	0.72	4
BV006	6	″	High	0.13	–0.03	0.69	4
BN012	12	″	Low	0.07	–0.14		1
BV012	12	″	High	0.04	+0.23	0.26	6
BN018	18	″	Low	0.13			
BV018	18	″	High	0.14	+0.23	0.17	5
BN024	24	″	Low	0.06			
BV024	24	″	High	0.13	–0.28	0.47	4
BN030	30	″	Low	0.07			
BV030	30	″	High	0.18	–0.14		1
SN006	6	Poorly pronounced	Low	0.07	+0.12		1
SV006	6	″	High	0.12	0.0		1
SV018	18	″	High	0.17			
MN006	6	Clearly pronounced	Low	0.05	–0.36		1
MV006	6	″	High	0.11			
Standard	6	Absent		0.10	(reference)		

Note: Δ is the deviation of the substrate cut from the (0001) plane, *M* indicates the presence of small-angle boundaries, *T* is the temperature of the annealing of a wafer after cutting, *R* is the surface roughness according to the AFM data, ⟨*F*⟩ is the average relative difference between the rocking-curve width for the (0004)GaN layer and the layer on a standard substrate (see Eq. (1)); σ is the variance of ⟨*F*⟩, and *n* is the number of experiments.

annealing, higher hills are formed on the surface. Many images show clear steps separated by terraces. These steps are related to the vicinal structure of the wafer surface cut off with a deviation from an atomic plane. As the deviation angle increases, the width of a terrace (atomic plane) regularly decreases.

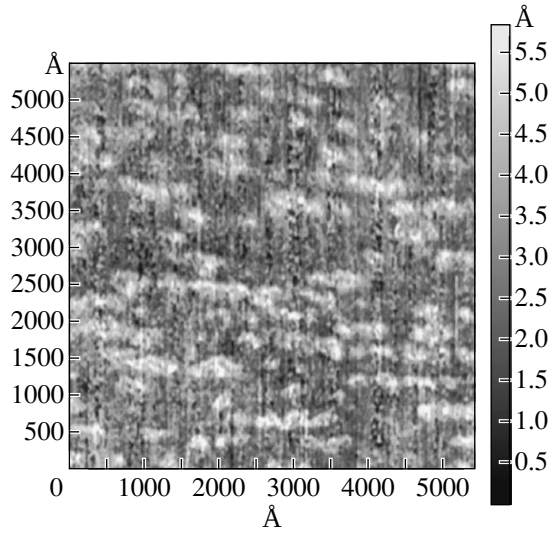

Fig. 2. AFM image of the surface of substrate BV024.

The difference between the X-ray diffraction rocking curves of wafers from different series was insignificant due to the large penetration depth of X-rays in the crystal matrix and the bulk nature of the diffraction-pattern formation.

3. GROWTH OF GaN EPITAXIAL LAYERS

GaN and AlN epitaxial layers were grown by metal–organic vapor-phase epitaxy (MOVPE) in a vertical quartz reactor with the inductive heating of a substrate. Trimethylgallium, trimethylaluminum, and ammonia served as Ga, Al, and N sources, respectively. Hydrogen was used as a carrier gas.

After the preliminary procedures of high-temperature annealing and nitridization of the substrate surface, we grew an AlN or GaN buffer layer ~20 nm thick. Lastly, the buffer layer was annealed, and the basic GaN layer was deposited at a temperature of 1000 to 1100°C.

4. COMPARATIVE ANALYSIS OF LAYERS

According to the X-ray diffraction data, the epitaxial films are mosaic single crystals of the hexagonal modification of α-GaN(0001). The θ/2θ-scanning spectra contain only peaks from the substrate and the epitaxial layer. The rocking-curve width for GaN(0004) grown with the current level of technology is FWHM =

0.06°, which, according to the data in the literature, corresponds to the crystal quality appropriate for most applications [3].

The SIMS data indicate that a GaN layer is homogeneous throughout its thickness. However, we should note the presence of a strong diffusion of aluminum from the buffer AlN sublayer in structures with this type of sublayer.

Direct comparison of the quality of the substrates' GaN layers was impossible because the parameters varied from process to process during the development of the regimes. For this reason, a reference method was used. In each experiment, two substrates were used: one from the series under investigation and the other from the same set in all the experiments. The reference substrates had a certain standard quality and made it possible to compare the experimental sets of substrates with each other. As a numerical parameter, we used the relative difference in the widths of X-ray diffraction rocking curves of the GaN(0004) layers on two substrates

$$F = 2(\mathrm{FWHMs} - \mathrm{FWHM})/(\mathrm{FWHMs} + \mathrm{FWHM}), \quad (1)$$

where FWHMs is the rocking-curve width for GaN(0004) on the reference substrate. Having the set of values for F in a series, we calculated the average value of $\langle F \rangle$ and the variance σ.

The results listed in the table show that a statistically significant decrease in $\langle F \rangle$ was observed only for substrates BV018 with a cut deviation of 0.3°. In other cases, we observed either an increase or a decrease, which, however, did not exceed the variance. The photoluminescence line intensity varied significantly over the layer surface, which made it impossible to distinguish the layers in this parameter. The table also shows that the statistics could not be collected for all the series. In addition, the FWHM decreased during the experiments from 1° to less than 0.1°, which affected the value of variance. The procedure for comparing the substrates is likely to be more correct under the conditions of a well developed process where the fine tuning of the parameters for each type of substrate is completed individually. It is difficult to single out the effect of the substrate because the growth conditions for the buffer sublayer significantly affect the GaN-layer quality. According to the published data, the reason is that the buffer, or even several Al monolayers, set the polarity of the growth surface of the subsequent GaN layer. The [0001] direction in the GaN crystal is polar, and the Ga(0001) growth surface yields a more perfect crystal than the N$(000\bar{1})$ surface [4].

It should be noted that the previously performed replacement of old substrates, produced several years ago, with substrates of standard quality resulted in a pronounced improvement in the quality of layers ($F > 0.5$).

5. CONCLUSIONS

In this study, we investigated the effect of certain types of treatment for sapphire substrates on the properties of MOVPE-grown GaN layers.

The roughness of the face surface of the substrates measured by AFM in a field of 0.5×0.5 μm^2 does not exceed 0.2 nm and, in most cases, is somewhat lower for substrates annealed at low temperatures. On many substrates, one can clearly see steps separated by terraces, which are due to the vicinal atomic structure of the wafer surface.

The results of this study show that a statistically significant decrease in the width of X-ray diffraction rocking curves for GaN(0004) layers was obtained for substrates with misorientation angle of 0.3° and without small-angle boundaries, which were annealed after cutting at high temperature. In other cases, we observed either an increase or decrease in the rocking-curve width, which, however, was smaller than its variance.

REFERENCES

1. T. Someya, K. Hoshino, and Y. Arakawa, Appl. Phys. Lett. **79**, 1992 (2001).
2. Yu. G. Nosov and L. I. Derkachenko, Zh. Tekh. Fiz. **73** (10), 139 (2003) [Tech. Phys. **48**, 1354 (2003)].
3. R. Dimitrov, M. Murphy, J. Smart, *et al.*, J. Appl. Phys. **87**, 3375 (2000).
4. D. H. Lim, K. Xu, S. Arima, *et al.*, J. Appl. Phys. **91**, 6461 (2002).

Translated by V. Bukhanov

Semiconductors, Vol. 39, No. 1, 2005, pp. 100–102. Translated from Fizika i Tekhnika Poluprovodnikov, Vol. 39, No. 1, 2005, pp. 112–114.

LOW-DIMENSIONAL SYSTEMS

Special Features of Structural Interaction in (AlGaIn)N/GaN Heterostructures Used as Dislocation Filters

I. P. Soshnikov*^, N. N. Ledentsov*, A. F. Tsatsul'nikov*, A. V. Sakharov*, W. V. Lundin*, E. A. Zavarin*, A. V. Fomin*, D. Litvinov, E. Hahn**, and D. Gerthsen****

**Ioffe Physicotechnical Institute, Russian Academy of Sciences, St. Petersburg, 194021 Russia*

^e-mail: Ipsosh@beam.ioffe.ru

***University of Karlsruhe, Karlsruhe, Germany*

Submitted June 1, 2004; accepted for publication June 16, 2004

Abstract—The behavior of threading dislocations in AlGaN and InGaN layers incorporated into GaN-based heterostructures is studied. It is shown that InGaN layers with an intermediate composition can be used as the most effective dislocation filters. Estimations of the stresses generated by dislocations and nanodomains show good agreement between the theory and experiment. © *2005 Pleiades Publishing, Inc.*

1. INTRODUCTION

Heterostructures based on GaN are the most important components of optoelectronic devices designed for the blue–green and ultraviolet regions of the spectrum [1–5]. However, the development of these devices is restricted owing to the problem of the high density of threading dislocations in the structures [4–6], which represent an effective channel for the nonradiative recombination of electron–hole pairs.

Several types of filters for threading dislocations are known. In particular, they can be formed using lateral epitaxial overgrowth (LEO) [6, 7], or, alternatively, we can use AlGaN/GaN superlattices [8, 9] to serve as the filters under consideration. However, the dislocation filters based on the AlGaN/GaN superlattices exhibit a low efficiency and poorly restrict the growth of threading dislocation, which is apparently caused by the extent (spread) of heteroboundaries when the superlattices are grown by metal-organic chemical-vapor deposition (MOCVD). The technology of dislocation filters (DFs) based on the LEO structures also encounters serious problems related to growth; in particular, it is necessary to terminate the growth and form the intermediate layers in another chamber. Amano and Akasaki [6] studied the effect of the temperature of GaN growth on the formation of dislocations and showed that the aforementioned filters can lead to the annihilation of a fraction of the dislocations if the density of the latter is high. At the same time, it is known, for the case of heterostructures that are formed from GaAs and include InGaAs nanoinclusions [10] or are formed of Si with SiGe nanoinclusions [11], that dislocation filters based on layers with nanoinclusions can produce good results if the lattice parameter of the material of nanoinclusions differs widely from that of the matrix. However, the formation of dislocation filters based on heterostructures with InGaN layers and/or on a combination of a DF based on AlGaN layers and superlattices have been studied inadequately so far. Therefore, in this paper, we report the results from studying the behavior of threading dislocations in various combinations of the layers incorporated into the (AlGaIn)N/GaN heterostructures grown by MOCVD.

2. EXPERIMENTAL

Experiments with the growth of heterostructures were performed using an AIXTRON AIX 2000/HT system. We used conventional polished sapphire wafers as substrates. The sequence of layers in the grown heterostructure is shown in Fig. 1 and includes GaN layers, a layer of the main dislocation filter, and two $Al_{0.18}Ga_{0.82}N$/GaN (8/300 nm) layers. The grown series of heterostructures includes various combinations of the (AlGaIn)N layers, including separate (separated)

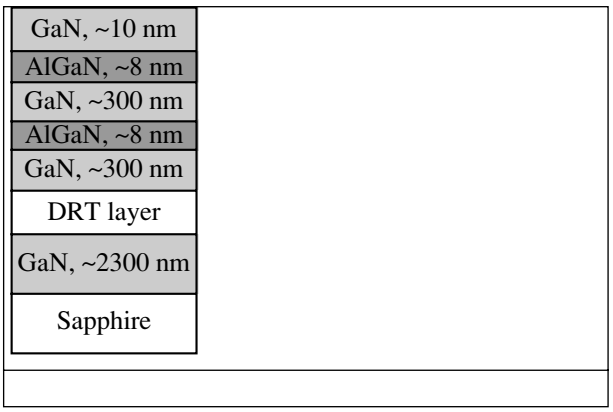

Fig. 1. A generalized schematic representation of grown heterostructures. DRT stands for defect reduction technique.

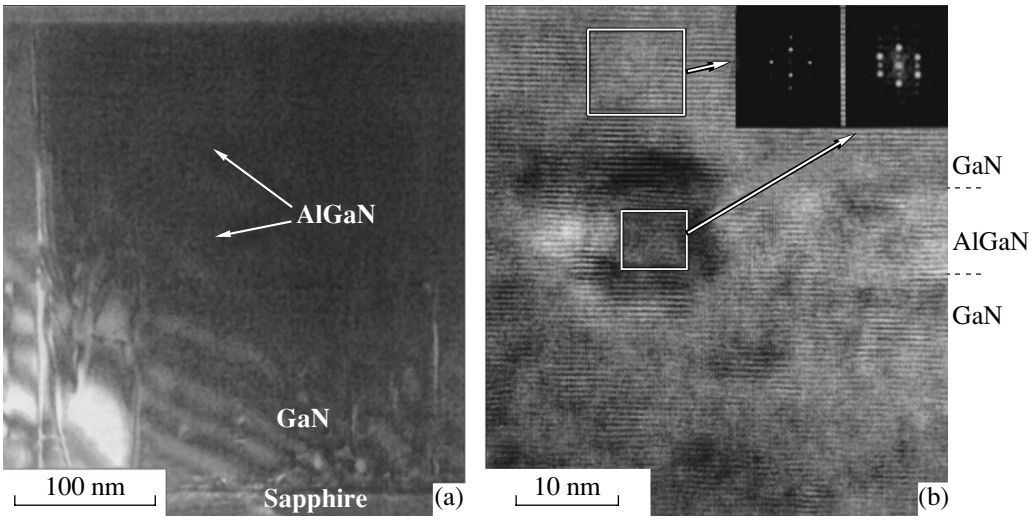

Fig. 2. (a) The dark-field and (b) high-resolution electron-microscopic images of the $(11\bar{2}0)$ cross section of a sample with AlGaN layers in the GaN matrix.

AlGaN and InGaN with different compositions. It is worth noting that, in this series, we used InGaN and AlGaN layers that had a graded composition and were grown at a comparatively low temperature using an interruption in the growth. In addition, we tested a method for overgrowing the InGaN layer with an GaN layer at a low rate, which ensured an efficient migration of adatoms over the surface. It is noteworthy that the total indium concentration in the layers was retained an almost constant level.

The structural characterization of the samples was attained by transmission electron microscopy (TEM) using a Philips CM200FEG microscope. The samples were prepared for study with TEM according to the conventional procedure that included etching with 4-keV Ar^+ ions at the final stage. The images obtained were processed using a DiAnaTEM software package [12].

3. RESULTS AND DISCUSSION

Our studies show that the threading dislocations penetrate through the (AlGa)N layers in the samples containing these layers (Fig. 1). In addition, the formation of nanoinclusions whose characteristic sizes are in the order of 10 nm is observed in the (AlGa)N layers. The Fourier transforms of the high-resolution images of the main lattice and a nanoinclusion are shown in the insets in Fig. 2. A comparison of the obtained Fourier transforms shows that the nanoinclusions have the cubic structure of a sphalerite type.

A study of heterostructures with InGaN layers that have different thickness and composition shows that the most efficient dislocation filter is attained if the InGaN layer with an indium content amounting to $x \approx 0.10$ is deposited (Fig. 3). In this case, the formation of InGaN nanodomains is observed at the upper boundary of the threading dislocations.

An increase in the indium content of the layer to $x \approx 0.2$–0.3 gives rise to the inverse effect: large nanodomains highly enriched with indium are observed. These nanodomains can produce new defects.

The stresses generated by threading dislocations can be estimated from the formula [13, 14]

$$\tau_{\text{eff}} = S\varepsilon\left[\frac{2G(1+\nu)}{1-\nu}\right]$$

$$-\left(\ln\frac{\beta h}{b}+1\right)\frac{Gb(1-\nu\cos^2\alpha)\cos\phi}{4\pi h(1-\nu)},$$

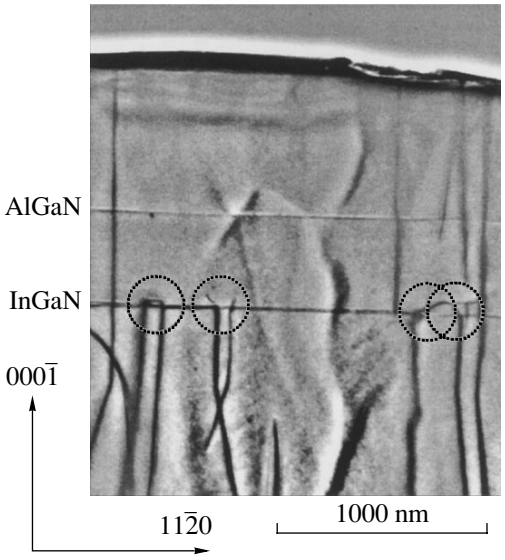

Fig. 3. A (2200) dark-field electron-microscopic image of the $(11\bar{2}0)$ cross section for a sample containing an InGaN layer with an In content amounting to $x \approx 0.1$.

where G is the shear modulus, b is the Burgers vector, L is the dislocation length, and ν is the Poisson ratio.

The stresses induced by the InGaN nanoinclusions can be estimated in terms of the Treacy–Gibson concepts [15, 16]. A comparison of the stresses induced by dislocations with those induced by InGaN nanoinclusions shows that these particular stresses become equal to each other at some intermediate (critical) content of In. If the In content is higher than this critical value, the stresses induced by InGaN nanodomains exceed those induced by dislocations. As a result, new dislocations are generated.

4. CONCLUSION

We studied the behavior of threading dislocations in the AlGaN and InGaN layers incorporated into the heterostructures based on GaN.

We showed that nanoinclusions of a cubic phase with characteristic sizes in the order of 10 nm are formed in the AlGaN layers. The AlGaN/GaN heterostructures exhibit a low efficiency when used as dislocation filters.

It is shown that the most effective filtering of dislocations is observed in InGaN layers with an In content in the order of 10%. An increase in the effective In content in the InGaN layers leads to the generation of new dislocations.

A comparison of the stresses induced by threading dislocations with those induced by InGaN layers shows that the dislocation filter is most effective if these two types of stresses are equal to each other.

ACKNOWLEDGMENTS

This study was supported by the Russian Foundation for Basic Research, and a program of scientific cooperation between the Ioffe Physicotechnical Institute and the Industrial Technology Research Institute.

REFERENCES

1. S. Nakamura, G. Fasol, and S. J. Pearton, *The Blue Laser Diode: the Complete Story*, 2nd ed. (Springer, Berlin, 2000).
2. S. Nakamura, Proc. SPIE **3749**, 2 (1999).
3. I. L. Krestnikov, N. N. Ledentsov, A. Hoffmann, *et al.*, Phys. Rev. B **66**, 155310 (2002).
4. X. Hu, J. Deng, N. Pala, *et al.*, Appl. Phys. Lett. **82**, 1299 (2003).
5. M. S. Shur, A. D. Bykhovski, R. Gaska, *et al.*, Appl. Phys. Lett. **76**, 3298 (2000).
6. H. Amano and I. Akasaki, Opt. Mater. **19**, 219 (2001).
7. H. Marchand, X. H. Wu, J. P. Ibbetson, *et al.*, Appl. Phys. Lett. **73**, 747 (1998).
8. D. Huang, M. A. Reshchikov, F. Yun, *et al.*, Appl. Phys. Lett. **80**, 216 (2002).
9. M. D. Craven, S. H. Lim, F. Wu, *et al.*, Appl. Phys. Lett. **81**, 1201 (2002).
10. E. Bellet-Amalric, C. Adelmann, E. Sarigiannidou, *et al.*, J. Appl. Phys. **95**, 1127 (2004).
11. Yu. B. Bolkhovityanov, O. P. Pchelyakov, L. V. Sokolov, and S. I. Chikichev, Fiz. Tekh. Poluprovodn. (St. Petersburg) **37**, 513 (2003) [Semiconductors **37**, 493 (2003)].
12. I. P. Soshnikov, O. M. Gorbenko, A. O. Golubok, and N. N. Ledentsov, Fiz. Tekh. Poluprovodn. (St. Petersburg) **35**, 361 (2001) [Semiconductors **35**, 347 (2001)].
13. J. W. Matthews and A. E. Blackeslee, J. Cryst. Growth **27**, 11 (1974).
14. D. C. Houghton, J. Appl. Phys. **70**, 2136 (1991).
15. M. M. J. Treacy and J. M. Gibson, J. Vac. Sci. Technol. B **4**, 1458 (1986).
16. D. Gerthsen, E. Hahn, B. Neubauer, *et al.*, Phys. Status Solidi C **0**, 1668 (2003).

Translated by A. Spitsyn

Semiconductors, Vol. 39, No. 1, 2005, pp. 103–106. Translated from Fizika i Tekhnika Poluprovodnikov, Vol. 39, No. 1, 2005, pp. 115–117.

LOW-DIMENSIONAL SYSTEMS

Lateral Photoconductivity of AlGaAs/InGaAs Structures with Quantum Wells and Self-Organized Quantum Dots Under Interband Illumination

O. A. Shegai^, A. K. Bakarov, A. K. Kalagin, and A. I. Toropov

Institute of Semiconductor Physics, Siberian Division, Russian Academy of Sciences, pr. Akademika Lavrent'eva 13, Novosibirsk, 630090 Russia

^e-mail: shegai@thermo.isp.nsc.ru

Submitted June 1, 2004; accepted for publication June 16, 2004

Abstract—The results of studying the special features of the dependence of lateral photoconductivity in AlGaAs/InGaAs structures with quantum dots and quantum wells on the intensity of interband light at low temperatures are reported. It is found that there is a threshold for the increase in photoconductivity. Oscillations of photoconductivity are observed at relatively high pulling fields. The effects of the pulling field and temperature on the photoconductivity are studied. The results are analyzed in terms of the theory of percolation of nonequilibrium charge carriers over localized states, taking into account the relaxation of stresses around quantum dots.

1. INTRODUCTION

Studies of the mechanisms of lateral interband photoconductivity in AlGaAs/InGaAs structures with self-organized InGaAs quantum dots (QDs) and quantum wells (QWs) are important as these structures can be used in the fabrication of new devices [1]. In the structures under consideration, the energy-band diagram is of type 1, where the region within a QD (or a QW) represents a well for both electrons and holes. It initially seems that nonequilibrium charge carriers generated by interband excitation should be trapped at the states in a QD (or a QW) and then recombine radiatively, which should not give rise to any special features in the interband photoconductivity. However, the nonuniform distribution of stresses around a QD, as was recently shown for Si/Ge structures with Ge QDs [2, 3], can affect photoconductivity in AlGaAs/InGaAs structures (the Si/Ge structures have an energy-band diagram of type 2 [2, 3]).

In this paper, we report the experimental results from studying the special features of the dependence of the lateral photoconductivity in AlGaAs/InGaAs structures with QDs and QWs on the intensity of interband light at low temperatures. We observed a stepwise increase in, as well as oscillations of, the photoconductivity in the structures under consideration. We also studied the effect of the pulling field on the observed special features of the photoconductivity. The results are analyzed using the theory of the percolation of nonequilibrium charge carriers over localized states, taking into account the relaxation of stresses around a QD.

2. RESULTS AND DISCUSSION

The structures with QDs were obtained using molecular-beam epitaxy and according to the Stranski–Krastanov self-organization mechanism: a buffer AlGaAs layer was grown first on a substrate of semi–insulating GaAs (001), an InGaAs layer with a nominal thickness of 2.5 monolayers (ML) was then grown at a temperature of 510°C, and finally another AlGaAs layer was grown and was then overgrown with a 20-nm-thick GaAs surface layer. The QD concentration was $\sim 10^{10}$ cm^{-2}, and the lateral size of the QDs ranged from 30 to 40 nm. QWs were also grown in some of the structures with QDs. In those structures, the sizes of the GaAs QWs were 8.5 and 5 nm and they were separated by a 25-nm-thick AlGaAs layer.

The area of the studied samples was 2×4 mm^2; the illuminated area was $\sim 2 \times 2$ mm^2. Ohmic contacts to the structures were formed of indium using the conventional procedure. The photoconductivity was measured at low temperatures using a red light-emitting diode as the source of interband photoexcitation (previously described in more detail in [3]).

In Fig. 1, we show the dependences of the lateral photoconductivity in AlGaAs/GaAs structure 477, which has two QWs with widths of 8.5 and 5 nm separated by a 25-nm-thick AlGaAs layer, on the interband-light intensity I at $T = 4.2$ K and at various values of the pulling voltage U. In the region of small values of I, an increase in the photoconductivity is observed as I increases, starting with a certain threshold intensity I_{th}. As the voltage U increases, the slope of the photoconductivity curves increases, attains a maximum at $U \approx 12$ V,

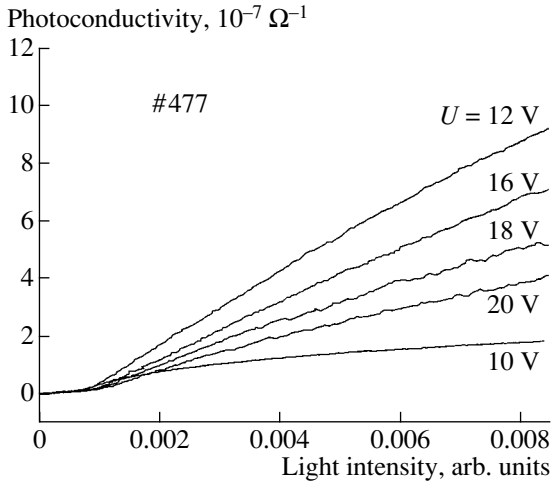

Fig. 1. Dependences of the lateral photoconductivity on the intensity of interband light for an AlGaAs/GaAs structure that has two quantum wells with widths of 8.5 and 5 nm separated by a 25-nm-thick AlGaAs layer. The dependences were measured at T = 4.2 K and at several values of the pulling voltage U in a range from 10 to 20 V.

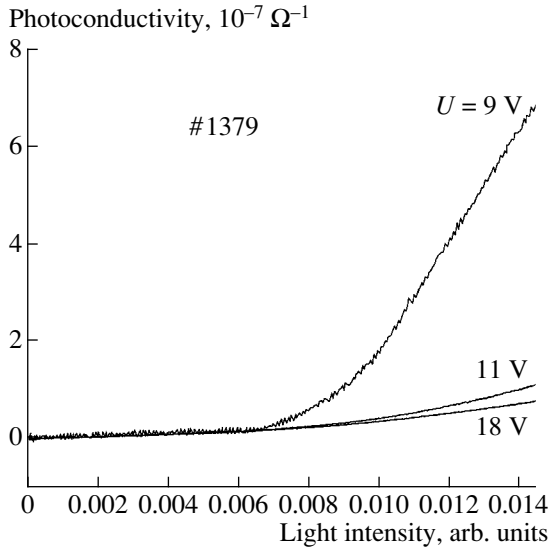

Fig. 2. Dependences of the lateral photoconductivity on the intensity of interband light for a structure with a single InAs quantum-dot layer in the AlAs matrix at several values of the pulling voltage U = 9–18 V. The dependences were measured at T = 4.2 K.

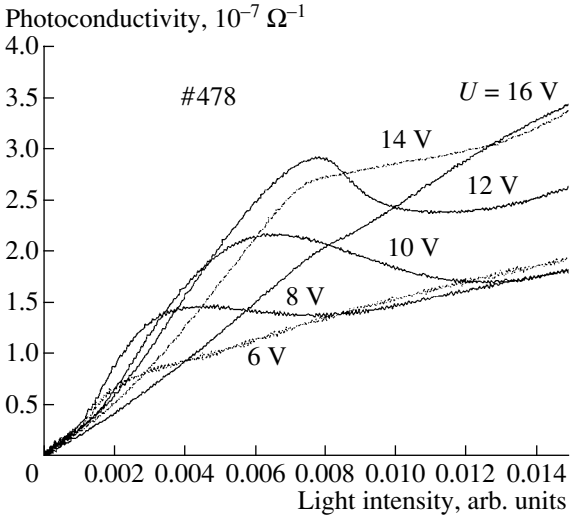

Fig. 3. Dependences of the lateral photoconductivity on the intensity of interband light for a structure with an InGaAs quantum dot and two GaAs quantum wells in the AlGaAs matrix at various values of the pulling voltage. The dependences were measured at T = 4.2 K.

and then decreases. It is noteworthy that the value of I_{th} depends on U only slightly, in contrast to what was observed in the case of Ge QDs [3].

In Fig. 2, we show the dependences of lateral photoconductivity in AlAs/InAs structure 1379, which has a single InAs QD layer, on the interband-light intensity I at T = 4.2 K and at several values of the pulling voltage U. It can be seen that the threshold increase in the photoconductivity sets in at an I_{th} that is much larger (approximately, by an order of magnitude) than the I_{th} for the structure with QWs (Fig. 1). As U increases, the slope of the photoconductivity curves decreases. The value of I_{th} is also almost independent of U.

In Fig. 3, we show the dependences of lateral photoconductivity in AlGaAs/InGaAs structure 478, which has an InGaAs QD and two GaAs QWs in the AlGaAs matrix, on the interband-light intensity I at T = 4.2 K and at U in the range 6 to 16 V. It can be seen from Fig. 3 that, as U increases, a peak in the photoconductivity curves appears and increases in magnitude. This peak shifts gradually to the region of higher intensities and then disappears as U increases to 16 V. In our opinion, the descending portion of the photoconductivity curve is of particular interest here. It is noteworthy that, in the photoconductivity curve measured for bulk GaAs, only a steady increase is observed in the photoconductivity as the interband-light intensity is increased.

For sample 477, the photoconductivity signal becomes nonsteady as U increases, and oscillations appear in the dependence of photoconductivity on I at voltages higher than about 50 V, as shown in Fig. 4. It can be seen that these oscillations appear starting with a certain light intensity and that the period in which they occur increases with increasing U and decreases with increasing I. As the rate of increase in the light intensity was varied, the period of oscillations varied as well, but they were preserved at a certain fixed intensity of illumination of the structures. This means that the observed oscillations of photoconductivity occur over time. Similar oscillations of photoconductivity in the region of large values of U were also observed for some structures with QDs. An increase in

the measurement temperature leads to the disappearance of the threshold behavior of photoconductivity and to a decrease in the period of oscillations until the point of their complete disappearance.

The results obtained were analyzed in the context of the percolation theory [4]. We will relate the stepwise increase in photoconductivity in the structures with QDs to fluctuations of the QD thickness in the structure plane [5]. The consequence of these fluctuations is a broadening of the dimensional-quantization levels in a QD and formation of localized states in the regions where the fluctuation in the QD thickness attains a maximum. As the light intensity increases, the occupancy of these localized states also increases, and at $I = I_{th}$, the nonequilibrium charge carriers in these states reach the percolation level. A numerical analysis for $I > I_{th}$ shows that the photoconductivity signal for the structures with QDs increases according to the power law $(I - I_{th})^p$, where the exponent p is equal to 0.5 at U = 10 V and increases steadily as U increases.

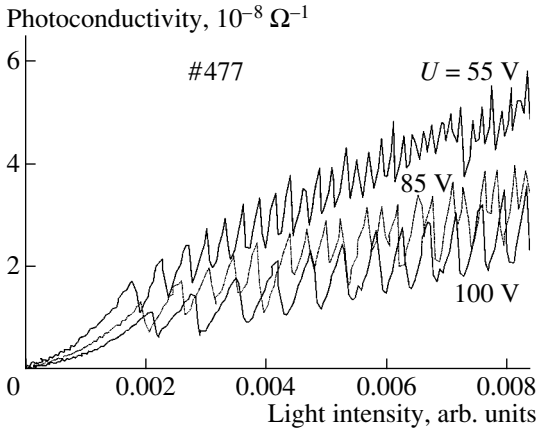

Fig. 4. Dependences of the lateral photoconductivity on the intensity of interband light for a structure that has two GaAs quantum wells with widths of 8.5 and 5 nm separated by a 25-nm-thick AlGaAs layer. The dependences were measured at T = 4.2 K and U = 55, 85, and 100 V.

The dependence of the photoconductivity signal on I when I is approximately equal to I_{th} also follows the power law for structure 1379; however, the exponent exceeds unity at U = 9 V. This exponent was previously found to be equal to ~1.4 for the structures with Ge QDs and was identified as the critical index t in the percolation theory [3].

The fact that the structure with QDs has an appreciably larger value of the threshold light intensity than the structure with QWs, indicates that the profile induced by stressed QDs exceeds that induced by fluctuations in the QW thickness. It is also noteworthy that the threshold behavior of photoconductivity was not observed for a number of structures with QWs. This observation indicates that the thickness fluctuations are insignificant in these structures.

We now relate the origin of the oscillations in the photoconductivity signal to the behavior of localized charge carriers in the vicinity of the percolation threshold. A more careful consideration shows that the photoconductivity oscillations are asymmetric; i.e., a steady increase in the photoconductivity signal occurs first and the then it decreases abruptly. At small values of U, the recombination of electrons and holes in localized states reduces the occupancy of these states so that the oscillations are not observed. At large values of U, the nonequilibrium charge carriers of opposite signs become separated; as a result, the recombination is suppressed. At a fixed value of I, the evolution of the accumulation of electrons and holes in the localized states under consideration occurs as long as these states do not intersect, in which case the recombination is resumed, which manifests itself in a drastic decrease in the photoconductivity signal. The repetition of this cyclic process leads to the observed oscillations in photoconductivity. An increase in the period of oscillations as U increases is the result of an increase in the spatial separation of electrons and holes in localized states. A decrease in the period of oscillations in conjunction with an increase in illumination intensity is accounted for by a rise in the concentration of nonequilibrium charge carriers, which leads to a faster occupation of the localized states. An increase in the measurement temperature leads to an increase in the frequency of photoconductivity oscillations; as a result, the oscillations disappear completely at a certain temperature. In this case, the thermal energy of electrons in localized states becomes larger than the barrier height, and charge carriers are insensitive to the profile related either to fluctuations in the QW thickness in the structures with QWs or to the relaxation of stresses around QDs in the structures with QDs; as a result, oscillations disappear.

Both QDs and QWs are incorporated into structure 478. The threshold-type increase in the photoconductivity signal for this structure occurs at a small value of I_{th} (Fig. 3), as in the case of structure 477 with QWs (Fig. 1), which can be related to fluctuations in the QW thickness in the structure. However, a portion of the steady decrease in the photoconductivity signal with increasing I is apparently caused by a decrease in the number of charge carriers in localized states as a result of the tunneling of the carriers to the dimensional-quantization levels in a QD.

Thus, we find that lateral photoconductivity in the AlGaAs/GaAs structures with GaAs QWs and in AlGaAs/InGaAs structures with self-organized InGaAs QDs depends in a thresholdlike manner on the intensity of interband light. We observed oscillations in the interband-excited photoconductivity in the region of relatively high pulling fields. These special features are accounted for using the model of percolation of nonequilibrium charge carriers over localized states.

ACKNOWLEDGMENTS

This study was supported by the Russian Foundation for Basic Research, project no. 03-02-16466.

REFERENCES

1. V. A. Shchukin and D. Bimberg, Rev. Mod. Phys. **71**, 1125 (1999).
2. O. A. Shegaĭ, K. S. Zhuravlev, V. A. Markov, *et al.*, Fiz. Tekh. Poluprovodn. (St. Petersburg) **34**, 1363 (2000) [Semiconductors **34**, 1311 (2000)].
3. O. A. Shegai, V. A. Markov, A. I. Nikiforov, *et al.*, Phys. Low-Dimens. Semicond. Struct., Nos. 1–2, 261 (2002).
4. B. I. Shklovskiĭ and A. L. Éfros, *Electronic Properties of Doped Semiconductors* (Nauka, Moscow, 1979; Springer, New York, 1984).
5. V. A. Gaĭsler, D. A. Ténné, N. T. Moshegov, *et al.*, Fiz. Tverd. Tela (St. Petersburg) **38**, 2242 (1996) [Phys. Solid State **38**, 1235 (1996)].

Translated by A. Spitsyn

Semiconductors, Vol. 39, No. 1, 2005, pp. 107–112. Translated from Fizika i Tekhnika Poluprovodnikov, Vol. 39, No. 1, 2005, pp. 118–123.

LOW-DIMENSIONAL SYSTEMS

Spin Effects in Magnetoresistance Induced in an n-$In_xGa_{1-x}As$/GaAs Double Quantum Well by a Parallel Magnetic Field

M. V. Yakunin*^, G. A. Al'shanskiĭ*, Yu. G. Arapov*, V. N. Neverov*, G. I. Kharus*, N. G. Shelushinina*, B. N. Zvonkov, E. A. Uskova**, A. de Visser***, and L. Ponomarenko*****

**Institute of Metal Physics, Ural Division, Russian Academy of Sciences, Yekaterinburg, 620219 Russia*

^e-mail: yakunin@imp.uran.ru

***Physicotechnical Research Institute at Lobachevsky State University, Nizhni Novgorod, 603600 Russia*

****Van der Waals–Zeeman Institute, University of Amsterdam, The Netherlands*

Submitted June 1, 2004; accepted for publication June 16, 2004

Abstract—Magnetoresistance in n-$In_xGa_{1-x}As$/GaAs ($x \approx 0.18$) heterostructures with double quantum wells (DQWs) was studied in the magnetic field parallel to the DQW layer. Specific features of the magnetoresistance, related to the passing of the tunnel gap edges across the Fermi level, are revealed and studied. Agreement between the calculated and experimental positions of the observed features is obtained when the spin splitting of the energy spectrum is taken into account. Earlier, similar features were observed in the magnetoresistance of n-GaAs/$Al_xGa_{1-x}As$ DQW heterostructures, but the spin effects did not manifest themselves.

A system of coupled 2D conducting layers, or a double quantum well (DQW), is an object of interest both because of its possible applications (see, e.g., [1]) and the fundamental physics involved [2]. It attracts attention due to the possible existence of collective correlated interlayer states, which give rise to new electronic phases or lead to a broadening of the existing range of phases known in a separate 2D layer [2, 3]. Furthermore, the recent attention given to studies of spin transport (spintronics) has increased the interest in the spin effects of processes in DQWs, and several experiments indicate the existence of nontrivial effects (see, e.g., [4]). We should note that, all over the world, the vast majority of research into DQWs is performed in a GaAs/$Al_xGa_{1-x}As$ heterosystem, because it provides the best quality layers, owing to a minimum lattice mismatch. We have studied the magnetoresistance and Hall effect in a DQW formed in an n-$In_xGa_{1-x}As$/GaAs heterosystem in a magnetic field normal ($B_\perp$) or parallel ($B_\parallel$) to the layers of the structure. In contrast to a GaAs/$Al_xGa_{1-x}As$ system, in which the spin splitting of the conduction band of GaAs is very small, the spin effects in the $In_xGa_{1-x}As$/GaAs system may be much more pronounced. This is because the g-factor of electrons in InAs, which is one of the components of the $In_xGa_{1-x}As$ solid solution that forms the potential well, is larger than in GaAs by a factor of about 35.

The structures under study consist of two $In_{0.18}Ga_{0.82}As$ potential wells, 5 nm in width and separated by a thin GaAs barrier, and of adjacent GaAs side barriers, each containing a Si δ-doped layer separated from the nearest $In_{0.18}Ga_{0.82}As$ layer by an undoped spacer of 19 nm in width. In this study we present the data for two samples, nos. 2981 and 2984, whose parameters are listed in the table: n_s is the total density of the electron gas in two layers; μ, the mobility at low temperatures; Δ_{SAS}, the tunnel gap between the energies of the symmetric and antisymmetric states; and E_F, the Fermi level. The last two quantities, and also the potential profiles of the structures, were obtained using a self-consistent solution of the Schrödinger and Poisson equations in a zero field.

In the magnetic field normal to the structure plane, a clear picture of the quantum Hall effect (Fig. 1) is observed, which corresponds to the complicated structure of DQW levels quantized by the magnetic field. The interest in studies focusing on the magnetic field parallel to the structure plane is related to the fact that it is possible to observe and analyze features in the energy spectrum that are not masked by quantization.

In layers of finite thickness, the effect of the magnetic field parallel to the structure plane $B_\parallel$ consists in the following:

(i) a diamagnetic shift of the quantum-confinement levels E_i so that the spacing between these levels increases;

Table

Sample no.	Barrier width, nm	n_s, 10^{15} m^{-2}	μ, m^2 V^{-1} s^{-1}	Δ_{SAS}, meV	E_F, meV
2981	7	2.05	2.6	7.4	8
2984	3.5	2.34	1.6	23.1	9.5

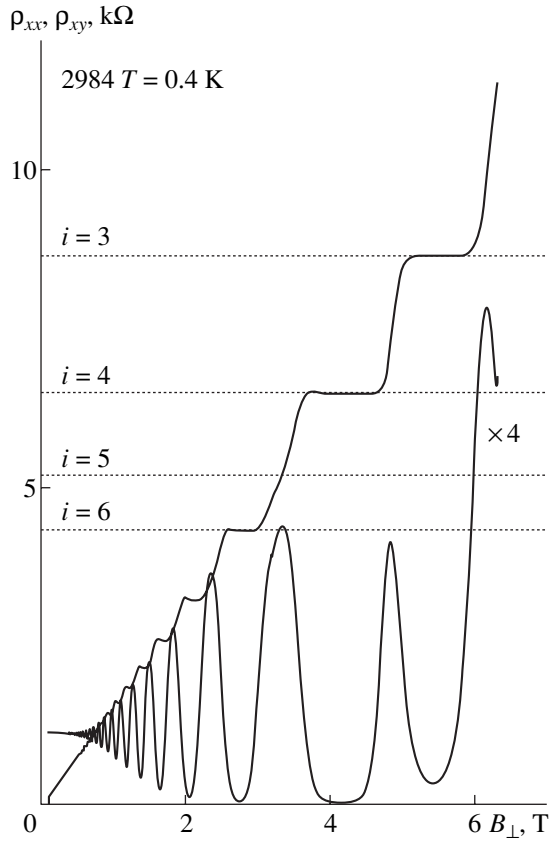

Fig. 1. The quantum Hall effect and magnetoresistance in sample no. 2984.

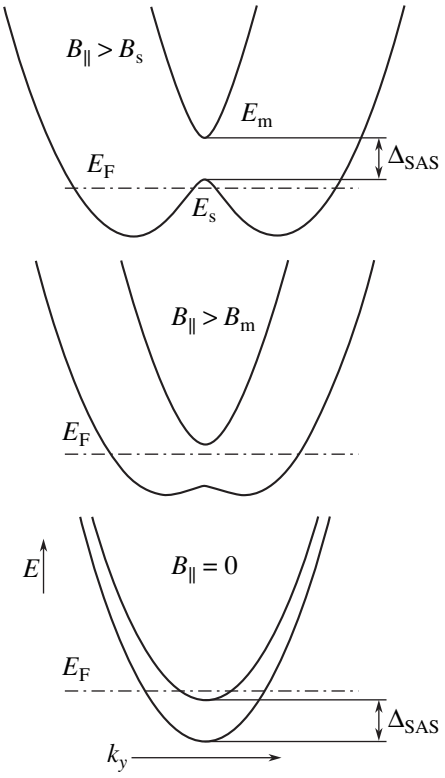

Fig. 2. The evolution of the energy structure of the DQW in the magnetic field $B_\|$ parallel to the structure plane.

(ii) a shift of the constant-energy surfaces $E_i(k_\|)$, $k_\| = (k_x, k_y)$ along the k_y direction [5].

The last factor is important in DQWs, because the energy-dispersion surfaces of the two layers $E_i^{1,2}(k_\|)$ are shifted with respect to each other by $\Delta k_{yi} = eB_\| d_i/\hbar$ (Fig. 2), where d_i is the effective spacing between the centers of mass in layers for the ith subband [6]. Furthermore, we only discuss the processes related to the evolution of the ground subband, so the index i will be omitted. If tunneling between the layers is possible, the level of a separate well in a DQW is split into two levels with symmetric (S) and antisymmetric (AS) wave functions and separated by the tunnel gap Δ_{SAS}. At a relative lateral shift in the k-space of $E^{1,2}(k_\|)$ paraboloids in parallel magnetic field, the gap Δ_{SAS} is bound to the line of their intersection (Fig. 2). As a result, a complex surface of constant energy $E(k_\|)$ is formed in the DQW. It consists of an inner surface with the minimum E_m at $k = 0$, which corresponds to the upper edge of Δ_{SAS}, and an outer surface with a saddle point E_s at $k = 0$, corresponding to the lower edge of the gap. As the magnetic field increases and the paraboloids move farther apart in the k_y direction, the gap is shifted upwards.

As can be seen in the table, initially, in a zero field, the Fermi level E_F in sample no. 2981 lies above the gap Δ_{SAS}. Therefore, in a field B_m the Fermi level will be crossed by the minimum E_m, and after that, in the field $B_s > B_m$, by the saddle point (Fig. 2). As a result, the total density of the states at the Fermi level decreases stepwise at $B_\| > B_m$, and the intersubband transitions will be switched off, which will induce a stepwise decrease or a minimum in the magnetoresistance $\rho(B_\|)$ at $B_\| \approx B_m$. The van Hove singularity in the density of the states is related to the saddle point E_s; this singularity will cause the magnetoresistance maximum in the field $B_\| \approx B_s$. Indeed, in this sample we did observe a minimum and maximum in the magnetoresistance $\rho(B_\|)$ (see Fig. 3). At the same time, in sample no. 2984, which had a barrier two times thinner and, consequently, a significantly wider gap Δ_{SAS}, the Fermi level lay in the gap below the minimum E_m even in a zero field. Therefore, in this case, there is no reason for the formation of a minimum in magnetoresistance at $B_\| \approx B_m$, and only a maximum can exist at $B_\| \approx B_s$, which we did observe in the pulsed magnetic field at about $B_s \approx 30$ T (Fig. 3). Features of this kind were earlier observed in $\rho(B_\|)$, but only in DQWs formed in GaAs/Al$_x$Ga$_{1-x}$As structures [7].

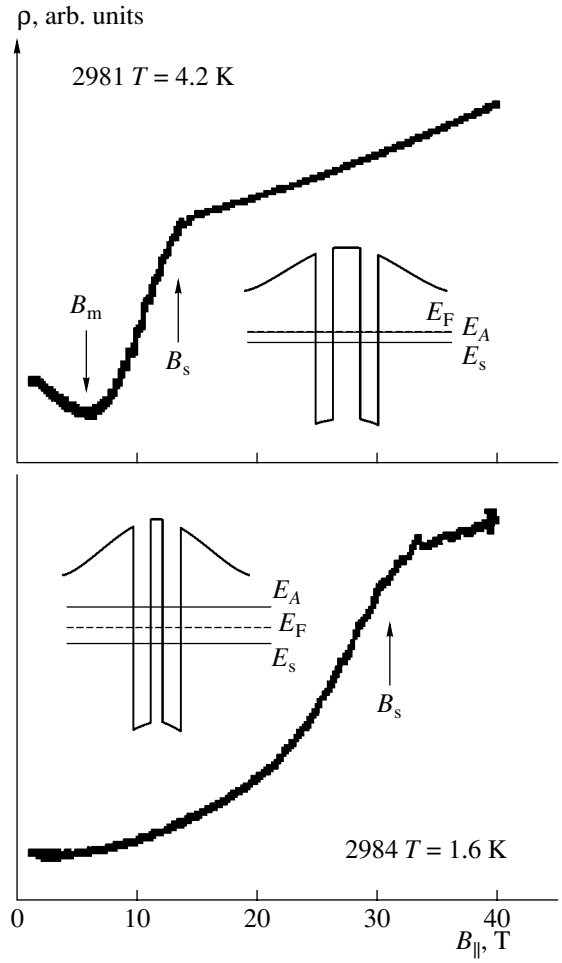

Fig. 3. Resistance $\rho(B_\parallel)$ vs. the intensity of the magnetic field parallel to the structure plane. Insets: calculated potential profiles and energy levels.

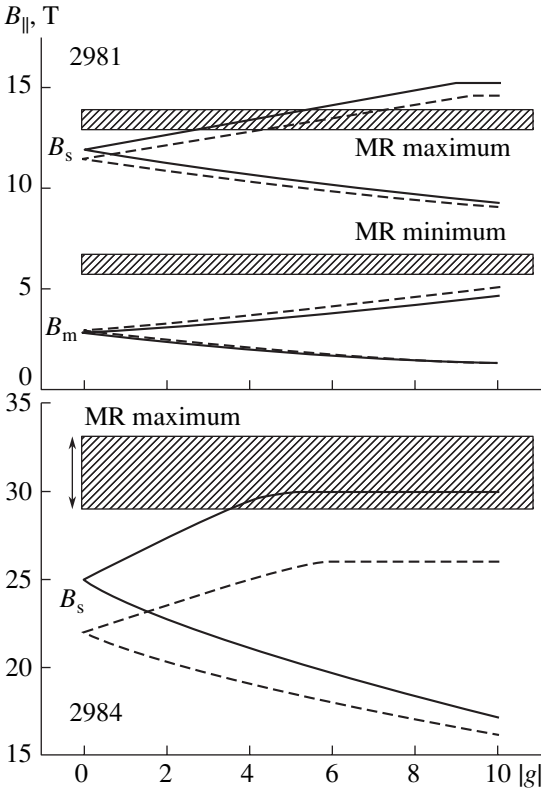

Fig. 4. A comparison of the measured values of $B_\parallel$, corresponding to the maximum and minimum of the magnetoresistance (shaded areas) with the values calculated as functions of the g-factor. The dashed lines represent simplified calculations on the assumption $\langle s|z^2|s\rangle = \langle a|z^2|a\rangle = 0$ [6]; and the solid lines, the data of more precise calculations.

The energy dispersion in the DQW in the parallel field was calculated in terms of a two-level model:

$$E_{1,2} = \frac{\hbar^2(k_x^2 + k_y^2)}{2m} + \frac{H_{ss} + H_{aa}}{2} \pm \frac{1}{2}\sqrt{(H_{ss} - H_{aa})^2 + 4H_{sa}^2}, \quad (1)$$

where

$$H_{ss} = E_s + \frac{m}{2}\omega^2\langle s|z^2|s\rangle,$$

$$H_{aa} = E_a + \frac{m}{2}\omega^2\langle a|z^2|a\rangle,$$

$$H_{sa} = -\hbar\omega k_y\langle s|z|a\rangle,$$

$\omega = eB_\parallel/m$; m is the effective electron mass; $|s\rangle$ and $|a\rangle$, the symmetric and antisymmetric wave functions in the DQW; and E_s and E_a, the lower and upper edges of the gap in the zero magnetic field.

The simplest approximation was used in [6], where the assumption $\langle s|z^2|s\rangle = \langle a|z^2|a\rangle = 0$ was employed. In this case, the gap

$$H_{aa} - H_{ss} = E_a - E_s = \Delta_{SAS}$$

does not vary with the magnetic field. This approximation is sufficiently precise to estimate the magnetic field B_s for sample no. 2981, which has a wide barrier, but is too inaccurate in the case of the wide gap in sample no. 2984, which has a thin barrier (Fig. 4). Calculations made without this approximation show that, in fact, the gap increases as the field increases, and becomes, in a field of 30 T, nearly twice as large as in a zero field (Figs. 5a, 5d).

A comparison between the calculated and experimental positions of the features in the magnetoresistance (Fig. 4, $g = 0$) shows a reasonable agreement for the position of the maximum, B_s, for sample no. 2981, but the position of the minimum, B_m, is underestimated in the calculations. Figure 4 shows the results calculated for infinitely narrow levels.

Our calculations of the total density of the states at the Fermi level, DOS(E_F), as function of the magnetic field $B_\parallel$ show that the broadening of levels dE leads to a

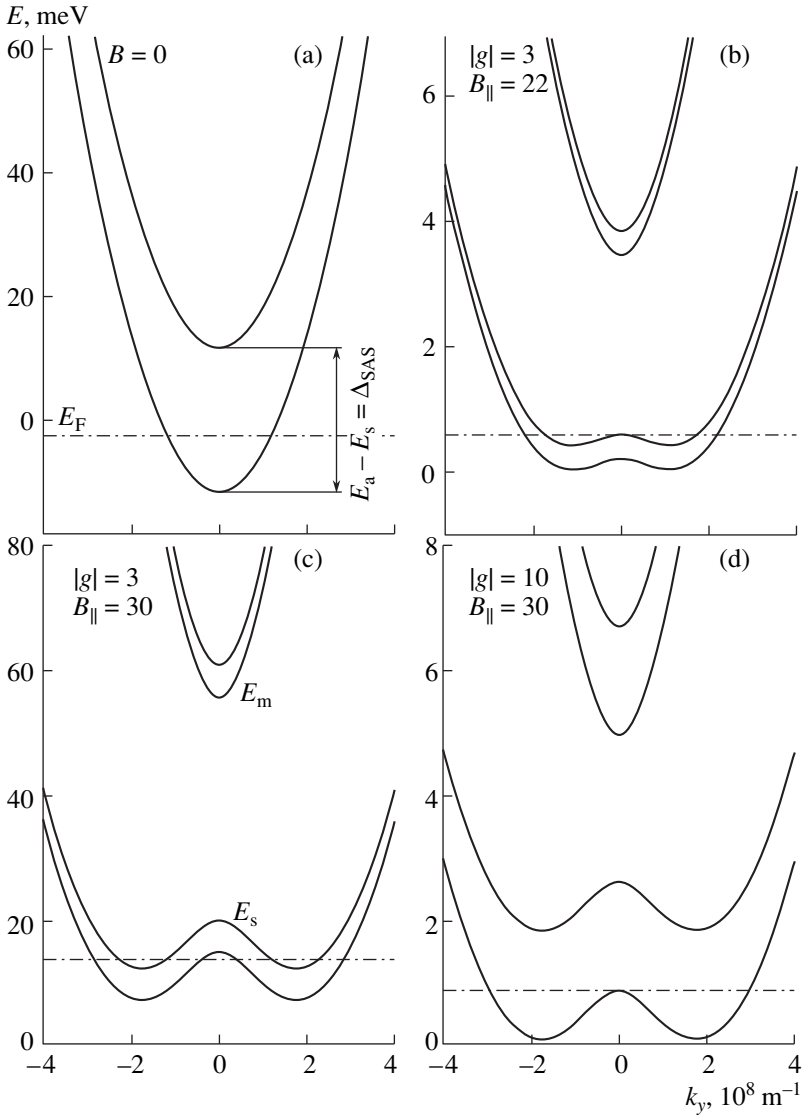

Fig. 5. The energy dispersion in the conduction band along k_y for sample no. 2984, calculated for different values of $B_\parallel$ (in tesla) and the g-factor, denoted in the figure.

considerable shift of the B_m minimum to a higher $B_\parallel$ (Fig. 6a), and the calculated data agree with the experiment. This shift is related to the fact that, in a zero field, the Fermi level lies in the upper subband, in the immediate vicinity of its edge, and is on the verge of departing from it. As the field increases in the range of weak fields, it moves nearly in parallel with the lower spin sublevel. More reliable conclusions follow from an analysis of the magnitude of the field B_s, which is not varied when the levels are broadened.

For sample no. 2984, the calculation of the position of the maximum in $\rho(B_\parallel)$ using the approximate method yields a strongly underestimated magnitude of the field, B_s (see Fig. 4, the point of convergence of dashed lines for sample no. 2984 at $g = 0$). This discrepancy can be noticeably diminished in more precise calculations (see Fig. 4, the point of convergence of solid lines for sample no. 2984 at $g = 0$) but not eliminated. Elimination only becomes possible if the spin splitting of the states is taken into account. In this case, summands $\pm g\mu_B B_\parallel/2$ are introduced into (1), where μ_B is the Bohr magneton (Fig. 4). Then, the calculated value of B_s for the saddle point of the lower spin-split subband agrees with the experiment for a g-factor with $|g| > 3$. The interpolation between InAs and GaAs ($g = -15$ and $g = -0.44$, respectively) yields $g \approx -3$ for $In_{0.18}Ga_{0.82}As$. The spin splitting in our samples is distinctly observed in perpendicular fields (Fig. 1), where it manifests itself even in the field $B_\perp \approx 5$ T as a feature of the quantum Hall effect for the odd integer $i = 3$ at the Hall resistance $\rho_{xy} = h/e^2 i$. The initiation of the state for $i = 5$ in a field of ~3 T can also be seen.

A comparison of Figs. 5b and 5c offers a possible explanation of the fact that the features related to the

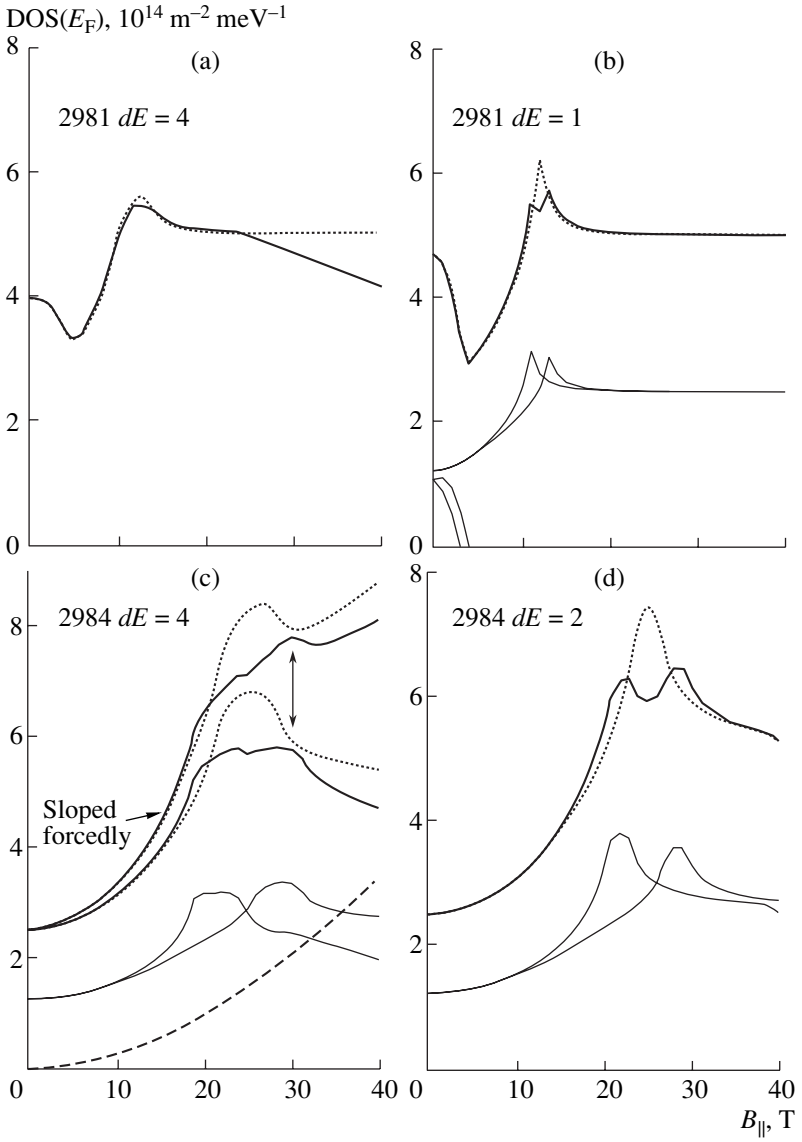

Fig. 6. The density of the states at the Fermi level, DOS(E_F), calculated for (a, b) sample no. 2981 and (c, d) sample no. 2984: g = 3 (solid lines) and g = 0 (dotted lines). The level broadening dE: (a, c) 4, (b) 1, and (d) 2 meV. Thin solid lines represent the result of calculations for separate subbands; and thick lines, the sum of these. An increasing function (dashed line) is added to reflect the rise in the background component of the magnetoresistance as the field increases (c); the total density of the states that account for this artificial rise is shown by the two upper lines in the figure.

saddle point in the upper of the spin-split subbands are not observed in the $\rho(B_{||})$ dependence for sample no. 2984. In the field $B_{||}$ = 22 T, the saddle point is not formed yet, and the corresponding change in the density of the states is masked by features in that density, which are related to side minima of the same subband with close energies. In contrast, at 30 T the saddle points are resolved; i.e., they lie far enough, in terms of energy, from the minima of their subbands. Moreover, as can be seen in Fig. 5c, at $|g|$ = 3 the saddle point of the lower subband almost coincides with the minima of the upper subband, which can enhance the total density-of-states peak at the Fermi level in a field of ~30 T.

These arguments are supported, to some extent, by a calculation of the density of the states at the Fermi level, DOS(E_F), as a function of the magnetic field. As can be seen in Fig. 6c, at a certain broadening of the levels, the features in the density of the states in the upper subband are smeared, but the feature related to the saddle point in the lower subband remains discernible (marked with a vertical arrow). However, calculations of only the density of the states fail to provide a complete description of the dependence of the resistance on a magnetic field. The features related to the upper spin sublevel are manifested in the calculated data in the form of a wide shoulder on the $\rho(B_{||})$ dependence, in fields below 30 T, which is not the case in the experi-

ment. Furthermore, the calculated total DOS(E_F) decreases as the field increases in the range of high fields (Figs. 6a, 6c), which occurs because the Fermi level passes into the lower spin subband, whereas in the experiment, in contrast, the magnetoresistance increases in both samples.

A strong positive magnetoresistance in single layers in the parallel field was observed in several studies [8, 9], where the spin polarization of the electron gas was suggested as the possible mechanism responsible for this effect. In our experiments, we also observed a spin polarization when the upper spin subband is depleted in the field $B_\| > B_s$. It is necessary to note, however, that in the mentioned studies, a metal-type behavior of the resistance was observed, and it was assumed that the spin polarization depresses the mechanisms responsible for this metal-type behavior. In contrast, in our samples, the resistance steadily increases as the temperature decreases in the whole range studied, down to $T \approx 0.3$ K. At the same time, in [9], a positive magnetoresistance was observed, also at low densities, in the region of the insulating state. Thus, the reason why the resistance grows as $B_\|$ increases is not clear yet.

A comparison of Figs. 5c and 5d allows us to understand why the $B_s(|g|)$ dependences (Fig. 4) level off: after the total depletion of the upper spin subband, the Fermi level becomes rigidly fixed within the lower subband.

An estimation of the level broadening from the mobility values gives $dE \approx 1$ meV. The somewhat higher values of dE, which were to be used in our calculations, to fit the experiment, can be justified by the fact that level broadening is defined by the quantum lifetime of electrons (which depends on all the scattering processes). This period can be several times shorter than the transport lifetime determined from the mobility. Figures 6b and 6d show the magnetoresistance behavior that would be expected at a smaller broadening of levels.

ACKNOWLEDGMENTS

The study was supported by the Russian Foundation for Basic Research (project nos. 02-02-16401 and 04-02-614) and a Program of the Russian Academy of Sciences: “Physics of Solid-State Nanostructures.”

REFERENCES

1. V. V. Popov, T. V. Teperik, G. M. Tsymbalov, *et al.*, Semicond. Sci. Technol. **19**, S71 (2004).
2. J. P. Eisenstein, in *Perspectives in Quantum Hall Effects*, Ed. by S. Das Sarma and A. Pinczuk (Wiley, New York, 1997), Chap. 2; S. Girvin and A. H. MacDonald, *Perspectives in Quantum Hall Effects*, Ed. by S. Das Sarma and A. Pinczuk (Wiley, New York, 1997), Chap. 5.
3. J. P. Eisenstein, M. Kellogg, I. B. Spielman, *et al.*, Physica E (Amsterdam) **20**, 111 (2003).
4. L. Kłopotovski, M. Nawrocki, J.-D. Ganiere, *et al.*, Semicond. Sci. Technol. **19**, S380 (2004).
5. T. Ando, J. Phys. Soc. Jpn. **39**, 411 (1975).
6. G. S. Boebinger, A. Passner, L. N. Pfeifer, and K. W. West, Phys. Rev. B **43**, 12673 (1991).
7. J. A. Simmons, S. K. Lyo, N. E. Harff, and J. F. Klem, Phys. Rev. Lett. **73**, 2256 (1994); M. A. Blount, J. A. Simmons, and S. K. Lyo, Phys. Rev. B **57**, 14882 (1998); T. Jungwirth, T. S. Lay, L. Smrcka, and M. Shayegan, Phys. Rev. B **56**, 1029 (1997).
8. D. Simonian, S. V. Kravchenko, M. P. Sarachik, and V. M. Pudalov, Phys. Rev. Lett. **79**, 2304 (1997); V. M. Pudalov, G. Brunthaler, A. Prinz, and G. Bauer, Pis’ma Zh. Éksp. Teor. Fiz. **65**, 887 (1997) [JETP Lett. **65**, 932 (1997)].
9. J. Yoon, C. C. Li, D. Shahar, *et al.*, Phys. Rev. Lett. **84**, 4421 (2000).

Translated by D. Mashovets

Semiconductors, Vol. 39, No. 1, 2005, pp. 11–13. Translated from Fizika i Tekhnika Poluprovodnikov, Vol. 39, No. 1, 2005, pp. 17–20.

SEMICONDUCTOR STRUCTURES, INTERFACES, AND SURFACES

Growth of BGaAs Layers on GaAs Substrates by Metal–Organic Vapor-Phase Epitaxy

D. A. Pryakhin*^, V. M. Danil'tsev*, Yu. N. Drozdov*, M. N. Drozdov*, D. M. Gaponova*, A. V. Murel'*, V. I. Shashkin*, and S. Rushworth**

**Institute for Physics of Microstructures, Russian Academy of Sciences, Nizhni Novgorod, 603950 Russia*
^e-mail: pda@ipm.sci.nnov.ru
***Epichem Group, Power Road, Bromborough, Wirral, CH62 3QF, UK*
Submitted June 1, 2004; accepted for publication June 16, 2004

Abstract—$B_xGa_{1-x}As$ layers were grown on GaAs substrates using low-pressure metal–organic vapor-phase epitaxy. Triethylboron, trimethylgallium, and arsine were used as boron, gallium, and arsenic sources. Optimum growth conditions were selected. The layers were studied using X-ray diffraction, secondary-ion mass spectrometry (SIMS), and photocurrent spectroscopy (PCS). The SIMS results showed a uniform boron distribution over the layer thickness. According to the PCS data, the BGaAs band gap decreases as the boron concentration increases. © *2005 Pleiades Publishing, Inc.*

1. INTRODUCTION

Progress in optoelectronics requires the continuous development of new materials. When GaAs substrates are used, the basic materials for epitaxial layers are alloys based on III–V compounds. At present, nitrogen-containing alloys are being actively studied. The new materials in this series are alloys based on III–V compounds that have undergone the substitution of III cations with boron atoms. The feasibility of growing $B_xGa_{1-x}As$ epitaxial layers is based, in particular, on the use of triethylboron in metal–organic vapor-phase epitaxy (MOVPE). The studies in this field are at an initial stage, and only a small number of them deal with the MOVPE of the BGaAs alloy and analysis of its properties [1–5].

According to [6–8], the BAs band gap is E_g = 1.46 eV; hence, the introduction of boron into GaAs makes it possible to vary E_g, but only in a narrow range. In [9], a 50-meV decrease in the band gap was found at a boron concentration of 0.06%. The reverse effect was observed in [3], where E_g increased by 4–8 meV per 1% of introduced boron. These discrepancies suggest that the above problem has not been adequately studied.

What is quite obvious is the decrease in the lattice parameter when the boron concentration in $B_xGa_{1-x}As$ is increased, since the boron atom is characterized by a much smaller tetrahedral covalent radius than Ga. For cubic BAs, the lattice parameter is 0.477 nm [6–8]. Therefore, elastically stretched epitaxial $B_xGa_{1-x}As$ layers on the GaAs substrate can be used to compensate for elastic strains in heterostructures with elastically compressed $In_xGa_{1-x}As$ layers. In the case of a simultaneous introduction of B and In atoms, a $B_xIn_yGa_{1-x-y}As$ quaternary compound can be grown, which is lattice-matched with the GaAs substrate.

In this paper, we present the results of our study concerned with the growth of BGaAs epitaxial layers by MOVPE.

2. EXPERIMENTAL

BGaAs layers were grown using an "EPIQUIP" low-pressure (100 Torr) MOVPE setup with a horizontal reactor. Triethylboron (TEB), trimethylgallium (TMG), and arsine were used as In, Ga, and As sources, respectively. The growth temperature was 600°C. The layers were grown on semi-insulating or doped GaAs substrates. As preparation, a GaAs buffer layer ~0.1 μm thick was grown on the substrate, also at 600°C.

Hydrogen was used as a carrier gas. The total flow through the reactor was 8 l/min. The layers were grown at partial pressures of reagents from 10^{-2} to 5×10^{-2} mbar for triethylboron and from 2×10^{-3} to 5.6×10^{-3} mbar for trimethylgallium. To maintain these values, corresponding temperatures of bubblers and the carrier gas flows through them were set. The triethylboron vapor pressure P was calculated using the formula (see [5])

$$\log P = 2.91408 - \frac{753.261}{T - 112.631},$$

where T is the Kelvin temperature and P is pressure in mbar.

The boron concentration in the vapor phase can be characterized by the mole fraction of triethylboron X_V:

$$X_V = \frac{[\mathrm{TEB}]}{[\mathrm{TEB}] + [\mathrm{TMG}]},$$

1063-7826/05/3901-0011$26.00 © 2005 Pleiades Publishing, Inc.

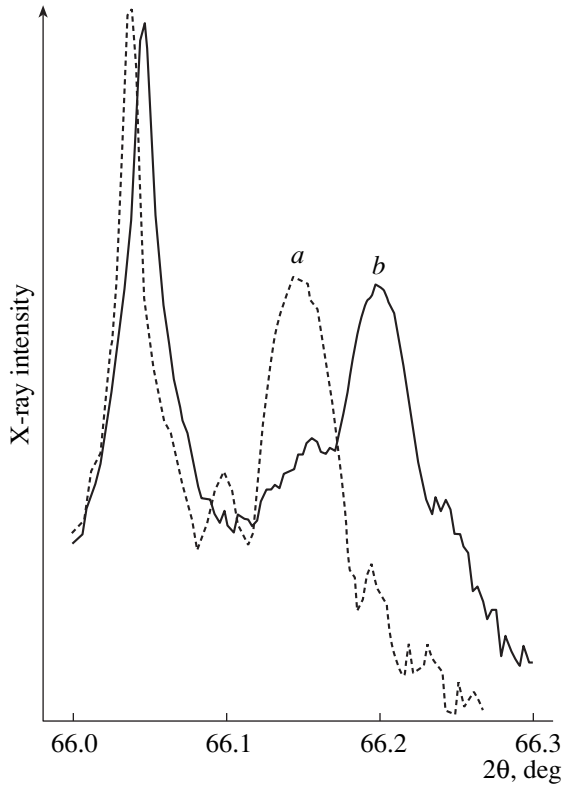

Fig. 1. X-ray diffraction spectra of $B_xGa_{1-x}As$ samples: (*a*) doped substrate (100), misorientation 2° along the [110] direction, $x = 0.5\%$; (*b*) semi-insulating substrate (100), misorientation 0° along the [110] direction, $x = 0.7\%$.

where [TEB] and [TMG] are the partial pressures of the components in the vapor phase. During the experiment, X_V was varied from 0.3 to 0.9.

The grown epitaxial layers were studied by X-ray diffraction (XRD) on a DRON-4 diffractometer (Ge(400) monochromator and Cu$K\alpha_1$ radiation). The depth distribution of elements in the epitaxial layers was determined by SIMS on a Shipovnik-3 mass spectrometer (O_2^+ beam and 10 keV, 600×600 μm^2 raster). The samples were also studied using *C–V* profiling and photocurrent spectroscopy.

3. RESULTS AND DISCUSSION

The thickness of the grown $B_xGa_{1-x}As$ epitaxial layers, determined by *C–V* profiling and XRD, varied from 0.2 to 0.5 μm. In contrast to GaAsN layers, they have *n*-type conductivity. The boron concentration was determined from the XRD spectra by taking into account elastic strain in the layer. An example of XRD spectra in the vicinity of (004)GaAs is shown in Fig. 1. It should be noted that the boron concentration in the layer grown on the semi-insulating substrate ((100), misorientation is 0° along the [110] direction) is higher than in the layer grown on the doped substrate ((100), misorientation is 2° along the [110] direction) in all the samples.

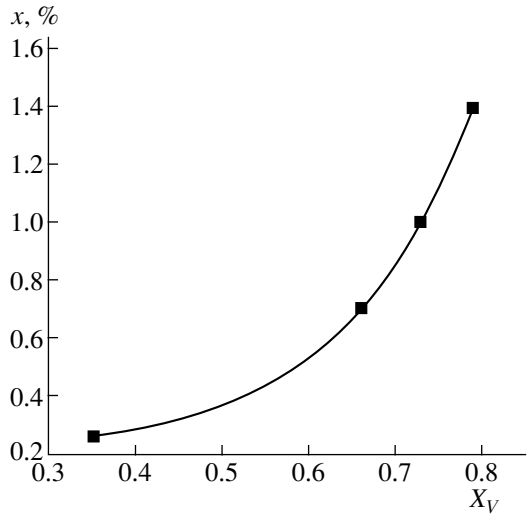

Fig. 2. The dependence of the BAs concentrations (x) in the $B_xGa_{1-x}As$ layer on the triethylboron mole fraction X_V in the vapor phase.

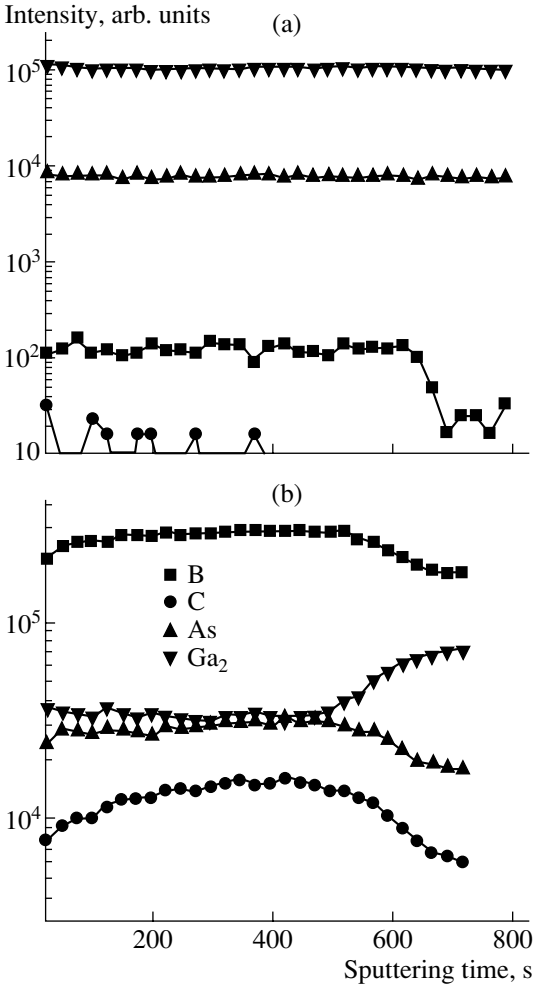

Fig. 3. SIMS profiles of elements in the $B_xGa_{1-x}As$ epitaxial film for (a) the sample with $x = 0.7\%$ and (b) the sample grown at $X_V = 0.9$.

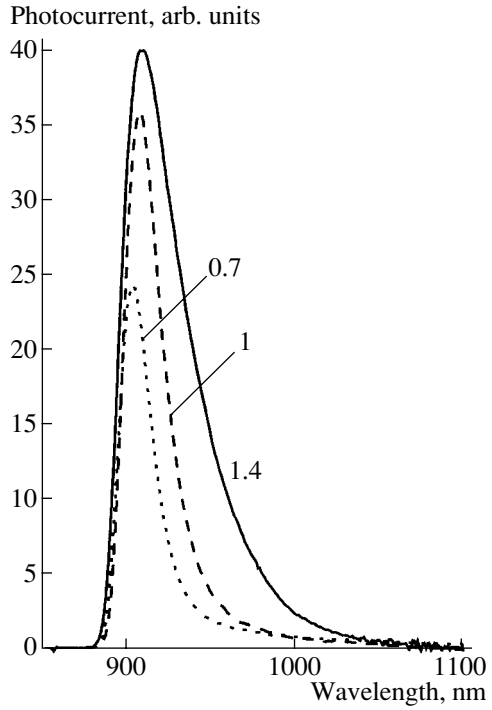

Fig. 4. Photoconductivity spectra of $B_xGa_{1-x}As$ epitaxial layers for x = 0.7, 1, and 1.4%.

The influence of variations in the composition of the initial gas mixture on the boron introduction and quality of the grown layers was found to be highly significant. A decrease in the trimethylgallium partial pressure results in a decrease in the growth rate and an increase in the number of vacancies of group-III elements, which increases the degree of boron introduction (Fig. 2). However, epitaxial growth is suppressed when the triethylboron mole fraction X_V in the vapor phase exceeds 0.85, and a polycrystalline or amorphous layer with a very high boron content is formed on the surface. The same effect was observed when the triethylboron flow increased. Probably, this is caused by spurious vapor-phase reactions and the formation of polycrystalline boron arsenide, elemental polycrystalline or amorphous boron on the surface.

The degree of boron introduction also increases along with arsine flow. In the experiments we performed, the ratio of the concentrations of group-III and group-V elements ([III]/[V]) was up to 52.

The SIMS data for the $B_xGa_{1-x}As$ epitaxial layer with x = 0.7% are shown in Fig. 3a. As can be seen, the depth distribution of elements in the layer is uniform. Figure 3b shows the distribution for the sample grown under the conditions of epitaxial growth suppression. In comparison with the former layer, the boron concentration increases by approximately two orders of magnitude. The high carbon content indicates a large amount of products from the incomplete decomposition of organometallic compounds, which may confirm the version of events where spurious heterogeneous reactions occur in the vapor phase.

Figure 4 shows the photoconductivity spectra for three $B_xGa_{1-x}As$ samples with various boron concentrations. An increase in the boron concentration results in an elongation of the long-wavelength photocurrent slope, which suggests that there are optical transitions in boron-containing samples whose energies are lower than the GaAs band gap. In [5], these transitions are associated with the transition from the conduction band to the level of light holes in the valence band. When boron is introduced, the light-hole band is split off from the heavy-hole band due to strong tensile stresses in the BGaAs–GaAs system.

4. CONCLUSION

$B_xGa_{1-x}As$ epitaxial layers were grown on GaAs substrates using low-pressure MOVPE. The highest BAs content in the layers is x = 1.4%. Photocurrent spectroscopy showed that the band gap E_g of the grown BGaAs layers decreases as the boron concentration increases. The estimated value of ΔE_g is ~100 meV for a layer with the highest BAs content.

ACKNOWLEDGMENTS

This study was supported by the Russian Foundation for Basic Research, project no. 04-02-17180.

We thank the EPICHEM Group for supplying the organoelemental compounds.

REFERENCES

1. H. Dumont, J. Dazord, Y. Monteil, *et al.*, J. Cryst. Growth **248**, 463 (2003).
2. H. Dumont, D. Rutzinger, C. Vincent, *et al.*, Appl. Phys. Lett. **82**, 1830 (2003).
3. J. F. Geinsz, D. J. Friedman, J. M. Oslon, *et al.*, Appl. Phys. Lett. **76**, 1443 (2000).
4. J. F. Geinsz, D. J. Friedman, Sarah R. Kurtz, *et al.*, J. Electrochem. Soc. **30**, 1387 (2001).
5. V. Gottschalch, G. Leibiger, and G. Benndorf, J. Cryst. Growth **248**, 468 (2003).
6. H. M. Manasevit, W. B. Hewitt, A. J. Nelson, and A. R. Mason, J. Electrochem. Soc. **136**, 3070 (1989).
7. S. M. Ku, J. Electrochem. Soc. **113**, 813 (1966).
8. T. L. Chu and A. E. Hyslop, J. Electrochem. Soc. **121**, 412 (1974).
9. V. K. Gupta, M. W. Koch, N. J. Watkins, *et al.*, J. Electron. Mater. **29**, 1387 (2000).

Translated by A. Kazantsev

Semiconductors, Vol. 39, No. 1, 2005, pp. 113–118. Translated from Fizika i Tekhnika Poluprovodnikov, Vol. 39, No. 1, 2005, pp. 124–130.

LOW-DIMENSIONAL SYSTEMS

Terahertz Oscillator Based on Nonlinear Frequency Conversion in a Double Vertical Cavity

Yu. A. Morozov*^, I. S. Nefedov*, V. Ya. Aleshkin, and I. V. Krasnikova*****

**Institute of Radio Engineering and Electronics, Russian Academy of Sciences, Saratov, 410019 Russia*

^e-mail: mor@ire.san.ru

***Institute for Physics of Microstructures, Russian Academy of Sciences, Nizhni Novgorod, 603600 Russia*

****Saratov State Technical University, Saratov, 410016 Russia*

Submitted June 1, 2004; accepted for publication June 16, 2004

Abstract—The feasibility of producing a vertical-cavity laser that operates in the far IR region and is based on the three-wave mixing due to the lattice nonlinearity of a GaAs/AlGaAs system is analyzed. It is shown that the use of a double Bragg cavity with the parameters tuned both to high-frequency oscillations (sources of nonlinear polarization) and to the difference frequency allows one to raise the intensity of the radiation in the far IR region. The power density of the radiation at a wavelength of 49.5 μm equals approximately 5×10^{-4} μW/μm^2 at a drive current density of 5 kA/cm^2. It is suggested that a drive current should be supplied with the use of intercavity contacts, to be located in the vicinity of a node in the difference mode; then, the absorption of radiation by free charge carriers will be reduced to a minimum. © *2005 Pleiades Publishing, Inc.*

1. INTRODUCTION

The development of coherent light sources for the middle and far IR regions remains a topical problem despite the appreciable recent progress due to the advent of quantum-cascade lasers [1]. An alternative approach to lasing in the far and middle IR regions can apparently be based on the principle of nonlinear frequency conversion. This concept has been actively developed since the early 1970s for applicaton to devices where nonlinear three-wave mixing takes place in an external nonlinear crystal (see, e. g., [2]). In recent years, a number of new lasers have appeared where a nonlinear frequency conversion with the difference frequency falling in the middle IR region is realized in the laser itself [3–5]. Under these conditions, it is assumed that two-frequency radiation in the near IR region gives rise to nonlinear polarization in the medium. In a strip-structure laser with the radiation output through the end face, as suggested in [3], a realization of the laser's optimal characteristics is particularly hindered by the difficulty of providing for the phase-matching conditions between the nonlinear polarization at the difference frequency and the waveguide mode at the same frequency. We have recently suggested [5] a vertical-cavity laser that eliminates this problem, since the cavity length does not exceed the coherence length $l_c = \pi/\Delta k$ (Δk is the difference between the wave numbers of the nonlinear polarization wave and the waveguide mode at the difference frequency). As well as this, in a vertical-cavity laser, the electric field of the high-frequency oscillations responsible for second-order nonlinear polarization can exceed that of a stripe laser by more than an order of magnitude. Furthermore, a vertical-cavity laser apparently allows one to attain a higher overlapping factor (in a transverse cross section) between the induced nonlinear polarization and the difference mode. We extended the basic principle incorporated into the laser [5] to a light-emitting structure with a double vertical cavity [6]. The latter study shows that the use of an additional cavity tuned to the difference frequency provides a 1 to 1.5 orders of magnitude rise of the power density in the middle IR range (13 μm). Note that a vertical-cavity laser using frequency doubling based on the lattice nonlinearity of a GaAs/AlGaAs system is considered in [7].

In this study, we numerically investigate the characteristics of far-IR radiation (~50 μm) that stem from nonlinear frequency conversion, which was suggested for the first time in [6]. It should be noted that a quantum-cascade laser for the far-IR region (66 μm) [8] is efficient only if cooled to about 10–50 K.

2. THE LASER STRUCTURE

A schematic diagram of the laser structure under consideration is shown in Fig. 1. The two quantum-dimensional $In_xGa_{1-x}As/GaAs$ active layers (*7*) responsible for near infrared lasing at $\lambda_{1,2}$ (~1 μm) are separated by an $Al_{0.2}Ga_{0.8}As$ layer. The thickness of the latter is about one quarter of λ_m, which is the mean value of $\lambda_{1,2}$ (taking into account the refractive index). In this case, the longitudinal distribution of a field in the active regions is managed so that the antinodes of one of the high-frequency modes coincide closely with the nodes of the other mode. This circumstance reduces the influence of each active layer on the amplified (or attenuated) field in the neighboring active layer. The layers

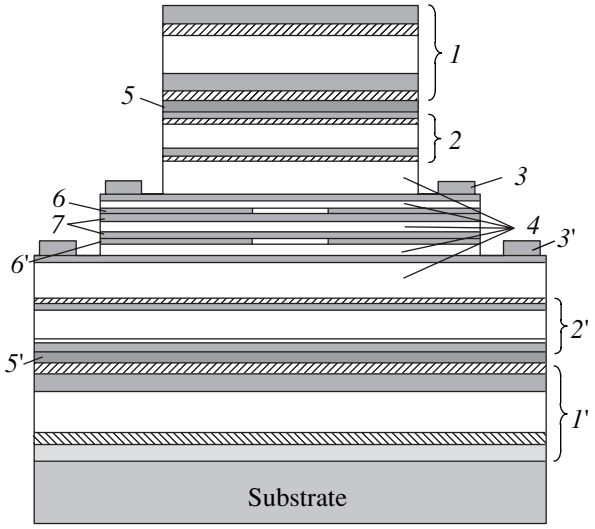

Fig. 1. A schematic representation of the laser structure: (*1*, *1*') and (*2*, *2*') are the upper and the lower Bragg reflectors (sets 2 and 1, respectively); (*3*, *3*') are the *p*- and *n*-contacts; (*4*) are nonlinear-conversion layers; (*5*, *5*') are the tuning layers; (*6*, *6*') are the oxide windows; and (*7*) are the active layers.

where the nonlinear three-wave mixing giving rise to the generation of the difference mode (corresponds to the wavelength λ_r in air) is most efficient will be referred to as the layers (*4*) of nonlinear conversion ($Al_{0.2}Ga_{0.8}As$). We suggest using two sets of Bragg reflectors consisting of alternating quarter-wave GaAs/AlAs layers. One of these sets (*2*, *2*') (the first, for clarity) confines the vertical cavity that is matched with the waves $\lambda_{1,2}$; i. e., these waves belong to the neighboring longitudinal modes of this cavity, providing for its minimal sizes. The Bragg reflectors (*1*, *1*') of set two represent the difference wave and are transparent at the wavelengths $\lambda_{1,2}$. Thus, the laser structure is formed by two vertical cavities, one of which is incorporated into the other. The internal cavity ensures the lasing conditions in the near IR region. The external cavity, when it is precisely tuned to the wavelength λ_r, considerably amplifies the field at the difference frequency in the region where it interacts with the nonlinear polarization at this frequency. The analysis shows that there is a noticeable increase in the conversion efficiency and, therefore, in the power density of the radiation in the mid-IR region. The additional (tuning) AlAs layers (*5*, *5*') adjoining the Bragg reflectors (BRs) of set two from inside make it possible to accurately tune the resonant frequency of the external cavity to the difference frequency. It is clear that the BR thickness for far-IR radiation is about several micrometers. Therefore, it seems reasonable to use a deposition method of production, including the deposition of the other pair of semiconductor (insulating) materials that are transparent in the aforementioned spectral region.

It is known that absorption by free charge carriers is one of the main causes of radiation loss in the far-IR region. Therefore, an acceptable Q-factor of the cavity tuned to the wavelength λ_r can be ensured by formulating the Bragg reflectors using undoped layers. According to our analysis, at a given geometry of the sources, the profile of a standing wave of the second-order nonlinear polarization is such that its node is located between the active layers. Because of this reason, a drive current can be supplied via highly doped *p*- and *n*-type contact layers (*3*, *3*') that are located inside the cavities near the active layers and, hence, near the node of the difference wave. As a result, the absorption of far-IR radiation is reduced to a minimum. In order to limit the current and the optical fields in the transverse section of the laser, we use oxide (AlO) apertures (windows). It turns out that an acceptable power value in the far-IR region can only be attained when oxide windows with a diameter considerably exceeding the wavelength at the difference frequency are used. Therefore, a geometric-optics approximation of plane uniform waves propagating in a vertical direction (across the layers) can serve as the first approximation for analyzing the electrodynamic characteristics of lasing. In the subsequent studies, we will consider the influence of a multimode transverse structure of radiation on the power and spectral characteristics of lasing.

3. MATHEMATICAL BACKGROUND AND NUMERICAL RESULTS

We calculated the field distribution in high-frequency modes and the gain in the active layers of laser by solving a boundary eigenvalue problem for the wave equation in the space of a complex variable. Note that one of the parts (real or imaginary) of the first complex eigenvalue defines the geometry of the structure for the given mode λ_1 and the other characterizes the gain in the first active layer. The second eigenvalue defines the wavelength and the gain in the second active layer. We took into account both the radiation loss in a multilayer structure and the loss due to the emission of radiation through the upper BRs. The threshold currents were determined from a stationary solution of the rate equation for the carrier concentration in the active layers. This approach is described in detail in [5].

It is known that zinc blende crystals grown on (100)-oriented substrates do not admit nonlinear mixing of plane co-propagating waves. However, in structures with an inclined substrate, this nonlinear conversion is feasible, and was successfully attained in [7]. In that study, a second harmonic generation (0.5 μm) was accomplished in a vertical-cavity laser based on a GaAs/AlGaAs system on an inclined (311)-oriented substrate. In view of the above, to provide clarity, we assume that the double vertical cavity laser under study

is also grown on a (311)-oriented GaAs substrate. Taking into account the transformation of field components caused by the rotation of the coordinate system, we can express the second-order nonlinear polarization as $\rho = 2\chi\varepsilon_0 d_{14} E^{(1)} E^{(2)}$. Here, d_{14} is the component of the nonlinear susceptibility tensor, $\chi = 27/(11/\sqrt{22}) \approx 0.523$ is the coefficient related to the rotation from plane (100) to (311), ε_0 is the permittivity of free space, and $E^{(1, 2)}$ are the electric fields of the source waves $\lambda_{1, 2}$.

First, to obtain a correct estimation of the optical power resulting from nonlinear conversion, one needs to analyze the dispersion of the nonlinear susceptibility (coefficient d_{14}) of gallium arsenide in the vicinity of the phonon (transverse optical phonon) resonance frequency. The data of the recently performed experiment [9] allows us to improve the parameters $C_{1, 2, 3}$ that define the frequency dependence of $d_{14}(\omega_3, \omega_2, \omega_1)$ in accordance with expression (8) from the article by Mayer and Keilmann [10]. Figure 2 shows the normalized nonlinear susceptibility $d_{14}(\lambda_r, \lambda_1, \lambda_2)/d_{14}^e$ versus the wavelength λ_r under the condition that $\lambda_{1, 2}$ is symmetric about the mean value λ_m, i.e., $\lambda_{2, 1} = \lambda_m \pm \delta$. Here, $d_{14}^e = 170 \times 10^{-12}$ m/V [7] is the electronic contribution to nonlinear susceptibility. For our calculations, we used the frequency values $\nu_{TO} = 8.02$ THz and the attenuation parameter $\gamma_{TO} = 0.06$ THz of a transverse optical phonon, as given in the review by Blakemore [11]. The plot indicates that second-order nonlinearity considerably increases in the vicinity of the resonance, nearly disappears at $\lambda_r \approx 60$ μm, and increases again as the frequency of the difference mode increases further. Hence it follows that the method of nonlinear frequency conversion by means of GaAs lattice nonlinearity is apparently inefficient in the close vicinity of 60 μm. However, it is probably possible to produce a laser with practically interesting output characteristics near the phonon resonance under the condition of a reasonable balance between the increase in the nonlinear susceptibility and the losses (which also increase in the vicinity of the frequency ν_{TO} and, thus, decrease the efficiency of the three-wave mixing). As an example illustrating this possibility, we consider a laser with a difference harmonic wavelength of about 50 μm. This value corresponds to $d_{14} \approx 60 \times 10^{-12}$ m/V.

In order to find the electric field E_r at the difference frequency, we solved an inhomogeneous wave equation with given external sources:

$$\nabla^2 + \gamma^2 E_r = -\frac{\gamma^2}{\varepsilon\varepsilon_0} p = \Re, \tag{1}$$

where $\nabla^2 = d^2/dz^2$ is the Laplace operator, $\gamma = k_0\sqrt{\varepsilon}$ is the wave number, ε is the relative permittivity, and $k_0 = 2\pi/\lambda_r$. The general solution of this equation in a homogeneous layer with the boundary conditions $E_r(0) = E_{r0}$ and $dE_r(0)/dz = E'_{r0}$ is known:

$$E_r(z) = E_{r0}\cos\gamma z + \frac{E'_{r0}}{\gamma}\sin\gamma z + \frac{1}{\gamma}\int_0^z \sin\gamma(z-\tau)\Re(\tau)d\tau. \tag{2}$$

Therefore, the electric field and its derivative at the boundaries of a layer with the thickness h can be related via the following matrix expression:

$$\begin{pmatrix} E_r(h) \\ E'_r(h) \end{pmatrix} = \hat{m}\begin{pmatrix} E_r(0) \\ E'_r(0) \end{pmatrix} + \int_0^h \begin{pmatrix} \frac{1}{\gamma}\sin\gamma(h-\tau) \\ \cos\gamma(h-\tau) \end{pmatrix}\Re(\tau)d\tau, \tag{3}$$

where

$$\hat{m} = \begin{pmatrix} \cos\gamma h & \frac{1}{\gamma}\sin\gamma h \\ -\gamma\sin\gamma h & \cos\gamma h \end{pmatrix}$$

is the transfer matrix of the layer. The electric field strength and its derivative with respect to the longitudinal coordinate (proportional to the magnetic-field strength) must be continuous at the boundaries of homogeneous layers. Therefore, sequentially perform-

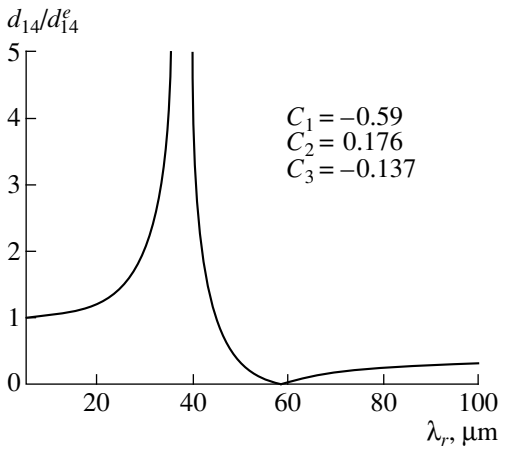

Fig. 2. The Normalized component of the nonlinear susceptibility tensor d_{14} vs. the difference-mode wavelength.

The parameters of the structure

Layer	Thickness, μm	Conductivity type/Concentration, 10^{18} cm^{-3}	α_r, cm^{-1}
GaAs (BR 2)	3.182	Undoped	20
AlAs (BR 2)	3.78	Undoped	5
GaAs (BR 1)	0.071	Undoped	20
AlAs (BR 1)	0.084	Undoped	5
$Al_{0.2}Ga_{0.8}As$ nonlinear converter	2.747	Undoped	20
GaAs contact	0.03	*n*/10	41200
$Al_{0.2}Ga_{0.8}As$ nonlinear converter	0.1	*n*/1	6900
InGaAs/GaAs (QW 1 + barrier 1)	0.03	Undoped	2000
$Al_{0.2}Ga_{0.8}As$ nonlinear converter	0.042	Undoped	1500
InGaAs/GaAs (QW 2 + barrier 2)	0.03	Undoped	2000
$Al_{0.2}Ga_{0.8}As$ nonlinear converter	0.1	*p*/1	950
GaAs contact	0.03	*p*/10	6700
$Al_{0.2}Ga_{0.8}As$ nonlinear converter	2.67	Undoped	20

ing transformation (3), we obtain the relationship for the fields at the boundaries of a structure with the length L:

$$\begin{pmatrix} E_r(L) \\ E_r'(L) \end{pmatrix} = \hat{M}_1 \begin{pmatrix} E_r(0) \\ E_r'(0) \end{pmatrix} + \sum_{i=1}^{N} \hat{M}_{i+1} \int_{d_i}^{d_{i+1}} \begin{pmatrix} \frac{1}{\gamma_i}\sin\gamma_i(d_{i+1}-\tau) \\ \cos\gamma_i(d_{i+1}-\tau) \end{pmatrix} \Re(\tau)d\tau. \quad (4)$$

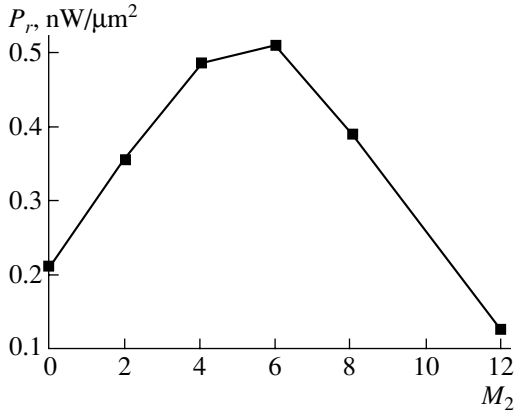

Fig. 3. The power density of the difference mode vs. the number of pairs of layers in the BRs of set 2.

Here, $\hat{M}_j = \prod_{i=j}^{N} \hat{m}_i$ is the product of the transfer matrices starting with layer j and continuing to the last layer N, $\hat{M}_{N+1} = \hat{I}$ is the unit matrix, $d_1 = 0$, and $d_{N+1} = L$. At the given boundary conditions, i.e., $E_r'(0) = 0$ (the magnetic wall at the lower boundary) and $E_r'(L) = -jk_0E_r(L)$ (a running wave in free space), formula (4) represents a system of inhomogeneous algebraic equations. By solving this system, we determine the power density at the difference frequency in the form $P_r = |E_r|^2/(2\rho_0)$, where $\rho_0 = 120\pi$ is the wave impedance in free space. The above approach does not imply the expansion of a field induced by external sources in the eigenwaves of the problem. It is known that solving the eigenvalue problem, in an exact formulation, for systems with losses requires a nonstationary approach and, therefore, meets serious difficulties [12].

The parameters used in the calculations are listed in the table. The values of these parameters correspond to the following wavelengths of high-frequency oscillations: $\lambda_1 = 0.99$ μm, $\lambda_2 = 1.0102$ μm, and $\lambda_r = 49.5$ μm for the difference harmonic. As was mentioned above, the efficiency of the difference-mode generation depends heavily on the losses caused by the absorption of waves involved in the nonlinear conversion process. This statement is also true for the near-IR waves, which form nonlinear polarization, and, to a greater extent, for the difference mode. Indeed, the attenuation of the waves that are the sources of nonlinear polarization defines the necessary level of the gain in the active regions and, therefore, the threshold current for the excitation of the waves $\lambda_{1,2}$. At the same time, the energy density of high-frequency electric fields depends on the excess of the operating current over the threshold value. In addition, it is intuitively understood, and also confirmed by the analysis of formula (4), that the power density at the difference frequency is suppressed as a result of an increase in the damping constant α_r of waves at this frequency. The values of α_r are listed in the rightmost column of the table. We considered the absorption by free carriers as the main mechanism responsible for the damping in *n*-type layers, and used the results of reviews [11, 13]. An appreciable loss in the contact *n*-type doped layer can be explained by the fact that, at a certain doping level, the difference frequency falls in the vicinity of the plasma resonance. It is known that, for acceptor-doped layers, intersubband scattering in the valence band also plays an important part along with free carrier absorption. Therefore, for *p*-type layers, the data were obtained by processing the experimental results reported in [14, 15].

Figure 3 shows the power density at the difference frequency versus the number of pairs M_2 of layers that make up the external reflectors (set 2). The reflectors of set 1 are assumed to include 35 pairs of layers. The drive current is assumed to be equal to 5 kA/cm^2. As follows from Fig. 3, at the given parameters, there is an

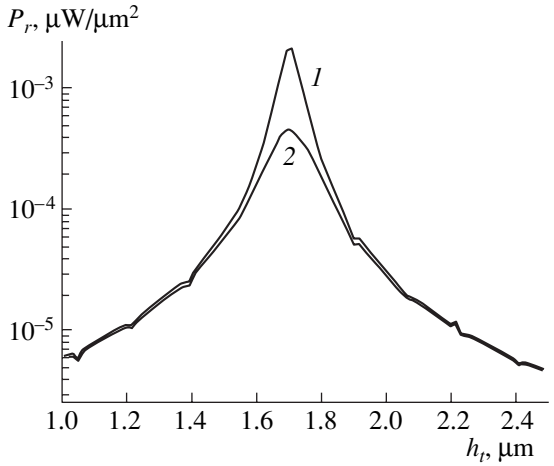

Fig. 4. The power density of the difference mode vs. the tuning layer thickness (*1*) in the absence and (*2*) in the presence of losses.

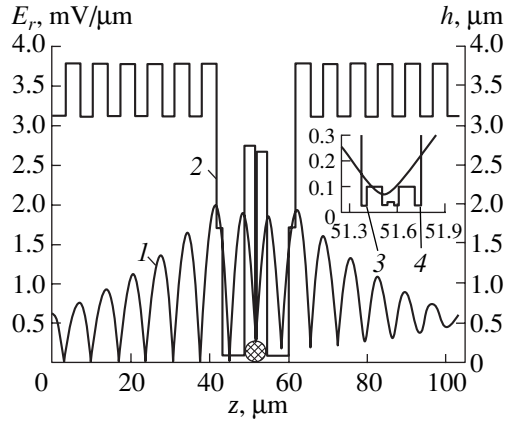

Fig. 5. (*1*) The electric-field amplitude of the difference wave and (*2*) the layer thickness vs. the longitudinal coordinate *z*. Inset: the same in the doped layers including the (*3*) *n*-type and (*4*) *p*-type contacts on an enlarged scale.

optimal number of pairs of layers that form the external reflectors. The analysis by formula (4) shows that, in the absence of absorption in the bulk of the layers, the power density increases proportionally to $(n_1/n_2)^{2M_2}$, where n_1 and n_2 are the refractive indices of layers that form the external BRs. In the presence of optical losses, this dependence levels off and the output power drops as the number of the BR layers increases further. As can be seen from the plot, the presence of an additional cavity tuned to the difference frequency gives, approximately, a 2.5-time gain for a laser in the range considered.

Figure 4 shows the resonance curves; i. e., the power density of the difference mode versus the thickness h_t of the tuning layers at $M_2 = 6$. It can be seen that losses in the bulk of the layers significantly affect the maximal intensity of the radiation. The resonance peaks are comparatively narrow, which can be explained, first, by the fact that the oscillations induced by nonlinear polarization should represent the cavity eigenfunctions and, second, by the fact that the profile of nonlinear polarization should feature maximal spatial overlapping with the field of the difference wave. The position of resonances along the abscissa axis is almost unaffected by the presence or absence of losses.

Figure 5 shows the amplitude of the electric field of the difference mode in the same laser at a resonance tuning of the external cavity. The thickness of the layers along the longitudinal coordinate is also shown. The inset shows the same values in the region of doped layers, i. e., between the contacts (the region is marked by the hatched circle in the main plot), on an enlarged scale. It can be seen that the electric-field amplitude in the doped layers is small (no larger than 0.2×10^{-3} V/μm). The position of the contacts in the vicinity of the wave node makes it possible to reduce the losses caused by the absorption inside the structure to a minimum. It also follows from Fig. 5 that the field of the difference wave

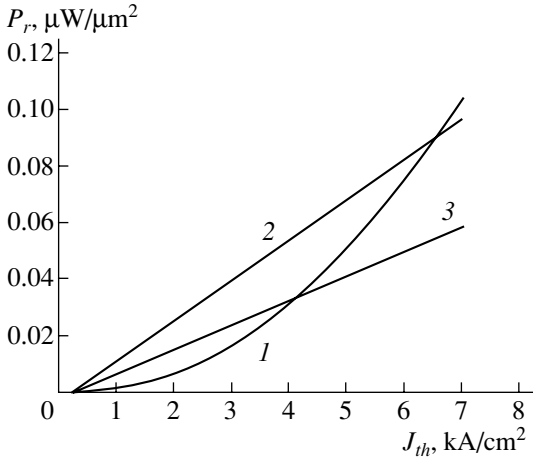

Fig. 6. The intensity of radiation in the (*1*) far and (*2*, *3*) near IR regions vs. the drive current density. For curve *1*, the scalet at the ordinate axis is enlarged by 100 times.

considerably differs from that of the standing wave in the vicinity of the exit cross section. This circumstance is mainly due to the emission of a wave from the output surface and, along with this, to the attenuation in the bulk of the layers.

Figure 6 shows the intensities of the difference mode and the waves with $\lambda_{1,2}$ versus the drive-current density *J*th in a laser that has an optimal number of the pairs of layers that form the external cavity. As would be expected, the power of the difference mode increases almost quadratically with *J*th and attains a value of 5×10^{-4} μW/μm^2 at the current density 5 kA/cm^2. Because the vicinity of $\lambda_{1,2}$ corresponds to the maximal reflection coefficient for the BRs of set 1, the modes of the source waves appear to be largely locked within the cavity: their power is only two orders of magnitude higher than that of the difference mode. (For compari-

son, in a mid-IR laser [6], the output intensity of the sources exceeds the intensity of the radiation that results from nonlinear mixing by more than three orders of magnitude.)

4. CONCLUSION

The characteristics of far-IR radiation obtained from a semiconductor laser that is based on nonlinear frequency conversion in a structure with a double vertical cavity are numerically studied.

It is suggested that a driving current is supplied by means of intracavity contacts located in the vicinity of the node of the difference wave field. This approach, via the Drude mechanism, ensures the lowest attenuation of IR radiation by free charge carriers.

The excitation of the laser structure by nonlinear polarization at the difference frequency is analyzed without using the expansion of a field in the eigenfunctions of the waveguide structure (the cavity). This is a general approach and can be applied to almost any structure consisting of uniform layers and excited by given external sources.

It is shown that the intensity of the difference mode is a quadratic function of the drive-current density and attains 5×10^{-4} μW/μm^2 at a drive-current density of 5 kA/cm^2 under the conditions of resonant tuning. The power density of the high-frequency oscillations that induce the nonlinear polarization is approximately two orders of magnitude higher at the same drive current.

The effect of absorption in the bulk of the cavity on the output characteristics of the laser is determined. It is shown that damping of far-IR radiation, as a result of the absorption by free charge carriers and scattering by the phonons at a frequency close to the phonon resonance, is the main factor that retards the growth of the power density of the radiation. In the absence of losses, the output intensity would grow proportionally to $(n_1/n_2)^{2M_2}$. At the given attenuation constant in the bulk of the layers, the presence of an additional cavity tuned to the resonance with the difference frequency results in, approximately, a 2.5-fold increase in the output power. The optimal number of periods in the BRs of set 2 is six when the period consists of GaAs/AlAs layers. The total thickness of the structure is about 100 μm.

The distribution of the electric field at the difference frequency along the structure is analyzed. It is shown that one of the minima of the field is located within the doped layers, which provides for the low field strength at the contacts. As a result, the losses due to free-carrier absorption decrease. It is also shown that the field profile in the vicinity of the output section considerably differs from that of the standing wave. This fact is due to both the loss in the bulk of the layers and the surface emission of the radiation.

ACKNOWLEDGMENTS

This study was supported by the Russian Foundation for Basic Research and the Belarussian Republican Foundation for Fundamental Research, project no. 02-02-81036-Bel2002_a; the Russian Foundation for Basic Research, project no. 04-02-17432; and the International Science and Technology Center (ISTC), project no. 2293.

REFERENCES

1. M. Beck, D. Hofstetter, T. Aellen, *et al.*, Science **295**, 301 (2002).
2. O. Levi, T. Pinguet, T. Skauli, *et al.*, Opt. Lett. **27**, 2091 (2002).
3. V. Ya. Aleshkin, A. A. Afonenko, and N. B. Zvonkov, Fiz. Tekh. Poluprovodn. (St. Petersburg) **35**, 1256 (2001) [Semiconductors **35**, 1203 (2001)].
4. A. A. Belyanin, D. Deppe, V. V. Kocharovskiĭ, *et al.*, Usp. Fiz. Nauk **173**, 1015 (2003) [Phys. Usp. **46**, 986 (2003)].
5. Yu. A. Morozov, I. S. Nefedov, and V. Ya. Aleshkin, Zh. Tekh. Fiz. **74** (5), 71 (2004) [Tech. Phys. **49**, 592 (2004)].
6. Yu. A. Morozov, I. S. Nefedov, and V. Ya. Aleshkin, Fiz. Tekh. Poluprovodn. (St. Petersburg) **38**, 1392 (2004) [Semiconductors **38**, 1350 (2004)].
7. Y. Kaneko, S. Nakagawa, Y. Ichimura, *et al.*, J. Appl. Phys. **87**, 1597 (2000).
8. M. Rochat, L. Ajili, H. Willenberg, *et al.*, Appl. Phys. Lett. **81**, 1381 (2002).
9. T. Dekorsy, M. Helm, V. Yakovlev, *et al.*, Phys. Rev. Lett. **90**, 055508 (2003).
10. A. Mayer and F. Keilmann, Phys. Rev. B **33**, 6954 (1986).
11. J. Blakemore, J. Appl. Phys. **53**, R123 (1982).
12. A. S. Il'inskiĭ and G. Ya. Slepyan, *Oscillations and Waves in Electrodynamical Systems with Losses* (Mosk. Gos. Univ., Moscow, 1983) [in Russian].
13. S. Adachi, J. Appl. Phys. **58**, R1 (1985).
14. W. Songprakob, R. Zallen, D. Tsu, and W. Liu, J. Appl. Phys. **91**, 171 (2002).
15. W. Songprakob, R. Zallen, W. Liu, and K. Bacher, Phys. Rev. B **62**, 4501 (2000).

Translated by A. Sidorova

Semiconductors, Vol. 39, No. 1, 2005, pp. 119–123. Translated from Fizika i Tekhnika Poluprovodnikov, Vol. 39, No. 1, 2005, pp. 131–135.

LOW-DIMENSIONAL SYSTEMS

Localization of Holes in an InAs/GaAs Quantum-Dot Molecule

M. M. Sobolev, G. E. Cirlin, Yu. B. Samsonenko, N. K. Polyakov, A. A. Tonkikh, and Yu. G. Musikhin

Ioffe Physicotechnical Institute, Russian Academy of Sciences, Politekhnicheskaya ul. 26, St. Petersburg, 194021 Russia

Submitted June 1, 2004; accepted for publication June 16, 2004

Abstract—Deep-level transient spectroscopy is used to study the emission of holes from the states of a vertically coupled system of InAs quantum dots in *p–n* InAs/GaAs heterostructures. This emission was considered in relation to the thickness of a GaAs interlayer between two layers of InAs quantum dots and to the reverse-bias voltage U_r. It is established that hole localization at one of the quantum dots is observed for a quantum-dot molecule composed of two vertically coupled self-organized quantum dots in an InAS/GaAs heterostructure that has a 20-Å-thick or 40-Å-thick GaAs interlayer between two layers of InAs quantum dots. For a thickness of the GaAs interlayer equal to 100 Å, it is found that the two layers of quantum dots are incompletely coupled, which results in a redistribution of the hole localization between the upper and lower quantum dots as the voltage U_r applied to the structure is varied. The studied structures with vertically coupled quantum dots were grown by molecular-beam epitaxy using self-organization effects. © *2005 Pleiades Publishing, Inc.*

1. INTRODUCTION

At present, one the most interesting fields in current semiconductor physics is related to the problem of the coupling and hybridization of quantum states in self-organized quantum dots (QDs). Vertically coupled structures are promising for the development of lasers with QDs [1]; components of optical memory [2]; and, possibly, quantum-mechanical computers [3]. It is believed that a vertically coupled system that is composed of two planar arrays of QDs separated by an interlayer can serve as a single qubit [4]. A necessary condition for the accomplishment of a single qubit is the quantum-mechanical coupling of the wave functions of two QDs, similar to that which is realized in molecules. The formation of molecular states for vertically coupled QDs attracts the active attention of both theoreticians [3–7] and experimentalists [7–11]. It was shown theoretically by Partoens and Peeters [5] that two QDs can be found in the state of either a single atomic dot or a molecule, depending on the distance between these QDs. The condition for strong coupling should be satisfied if the distance between the QDs is small as, in this case, the QD pair behaves like a single QD. The QDs behave like uncoupled QDs if they are widely separated. As was shown previously [5], the QDs should behave like a new type of molecule if the distance between them is intermediate. If the QDs are coupled, the levels should be split between the bonding and antibonding states, with the position of the levels depending on the distance between the QDs [3–6]. It follows from theoretical results [2] that the formation of the bonding and antibonding states can occur only for the electron states of a quantum molecule. However, it is believed [8] that the bonding and antibonding quantum states for holes are not formed as a result of a large effective mass of holes, but, rather, the holes should be localized within QDs. It was suggested previously [3, 6, 7] that, depending in the distance between QDs, the bonding and antibonding states related to holes can be formed in quantum molecules. A coherent two-level system can be controlled using either short optical pulses [7] or an electric field applied to the heterostructure, which affects the localization of holes within a quantum molecule [8, 9]. The relevant studies were performed using the resonance-tunneling effect [11] or by recording measurements of microphotoluminescence [7, 9]. In addition, an enhancement of the effect of the hybridization of electronic states in two QDs in relation to the thickness of the barrier between them was previously reported [9, 10].

We previously showed that there are the following effects in the InAs/GaAs heterostructures with vertically coupled QDs:

(i) the Coulomb interaction between charge carriers localized within QDs and ionized lattice defects located in the near proximity to a QD, and (ii) the quantum-dimensional Stark effect [12, 13].

The manifestation of either of the above effects is related to the shift of a peak in the spectrum of deep-level transient spectroscopy (DLTS). In the case of the Coulomb interaction, the shift of the peak depends on the conditions of preliminary isochronous annealing (the presence or absence of a reverse voltage applied during annealing) and is controlled by the formation of a dipole whose built-in electrostatic field affects the height of the barrier for the emission of charge carriers. In the Stark effect, this shift is specified by the heavy dependence of the position of the energy levels for the

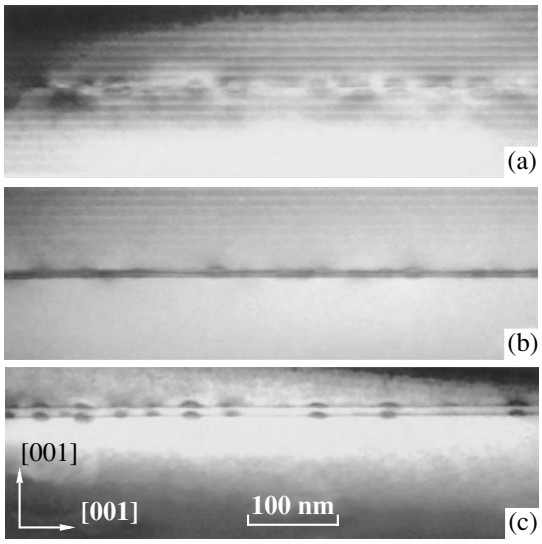

Fig. 1. A microphotograph of a cross section of the samples with two layers of InAs quantum dots separated by a GaAs interlayer with the thickness d_{GaAs} = (a) 20, (b) 40, and (c) 100 Å. The images were obtained using transmission electron microscopy.

states of vertically coupled QDs on the strength of the applied external electric field. The manifestation of these two effects makes it possible to compare the observed DLTS peaks with the quantum states in InAs/GaAs heterostructures that incorporate vertically coupled QDs, and also to determine whether these states correspond to the levels of localized bonding or antibonding *s* and *p* states in vertically coupled QDs. The use of this approach for a vertically coupled QD structure composed of six rows of InAs QDs separated by a GaAs interlayer with a thickness of d_{GaAs} = 40 Å allowed us to establish that the formation of the bonding and antibonding *s* and *p* states for holes occurs for this type of system of coupled QDs [12, 13].

In this paper, we report the results of studying the capacitance–voltage (*C–V*) characteristics and DLTS spectra of quantum states in InAs/GaAs heterostructures that had two rows of vertically coupled QDs in relation to both the thickness of the GaAs interlayer and the reverse-bias voltage U_r. The InAs/GaAs heterostructures with vertically coupled QDs under study were grown by molecular-beam epitaxy (MBE) using self-organization effects.

2. EXPERIMENTAL

The InAs/GaAs heterostructures that include the vertically coupled QDs, and are studied by us, were grown by MBE on n^+-GaAs substrates with a (100) orientation. The QD array was formed as a result of the double deposition of two InAs monolayers that were separated by a GaAs interlayer with a thickness of 20, 40, or 100 Å. The vertically coupled QDs were formed in the midplane of p^0-GaAs with a thickness of 0.90 μm. The p^0-GaAs layer was overgrown with a p^+-GaAs layer. The DLTS studies of the deep traps in the heterostructures were performed using a DL4600 spectrometer, operating as a two-gate integrator, produced by the BIO-RAD Company. In order to carry out the DLTS measurements, we thermally deposited ohmic contacts on the n^+-GaAs substrate and the p^+-GaAs layer. Prior to each DLTS measurement, the sample was annealed isochronously for 1 min at a fixed temperature either in the presence ($U_{ra} < 0$) or in the absence ($U_{ra} = 0$) of applied reverse-bias voltage. The sample was initially heated to 450 K and, if the annealing was performed at $U_{ra} < 0$, was kept at this temperature for 1 min at the zero-bias voltage $U_{ra} = 0$. It was then cooled to the annealing temperature. The sample was kept for some time at $U_{ra} < 0$ if the annealing was performed at $U_{ra} = 0$. The annealing temperature was varied in the range from 80 to 450 K. After annealing, the sample was cooled to 80 K at either $U_{ra} < 0$ or $U_{ra} = 0$. The DLTS measurements were then performed in darkness, unless otherwise specified, or under exposure to white light. In order to determine the concentration profile of the charge carriers in the heterostructures, we measured the *C–V* characteristics. The thermal-activation energy E_a and the cross sections for the charge-carrier capture by traps $\sigma_{n,p}$ were determined by varying the rate windows in the standard DLTS measurements.

3. RESULTS AND DISCUSSION

In Fig. 1, we show microphotographs, obtained using transmission electron microscopy, of the samples with two InAs QD layers separated by a GaAs interlayer with a thickness d_{GaAs} = 20, 40, or 100 Å. The formation mechanism of InAs/GaAs vertically coupled QDs has previously been studied in detail [14]. It was shown that the vertically coupled QDs are formed owing to a self-organization effect that involves the transfer of InAs from the lower QDs to the upper QDs with a subsequent replacement of InAs by GaAs [14]. As can be seen from Fig. 1, the lateral sizes of the lower islands in the system of vertically coupled InAs QDs with d_{GaAs} = 20 or 40 Å do not exceed 170 Å. The lateral sizes of the upper islands are increased to 210–220 Å. For a structure with the interlayer thickness d_{GaAs} = 100 Å, the lateral sizes of the lower and upper islands in the system of vertically coupled InAs QDs are identical and equal to 200–230 Å.

We measured the *C–V* characteristics of *p–n* InAs/GaAs heterostructures with vertically coupled QDs at T = 82 K. The dependences of the capacitance on the bias voltage U_r exhibited a behavior typical of localized states [12]. A single peak was observed in the free-hole concentration profiles $p^*(U_r)$ determined from the *C–V* measurements for the structures with d_{GaAs} = 20 or 40 Å (Fig. 2, curves *1*, *2*). This peak is related to the release of charge carriers from the quantum states of QDs. Two peaks were observed in the

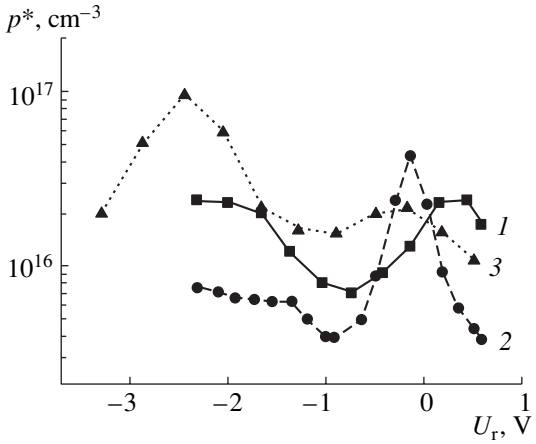

Fig. 2. Concentration profiles $p^*(U_r)$ for the *p–n* InAs/GaAs heterostructures with two layers of InAs quantum dots separated by a GaAs interlayer with the thickness d_{GaAs} = (*1*) 20, (*2*) 40, and (*3*) 100 Å. The profiles were determined from the measurements of *C–V* characteristics at T = 82 K after preliminary isochronous annealing under the reverse-bias voltage $U_{ra} < 0$.

hole-concentration profiles $p^*(U_r)$ for the structures with d_{GaAs} = 100 Å (Fig. 2, curve *3*).

Using the *C–V* measurements, we determined the bias-voltage ranges for which the signals related to the emission of charge carriers from the states of vertically coupled QDs should be observed in the DLTS spectra. In order to determine both the spatial localization of the DLTS signals and the origin of the levels related to them, we measured the spectra at a constant amplitude of the filling-pulse voltage U_f; moreover, we varied the voltage U_r at which the DLTS signal was detected. The results obtained using transmission electron microscopy show that a two-layer system of QDs coupled in the vertical direction exists between the InAs layers of the structures with the GaAs-interlayer thickness d_{GaAs} = 20 or 40 Å. The wave functions of the islands overlap so that electronic properties of vertically coupled QDs belong to a single object. The formation of a two-layer system of QDs is also observed for the structures with the interlayer thickness d_{GaAs} = 100 Å; however, these QDs are not coupled in the vertical direction. The upper and lower QDs have approximately identical lateral sizes, and, in this case, two rows of isolated QDs are observed. Measurements of the *C–V* characteristics show that the peaks related to the localization of charge carriers at the quantum states of vertically coupled QDs are present in the $p^*(U_r)$ profiles of the structures under study. The results of our DLTS studies show that each of these peaks corresponds to peaks in the DLTS spectra (Figs. 3a, 3b). For the structures with two QD layers with an interlayer thickness d_{GaAs} = 20 or 40 Å, two DLTS peaks, $HD1_{20(40)}$ and $HD2_{20(40)}$, are observed in the spectra when U_r varies from –1.25 to –0.25 V and from –0.25 to 0.25 V (Fig. 3b). The DLTS spectrum of the structure with the GaAs interlayer thickness d_{GaAs} =

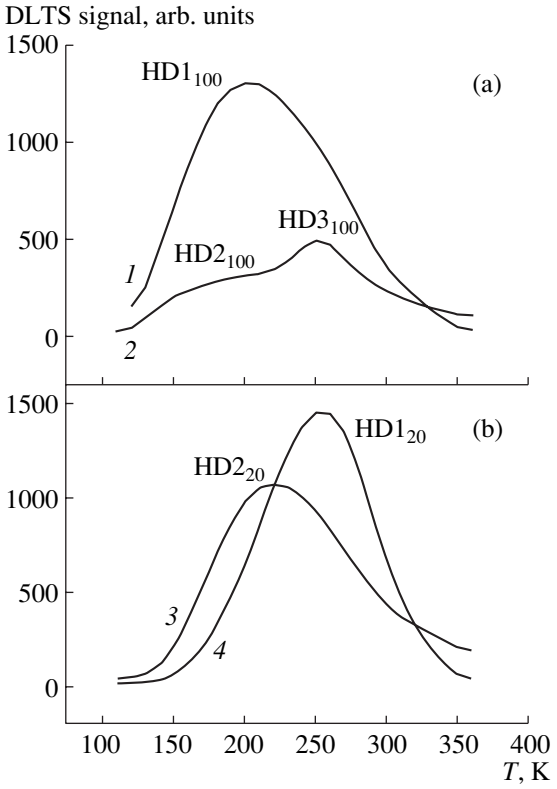

Fig. 3. The DLTS spectra for *p–n* heterostructures with two layers of InAs quantum dots separated by a GaAs interlayer with the thickness d_{GaAs} = (a) 100 and (b) 20 Å. All the spectra were measured at voltages of the reverse-bias pulse U_r = (*1*) 0.08, (*2*) –1.35, (*3*) –0.27, and (*4*) 0.02 V. The emission-rate window was 200 s^{-1}, the filling-pulse amplitude U_f = 0.5 V, and the filling-pulse duration was 25 μs.

40 Å is not shown since this spectrum is identical to that of the structure with d_{GaAs} = 20 Å. The structures with d_{GaAs} = 100 Å also exhibited two DLTS peaks ($HD1_{100}$ and $HD2_{100}$) in the same range of variations in U_r. In addition, as the reverse voltage attains the value $U_r \approx$ 1.35 V, a further DLTS peak ($HD3_{100}$) appears (Fig. 3a).

In order to determine the origin of the above levels, we studied the dependences of the DLTS spectra in the conditions of preliminary isochronous annealing (under conditions of $U_{ra} < 0$ or $U_{ra} = 0$) for the values of U_r that corresponded to characteristic variations in the behavior of the DLTS spectra [12]. For all the structures in this study, as the isochronous-annealing conditions were changed, we observed temperature shifts in the positions of every DLTS peak observed. These shifts are controlled by electrostatic bistable dipoles formed by the charge carriers localized within a QD and by ionized deep-level defects, which is a characteristic feature used to identify the DLTS peaks with the QD states [12]. This circumstance made it possible to compare the DLTS peaks with the quantum states of the vertically coupled QDs. The dependence of the position of the DLTS peaks identified in the above-described way on

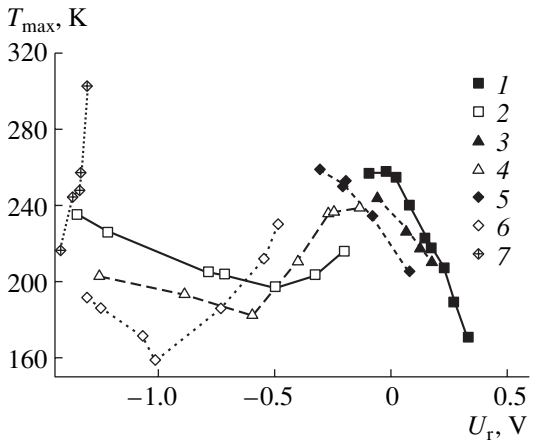

Fig. 4. Dependences of the temperature positions of the DLTS peaks on the voltage of the reverse-bias pulse U_r for the peaks (*1*) $HD1_{20}$, (*2*) $HD2_{20}$, (*3*) $HD1_{40}$, (*4*) $HD2_{40}$, (*5*) $HD1_{100}$, (*6*) $HD2_{100}$, and (*7*) $HD3_{100}$.

the value of U_r was also observed. As was mentioned above, three DLTS peaks ($HD1_{100}$, $HD2_{100}$, and $HD3_{100}$) were observed for the structure with the GaAs interlayer thickness of 100 Å (Fig. 3a). We plotted the dependences of the temperature position of the peaks under consideration on the value of U_r (Fig. 4, curves *5–7*). A shift to higher temperatures in conjunction with an increase in the magnitude of U_r was observed for the $HD1_{100}$ peak (curve *5*). The $HD2_{100}$ DLTS peak shifts to lower temperatures as U_r varies from –0.5 to –1.0 V (curve *6*) and shifts to higher temperatures as U_r varies from –1.0 to –1.5 V. This behavior corresponds to the variation in the thermal-activation energy from 395 to 267 meV (and then to 285 meV). For the $HD3_{100}$ DLTS peak (curve *7*), we managed to observe only a shift of the peak position to lower temperatures as U_r varied from –1.25 to –1.5 V, which corresponded to the variation in E_a from 486 to 431 meV. The observed dependences can be related to the manifestation of the following two effects:

(i) a decrease in the height of the barrier for thermal emission as a result of the manifestation of the field effect [15]; and

(ii) the Stark shift of the energy level of the quantum state [16].

The independent behavior of peaks $HD2_{100}$ and $HD3_{100}$ makes it possible to conclude that they are related to the states of two QDs that are coupled only slightly and separated by a GaAs interlayer. This assumption is also supported by the presence of two peaks in the $p^*(U_r)$ profile for these structures. There are two hypotheses concerning the origin of peak $HD1_{100}$: this peak is either related to the state of the first QD or, which is more likely, related to an interface state at the boundary between the wetting layer and the first QD.

Similar dependences on the value of U_r were observed for the $HD1_{20}$, $HD2_{20}$, $HD1_{40}$, and $HD2_{40}$ peaks that were present in the DLTS spectra of the structures with two rows of QDs and d_{GaAs} = 20 or 40 Å (Fig. 4, curves *1–4*). The thermal-activation energy E_a of the $HD2_{20}$ level (curve *2*) for the structure with d_{GaAs} = 20 Å decreased first from 322 to 195 meV as U_r increased and then increased to 241 meV. We did not observe a peak related to the second QD for the structures with d_{GaAs} = 20 or 40 Å. The results obtained for these structures suggest that, in this case, hybridization of the hole states in the QDs does not occur; rather, we observe the localization of holes at some location in the quantum molecule due to quantum-mechanical tunneling without the formation of bonding and antibonding states (this localization was predicted previously in [7, 17]). This behavior differs from the situation where the hybridization of quantum states is observed for the structures with six rows of QDs. In addition, as can be seen in Fig. 4, a decrease in the thickness of the GaAs interlayer leads to an increase in the energy of the hole states in a QD molecule, which is consistent with the theoretically obtained results [7, 17].

4. CONCLUSION

We established that holes are localized in one of the quantum dots in a quantum molecule composed of two vertically coupled self-organized quantum dots in InAs/GaAs heterostructures with two InAs quantum-dot layers separated by a GaAs interlayer with a thickness of 20 or 40 Å. Incomplete coupling of two quantum-dot layers was observed if the thickness of the GaAs interlayer was 100 Å. This circumstance leads to the redistribution of the hole localization between the upper and lower quantum dots as the reverse-bias voltage applied to the structure is varied.

ACKNOWLEDGMENTS

This study was supported by the scientific program "Physics of Solid-State Nanostructures" and the Russian Foundation for Basic Research (project no. 00-02-16848).

REFERENCES

1. M. V. Maximov, Yu. M. Shernyakov, A. F. Tsatsul'nikov, *et al.*, J. Appl. Phys. **83**, 5561 (1998).
2. T. Lundstrom, W. Schoenfeld, H. Lee, and P. M. Petroff, Science **286**, 2312 (1999).
3. M. Korkusinski and P. Hawrylak, Phys. Rev. B **63**, 195311 (2001).
4. X. Q. Li and Y. Arakawa, Phys. Rev. A **63**, 012302 (2001).
5. B. Partoens and F. M. Peeters, Phys. Rev. Lett. **84**, 4433 (2000).
6. F. Troiani, U. Hohenester, and E. Molinari, Phys. Rev. B **65**, 161301 (2002).

7. M. Bayer, P. Hawrylak, K. Hinzer, *et al.*, Science **291**, 451 (2001).
8. W. Sheng and J.-P. Leburton, Phys. Rev. Lett. **88**, 167401 (2002).
9. I. Shtrichman, C. Metzner, B. D. Gerardot, *et al.*, Phys. Rev. B **65**, 081303 (2002).
10. H. J. Krenner, A. Zrenner, and G. Abstreiter, in *Abstracts of 26th International Conference on the Physics of Semiconductors* (Edinburgh, Scotland, 2002), Part 1, p. 204.
11. T. Bryllet, M. Borgstrom, T. Sass, *et al.*, in *Abstracts of 26th International Conference on the Physics of Semiconductors* (Edinburgh, Scotland, 2002), Part 3, p. 2.
12. M. M. Sobolev, V. M. Ustinov, A. E. Zhukov, *et al.*, Fiz. Tekh. Poluprovodn. (St. Petersburg) **36**, 1089 (2002) [Semiconductors **36**, 1013 (2002)].
13. M. M. Sobolev, V. M. Ustinov, and G. E. Cirlin, Physica B (Amsterdam) **340–342**, 1103 (2003).
14. N. N. Ledentsov, V. A. Shchukin, M. Grundmann, *et al.*, Phys. Rev. B **54**, 8743 (1996).
15. S. Anand, N. Carlsson, M.-E. Pistopl, *et al.*, J. Appl. Phys. **84**, 3747 (1998).
16. A. Patanè, A. Levin, A. Polimeny, *et al.*, Appl. Phys. Lett. **77**, 2979 (2000).
17. W. Sheng and J.-P. Leburton, Appl. Phys. Lett. **81**, 4449 (2002).

Translated by A. Spitsyn

Semiconductors, Vol. 39, No. 1, 2005, pp. 124–126. Translated from Fizika i Tekhnika Poluprovodnikov, Vol. 39, No. 1, 2005, pp. 136–139.

AMORPHOUS, VITREOUS, AND POROUS SEMICONDUCTORS

The Engineering and Properties of InAs Quantum Dot Molecules in a GaAs Matrix

Yu. B. Samsonenko[1]^, G. E. Cirlin[1], A. A. Tonkikh[1], N. K. Polyakov[1], N. V. Kryzhanovskaya[2], V. M. Ustinov[2], L. E. Vorob'ev[3], D. A. Firsov[3], V. A. Shalygin[3], N. D. Zakharov[4], P. Werner[4], and A. Andreev[2, 5]

[1]*Institute for Analytical Instrumentation, Russian Academy of Sciences, St. Petersburg, 198103 Russia*
^*e-mail: samsonenko@beam.ioffe.ru*
[2]*Ioffe Physicotechnical Institute, Russian Academy of Sciences, St. Petersburg, 194021 Russia*
[3]*St. Petersburg State Polytechnical University, St. Petersburg, 195251 Russia*
[4]*Max Planck Institute of Microstructure Physics, 06120 Halle (Saale), Germany*
[5]*Department of Physics, University of Surrey, Guildford, GU2 7XH, UK*
Submitted June 1, 2004; accepted for publication June 14, 2004

Abstract—Arrays of InAs quantum dot (QD) molecules in the GaAs matrix, which consist of pairs of vertically aligned InAs QDs, have been synthesized by molecular beam epitaxy. A study of the resulting structures by transmission electron microscopy demonstrated that the vertically aligned QDs are equal in size. Photoluminescence measurements revealed that the spectra of the samples under study contain bands corresponding to electronic states in QD molecules. © *2005 Pleiades Publishing, Inc.*

1. INTRODUCTION

The properties of semiconductor quantum dots (QDs) have recently been extensively studied. The interest in the phenomenon of QDs is due to their unique properties, existence of techniques for their reproducible fabrication, and possibility of their use in modern micro- and optoelectronics. The electronic structure of a QD is discrete, which is why QDs are frequently named "artificial atoms." A semiconductor QD molecule is an object composed of two or more QDs lying in the immediate vicinity of each other. In the context of this study, two identical QDs coupled by tunneling will be referred to as a QD molecule (QDM). The electronic structure of a QDM constituted by a pair of identical QDs contains split states of separate QDs [1]. The possibility of obtaining terahertz emission via electron transitions from the upper to lower split levels of QDMs has been discussed [2, 3]. Accordingly, QDMs can be regarded as potential terahertz emitters of light.

One of the most extensively used methods for the fabrication of QDs is their epitaxial growth in lattice-mismatched heteroepitaxial systems via self-assembly. One technique that can be used grow QDs in such a way is molecular-beam epitaxy (MBE). In an InAs/GaAs system, the lattice mismatch is as high as 7%. As a result, in epitaxial growth of an InAs layer on the surface of a GaAs substrate, the elastically strained InAs layer disintegrates at a certain instant of time into an array of three-dimensional (3D) InAs islands and a residual quasi-2D InAs layer (wetting layer). As was shown previously in [4], these InAs islands are QDs in which the motion of electrons and holes is confined in every direction. Thus, MBE produces QDs in a natural way, and it is only necessary to terminate the epitaxy at a certain instant of time and to cover the array of InAs QDs with a GaAs layer. Fabrication of QDMs is a more complicated technological task.

It has been shown previously [5] that, if two or more layers of InAs QDs are grown, separated by a thin GaAs spacer, a vertical alignment effect is observed, with the QDs of the upper layer formed directly above the QDs of the lower layer. This effect can be used to obtain closely spaced QDs, which are a prototype of QDMs. A negative phenomenon in the case of vertical alignment is that the size of QDs in the upper layer exceeds those in the lower layer. An approach in which pairs of vertically aligned QDs can be obtained, with each QD having the same size and composition, was suggested in [6]. Nevertheless, the fact that the number of publications devoted to this issue is small means that the fabrication of vertically aligned pairs of identical QDs is a rather complicated technological task inviting additional examination.

The goal of the present study was to develop a reproducible technique for the fabrication of InAs QDMs in a GaAs matrix by MBE and to analyze their properties using transmission electron microscopy (TEM) and the photoluminescence (PL) method.

2. EXPERIMENTAL

The growth experiments were carried out on an EP1203 MBE machine on semi-insulating (100) GaAs

substrates. Several sets of samples with two QD layers separated by a GaAs spacer were grown. In optimizing the technique of QDM fabrication, the following parameters of the structure were varied: the effective thicknesses of InAs in the first and second QD layers, the thickness of the GaAs spacer, and the intermediate-annealing conditions of layers that had QDs.

The structure of the samples was analyzed by diffraction electron microscopy on an SM20 electron microscope at an accelerating voltage of 200 kV.

The electronic structure of the samples was studied using the stationary PL method at a temperature of 77 K. The optical excitation was effected by an Ar^+ laser at a wavelength of 514.5 nm, and the PL signal was detected by a cooled Ge photodetector.

3. RESULTS AND DISCUSSION

The development of the technique for QDM fabrication required that several sets of growth experiments should be carried out.

In the first stage, the influence exerted by high-temperature annealing (HTA) on the uniformity of QDs in the first and second layers of the structure was studied [7]. The HTA was necessary because segregation of In is possible during the growth of QDs and their subsequent overgrowth with a GaAs layer [7]. Thus, at equal thicknesses of deposited InAs in both QD layers, the effective thickness of InAs in the upper layer is greater.

To study the effect of HTA on the uniformity of QDs in different layers, the samples were grown in the following configuration: The effective thickness of InAs in both layers was chosen as 2.5 monolayers (ML), and that of the GaAs spacer, 30 nm. A spacer of this thickness is sufficient for eliminating the influence of the elastic stresses created by the lower layer of QDs on the second QD layer. Moreover, a 30-nm-thick spacer precludes electron tunneling between the QDs of the first and second layers. The InAs QDs formed at 485°C were overgrown with a 5-nm-thick GaAs layer, after which the sample temperature was raised to 610°C and maintained at this level for 1 min (HTA). Then, the sample temperature was lowered to 550°C and the rest of the GaAs spacer (25 nm) was deposited. The QDs of the second layer were formed in a similar manner, with the use of the HTA procedure. The uniformity of the QD array in the first and second layers was assessed by comparing the halfwidths of PL bands for samples with one and two QD layers. The application of the HTA procedure described above did not lead to a broadening of the PL spectra for structures with two QD layers. Consequently, the QD arrays in the first and second QD layers are sufficiently uniform in size.

In the second stage of the study, the thickness of the GaAs spacer was diminished to 10 nm in order to reveal the influence exerted by the elastic stresses produced by the QDs of the first layer on the shape and size of QDs in the second layer. The effective thicknesses of the InAs layers were 2 ML for both QD layers. Figure 1 shows a TEM image of a structure of this kind. It can be seen that the QDs of the second layer exceed the size of those of the first layer. The PL spectra obtained from a sample shown in Fig. 1 contain two PL bands. A study of the influence exerted by the excitation power density on the relative intensities of the PL bands for QDs demonstrated that the ratio of the integral intensities of the two PL bands is the same for any excitation power. Thus, the PL measurements confirmed the existence of two groups of QDs with different sizes in the sample under study.

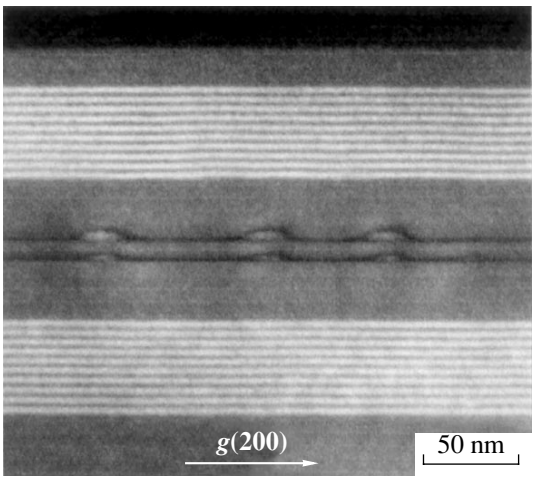

Fig. 1. A cross-sectional TEM image of a structure with two layers of InAs QDs separated by a 10-nm-thick GaAs spacer. The effective thickness of InAs in each layer is 2 ML.

The analysis in the first and second stages of the study demonstrated that it is necessary to use HTA and that, for the QDs in the second layer to be equal in size to the QDs of the first layer, the second InAs layer should have a smaller thickness.

In the third stage, the thickness of the GaAs spacer was chosen as 5 nm. This spacer thickness is sufficient both for the vertical alignment of the second-layer QDs and for the electron tunneling between the vertically aligned QDs to be possible. The primary goal of this stage was to choose the effective InAs thicknesses in the first and second layers in order to obtain QDs of identical size in these layers. Figure 2 shows a TEM image of a structure with two layers of InAs QDs, separated by a 5-nm-thick GaAs spacer, with the effective InAs thicknesses of 4 and 2 ML for the first and second layers, respectively. It can be seen from Fig. 2 that the vertically aligned QDs of the first and second layers are equal in size. The PL spectra measured from this sample at a temperature of 77 K and varied excitation power density are shown in Fig. 3.

It can be seen that the PL spectra contain two peaks $P1$ and $P2$ at any excitation power. This situation is similar to that observed in the sample with a 10-nm spacer and equal effective thicknesses of InAs in both QD layers.

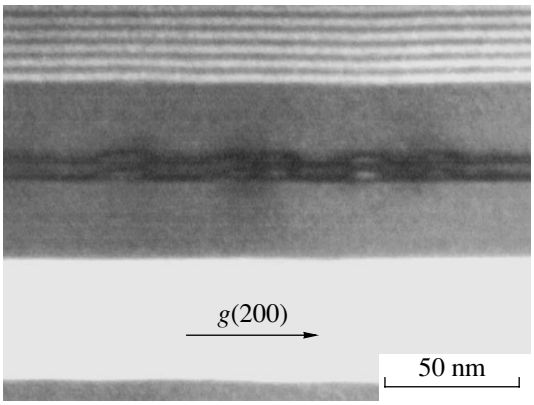

Fig. 2. A cross-sectional TEM image of a sample with two layers of InAs QDs separated by a 5-nm-thick GaAs spacer.

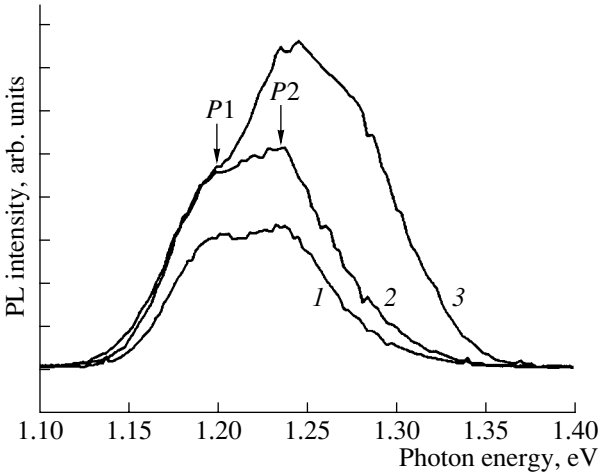

Fig. 3. PL spectra of the sample in Fig. 2, measured at 77 K and an excitation power W: (*1*) W_0, (*2*) $5W_0$, and (*3*) $20W_0$.

However, in the case of the sample with a 5-nm-thick GaAs spacer and varied effective thickness of InAs, the integral intensity of a $P2$ band grows faster than that of a $P1$ band as the excitation power increases. This circumstance is presumably due to the splitting into symmetric and antisymmetric states. To reveal the true mechanism responsible for the appearance of the $P1$ and $P2$ bands, an additional study was performed by means of the time-resolved PL method [8]. The data obtained, as well as the good agreement between the energy of splitting of the $P1$ and $P2$ bands and the results of a theoretical calculation performed for a model sample with a 5-nm GaAs spacer, confirm the formation of QDM in this sample.

4. CONCLUSION

Thus, a procedure has been developed for the fabrication of tunnel-coupled pairs of identical QDs, QD molecules, by MBE. A TEM study of samples that had QDMs demonstrated that vertically aligned pairs of QDs of the same size, separated by a 5-nm-thick spacer, are present in their structure. The results of a PL study of samples with vertically aligned tunnel-coupled QDs are in a good agreement with the calculations performed for QDMs of the configuration under discussion.

ACKNOWLEDGMENTS

The study was supported by INTAS, project no. 2001-0615, and the Russian Foundation for Basic Research.

REFERENCES

1. M. Bayer, P. Hawrylak, K. Hinzer, *et al.*, Science **291**, 451 (2001).
2. P. Boucaud, J. B. Williams, K. S. Gill, *et al.*, Appl. Phys. Lett. **77**, 4356 (2000).
3. P. Boucaud, K. S. Gill, J. B. Williams, *et al.*, Appl. Phys. Lett. **77**, 510 (2000).
4. D. Bimberg, M. Grundmann, and N. N. Ledentsov, *Quantum Dot Heterostructures* (Wiley, Chichester, 1998).
5. L. Goldstein, F. Glas, J. Y. Marzin, *et al.*, Appl. Phys. Lett. **47**, 1099 (1985).
6. S. Fafard, M. Spanner, J. P. McCaffrey, and Z. R. Wasilewski, Appl. Phys. Lett. **76**, 2268 (2000).
7. Z. R. Wasilewski, S. Fafard, and J. P. McCalrey, J. Cryst. Growth **201–202**, 1131 (1999).
8. V. G. Talalaev, J. W. Tomm, N. D. Zakharov, *et al.*, Fiz. Tekh. Poluprovodn. (St. Petersburg) **38**, 723 (2004) [Semiconductors **38**, 696 (2004)].

Translated by M. Tagirdzhanov

Semiconductors, Vol. 39, No. 1, 2005, pp. 127–131. Translated from Fizika i Tekhnika Poluprovodnikov, Vol. 39, No. 1, 2005, pp. 140–144.

AMORPHOUS, VITREOUS, AND POROUS SEMICONDUCTORS

Resonant Raman Scattering and Atomic Force Microscopy of InGaAs/GaAs Multilayer Nanostructures with Quantum Dots

M. Ya. Valakh*^, V. V. Strelchuk*, A. F. Kolomys*, Yu. I. Mazur, Z. M. Wang**, M. Xiao**, and G. J. Salamo****

**Institute of Semiconductor Physics, National Academy of Sciences of Ukraine, Kiev, 03028 Ukraine*

^e-mail: valakh@isp.kiev.ua

***University of Arkansas, Department of Physics, 72701 Arkansas, USA*

Submitted June 1, 2004; accepted for publication June 16, 2004

Abstract—The transition from two-dimensional (2D) pseudomorphic growth to the three-dimensional (3D) (nanoisland) growth in $In_xGa_{1-x}As/GaAs$ multilayer structures grown by molecular-beam epitaxy was investigated by atomic force microscopy, photoluminescence, and Raman scattering. The nominal In content x in $In_xGa_{1-x}As$ was varied from 0.20 to 0.50. The thicknesses of the deposited $In_xGa_{1-x}As$ and GaAs layers were 14 and 70 monolayers, respectively. It is shown that, at these thicknesses, the 2D–3D transition occurs at $x \geq 0.27$. It is ascertained that the formation of quantum dots (nanoislands) does not follow the classical Stranski–Krastanov mechanism but is significantly modified by the processes of vertical segregation of In atoms and interdiffusion of Ga atoms. As a result, the $In_xGa_{1-x}As$ layer can be modeled by a 2D layer with a low In content ($x < 0.20$), which undergoes a transition into a thin layer containing nanoislands enriched with In ($x > 0.60$). For multilayer $In_xGa_{1-x}As$ structures, lateral alignment of quantum dots into chains oriented along the $[\bar{1}10]$ direction can be implemented and the homogeneity of the sizes of quantum dots can be improved. © *2005 Pleiades Publishing, Inc.*

1. INTRODUCTION

An important line of development of fundamental and applied solid-state physics is investigating the processes of self-assembled formation of semiconductor quantum dots (QD) upon molecular-beam growth of strained heterostructures. It is believed that this process follows the Stranski–Krastanov mechanism; i.e., when the thickness of a deposited layer attains some critical thickness, elastic strain relaxation occurs with the formation of three-dimensional (3D) nanoislands (QDs) on a thin (several monolayers) two-dimensional (2D) wetting layer.

Most attention has been paid to InAs QDs, which are formed as a result of the 2D–3D transition under epitaxial growth of strained InAs/GaAs heterostructures. Some recent results indicate that the initiation and the growth of InAs QDs cannot be described in terms of the classical Stranski–Krastanov mechanism. It was indicated that these processes may be affected by the vertical segregation of In atoms and interdiffusion of Ga atoms [1]. For $In_xGa_{1-x}As$ QDs formed in a GaAs matrix, the situation is even more complicated due to the simultaneous deposition of cations of two types. In addition, despite the fact that arrays with high densities (~10^{11} cm^{-2}) of $In_xGa_{1-x}As$ QDs have been obtained, the spread of sizes and shapes of QDs hinder their wide application in practice. The use of multilayer structures makes it possible to solve in general the problem of vertical alignment of QDs along the growth direction and improve the homogeneity of their sizes [2, 3], but lateral alignment (in the interface plane) is still a problem [4–6]. In the case of multilayer nanoisland structures $In_xGa_{1-x}As/GaAs$, the alignment critically depends on the surface elastic anisotropy of the matrix material [7] and the crystallographic orientation of the surface [8]. Previously, we showed for a multilayer system that, with the use of growth interruption upon deposition of a separating GaAs layer, lateral alignment of QDs into a line can be implemented with an increasing number of layers. The QD parameters and the features of their spatial alignment are controlled by the epitaxial growth conditions.

In this study, we investigated the formation and optical properties of QDs in $In_xGa_{1-x}As$ multilayer structures by methods of atomic force microscopy, resonant Raman scattering, and photoluminescence. It is shown that laterally ordered QD arrays can be formed in such structures upon deposition of $In_{0.5}Ga_{0.5}As$ solid solution onto a (100) plane.

2. EXPERIMENTAL

$In_xGa_{1-x}As/GaAs$ multilayer structures with quantum wells (QWs) and QDs were grown on semi-insulating GaAs(100) substrates by molecular-beam epitaxy. After removal of the oxide layer from the surface, a buffer GaAs layer 0.5 μm thick was grown at a rate of one monolayer (ML) per second. All samples were grown at a constant As vapor pressure (10^{-5} Torr).

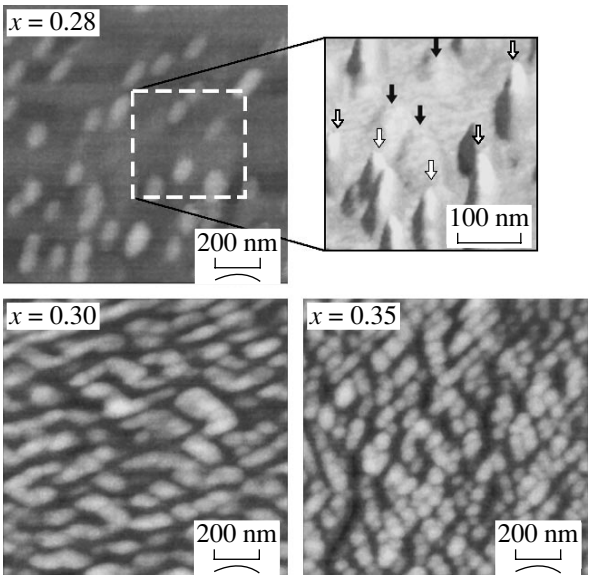

Fig. 1. AFM images of uncovered $In_xGa_{1-x}As$ layers with QDs in $In_xGa_{1-x}As/GaAs$ structures with different nominal In contents x. The inset shows the enlarged image of the sample with $x = 0.28$; the QDs of types A and B are denoted by open and closed arrows, respectively.

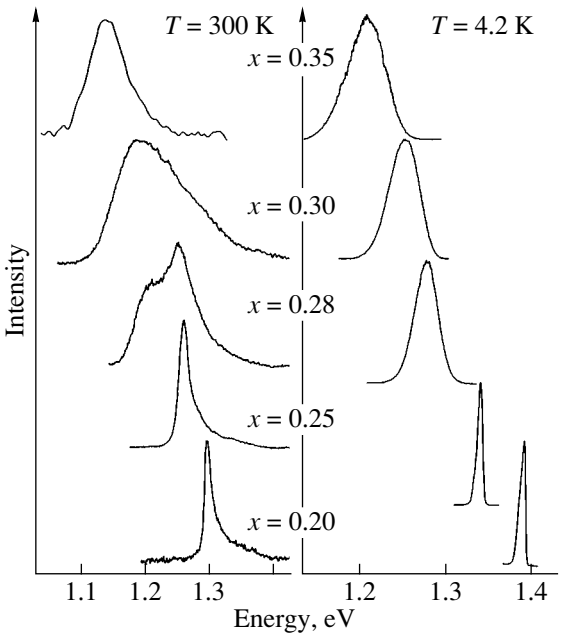

Fig. 2. PL spectra of $In_xGa_{1-x}As/GaAs$ multilayer structures with different In contents in $In_xGa_{1-x}As$ layers at T = 300 and 4.2 K. The energy of excitation photons is 2.54 eV.

The first series of 8-period $In_xGa_{1-x}As$ (14 ML)/GaAs(70 ML) structures was grown at a substrate temperature of 520°C. The nominal In content was x = 0.2, 0.25, 0.28, 0.30, and 0.35. The transition from the 2D pseudomorphic growth to the 3D growth was monitored by high-energy electron diffraction. At the noted thicknesses of $In_xGa_{1-x}As$ layers, the 2D–3D transition was not implemented for the samples with x = 0.2 and 0.25. For x = 0.28, 0.30, and 0.35, this transition was observed at thicknesses of $In_xGa_{1-x}As$ layers of 14.0, 10.7, and 7.4 ML, respectively.

The second series of $In_xGa_{1-x}As$(9.8 ML)/GaAs(60 ML) structures was grown at a substrate temperature of 540°C and growth rates of GaAs and $In_{0.5}Ga_{0.5}As$ layers of 0.4 and 0.2 ML/s, respectively. The separating GaAs layers were deposited using growth interruption.

Raman spectra were excited by a cw Nd YAG laser (λ = 1.0642 μm) and measured by a BOMEM Fourier interferometer. Photoluminescence (PL) spectra were excited by the 488-nm line of an Ar laser. The nanomorphology of the sample surfaces was investigated on an AFM Dimension 3000 atomic force microscope (DI Nano Scope IIIA).

3. RESULTS AND DISCUSSION

Figure 1 shows the atomic force microscopy (AFM) images of the upper uncovered layer of $In_xGa_{1-x}As$ QDs for 8-period $In_xGa_{1-x}As/GaAs$ structures with $x \geq 0.28$. At x = 0.28, QDs of two types can be seen: high 3D islands (type A) and flattened (2D) islands with a small ratio of height to lateral size (type B). In both cases, the QD bases are ellipses with major and minor axes oriented along the $[\bar{1}10]$ and [110] directions, respectively. With an increase in x, the density of islands increases, and their size distribution becomes more uniform. When x changes from 0.30 to 0.35, the average lengths of the major and minor ellipse axes decrease from 42 to 35 nm and from 22 to 15 nm, respectively. Although QDs come in contact with each other at x = 0.35, no coalescence with formation of large islands (characteristic of InAs QDs) was observed. This circumstance indicates that, as was noted above, the distribution of In and Ga atoms in the $In_xGa_{1-x}As$ layer may be nonuniform due to the vertical segregation of In atoms into the upper regions of $In_xGa_{1-x}As$ QDs [9].

At x = 0.2 and 0.25, the PL spectra (Fig. 2) contain a strong emission band of $In_xGa_{1-x}As$ QWs. The asymmetry of this band at T = 300 K is due to the thermally activated trapping of carriers into the regions with a lower In content and (or) monolayer fluctuations of the QW thickness. At T = 4.2 K, the PL lines show no asymmetry.

The morphological 2D–3D transition in the sample with x = 0.28 is responsible for the radical broadening of the PL band. Two overlapping emission bands are observed at room temperature. At T < 100 K, only the low-energy emission component manifests itself. At T > 100 K, the intensity is redistributed to the high-energy band. The activation energy of quenching of the

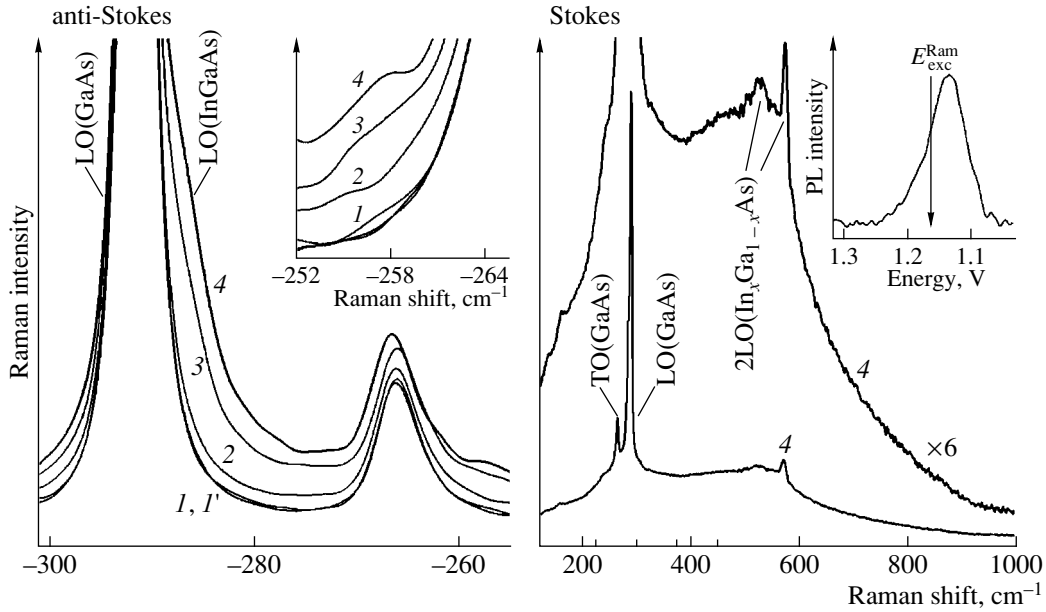

Fig. 3. Anti-Stokes and Stokes Raman spectra of $In_xGa_{1-x}As/GaAs$ multilayer structures with nominal In content x = (*1*) 0.2, (*2*) 0.28, (*3*) 0.30, and (*4*) 0.35. Curves *2–4* are shifted along the vertical axis. Curve *1*' corresponds to the GaAs/GaAs(100) structure. The inset in the Stokes region shows the PL spectrum of the structure with $x = 0.35$ at an energy of excitation photons of 2.54 eV. The arrow shows the energy of excitation photons for the Raman spectrum (R^{Ram}_{exc} = 1.165 eV). T = 300 K.

high-energy band (~47 meV), found from temperature measurements, corresponds exactly to the energy spacing between the maxima of these bands. We suggest that this redistribution is due to the thermally induced passage of carriers from large QDs enriched with In to small planar QDs with a lower In content (Fig. 1). The latter can be regarded as nucleation centers for 3D islands. An alternative explanation for the temperature redistribution of the band intensities—the involvement of excited states of QDs—contradicts the absence of any redistribution of the intensities of the bands considered at a significant change in the excitation level.

It is noteworthy that the efficiency of carrier trapping by QDs with subsequent emission is rather high. For example, the PL of fairly thick GaAs barrier layers was several hundred times lower. At the same time, in the samples without islands (x = 0.20 and 0.25), the intensity of emission from QWs was only several times higher than the PL intensity of the GaAs barrier layers.

Figure 3 shows the Raman spectra in the Stokes and anti-Stokes regions for the structures under study at T = 300 K. For comparison, curve *1*' shows the spectrum of an additional structure with an epitaxial GaAs layer deposited onto a GaAs(100) substrate under the same conditions. The thickness of the epitaxial layer is equal to the total thickness of the separating barrier and upper protective GaAs layers in the $In_xGa_{1-x}As/GaAs$ structures under study. The coincidence of curves *1* and *1*' indicates that, before the formation of QDs, the Raman spectrum is completely controlled by scattering only by LO (291.7 cm^{-1}) and TO (266.5 cm^{-1}) phonons in the GaAs protective, separating, and buffer layers. The weak scattering by TO phonons, which is forbidden for the (100) plane, manifested itself due to insignificant violations of the crystal structure in the GaAs separating layers.

For the structures with $x \geq 0.28$, the formation of nanoislands manifests itself in the additional scattering in the spectral ranges 280–288 and 255–260 cm^{-1}. We suggest that both these Raman signals are related to the contribution of the scattering by LO phonons in $In_xGa_{1-x}As$. As is well known, this solid solution belongs to materials with the so-called two-mode phonon reconstruction [10]. This type of phonon reconstruction is characterized by simultaneous manifestation of optical phonons in the frequency ranges typical of both binary components forming the solid solution. In the case under consideration, we are speaking of two LO(GaAs)-like modes due to the presence of two sublayers in the $In_xGa_{1-x}As$ layer with significantly different In contents. This is in agreement with the above-noted manifestation of the vertical segregation of In atoms.

More evident proof of the existence of two regions with different In contents follows from the analysis of the two-phonon 2LO-Stokes Raman spectrum for the sample with x = 0.35. In this case, nearly exact conditions for the output resonance with the electronic excitation of QDs enriched with In were implemented (see inset in Fig. 3 in the Stokes region). Under the resonance conditions, the scattering by longitudinal optical

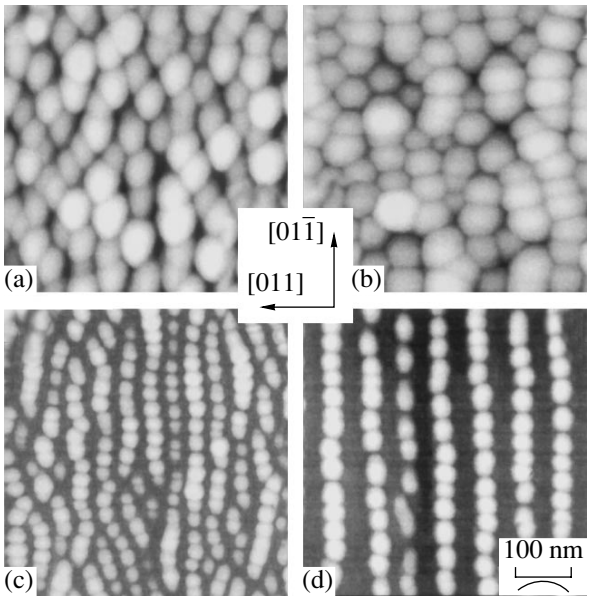

Fig. 4. AFM images of $In_xGa_{1-x}As$ layers uncovered with GaAs in $In_{0.5}Ga_{0.5}As/GaAs$ structures with QDs. The number of InGaAs layers is (a) 2, (b) 7, (c) 9, and (d) 17.

phonons should be enhanced due to the Fröhlich interaction. As can be seen from Fig. 3, two scattering peaks are observed in the second-order spectrum: a rather narrow peak at 573 cm^{-1} (Γ = 9.6 cm^{-1}) and a much wider peak at 528 cm^{-1} (Γ = 23 cm^{-1}). These values are in satisfactory agreement with the doubled frequencies of LO phonons observed in the first-order Raman spectrum.[1] Approximate estimation based on the values of the frequencies of LO(GaAs)-like phonons and the In content obtained from the known dependence of the phonon frequencies on the composition for bulk $In_xGa_{1-x}As$ [12] gave "true" values of x: x_{tr} = 0.15 and 0.65 in InGaAs layers and QDs, respectively. To determine the values of x_{tr} more accurately, one has to take into account the effects of spatial confinement and strain.

Thus, we can conclude that the main characteristic feature of the formation of $In_xGa_{1-x}As$ QDs in strained heterostructures is the formation of a 2D GaAs layer with a lower (in comparison with the nominal) In content at the interface with the GaAs substrate. The formation of this layer results from the tendency of the system to thermodynamic stability by decreasing the lattice mismatch between the substrate and the epitaxial layer. The components of InGaAs are redistributed due to the self-induced vertical segregation of In atoms and interdiffusion of Ga atoms into the interface region of the heterostructure. As a result, it turns out that 3D islands emerging from the 2D $In_xGa_{1-x}As$ layer (which is depleted with In) are characterized by the In content exceeding the nominal value by a factor of two. This two-step character (in the first-order approximation) of In distribution in $In_xGa_{1-x}As/GaAs$ multilayer structures was also confirmed by X-ray data [13].

As was noted above, a characteristic feature of the $In_xGa_{1-x}As$ QDs obtained is their elliptical base. This shape of the base is likely to be due to the anisotropy of the surface diffusion of In or Ga atoms (presumably, In atoms), which is induced by the strain anisotropy. In order to verify this hypothesis, we prepared another series of samples with $In_xGa_{1-x}As$ QDs (x = 0.5).

Figure 4 shows the AFM data for $In_{0.5}Ga_{0.5}As/GaAs(100)$ structures with InGaAs layers uncovered by GaAs. As can be seen from Fig. 4, the deposition of the second $In_{0.5}Ga_{0.5}As$ layer leads to the formation of an array of laterally unordered QDs with elliptical bases. With an increase in the number of periods, the homogeneity of QD sizes significantly improves. Even for the 9-period structure, lateral alignment of QDs in the form of chains along the [01$\bar{1}$] direction is observed. For the 17-period multilayer structure, the length of such QD chains is as high as 5 μm.

4. CONCLUSIONS

The investigation of the 2D–3D morphological transition induced by a change in the In content in 8-period $In_xGa_{1-x}As/GaAs$ structures showed that the $In_xGa_{1-x}As$ QDs with $x_{tr} \gg x$ are formed on a fairly thick $In_xGa_{1-x}As$ layer depleted with In ($x_{tr} < x$). This fact indicates that the nucleation of $In_xGa_{1-x}As$ QDs (nanoislands) does not follow the classical Stranski–Krastanov mechanism and is modulated to a large extent by the vertical segregation of In atoms and interdiffusion of Ga atoms. It is shown that the elliptical shape of the QD base may be much more pronounced in multilayer structures. As a result, lateral alignment of QDs in chains oriented along the [$\bar{1}$10] direction can be implemented and the homogeneity of their sizes can be improved.

REFERENCES

1. A. Rosenauer, D. Gerthsen, D. Van Dyck, *et al.*, Phys. Rev. B **64**, 245334 (2001); I. Kegel, T. H. Metzger, A. Lorke, *et al.*, Phys. Rev. B **63**, 035318 (2001); T. Walther, A. G. Gullis, D. J. Norris, and M. Hopkinson, Phys. Rev. Lett. **86**, 2381 (2001); N. Liu, J. Tersoff, O. Baklenov, *et al.*, Phys. Rev. Lett. **84**, 334 (2000).
2. C. Teichert, L. J. Peticolas, J. C. Bean, *et al.*, Phys. Rev. B **53**, 16334 (1996).

[1] It was reported [11] about the presence of interface modes of electrostatic nature in the resonance Raman spectra of self-assembled InAs/GaAs QDs. The interface modes may occur only in the presence of a sharp interface between separating GaAs layers and $In_xGa_{1-x}As$ QDs. However, in the case under consideration, the segregation of In atoms along the growth direction leads to a diffuse interface with respect to the value of x; hence, the occurrence of interface modes of electrostatic nature is unlikely.

3. G. S. Salamon, S. Komarov, J. S. Hariss, and Y. Yamamoto, J. Cryst. Growth **175–176**, 707 (1997).
4. Q. Xie, A. Madhukar, P. Chen, and N. Kabayashi, Phys. Rev. Lett. **75**, 2542 (1995).
5. S. Guha, A. Madhukar, and K. C. Rajkumar, Appl. Phys. Lett. **57**, 2110 (1990).
6. G. S. Salamon, J. A. Trezza, A. F. Marshall, and J. S. Harris, Jr., Phys. Rev. Lett. **76**, 952 (1996).
7. Z. M. Wang, K. Holmes, Yu. I. Mazur, and G. I. Salamo, Appl. Phys. Lett. **84**, 1931 (2004).
8. H. Wen, Z. M. Wang, and G. I. Salamo, Appl. Phys. Lett. **84**, 1756 (2004).
9. H. Li, Q. Zhuang, Z. Wang, and T. Daniels-Race, J. Appl. Phys. **87** (1), 188 (2000).
10. T. P. Persall, R. Carles, and J. L. Portal, Appl. Phys. Lett. **42**, 436 (1983).
11. Yu. A. Pusep, G. Zanelatto, S. W. Da Silva, *et al.*, Phys. Rev. B **58**, R1770 (1998).
12. G. Landa, R. Carles, and I. B. Runucci, Solid State Commun. **86**, 351 (1993).
13. V. V. Strel'chuk, V. P. Klad'ko, M. Ya. Valakh, *et al.*, Nanosist. Nanomater. Nanotekhnol. **1** (1), 309 (2003).

Translated by Yu. Sin'kov

Semiconductors, Vol. 39, No. 1, 2005, pp. 132–135. Translated from Fizika i Tekhnika Poluprovodnikov, Vol. 39, No. 1, 2005, pp. 145–148.

AMORPHOUS, VITREOUS, AND POROUS SEMICONDUCTORS

Photoluminescence and the Raman Scattering in Porous GaSb Produced by Ion Implantation

Yu. A. Danilov*^, A. A. Biryukov*, J. L. Gonçalves, J. W. Swart**, F. Iikawa***, and O. Teschke*****

**Physicotechnical Research Institute at Lobachevsky State University, Nizhnii Novgorod, 603950 Russia*
^e-mail: danilov@phys.unn.ru
***Centro de Componentes Semiconductores—UNICAMP, 13083-970 Campinas, SP, Brazil*
****Instituto de Fisica "Gleb Wataghin"—UNICAMP, 13081-970 Campinas, SP, Brazil*
Submitted June 1, 2004; accepted for publication June 16, 2004

Abstract—Atomic-force microscopy, photoluminescence, and Raman scattering are used to study the formation of the porous layer in ion-implanted GaSb. As the ion dose increases, first a system of hillocks is formed at the GaSb surface and then a porous layer is produced. The height of the step at the boundary between the porous layer and the unirradiated region can be as large as 1 μm. A broad band is observed in the photoluminescence spectrum in the range from 1.1 to 1.65 eV for ion-implanted GaSb; the intensity of this band increases with the ion dose. Additional lines peaked at 111 and 145 cm^{-1} are observed in the Raman spectra of porous GaSb. These lines are characteristic of an oxidized semiconductor. The data obtained indicate that the porous layer that formed as a result of ion implantation into GaSb exhibits properties that are characteristic of nanocrystalline systems. © *2005 Pleiades Publishing, Inc.*

1. INTRODUCTION

The discovery of intense luminescence in porous silicon [1, 2] caused an increased interest in studies of light-emitting semiconductor structures using this material. Porous Si is structurally a network of channels (voids); as a result, we have a system of crystallites of various sizes. The crystallites are surrounded by surface barriers and/or native-oxide layers. The smallest crystallites have sizes on the order of several nanometers. As a result, the quantum-dimensional broadening of the semiconductor band gap gives rise to the photoluminescence and electroluminescence of porous Si in the visible region of the spectrum. Porous layers can also be formed at the surface of other semiconductors, including SiC [3, 4], GaAs [5–7], InP [8], and GaP [9]. The aforementioned porous semiconductors are produced by electrochemical treatment of a single-crystal wafer; the electrolyte used in this treatment is specially chosen for each material. In this context, it is worth noting that a porous layer can be formed by ion implantation in some of III–V semiconductors (InSb [10], GaSb [11], and GaN [12]). However, the optical properties of these ion-implanted materials have not been studied adequately.

2. EXPERIMENTAL

In this study, single-crystal *n*-GaSb samples with (100) orientation were irradiated with medium-energy ions using doses D in the range from 1×10^{13} to 1×10^{16} cm^{-2} while the target was at room temperature. We used ions with various masses (from $^{11}B^+$ to $^{55}Mn^+$). All ion implantations were performed under conditions where the channeling was suppressed by tilting the sample by an angle of ~7° between the normal to the sample surface and the direction of the incident ion beam. The ion energy was 50 keV, unless otherwise specified.

Photoluminescence (PL) was measured at 77 K and was excited by radiation from the He–Ne or Ar lasers. The PL signal was detected using a photomultiplier or a Ge detector.

The Raman spectra were recorded at room temperature. We used an Ar^+ laser with the radiation at a wavelength of 514.5 nm as the excitation source. The laser beam was focused onto the sample surface using the lens system of a microscope. The Raman spectra were recorded in the backscattering geometry using a detector based on a charge-coupled device cooled to 77 K.

The morphology of implanted samples was studied using a TopoMetrix TMX 2000 atomic-force microscope (AFM) (IFGW-UNICAMP). The average step height h at the boundary between the irradiated and unirradiated areas of the wafer was measured using a DECTAK-3 ST system; the force applied to the tip was no greater than 0.1 N.

3. RESULTS AND DISCUSSION

An AFM study of the GaSb surface irradiated with ions revealed appreciable changes in the morphology of implanted regions; for example, the formation of hillocks with a height of ~10 nm, a pedestal diameter of

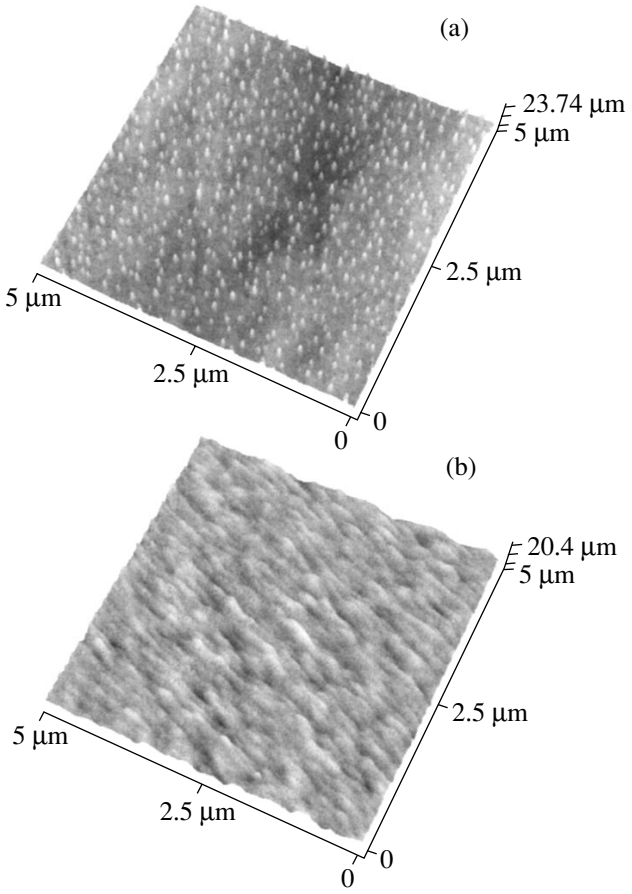

Fig. 1. The AFM images of the morphology of the GaSb surface irradiated with N^+ ions with doses of (a) 1×10^{15} and (b) 1×10^{16} cm^{-2}.

~60 nm, and a density of ~3×10^9 cm^{-2} were observed after implantation of N^+ ions with $D = 9 \times 10^{14}$–1×10^{15} cm^{-2} (Fig. 1a). As the dose increased to 1×10^{16} cm^{-2} (Fig. 1b), the formation of a morphological profile whose image is characteristic of a porous layer [13] was observed. The formation of a porous layer in our experiments correlated with the appearance of the profile step with the average height h at the boundary between the implanted and unimplanted regions. In particular, $h \approx 14$ nm in the case of irradiation with N^+ ions at a dose of 1×10^{16} cm^{-2}. Experiments with the implantation of the F^+ and Si^+ ions showed that similar changes in the GaSb surface also occurred as the radiation dose was increased. It is noteworthy that the doses characteristic of the aforementioned morphological changes decrease as the ion mass increases. For example, the threshold dose for the formation of hillocks decreases to ~5×10^{13} cm^{-2} for F^+ ions and to 5×10^{12} cm^{-2} for Si^+ ions. Thus, the changes in the morphology and the porous-layer formation are independent of the fact of whether the ions used are from gaseous elements (N^+) or not (Si^+); rather, these changes are caused by the generation of radiation defects produced as a result of the slowing-down of fast ions in the matrix. It is clear that an increase in the ion mass at the same ion energy leads to an increase in the concentration of the radiation defects produced in GaSb by each incident ion.

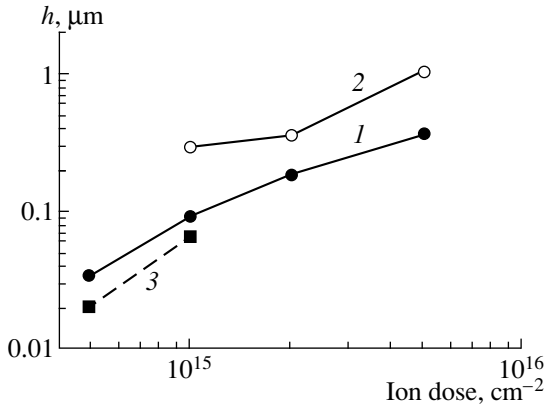

Fig. 2. The dependence of the step height h on the ion dose for (*1*) 40-keV Ar^+ ions, (*2*) 80-keV Ar^+ ions, and (*3*) 50-keV Si^+ ions.

The step height is controlled by the mass, energy, and ion dose and can be as large as 1 μm. In Fig. 2, we show the dependences of h on doses of the Ar^+ and Si^+ ions. It can be seen that, in the first approximation, the value of h is directly proportional to $D - D_{inc}$, where D_{inc} is the incubation void-formation dose, and is approximately equal to 2×10^{14} cm^{-2} for the Ar^+ ions with energies of 40–80 keV.

Only a fundamental band peaked at the photon energy of ≈0.75 eV is observed in the PL spectrum of the starting sample (Fig. 3, curve *1*); this band corresponds approximately to the GaSb band gap at the measurement temperature [14]. This band is not observed in the PL spectrum of ion-implanted GaSb. A broad band shifted to shorter wavelengths with respect to the fundamental band is observed in the PL spectra of the samples irradiated with ions in fairly high doses (exceeding those for the void formation). In Fig. 3 (curve *2*), we show the PL spectrum for the case of implantation with 200-keV Mn^+ ions (the dose was 1×10^{14} cm^{-2}). The spectrum consists of a band in the range of photon energies from 1.1 to 1.65 eV. The intensity of this broad band increases as the ion dose increases (see curve *3* in Fig. 3 for the Mn^+ ion dose of 1×10^{15} cm^{-2}). It is worth noting here that the appearance of a similar band in the short-wavelength (0.9–1.4 eV) region of the PL spectrum was reported previously [15] for GaSb irradiated with low-energy Ar^+ ions using doses of $\geq 4 \times 10^{17}$ cm^{-2} and was attributed to the formation of quantum dots at the sputtered surface.

The Raman spectrum for an unimplanted GaSb sample is shown in Fig. 4 (curve *1*). An intense line peaked at ≈234 cm^{-1} in this spectrum corresponds to a longitudinal optical (LO) phonon. The position of this

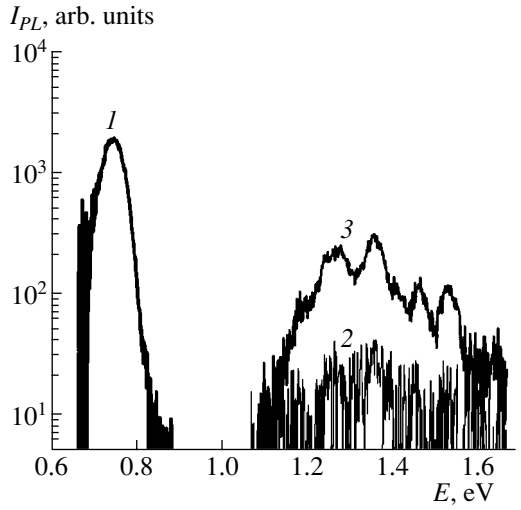

Fig. 3. The photoluminescence spectra at 77 K for (*1*) the as-grown GaSb sample, (*2*) the GaSb sample implanted with 200-keV Mn^+ ions at a dose of 1×10^{14} cm^{-2}, and (*3*) the GaSb sample implanted with Mn^+ ions at a dose of 1×10^{15} cm^{-2}.

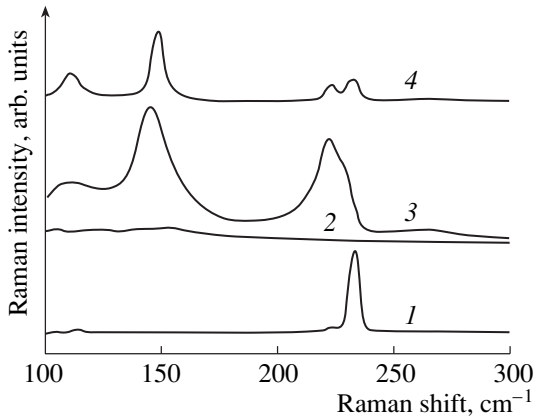

Fig. 4. The Raman spectra for (*1*) the as-grown GaSb sample, (*2*) the GaSb sample implanted with Si^+ ions with a dose of 5×10^{13} cm^{-2}, (*3*) the GaSb sample implanted with Si^+ ions with a dose of 1×10^{15} cm^{-2}, and (*4*) the unimplanted oxidized GaSb sample.

line is not much different from that described in the available published data (236 cm^{-1}) [16]. The appearance of this line is consistent with the selection rules for the (100) orientation. In addition, a low-intensity line at a wave number of ≈222 cm^{-1} is observed, which corresponds to a mode that is forbidden in the geometry under consideration and is related to a transverse optical (TO) phonon. The appearance of the line under consideration is caused by minor violations in the backscattering geometry and/or by deviation of the wafer orientation from the (100) plane.

The LO-line intensity decreases as a result of implantation, and, ultimately, this line is no longer observed. This behavior is illustrated by the Raman spectrum for GaSb irradiated with Si^+ ions at a dose of 5×10^{13} cm^{-2} (Fig. 4, curve *2*). As the ion mass is decreased, the LO line disappears at a higher dose, for example, at $D > 1 \times 10^{14}$ cm^{-2} for N^+ ions. Such behavior is characteristic of ion-implanted III–V semiconductors and is related to the disordering of the crystal structure in these materials [17]. However, as the dose is increased above that for the void-formation threshold (at $D > 1 \times 10^{14}$ cm^{-2} for Si^+), two new peaks appear in the Raman spectrum: a peak at 111 cm^{-1} with a lower intensity and a peak at 145 cm^{-1} with a higher intensity (Fig. 4, curve *3*). These peaks were not observed in the Raman spectrum of unirradiated GaSb. In addition, a fairly broad asymmetric line is observed; this line can be resolved into two Lorentzian lines peaked at 221 cm^{-1} (a line with a higher intensity) and 227 cm^{-1} (a line with a lower intensity). As the ion dose is increased further, the intensities of all the aforementioned peaks increase (at least, until the highest dose of 1×10^{15} cm^{-2} used in our experiments for Si^+ ions is attained).

Apparently, the lines peaked at 221 and 227 cm^{-1} can be attributed to the peaks shifted somewhat from the normal position and related to the GaSb TO and LO phonons, respectively. In order to clarify the origin of the Raman peaks at 111 and 145 cm^{-1}, we studied unirradiated GaSb samples oxidized in an oxygen flow for 15 min at 600°C. The Raman spectrum for one of these samples is shown in Fig. 4 (curve *4*). It can be seen that, in addition to the LO line at 233 cm^{-1} and the TO line at 224 cm^{-1} with a lower intensity characteristic of an unirradiated GaSb crystal, two low-frequency lines are observed. The satisfactory agreement between the positions of these lines in oxidized unimplanted GaSb and those of peaks at 111 and 145 cm^{-1} indicates that a significant oxide phase is present in implanted porous GaSb.

As a whole, the pattern of phenomena occurring in the course of ion implantation into GaSb can be conceived in the following way: As the ion dose increases, radiation defects are accumulated in the crystal, which leads to the disappearance of both the Raman LO peak and the PL fundamental band (as a result of the formation of the nonradiative-recombination centers). As the ion dose is increased further, the vacancy-containing complexes (voids) are formed, which gives rise to hillocks above the voids. The density and size of the voids increase with an increasing ion dose; as a result, the porous layer is ultimately formed. The surface exposure of the voids can give rise to a natural oxide over the entire developed surface of the implanted layer when the samples are transferred from the accelerator chamber to the air. This oxide is detected by the Raman scattering.

The porous layer can be considered as a system of crystallites of various sizes. The largest crystallites intergrow from the substrate and reach the surface. They can be responsible for the appearance of the Raman line that consists of two lines peaked at 221 and 227 cm^{-1}. A violation of the selection rules and some mis-

orientation with respect to the substrate give rise to a higher intensity of the TO line compared to that of the LO line, while the shift of these lines to longer wavelengths indicates that there is a nanocrystalline phase [17]. Gettering of radiation defects by large vacancy-containing complexes (voids) can be a cause of the preservation of crystallinity in these GaSb blocks. Small crystallites are responsible for the appearance of the short-wavelength band in the PL spectra that occurs as a result of quantum-mechanical broadening of the GaSb band gap. The sizes of these crystallites can be calculated using the empirical formulas suggested by Allan *et al.* [18]. The estimation based on the PL band at 1.1–1.65 eV and observed in ion-implanted GaSb yields a crystallite size in the range from 3.5 to 8.5 nm.

4. CONCLUSION

We showed that a porous layer is formed in single-crystal GaSb as a result of the accumulation of radiation defects in the course of implanting medium-energy ions. We determined the threshold ion doses for the porous-layer formation and measured the morphological characteristics of the irradiated surface. It is established using photoluminescence and Raman scattering that the porous layer formed as a result of ion implantation into GaSb exhibits properties that are characteristic of nanocrystalline systems.

ACKNOWLEDGMENTS

This study was supported by the Russian Foundation for Basic Research, project no. 03-02-16777.

REFERENCES

1. L. T. Canham, Appl. Phys. Lett. **57**, 1046 (1990).
2. Y. Kanemitsu, Phys. Rep. **263**, 1 (1995).
3. A. M. Danishevskiĭ, A. Yu. Rogachev, V. B. Shuman, and E. G. Guk, Fiz. Tekh. Poluprovodn. (St. Petersburg) **31**, 1387 (1997) [Semiconductors **31**, 1196 (1997)].
4. T. L. Rutenhouse, P. W. Bohn, T. K. Hossain, *et al.*, J. Appl. Phys. **95**, 490 (2004).
5. D. N. Goryachev and O. M. Sreseli, Fiz. Tekh. Poluprovodn. (St. Petersburg) **31**, 1383 (1997) [Semiconductors **31**, 1192 (1997)].
6. Yu. N. Buzynin, S. A. Gusev, Yu. N. Drozdov, and A. V. Murel', Zh. Tekh. Fiz. **70** (5), 128 (2000) [Tech. Phys. **45**, 650 (2000)].
7. N. S. Averkiev, L. P. Kazakova, É. A. Lebedev, *et al.*, Fiz. Tekh. Poluprovodn. (St. Petersburg) **34**, 757 (2000) [Semiconductors **34**, 732 (2000)].
8. G. Su, Q. Guo, and R. E. Palmer, J. Appl. Phys. **94**, 7598 (2003).
9. T. N. Zavaritskaya, V. A. Karavanskiĭ, A. V. Kvit, and N. N. Mel'nik, Fiz. Tekh. Poluprovodn. (St. Petersburg) **32**, 235 (1998) [Semiconductors **32**, 213 (1998)].
10. P. V. Pavlov, Yu. A. Danilov, and V. S. Tulovchikov, Dokl. Akad. Nauk SSSR **248**, 1111 (1979) [Sov. Phys. Dokl. **24**, 803 (1979)].
11. R. Callec, P. N. Favennec, M. Salvi, *et al.*, Appl. Phys. Lett. **59**, 1872 (1991).
12. S. O. Kucheyev, J. S. Williams, C. Jagadish, *et al.*, Appl. Phys. Lett. **77**, 1455 (2000).
13. O. Teschke, D. M. Soares, and L. A. O. Nunes, Appl. Phys. Lett. **70**, 2840 (1997).
14. P. S. Dutta, H. L. Bhat, and V. Kumar, J. Appl. Phys. **81**, 5821 (1997).
15. S. Facsko, T. Dekorsy, C. Koerdt, *et al.*, Science **285**, 1551 (1999).
16. S. G. Kim, H. Asahi, M. Seta, *et al.*, J. Appl. Phys. **74**, 579 (1993).
17. L. P. Avakyants, V. S. Gorelik, É. M. Temper, and S. M. Shcherbina, Fiz. Tverd. Tela (St. Petersburg) **41**, 1495 (1999) [Phys. Solid State **41**, 1369 (1999)].
18. G. Allan, Y. M. Niquet, and C. Delerue, Appl. Phys. Lett. **77**, 639 (2000).

Translated by A. Spitsyn

Semiconductors, Vol. 39, No. 1, 2005, pp. 136–138. Translated from Fizika i Tekhnika Poluprovodnikov, Vol. 39, No. 1, 2005, pp. 149–152.

AMORPHOUS, VITREOUS, AND POROUS SEMICONDUCTORS

Efficiency of Avalanche Light-Emitting Diodes Based on Porous Silicon

S. K. Lazarouk^, A. A. Leshok, V. A. Labunov, and V. E. Borisenko

Belarussian State University of Informatics and Radioelectronics, ul. Brovki 17, Minsk, 220013 Belarus

^e-mail: serg@nano.bsuir.edu.by

Submitted June 1, 2004; accepted for publication June 16, 2004

Abstract—Avalanche light-emitting diodes based on porous silicon were studied with the aim of improving the efficiency of these diodes. The highest external quantum efficiency of 1.4% was attained in the pulsed mode of operation with an off-duty factor of 100, in which case the light-emitting diodes operated at the largest amplitudes of input currents. However, increasing the quantum efficiency with increasing input currents is limited by the attainment of the leveling-off region related to the thermal heating of the diode structure. © *2005 Pleiades Publishing, Inc.*

The current state of the development of microelectronics makes it possible to fabricate the components of silicon integrated circuits that can operate in the gigahertz frequency region. However, a multilevel metallization system used at present for joining these components cannot operate satisfactorily at these frequencies owing to resistance–capacitance delay times. Therefore, the need arises to replace metallic interconnections by optical ones having faster response. The main problem in achieving silicon optical interconnections is related to fabrication of a silicon light-emitting device that can operate in the gigahertz range. Appreciable progress in solving this problem was attained for light-emitting diodes (LEDs) based on porous silicon [1–3]. Nevertheless, the LED efficiency level (10%) required for practical implementation of optical interconnections remains beyond reach at present. In this paper, we report the results of our efforts to increase the efficiency of emission from avalanche LEDs by improving heat transfer and using the pulsed mode of operation.

The main technological operations in the fabrication of both avalanche LEDs from porous silicon and a prototype of an optoelectronic pair on the basis of these LEDs were described previously [2, 4, 5]; here, we only describe the sequence and some of the main operations.

n-type silicon substrates with a resistivity of 0.01 Ω cm were used as the starting material. Porous silicon was formed by treating the substrates in a 1% aqueous solution of hydrofluoric acid. The thickness of the porous layer was 0.5 μm. We then deposited a 1-μm-thick aluminum film on top of this layer using magnetron sputtering of three aluminum targets in an Oratoriya-29 system. It is noteworthy that titanium inserts were incorporated into the second aluminum target; as a result, the aluminum films obtained by sputtering of this target contained 14 at % of titanium. Since the magnetron-sputtering deposition was effected in a situation where silicon wafers were moved beneath three sequentially positioned magnetrons, the titanium content varied gradually from zero at the bottom of the aluminum film to 14 at % in the middle part and then decreased again to zero at the top of the film. The concentration varied gradually, which was ensured by joint deposition when the wafers passed beneath two neighboring magnetrons. A 0.2-μm-thick niobium film was deposited on top of the aluminum film. A niobium mask was then formed using photolithography and etching. Finally, electrochemical anodic oxidation of the aluminum film was carried out through the niobium mask using a 5% aqueous solution of oxalic acid at a voltage of 50 V for 20 min. It is noteworthy that the titanium impurity atoms were also oxidized. Thus, a system of two avalanche LEDs based on the Schottky contacts between porous silicon and aluminum electrodes was formed. These two LEDs were connected by a waveguide formed of aluminum oxide and having a core doped with niobium oxide (see Fig. 1a).

As shown previously [2, 5], one of two diodes emits light if this diode is reverse-biased with a voltage that exceeds the avalanche-breakdown voltage (5 V). In this situation, the second diode exhibits light-sensitive properties at a reverse-bias voltage lower than 5 V (in the case under consideration, 4 V) and can detect the optical signal from the first diode. Consequently, the device structure formed can be considered a prototype of optical interconnections on a silicon substrate. A smaller waveguide length (5 μm between diodes), which reduced optical-signal losses, and a reduced area of aluminum electrodes (0.04 mm^2) represent the major differences from the analogue described previously [2]. A decrease in the area of aluminum electrodes leads to a decrease in the LED operating volume where heat is released. The thermal heating of the diode structure is controlled by the ratio between the volume of the heat-release source and the volume of the entire silicon chip through which this heat is transported. Consequently, the LEDs with smaller area are heated to a lesser extent and the heat in them is dissipated more effectively than

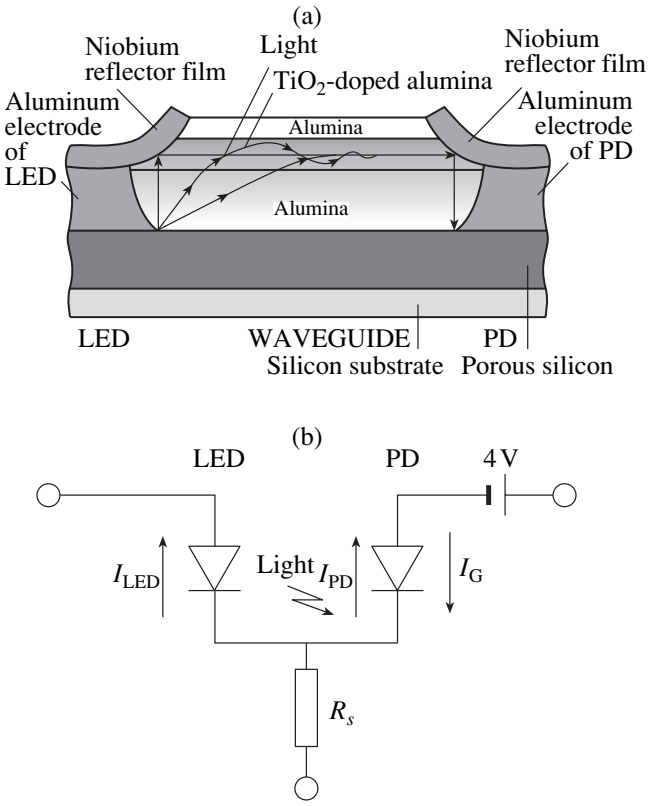

Fig. 1. (a) A cross section of silicon integrated optron pair (arrows indicate the propagation of light over the multilayer alumina waveguide) and (b) an equivalent circuit of the developed integrated optron pair. The abbreviation PD stands for photodiode (photodetector).

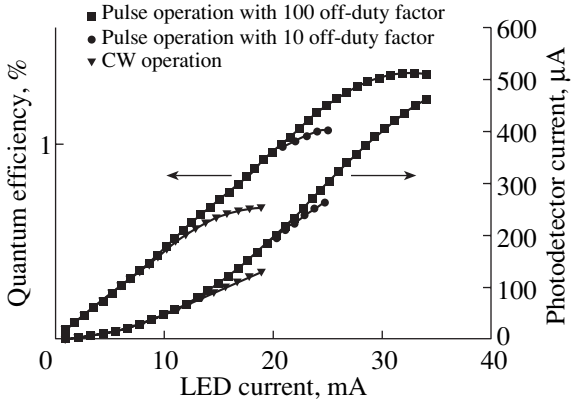

Fig. 2. Dependences of photodetector output current and external quantum efficiency of light-emitting diodes under study on the amplitude of input currents at different modes of operation.

in other LEDs with identical volume of silicon chip and for identical electrical-current densities. The optical response and external quantum efficiency of the LEDs were studied both in the constant-current and pulsed modes (at frequencies from 10 Hz to 1 kHz and at various off-duty factors for input-signal pulses).

An equivalent circuit of the formed prototype of an optron pair is shown in Fig. 1b. In a recent study [2], each of the components of a similar integrated optoelectronic device consisting of an LED and a photodetector was analyzed separately using either an external photodetector (in the case of the LED) or an external light source (in the case of the photodetector). In that case, the same dependences for the quantum efficiency of the LEDs under study were obtained; the detected signals in the case of an external optical source were also almost no different from those in the case of integrated LEDs. Thus, the studies performed suggest that the signal detected by the photodetector in the designed optoelectronic device represents the response to the LED optical signal. It is worth noting that, in the developed prototype of the optron pair, complete galvanic isolation is not ensured since electrical isolation of reverse-biased Schottky diodes is not perfect (both diodes are located on the same silicon substrate with the resistance R_s). However, the direction of the galvanic-coupling current is opposite to that of the photodiode current; i.e., we may state with confidence that the reverse current in the photodetector is caused by the optical signal of the LED. Furthermore, the photodetector signal was detected in the millisecond time range, which corresponded to the duration of the pulses under study. This circumstance made it possible to separate the input signal from parasitic capacitive currents whose duration was several microseconds.

In Fig. 2, we show the dependences of the photodetector output current on the LED input current under different conditions of LED operation. This dependence is nearly quadratic and transforms into a linear dependence at large values of the input current. It is worth noting that the dependence under study becomes linear at different values of the input current, depending on the mode of the LED operation. In particular, the beginning of the linear portion is observed at lower currents if the LED operates at a constant current; this behavior is accounted for by thermal heating of the LED. The latter inference is corroborated by the fact that the irreversible thermal breakdown of the diodes under study sets in if the input current is increased further.

If the LEDs operate in the pulsed mode, the heat released is dissipated during intervals between pulses, which prevents the structures under study from being thermally heated. Therefore, transition to the linear region and irreversible thermal breakdown are observed at higher amplitudes of input currents in this case.

It is evident that the larger the off-duty factor, the lower the thermal heating of the diode for the same pulse amplitudes. As a result, one can achieve operationwith the largest amplitudes of currents through the LED by increasing the off-duty factor.

The external quantum efficiency of an LED is defined as the ratio between the number of emitted photons and the number of charge carriers that pass through the LED at the same time. The major portion of emitted photons generate the photodiode current as they are absorbed. Therefore, the ratio between the photodiode and LED currents can be considered as the smallest

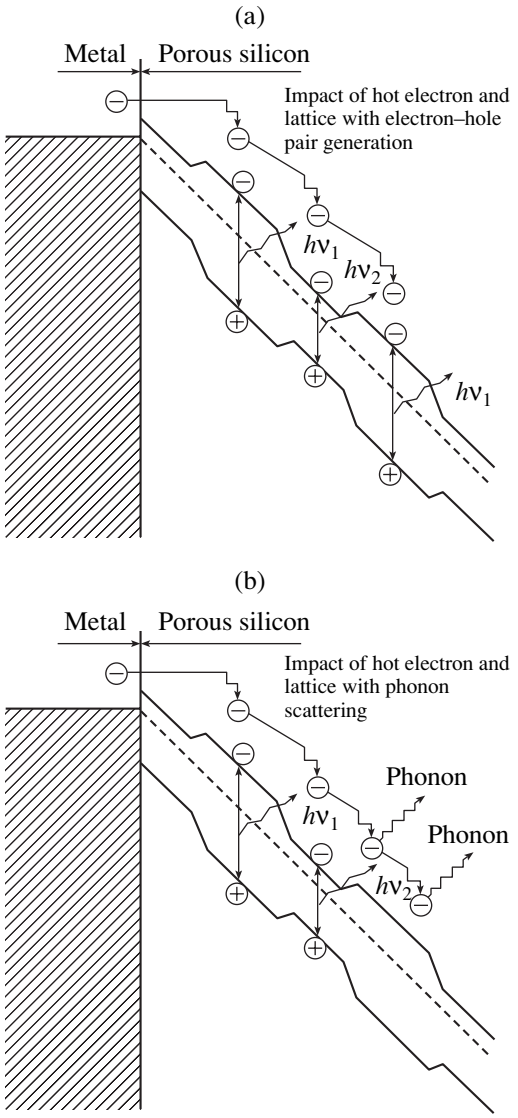

Fig. 3. Energy-band diagrams for the reverse-biased contact between metal and porous silicon at different temperatures of operation T_1 (a) < T_2 (b).

value of the external quantum efficiency of the LEDs under study with respect to the input current for various modes of operation of these LEDs. As can be seen from Fig. 2, the highest quantum efficiency of 1.4% is observed at the off-duty factor of 100 in the pulsed operation. It is in this case that the LEDs can operate at the largest amplitude of input currents. However, an increase in the quantum efficiency with increasing input current is limited. The attainment of leveling off of the efficiency is related to the thermal heating of the diode.

An increase in the efficiency of avalanche LEDs with increasing current is accounted for by a more efficient process of impact ionization at higher bias voltages, as illustrated schematically in the energy-band diagram in Fig. 3a. In this context, the following mechanisms of light emission should be mentioned: the band-to-band recombination of electron–hole pairs in nanocrystallites where the effect of quantum confinement manifests itself (the $h\nu_1$ emission in the visible region of the spectrum) and the band-to-band recombination of electron–hole pairs in larger nanocrystallites where there is no quantum confinement (the $h\nu_2$ emission in the infrared region of the spectrum) [6]. However, an increase in the current in LEDs also leads to an increase in operation temperatures, which, in turn, reduces the free-path length of hot electrons owing to collisions with lattice atoms and losses of energy due to scattering by phonons, as it is shown schematically in Fig. 3b. The energy dissipation due to scattering by phonons (along with the nonradiative processes of the Auger recombination) [7, 8] reduces the efficiency of the emission of light in the structures under study.

In conclusion, we note that the increase in the external quantum efficiency of avalanche LEDs was attained by improving heat transfer in the structures under study. For example, a decrease in the area of the aluminum electrode made it possible to attain quantum efficiency as high as 0.7% for an LED that operated at a constant current; this efficiency is twice as high as that reported previously [2]. The use of the pulsed mode of operation also made it possible to improve heat transfer and attain a quantum efficiency of 1.4%, which is unprecedentedly high for the types of LEDs under consideration [1, 3].

Thus, we have developed methods for increasing the emission efficiency in avalanche LEDs fabricated on porous silicon. It can be predicted that the attained value of the quantum efficiency can be increased severalfold by further decreasing the sizes of the structures and using materials with high thermal conductivity (for example, diamond-like films) for a better transfer and dissipation of heat. Therefore, avalanche LEDs based on porous silicon can be considered as promising components for the development of intrachip optical interconnections in integrated microcircuits.

REFERENCES

1. P. Calcot, in *Properties of Porous Silicon*, Ed. by L. Canham (INSPEC, London, 1997), Chap. 7.
2. S. K. Lasarouk, P. V. Jaguiro, A. A. Leshok, and V. E. Borisenko, Physica E (Amsterdam) **16**, 495 (2003).
3. B. Gelloz and N. Koshida, J. Appl. Phys. **88**, 4319 (2000).
4. S. K. Lasarouk, P. V. Jaguiro, S. Katsouba, *et al.*, Appl. Phys. Lett. **68**, 2108 (1996).
5. S. K. Lasarouk, P. V. Jaguiro, A. A. Leshok, and V. E. Borisenko, in *Physics, Chemistry and Application of Nanostructures*, Ed. by V. E. Borisenko, S. V. Gaponenko, and V. S. Gurin (World Sci., Singapore, 1999), p. 370.
6. S. K. Lazarouk, P. V. Jaguiro, A. A. Leshok, and V. E. Borisenko, Izv. Ross. Akad. Nauk, Ser. Fiz. **66** (2), 178 (2002).
7. S. K. Lazarouk and Yu. A. Berashevich, Izv. Belorus. Inzh. Akad. **11** (3), 48 (2001).
8. Th. Dittrich, V. Yu. Timoshenko, J. Rappich, and L. Tsybeskov, J. Appl. Phys. **90**, 2310 (2001).

Translated by A. Spitsyn

Semiconductors, Vol. 39, No. 1, 2005, pp. 139–141. Translated from Fizika i Tekhnika Poluprovodnikov, Vol. 39, No. 1, 2005, pp. 153–156.

PHYSICS OF SEMICONDUCTOR DEVICES

Observation of the Middle-Infrared Emission from Semiconductor Lasers Generating Two Frequency Lines in the Near-Infrared Region of the Spectrum

V. Ya. Aleshkin*, V. I. Gavrilenko*, S. V. Morozov*^, K. V. Marem'yanin*, B. N. Zvonkov, and S. M. Nekorkin****

**Institute for the Physics of Microstructures, Russian Academy of Sciences, Nizhni Novgorod, 603950 Russia*
^e-mail: more@ipm.sci-nnov.ru
***Physicotechnical Research Institute at Lobachevsky State University, Nizhni Novgorod, 603950 Russia*
Submitted June 1, 2004; accepted for publication June 14, 2004

Abstract—Simultaneous generation of several frequency bands of stimulated emission in a semiconductor laser with three quantum wells is experimentally studied. It is shown that different frequencies can be generated both in the fundamental and excited transverse modes of the waveguide. It is found that the simultaneous generation of stimulated emission in two- and three-frequency bands is possible. Dependences of the lasing power in different bands on the current are studied. A broadband Si:B extrinsic photodetector is used to detect the radiation in the middle-infrared spectral region in the emission from the semiconductor laser that generates two emission bands with an energy difference between the peaks of 50 meV (the wavelength $\lambda \approx 25$ μm). It is assumed that the middle-infrared emission is related to the generation of the difference harmonic. © *2005 Pleiades Publishing, Inc.*

1. INTRODUCTION

The interest in the semiconductor laser sources of middle- and far-infrared (IR) radiation is caused by their wide potential applications in communications, gas analysis, and spectroscopy. Developed cascade lasers of the mid-IR region operate successfully at room temperature [1], whereas it has been possible to attain lasing in cascade structures only at cryogenic temperatures [2]. Semiconductor lasers that are based on *p*-Ge [3, 4] and oscillate in the far-IR spectral region also only operate at low temperatures. An alternative approach to obtaining mid- and far-IR radiation consists in the use of nonlinear effects, which can ensure lasing at room temperature. In order to generate the difference mode in a laser that generates two short-wavelength modes, it was suggested that either the electronic nonlinearity in a quantum well (QW) containing three levels [5] was used or the nonlinear properties of the crystal lattice of the active-region material [6].

In this paper, we report the results of studying the laser emission that belongs to the mid-IR spectral region and is based on the difference frequency (due to the lattice nonlinearity in GaAs) in two-frequency lasers that operate at room temperature and include InGaAs/GaAs heterostructures with InGaAs QWs.

2. EXPERIMENTAL

The laser structures that contained three $In_xGa_{1-x}As$ QWs in the active region were grown using a metal–organic vapor-phase epitaxy at atmospheric pressure. The fraction of In in the structures of lasers with two-frequency generation was varied from 0.15 to 0.25 in the two outer QWs and from 0.3 to 0.35 in the middle QW. The width of the active region and the cavity length were equal to 100 and 500–1000 μm, respectively. The geometric parameters of the laser chip were L = 1000, b = 400, and d = 170 μm, where L was the chip length (the waveguide length); b, the chip width; and d, the total thickness of the structure. The mode composition of the laser radiation in the near-IR spectral region and the dependence of the lasing-line intensity on the pump current were studied using a KSVU-23 spectral system at T = 300, 77, and 4.2 K under conditions of continuous and pulsed pumping. The radiation in the mid-IR spectral range was detected at T = 4.2 K using a broadband extrinsic Si:B photodetector under conditions of pulsed pumping of the laser diodes with a pulse duration of 1–15 μs and a repetition frequency of 100 Hz.

3. RESULTS AND DISCUSSION

In Fig. 1, we show the spectral dependences of the intensity of the two-frequency generation (I_{LG}) on a scale of photon energies $h\nu$ for several values of the pump current I. The thresholdlike onset of the laser generation of a long-wavelength line was observed when the constant current that flowed through the structure exceeded ~220 mA. As the current was increased further, a short-wavelength line started to be seen; the intensity of this line increased linearly with the increasing current so that this intensity became equal to that of the long-wavelength line at the current I = 414 mA. We used the experimental data shown in Fig. 1 to plot the

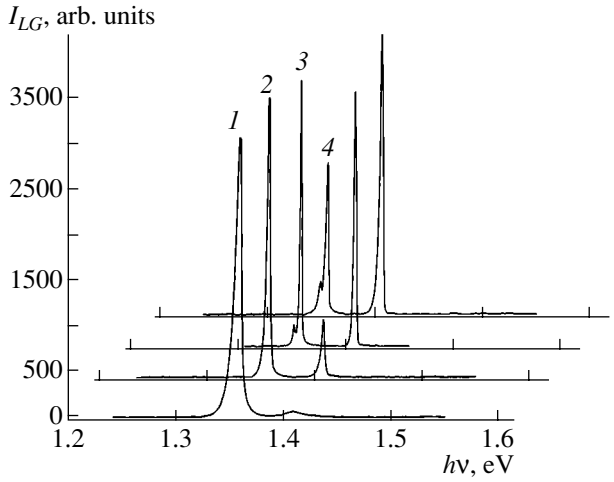

Fig. 1. Spectra of the two-frequency generation of a laser diode for the pump currents I = (*1*) 150, (*2*) 251, (*3*) 414, and (*4*) 483 mA. T = 77 K.

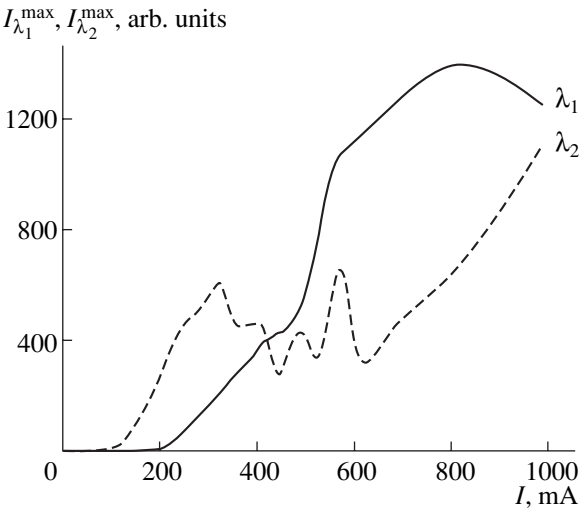

Fig. 2. The dependence of the generation-peak intensities on the pump current for the short-wavelength peak ($I_{\lambda_1}^{max}$) and the long-wavelength peak ($I_{\lambda_2}^{max}$). T = 77 K.

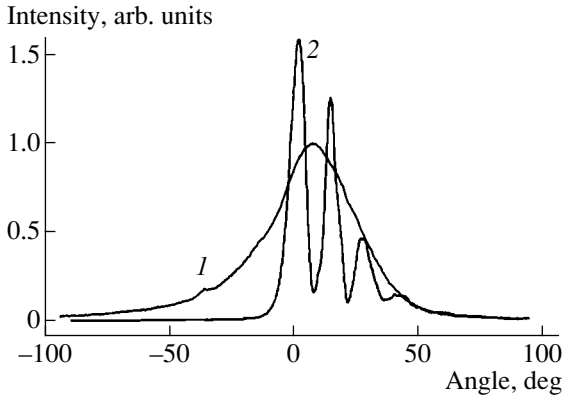

Fig. 3. The observed directivity patterns for emission in the plane perpendicular to the quantum-well layer: (*1*) generation of the main waveguide mode and (*2*) generation of several transverse waveguide modes.

dependences of the heights $I_{\lambda_1}^{max}$ and $I_{\lambda_2}^{max}$ of the peaks for the bands at wavelengths of λ_1 and λ_2 on the pump current for two-frequency lasing (Fig. 2). It can clearly be seen from Fig. 2 that the dependence of the intensity of the long-wavelength band on a current in the range of 300 to 600 mA is nonmonotonic. Probably, the decrease in emission intensity as the current increases is caused by the fact that photons emitted from the short-wavelength QW stimulate a recombination of specific electrons in the long-wavelength QW. The energy of these electrons corresponds to the energy of the transitions from the ground state of the electrons in the short-wavelength QW. As a result, the occupancy of the ground state of the electrons in the long-wavelength QW decreases, and a decrease in the emission intensity for the long-wavelength peak becomes possible as the current increases.

In order to analyze the mode composition of emission, we measured the directivity patterns. We observed two types of directivity patterns for different laser chips, as shown in Fig. 3. It is worth noting that the directivity patterns were identical for both types of emission. The directivity pattern shown by curve *1* corresponds to the generation of the main TE mode of the waveguide (referred to as the transverse mode). The unusual directivity pattern represented by curve *2* can correspond to the simultaneous generation of several transverse modes.

In Fig. 4, we show the spectra of two types of two-frequency lasing measured at room temperature under pulsed current pumping. It can be seen from Fig. 4 that the photon energies in different bands differ by about 50 meV (curve *1*) and 15 meV (curve *2*), which corresponds to the middle- and far-IR spectral regions. It is noteworthy that the two-band lasing was observed at room temperature in continuous-wave conditions as well.

As already mentioned above, we grew the structures with three QWs in our experiments; two of these QWs had a lower In content, were located symmetrically with respect to the center QW, and were identical. This special feature was intended to reduce the threshold current for short-wavelength lasing. However, three-frequency lasing in the middle IR spectral region was observed in some of the laser structures with three QWs in the active region; evidently, this lasing is related to the different composition of all three QWs (Fig. 4, curve *3*). Figure 4 also shows the spectrum of the second-harmonic generation for three-frequency lasing (curve *4*), which, once again, proves that the GaAs properties are clearly nonlinear.

In Fig. 5, we show the oscilloscope patterns of signals in the cases of two-frequency (curves *4*, *5*) and single-frequency (curve *3*) lasing. The patterns were

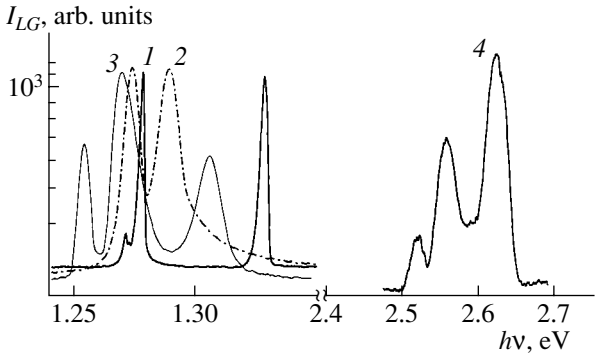

Fig. 4. Spectra of (*1*, *2*) two-frequency and (*3*) three-frequency generation for lasers that contain three quantum wells in the active region. Curve *4* represents the spectrum of second harmonics for the three-frequency generation. T = 300 K.

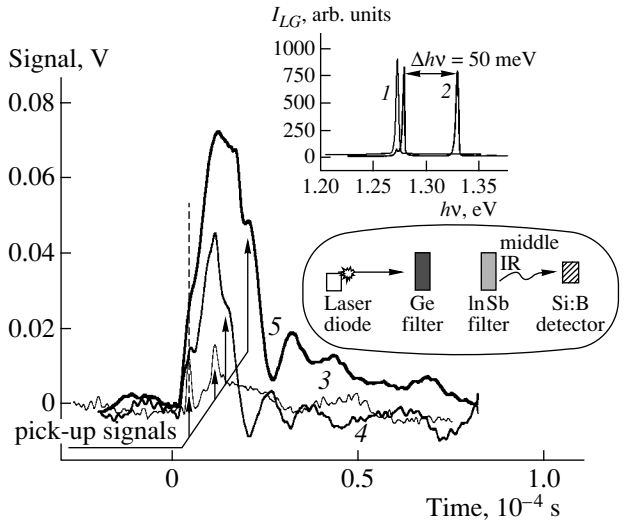

Fig. 5. Oscilloscope patterns of the signals in the middle-infrared region in the case of two-frequency lasing (traces *4* and *5* correspond to spectrum *2* in the upper inset) and single-frequency lasing (trace *3* corresponds to spectrum *1* in the upper inset) under pulsed pumping. The pulse duration τ = (*3*) 7, (*4*) 9, and (*5*) 15 μs. The upper inset shows the main modes of the (*1*) single-frequency and (*2*) two-frequency lasing. The lower inset shows a schematic representation of the experimental setup. The near-infrared emission was eliminated using Ge and InSb filters.

recorded using a broadband Si:B photodetector (the photosensitivity range was from ~10 to 30 μm). The near-IR emission of the main lasing modes (the upper inset) was suppressed using Ge and GaSb filters (see the lower inset). The measurements were carried out at the pulsed current pumping ($I \approx 3$ A) with the pulse duration τ = 7–15 μs at T = 4.2 K. It can be seen from Fig. 5 that, in the case of single-frequency lasing (curve *3*), a signal is not observed; only spurious signals at the pulse edges are clearly seen. In the case of two-frequency lasing (curves *4*, *5*), a signal whose amplitude increases with the pulse duration appears. The dependence of the signal amplitude on the pulse duration is related to the limited speed of the response of the Si:B detector. The characteristic buildup time for the detector's signal, as determined from the response time of the *RC* circuit in the measurement system, is equal to ~10 μs and is comparable to the pulse duration.

4. CONCLUSION

We established that semiconductor lasers with quantum wells can simultaneously generate stimulated radiation in two- and three-frequency bands. It is shown that both the main and excited transverse TE modes of the waveguide can be generated. We studied, experimentally, the dependence of the generation power in different frequency bands on the pump current. We observed two types of two-frequency lasing in laser structures with three quantum wells that differed in composition and were formed in the active region. The difference between the emission bands amounts to 15 and 50 meV, which corresponds to the far and middle infrared regions of the spectrum. A signal in the middle infrared region was observed in the case of two-frequency lasing with a difference of 50 meV between the emission bands; this signal can be related to the generation of the difference harmonic.

ACKNOWLEDGMENTS

This study was supported by the joint program "Basic Research and Higher Education" run by the US Civilian Research and Development Foundation and the Ministry of Education of the Russian Federation (grant no. REC-NN-001); grants from the Russian and Belarussian Foundations for Basic Research (project no. 02-02-81036); the Russian Foundation for Basic Research (project no. 04-02-17432); the International Science and Technology Centre (grant no. 2293); NATO (grant no. SfP-973799 Semiconductors), the Russian Academy of Sciences; and the Ministry of Industry, Science, and Technology of the Russian Federation.

REFERENCES

1. F. Capasso, A. Tredicucci, C. Gmachl, *et al.*, IEEE J. Sel. Top. Quantum Electron. **5**, 792 (1999).
2. M. Rochat, L. Ajili, H. Willenberg, and J. Faist, Appl. Phys. Lett. **81**, 1381 (2002).
3. A. Andronov and E. Gornik, Opt. Quantum Electron. **23**, 2 (1991).
4. I. V. Altukhov, M. S. Kagan, K. A. Korolev, *et al.*, Zh. Éksp. Teor. Fiz. **101**, 756 (1992) [Sov. Phys. JETP **74**, 404 (1992)].
5. A. A. Belyanin, F. Capasso, V. V. Kocharovsky, *et al.*, Phys. Rev. A **63**, 53803 (2001).
6. V. Ya. Aleshkin, A. A. Afonenko, and N. B. Zvonkov, Fiz. Tekh. Poluprovodn. (St. Petersburg) **35**, 1256 (2001) [Semiconductors **35**, 1203 (2001)].

Translated by A. Spitsyn

Semiconductors, Vol. 39, No. 1, 2005, pp. 14–16. Translated from Fizika i Tekhnika Poluprovodnikov, Vol. 39, No. 1, 2005, pp. 21–24.

SEMICONDUCTOR STRUCTURES, INTERFACES, AND SURFACES

Features of GaN Growth Attained by Metal–Organic Vapor-Phase Epitaxy in a Low-Pressure Reactor

O. I. Khrykin^, A. V. Butin, D. M. Gaponova, V. M. Danil'tsev, M. N. Drozdov, Yu. N. Drozdov, A. V. Murel, and V. I. Shashkin

Institute for Physics of Microstructures, Russian Academy of Sciences, Nizhni Novgorod, 603950 Russia

^e-mail: khrykin@ipm.sci-nnov.ru

Submitted June 1, 2004; accepted for publication June 16, 2004

Abstract—The properties of GaN layers grown by metal–organic vapor-phase epitaxy on sapphire substrates at atmospheric and reduced pressures were studied. The surface morphology, crystalline, luminescence, and electric transport properties of these structures were comparatively analyzed. The depth profiles of elements were measured using secondary-ion mass spectrometry. The carrier distribution in heavily doped structures with *p–n* junctions was analyzed by electrochemical *C–V* profiling. It was shown that GaN layers grown in a low-pressure reactor feature improved structural, electric, and optical characteristics. © *2005 Pleiades Publishing, Inc.*

1. INTRODUCTION

The application of wide-bandgap nitrides in optoelectronic devices operating in the blue and UV wavelength regions makes it possible to increase power, operating temperature, and stability in the face of external factors [1]. Therefore, great efforts have been undertaken in the technology of these materials in the last decade.

All the research teams developing methods of group-III nitride (III–N) growth employ two types of growth chambers for metal–organic vapor-phase epitaxy (MOVPE): low-pressure (LP) and atmospheric-pressure (AP) reactors [2]. LP reactors require pumping and pressure maintenance facilities; however, vapor-phase chemical interactions inside them are suppressed due to the low concentration of molecules. AP reactors require a special system for separating reagent flows up to the epitaxial growth zone. The complex dynamics of gas flows in the reactor complicates the growth of homogeneous layers on large areas.

The reactor we used was initially of an AP type; then, it was modernized to an LP reactor. This allowed us to compare the growth features and properties of GaN layers previously grown in the AP reactor [3, 4] with layers grown in the LP reactor.

The aim of this study is to determine the optimum conditions for growing high-quality GaN epitaxial layers on sapphire in an LP reactor and to compare these layers with those obtained in an AP reactor.

2. SAMPLE PREPARATION METHODS

Epitaxial GaN and AlN layers were grown by MOVPE in a vertical quartz reactor without a separate supply of reactants, with the inductive heating of a substrate holder, at a pressure of 75 Torr. Trimethylgallium (TMG), trimethylaluminum (TMA), and ammonia (NH_3) were used as Ga, Al, and N sources. Bis(cyclopentadienyl) magnesium served as the *p*-type dopant. The sapphire substrate orientation was (0001). Hydrogen or a hydrogen–nitrogen mixture was used as a carrier gas.

To study low-pressure growth, the setup described in [3] was modified. The main pumping facility was an NVPR-16-066 pump. The pressure was measured and controlled by an electronic pressure regulator (Bronkhorst) equipped with a domestic needle valve. In other respects, the vacuum and gas distribution facilities were similar to those of conventional MOVPE systems.

GaN layers were grown following a two-stage method [3]. After preliminary high-temperature annealing and "nitridization" of the substrate surface, an AlN or GaN buffer layer, ~20 nm thick, was deposited at a temperature of 600 to 650°C. The buffer layer was then annealed in an ammonia flow at 1050–1150°C for 5 min. Then the temperature was lowered and an epitaxial active GaN layer with a thickness of up to several micrometers was grown at temperatures of 600 to 1100°C.

3. RESULTS

The grown samples were studied using X-ray diffraction (XRD), on a DRON-4 diffractometer, and secondary-ion mass spectrometry (SIMS), on a Shipovnik-3 mass spectrometer. Photoluminescence spectra were measured using excitation by an He–Cd laser with a wavelength of 325 nm. The electrical characteristics (carrier mobility and concentration) were measured by the van der Pauw method.

The XRD data showed that the epitaxial layers are mosaic single crystals of a hexagonal modification of

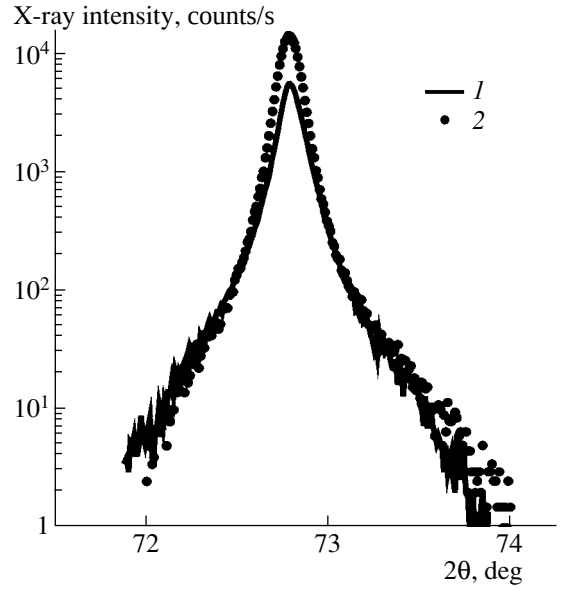

Fig. 1. θ/2θ scanning spectra (with a wide aperture in front of the detector) of H661 samples (solid curve) and a reference sample (dotted curve) in the region of the (0004) peak of GaN.

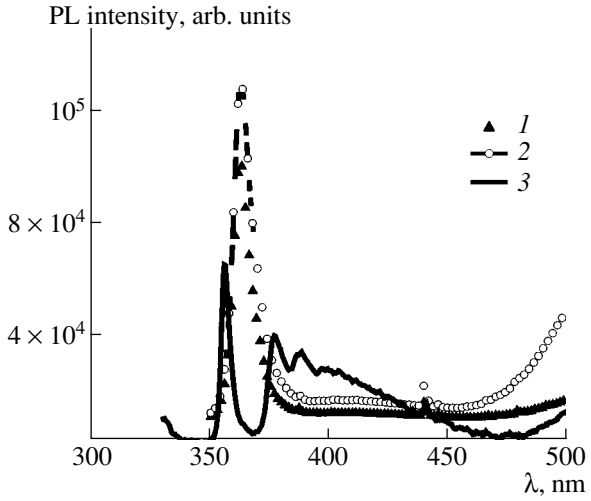

Fig. 2. Photoluminescence spectra of (*1*) the reference sample, (*2*) LP sample H660, and (*3*) AP sample H621.

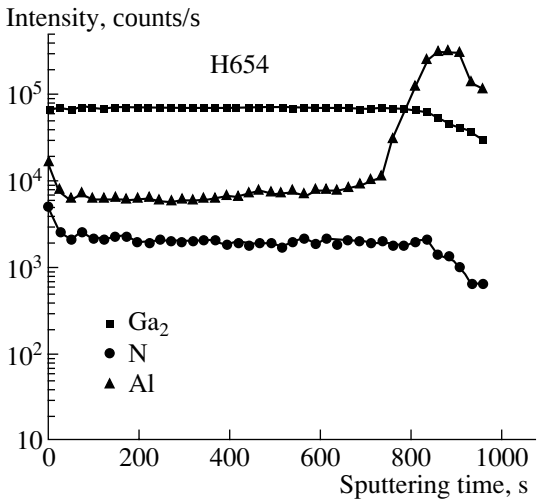

Fig. 3. SIMS profiles for the structure grown on an AlN buffer.

α-GaN(0001). The θ/2θ scanning spectra only contain peaks from the substrate and the epitaxial layer. The width of the rocking curve of GaN(0004) grown with the current level of technology is 0.06°, in terms of the sample rotation angle, which is (see Fig. 1) the same as for the reference high-quality GaN layer (such layers are used in the production of light-emitting diodes). Layer H661 is somewhat thinner than the reference layer; therefore, the peak is lower at the same width.

The photoluminescence spectra shown in Fig. 2 contain strong peaks in the vicinity of 3.4 eV. The spectrum of LP sample H660 is close to that of the reference sample. The spectrum of the AP sample includes a slightly shifted main peak, and a set of peaks, in the range of 2.9–3.3 eV, which seems to be caused by impurities contaminating the layer in the AP reactor.

Figure 3 shows the SIMS profiles for the structure with an AlN buffer. They demonstrate uniform depth distribution of the elements in the GaN epitaxial layer. Moreover, the layer contains Al with a concentration of $(1–5) \times 10^{18}$ cm^{-3}, which is caused by diffusion from the AlN buffer underlayer rather than from the sapphire substrate. This is demonstrated by an analysis of the structures grown without an AlN underlayer. At the same time, such an amount of aluminum has no significant effect on the electrical characteristics: the highest electron mobility was observed in the structure shown in Fig. 3. Much faster diffusion of Al, resulting in a concentration higher than 10^{20} cm^{-3}, is observed in the samples grown on the AlN buffer underlayer under nonoptimal conditions, which results in weak luminescence and low electron mobility in the upper GaN layers.

It was found that samples with low electron mobility had, as a rule, a larger half-width of XRD rocking curves (see table). This seems to be caused by the enhanced carrier scattering from grain boundaries in the layer as the misorientation angle between grains increases. For the samples grown in the AP reactor, the smallest width ω was 0.2° and the highest mobility was 120 cm^2 V^{-1} s^{-1}. We should note that the GaN samples grown on sapphire substrates with various deviations from the (0001) plane had identical carrier mobilities.

In order to study the carrier distribution, a technique for the electrochemical *C–V* profiling of various GaN structures with nonuniform doping was developed. An aqueous solution of KOH was used as an electrolyte. A quartz window disk, transparent for the UV spectral region of a halogen lamp, served as an electrochemical cell window. Nominally undoped samples were generally *n*-type ones with a doping level of 10^{17}–10^{18} cm^{-3}. Figure 4 shows the doping profile of an *p–n* junction

Parameters of GaN layers

Sample	ω, deg	μ, $cm^2 V^{-1} s^{-1}$	*n*, cm^{-3}
H633	0.33	50	3.8×10^{18}
H645	0.26	92	2.6×10^{18}
H651	0.16	150	2.5×10^{18}
H654	0.11	195	1.5×10^{18}
H655	0.13	230	1.2×10^{18}

Note: ω is the width of the XRD rocking curve of GaN(0004), μ is the carrier mobility, and *n* is the bulk carrier concentration.

including an upper *p*-type layer of about 0.4 μm thick, heavily doped with magnesium, and a lower *n*-type GaN layer.

4. DISCUSSION

As was noted in [2], the transition to a reduced pressure while retaining the same ratios of reactants in the vapor phase results in a sharp increase in the GaN growth rate. This is caused by a decrease in the number of spurious homogeneous vapor-phase reactions between organometallic compounds and ammonia at a chamber pressure below 330 Torr. Under the same growth conditions, the conversion to a reduced pressure resulted in a tenfold increase in the GaN growth rate in the experiments we performed. A nitrogen admixture in the carrier gas (H_2) flow at a reduced pressure did not cause significant changes in the growth rate. Pressure variation in the range of 75–150 Torr also had no appreciable effect on the GaN epitaxial growth rate. Some increase in the growth rate was observed as the epitaxial growth temperature was raised from 950 to 1100°C. It should be noted that, in order to obtain satisfactory parameters for the active layer, with a buffer layer grown at low temperatures, the NH_3 concentration in the gas mixture flow should be significantly (by a factor of 3–5) increased, since ammonia molecules are characterized by high thermal stability.

The buffer layer composition (AlN or GaN) had no significant effect on the structural and electrical properties of the epitaxial layers. The buffer layer thickness most significantly affected the properties of the GaN layers. With a thin buffer layer, the GaN film became continuous (and the growth became two-dimensional) after long-term epitaxial growth. To achieve a thick intermediate layer, it was necessary increase the active layer thickness to planarize the surface after passing to the two-dimensional growth mechanism. The electrical parameters of the GaN layer grown under optimized conditions correspond to those given in the literature for high-quality MOVPE GaN layers. The free electron concentration in undoped GaN layers was $(1–2) \times 10^{17}$ cm^{-3} and the carrier mobility was 200–250 $cm^2 V^{-1} s^{-1}$. The use of bis(cyclopentadienyl) magnesium made it possible to grow *p*-type GaN layers with a hole concentration of up to 10^{20} cm^{-3}.

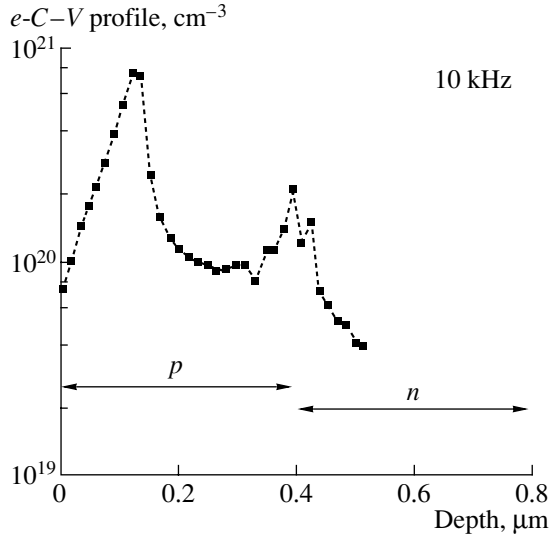

Fig. 4. An electrochemical *C*–*V* profile of the GaN structure with a *p*-doped upper layer.

5. CONCLUSIONS

The reduction of pressure in an MOVPE reactor makes it possible to increase the GaN growth rate by more than a factor of ten due to a decrease in the number of spurious homogeneous vapor-phase reactions.

The photoluminescence spectra of layers grown in an LP reactor do not contain the spurious peaks characteristic of layers grown at atmospheric pressure. This indicates the absence of spurious reactions during pyrolysis and the high perfection of the layers grown at low pressure.

High-quality *p*- and *n*-type GaN layers were grown on *c*-cut sapphire substrates by MOVPE in a low-pressure reactor.

ACKNOWLEDGMENTS

This study was supported by two programs of the Presidium of the Russian Academy of Sciences: “New Materials and Structures” and “Low-Dimensional Quantum Structures.”

REFERENCES

1. S. Nakamura, S. Pearton, and G. Fasol, *The Blue Laser Diode* (Springer, Berlin, 2000).
2. T. Sasaki and T. Matsuoka, J. Appl. Phys. **77**, 192 (1995).
3. O. I. Khrykin, N. V. Vostokov, D. M. Gaponova, *et al.*, in *Abstracts of VI Russian Conference on Physics of Semiconductors* (St. Petersburg, 2003), p. 162.
4. N. V. Vostokov, D. M. Gaponova, V. M. Danil’tsev, *et al.*, Izv. Ross. Akad. Nauk, Ser. Fiz. **68** (1), 101 (2004).

Translated by A. Kazantsev

Semiconductors, Vol. 39, No. 1, 2005, pp. 142–146. From Fizika i Tekhnika Poluprovodnikov, Vol. 39, No. 1, 2005, pp. 157–161.

PHYSICS OF SEMICONDUCTOR DEVICES

The Resonant Terahertz Response of a Slot Diode with a Two-Dimensional Electron Channel[1]

V. V. Popov[1]^, G. M. Tsymbalov[1], M. S. Shur[2], and W. Knap[2, 3]

[1]*Institute of Radio Engineering and Electronics, Saratov Division, Russian Academy of Sciences, Saratov, 410019 Russia*

^*e-mail: popov@ire.san.ru*

[2]*Department of Electrical, Computer, and System Engineering and RPI/IBM Center for Broadband Data Transfer, CII9015, Rensselaer Polytechnic Institute, Troy, New York, 12180 USA*

[3]*GES CNRS-Universite Montpellier2 UMR 5650, 34900 Montpellier, France*

Submitted June 1, 2004; accepted for publication June 14, 2004

Abstract—The terahertz response of a slot diode with a two-dimensional electron channel is calculated on the basis of the first principles of electromagnetism. It is shown that all characteristic electromagnetic lengths (scattering, absorption, and extinction lengths), as well as the impedance of the diode, exhibit resonances at plasmon excitation frequencies in the channel. The fundamental resonance behaves similarly to the current resonance in an *RLC* circuit. It has been concluded that, even at room temperature, a slot diode with a two-dimensional electron channel provides a resonant circuit at terahertz frequencies that couples effectively to external electromagnetic radiation with a loaded *Q*-factor exceeding unity. The diode resistance may be measured from contactless measurements of the characteristic electromagnetic lengths of the diode. © *2005 Pleiades Publishing, Inc.*

1. INTRODUCTION

The high-frequency response of field-effect transistors and diodes with two-dimensional electron channels is strongly affected by plasma oscillations in the channel. This phenomenon, in its various manifestations, can be used for the detection, frequency multiplication, and generation of terahertz (THz) radiation [1–13]. One of the main parameters of a device, which determines its high frequency properties, is the device impedance. The high-frequency impedance (admittance) of a slot diode was calculated for a capacitively [14] and conductively [15] contacted two-dimensional electron channel. This was performed within the framework of electrostatic theory and an equivalent circuit approach. In these approaches, the radiative contribution to the impedance (radiation resistance R_{rad} of the diode) is not considered, and intercontact geometrical capacitance C_g is either ignored altogether [14] or treated as a free parameter [15]. However, at ultrahigh (terahertz) frequencies (i) the radiation resistance of the diode may play the role of an additional damping mechanism, and (ii) the intercontact geometrical capacitance may effectively shunt the channel. Furthermore, the typical length of the side contacts in high-frequency high-electron-mobility transistors (HEMT) [12] is comparable to the THz radiation wavelength, which makes the electrostatic calculations of the intercontact capacitance inaccurate. Here we calculate the impedance of a slot diode with a conductively contacted two-dimensional electron channel using the full system of Maxwell's equations. In this way, we account for the radiation resistance and intercontact capacitance from first principles. In addition to its practical importance, the slot diode analyzed here is an idealization of the long ungated parts of the HEMT with an ultrashort nanometer gate. This HEMT was recently shown to exhibit a resonant THz emission that could be tuned using a bias voltage [12].

2. THEORETICAL MODEL

Consider a plane electromagnetic wave incident, normally from vacuum onto a perfectly conductive plane $z = 0$ with a slot of width w, which is located on the surface of a dielectric substrate. We assume that the electric field of the wave, $\mathbf{E}_0\exp(-i\omega t - ik_0 z)$ (where $k_0 = \omega/c$ and c is the speed of light in free space), is polarized across the slot (along the x-axis). The edges of the slot are connected by a two-dimensional electron channel with the areal conductivity described by the Drude model as

$$\sigma(\omega) = i\frac{Ne^2}{m^*(\omega + i\nu)},$$

where ν is the electron momentum scattering rate, N is the sheet electron density, and e and m^* are the charge and effective mass of electron, respectively.

Our theoretical procedure involves the following steps: We rewrite Maxwell's equations for the ambient medium and the substrate in the Fourier transform representation over the in-plane wave vector k_x. The Fou-

[1]This article was submitted by the authors in English.

rier transforms of the in-plane components of the electric and magnetic fields satisfy the following boundary conditions at $z = 0$:

$$\delta(k_x)E_0 + E_{x,a}^{(\mathrm{ind})}(k_x) = E_{x,s}^{(\mathrm{tot})}(k_x),$$
$$\delta(k_x)H_0 + H_{y,a}^{(\mathrm{ind})} - H_{y,s}^{(\mathrm{tot})}(k_x) = j(k_x),$$

where $j(k_x)$ is the Fourier transform of the surface electron current density, $\delta(k_x)$ is the Dirac δ-function, the subscripts a and s label the fields in the ambient medium and the substrate respectively, the superscripts (ind) and (tot) refer to induced and total fields, and E_0 and H_0 are the amplitudes of electric and magnetic fields in the incident wave. Then we relate the Fourier transform of the surface electron current density in the diode plane to that of the in-plane electric field in the same plane as

$$j(k_x) = G(k_x)E_x(k_x) + \frac{2}{Z_0}\delta(k_x)E_0,$$

where $E_x(k_x) = E_{x,s}^{(\mathrm{tot})}(k_x)$ is the Fourier transform of the in-plane component of the total electric field in the diode plane and Z_0 is the free space impedance. The k_x-space surface admittance $G(k_x)$ depends exclusively on the frequency and dielectric constants of the ambient medium ε_a (which we assume to be unity) and the substrate ε_x; therefore,

$$G(k_x) = \frac{\chi_a + \chi_s}{Z_0},$$

where

$$\chi_{a(s)} = \frac{\varepsilon_{a(s)}k_0}{\sqrt{k_0^2\varepsilon_{a(s)} - k_x^2}}.$$

Coming back to the real-space representation we have

$$j(x) = \frac{2E_0}{Z_0} + \int_{-\infty}^{\infty} dx' E_x(x') \int_{-\infty}^{\infty} dk_x G(k_x)\exp[ik_x(x - x')].$$

Using Ohm's law $j(x) = \sigma(\omega)E_x(x)$ for the two-dimensional electron channel and the condition $E_x = 0$ for the perfectly conductive contact half-planes, we obtain the following integral equation for an in-plane component of the total electric field within the slot:

$$\sigma(\omega)E_x(x) = \int_{-w/2}^{w/2} G(x, x')E_x(x')dx' + \frac{2E_0}{Z_0} \qquad (1)$$

with the kernel

$$G(x, x') = \int_{-\infty}^{\infty} dk_x G(k_x)\exp[ik_x(x - x')].$$

Integral Eq. (1) is solved numerically by the Galerkin method through its projection onto an orthogonal set of Legendre's polynomials within the interval $[-w/2, w/2]$. As a result, we find the induced electric field in the ambient medium is

$$\mathbf{E}_a^{(\mathrm{ind})}(\mathbf{r}) = \mathbf{E}_0\exp(ik_0z) + \int_{-\infty}^{\infty} \mathbf{E}_a^{(\mathrm{sc})}(k_x)\exp(i\mathbf{k}_a\mathbf{r})dk_x, \qquad (2)$$

and the total electric field in the substrate is

$$\mathbf{E}_a^{(\mathrm{tot})}(\mathbf{r}) = \int_{-\infty}^{\infty} \mathbf{E}_s^{(\mathrm{sc})}(k_x)\exp(i\mathbf{k}_s\mathbf{r})dk_x. \qquad (3)$$

The electric fields $\mathbf{E}_a^{(\mathrm{ind})}(\mathbf{r})$ and $\mathbf{E}_s^{(\mathrm{tot})}(\mathbf{r})$ have zero y-components, and $\mathbf{r}$ is the two-dimensional radius vector $\mathbf{r} = \{x, y\}$.

The wave vectors $\mathbf{k}_{a(s)}$ have k_x and $k_z = \pm\sqrt{k_0^2\varepsilon_{a(s)} - k_x^2}$ as their components. The integrals on the right-hand sides of Eqs. (2) and (3) describe the scattered fields in terms of the plane-wave continuum, while the first summand in Eq. (2) is the wave reflected normally from a perfectly conductive plane. The sign before the radical, in the expression for k_z, is chosen to correspond to the outgoing waves for $k_x < k_0\sqrt{\varepsilon_{a(s)}}$ and evanescent waves for $k_x > k_0\sqrt{\varepsilon_{a(s)}}$ in the respective medium.

Since only the outgoing plane waves (with $k_x < k_0\sqrt{\varepsilon_{a(s)}}$) contribute to radiative losses, we can calculate the fluxes of energy scattered per unit length of the slot in each medium as

$$P_{a(s)} = \frac{\pi}{Z_0}\int_{-k_0\sqrt{\varepsilon_{a(s)}}}^{k_0\sqrt{\varepsilon_{a(s)}}} \mathbf{n}_{a(s)}\frac{\mathbf{k}_{a(s)}}{k_0}\left|\mathbf{E}_{a(s)}^{(\mathrm{sc})}(k_x)\right|^2 dk_x,$$

where $\mathbf{n}_{a(s)}$ is the internal normal to the diode plane in the respective medium. Then we can define the scattering length as $L_{a(s)}^{(\mathrm{sc})} = P_{a(s)}/P_0$ in each medium, where P_0 is the energy flux density in the incident wave. We can also introduce the total scattering length as $L^{(\mathrm{sc})} = L_a^{(\mathrm{sc})} + L_s^{(\mathrm{sc})}$ and the absorption length as $L^{(\mathrm{ab})} = Q/P_0$, where

$$Q = \frac{1}{2}\int_{-w/2}^{w/2} |E_x(x, 0)|^2 \mathrm{Re}[\sigma(\omega)]dx$$

is the energy absorption rate (per unit length of the slot). The scattering and absorption lengths obey the energy conservation law in the form $L^{(\mathrm{sc})} + L^{(\mathrm{ab})} = L^{(\mathrm{ex})}$, where

$$L^{(\mathrm{ex})} = 4\pi\frac{\mathrm{Re}[\mathbf{E}_0^*\mathbf{E}_a^{(\mathrm{sc})}(k_x = 0)]}{|E_0|^2} \qquad (4)$$

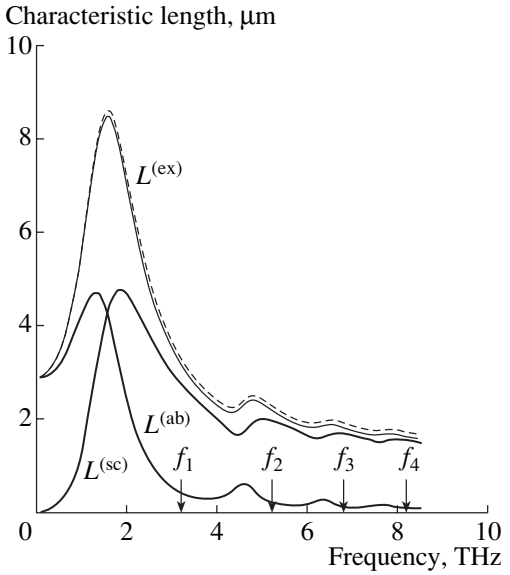

Fig. 1. Characteristic lengths vs. frequency for the slot diode with the parameters $N = 3 \times 10^{12}$ cm^{-2}, $\nu = 4.35 \times 10^{12}$ s^{-1}, $w = 1.3$ μm, $\varepsilon_s = 13.88$, and $m^* = 0.042m_0$.

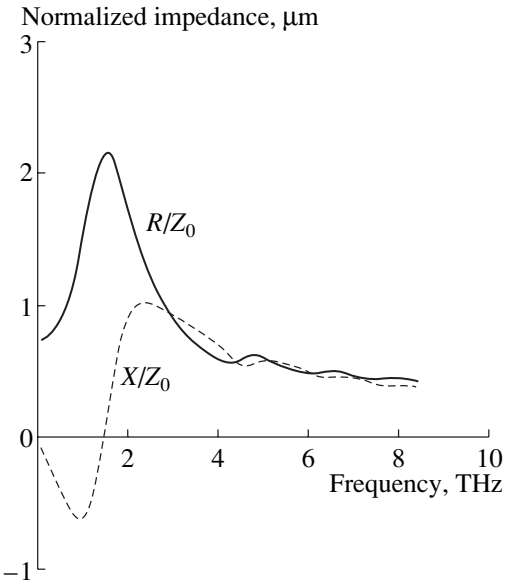

Fig. 2. Impedance of the slot diode with a two-dimensional electron channel vs. frequency.

is the extinction length, which is the ratio of the amount of energy picked out of the incident wave per unit time (per unit length of the slot) to that of the energy flux density in the incident wave. The formula analogous to Eq. (4) is the so-called optical theorem, in scattering theory [16].

3. RESULTS AND DISCUSSION

The calculated spectra of the scattering, absorption, and extinction lengths are shown in Fig. 1 for parameters typical of two-dimensional electron channels in gate-length HEMT of less than 100 nm at room temperature [12]. All characteristic lengths exhibit maxima at plasmon resonance frequencies in the channel. Note that, in order of magnitude, the extinction length exceeds the geometrical width of the slot even for the short electron relaxation time chosen for the calculations. The arrows in Fig. 1 mark the frequencies of ungated plasmons in an isolated two-dimensional electron channel with wave vectors $q_n = (2n - 1)\pi/w$ ($n = 1, 2, 3, \ldots$), which are estimated by a simple approximate formula [17]:

$$f_n = \frac{1}{2\pi}\sqrt{\frac{e^2 N q_n}{m^*\varepsilon_0(1+\varepsilon_s)}}. \quad (5)$$

It is evident from Fig. 1 that the plasma oscillations in the slot diode are softened because of the induction of image charges by these oscillations in the perfectly conductive contact half-planes.

In the equivalent circuit description, we can characterize the slot diode with a two-dimensional electron channel by its impedance. Within the channel, the total current is the sum of the electron current and the displacement current caused by oscillating charges in both the channel and contacts of the diode. Far away from the slot, the current in the contact planes is purely conductive and is determined by the amplitude of the incident wave. Since the total current is conserved along the circuit, we can define the diode impedance $Z = R + iX$ (per unit length of the slot) as

$$Z = \frac{1}{I}\int_{-w/2}^{w/2} E_x(x)dx,$$

where $I = 2E_0/Z_0$ is the surface-current density induced by the incident wave in the perfectly conductive contact planes.

The frequency dependence of the diode's normalized impedance, shown in Fig. 2, displays resonances at plasmon excitation frequencies. The reactance X exhibits a transition from inductive ($X < 0$) behavior, caused by the kinetic inductance of the electron channel, to a capacitive behavior ($X > 0$) at the frequency of the fundamental plasmon resonance, which corresponds to the current resonance in the equivalent circuit description. However, no current resonance is exhibited at higher plasmon resonant frequencies.

The normalized resistance R/Z_0 is, in essence, the matched width of the diode (measured along the slot), since the resistance of diode and the matched width is equal to the free-space impedance. The following theorem is valid: $4R = Z_0L^{(ex)}$. The extinction length calculated using this formula (dashed curve in Fig. 1), and by Eq. (4) (solid line), coincides with the accuracy of our numerical procedure. Accordingly, we can introduce the electron resistance R_e and radiation resistance R_{rad}, where $R_e = Z_0L^{(ab)}/4$ and $R_{rad} = Z_0L^{(sc)}/4$, respectively, so

that the total resistance of the diode is given by $R = R_e + R_{rad}$. Note that R does not vanish at high frequencies (but approaches R_{rad} instead).

One can see from Fig. 2 that the higher resonances are not nearly as pronounced as those predicted by the electrostatic description [15] because, at high frequencies, the $R_{rad}C_g$ circuit shunts plasma oscillations in the channel effectively. However, a sharp fundamental resonance, which corresponds to the current resonance in the equivalent circuit description, shows up even for room temperature parameters of the diode.

The frequency of the fundamental plasma resonance in the slot diode increases as the slot width decreases (according to formula (5), it varies roughly as a square root of the inverse of the slot width). Figures 3 and 4 exhibit absorption length and scattering length spectra for a 100 nm width of the slot for different electron scattering rates. Notice that the resonant absorption (the absorption excess at the resonance over the nonresonant Drude background) grows considerably as the width of the slot decreases (cf. Figs. 1 and 3). Clearly, the fundamental plasma resonance becomes narrower when the electron scattering rate is decreased. However, the width of the resonance remains finite due to the radiative damping of plasma oscillations, even with no electron scattering in the channel. The width of the scattering resonance in the absence of electron scattering (see curve *4* in Fig. 4) originates entirely from radiative damping. To minimize an error arising from the nonresonant background contribution, we estimate the radiative damping of plasmons γ_{rad} as the half width at half magnitude (HWHM) in the low-frequency slope of the scattering-resonance curve for $\nu = 0$ (curve *4* in Fig. 4), which yields $\gamma_{rad} = 4.27 \times 10^{12}$ s^{-1}. Then the electron scattering contribution to the resonance linewidth can be obtained as the difference between the HWHM measured in the low-frequency slope of the scattering resonance at any given $\nu \neq 0$ (or, which yields the same result, in the high-frequency slope of the corresponding absorption resonance) and the radiative damping. The scattering length at the plasma resonance monotonically grows as the electron scattering rate decreases, while the resonant absorption exhibits a maximum when the dissipative broadening (caused by the electron scattering in the channel) of the resonance linewidth becomes equal to the radiative broadening (curve *2* in Fig. 3 corresponds to this case). The weaker, as well as the stronger, electron scattering result in a smaller resonant absorption. Note that under the condition of maximal absorption, the scattering length of the diode is approximately equal to its absorption length, which puts the limit of the diode's ratio of absorption to scattering length close to unity.

We conclude that a slot diode with a two-dimensional electron channel provides a resonant circuit at terahertz frequencies that effectively couples to external electromagnetic radiation with the loaded Q-factor exceeding unity, even at room temperature. We also claim that the diode's high-frequency resistance may be measured from contactless measurements of the characteristic electromagnetic lengths of the diode.

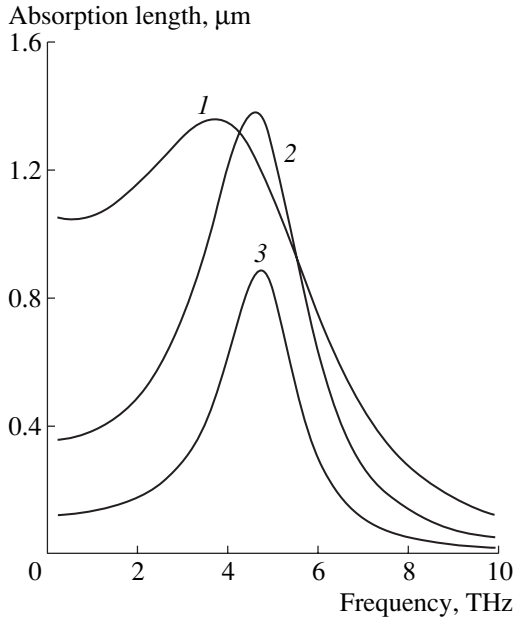

Fig. 3. Absorption length of the slot diode with the parameters $N = 3 \times 10^{12}$ cm^{-2}, $w = 0.1$ μm, $\varepsilon_s = 13.88$, and $m^* = 0.042m_0$ as a function of the frequency for different electron scattering rates: $\nu = 2 \times 10^{13}$ s^{-1} (curve *1*); 7×10^{12} s^{-1} (curve *2*); 2.3×10^{12} s^{-1} (curve *3*).

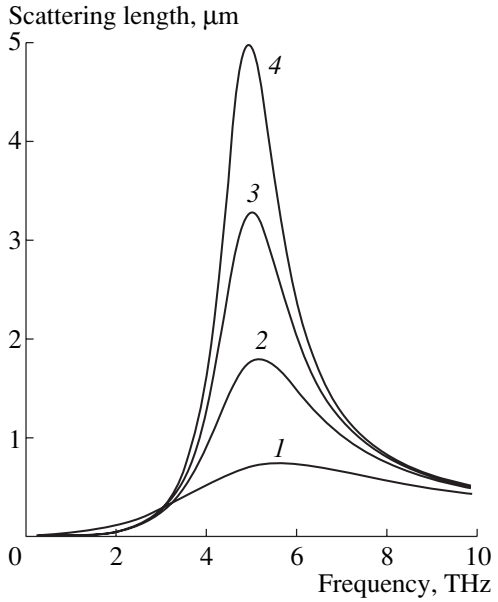

Fig. 4. Scattering length of the slot diode as a function of the frequency for different electron scattering rates: $\nu = 2 \times 10^{13}$ s^{-1} (curve *1*); 7×10^{12} s^{-1} (curve *2*); 2.3×10^{12} s^{-1} (curve *3*); $\nu = 0$ (curve *4*). The other parameters of the diode are the same as those in Fig. 3.

ACKNOWLEDGMENTS

This work has been supported by the Russian Foundation for Basic Research, grant no. 03-02-17219, and by the Russian Academy of Sciences program "Novel Materials and Structures." W.K. acknowledges the support of the CNRS-program "New THz Emitters and Detectors," Region Languedoc Roussillon, and from the French Ministry of Research and New Technologies, program ACI "Nanosciences and Nanotechnologies."

REFERENCES

1. M. S. Shur and V. Ryzhii, in *Terahertz Sources and Systems*, Ed. by R. Miles, P. Harrisson, and D. Lippens (Kluwer Academic, Dordrecht, 2001), p. 169.
2. M. Dyakonov and M. Shur, Phys. Rev. Lett. **71**, 2465 (1993).
3. M. Dyakonov and M. Shur, IEEE Trans. Electron Devices **43**, 380 (1996).
4. M. S. Shur and J.-Q. Lü, IEEE Trans. Microwave Theory Tech. **48**, 750 (2000).
5. W. Knap, V. Kachorovskii, Y. Deng, *et al.*, J. Appl. Phys. **91**, 9346 (2002).
6. W. Knap, Y. Deng, S. Rumyantsev, *et al.*, Appl. Phys. Lett. **80**, 3433 (2002).
7. X. G. Peralta, S. G. Allen, M. C. Wanke, *et al.*, Appl. Phys. Lett. **81**, 1627 (2002).
8. W. Knap, Y. Deng, S. Rumyantsev, and M. S. Shur, Appl. Phys. Lett. **81**, 4637 (2002).
9. V. V. Popov, O. V. Polischuk, T. V. Teperik, *et al.*, J. Appl. Phys. **94**, 3556 (2003).
10. V. V. Popov, T. V. Teperik, O. V. Polischuk, *et al.*, Phys. Solid State **46**, 153 (2004).
11. Y. Deng, R. Kersting, J. Xu, *et al.*, Appl. Phys. Lett. **84**, 70 (2004).
12. W. Knap, J. Lusakowski, T. Parenty, *et al.*, Appl. Phys. Lett. **84**, 2331 (2004).
13. A. V. Antonov, V. I. Gavrilenko, E. V. Demidov, *et al.*, Phys. Solid State **46**, 146 (2004).
14. P. J. Burke, I. B. Spielman, J. P. Eisenstein, *et al.*, Appl. Phys. Lett. **76**, 745 (2000).
15. V. Ryzhii, A. Satou, and M. S. Shur, J. Appl. Phys. **93**, 10041 (2003).
16. R. G. Newton, *Scattering Theory of Waves and Particles* (McGraw-Hill, New York, 1966; Mir, Moscow, 1969).
17. J. Alsmeier, E. Batke, and J. P. Kotthaus, Phys. Rev. B **40**, 12574 (1989).

Semiconductors, Vol. 39, No. 1, 2005, pp. 147–155. Translated from Fizika i Tekhnika Poluprovodnikov, Vol. 39, No. 1, 2005, pp. 162–170.

PHYSICS OF SEMICONDUCTOR DEVICES

Bloch Oscillations in Superlattices: The Problem of a Terahertz Oscillator

Yu. A. Romanov^ and Yu. Yu. Romanova

Institute for the Physics of Microstructures, Russian Academy of Sciences, Nizhni Novgorod, 603950 Russia

^e-mail: romanov@ipm.sci-nnov.ru

Submitted June 1, 2004; accepted for publication June 14, 2004

Abstract—The feasibility of designing a terahertz oscillator based on the Bloch oscillations of electrons in semiconductor superlattices is studied. It is shown that superlattices with high-Q Bloch oscillations can be used to generate a terahertz emission in pulsed electric fields with an off-duty factor that ensures the thermalization of electrons heated by the field. It is suggested that a terahertz oscillator is designed with a frequency that is tuned continuously by an electric field on the basis of anharmonic Bloch oscillations of electrons in semiconductor superlattices that have special miniband characteristics in which the major part of the effective electron mass is positive and increases as the electron energy increases. This circumstance makes it possible to eliminate the development of undesired domain instability (the Gunn effect). © *2005 Pleiades Publishing, Inc.*

1. INTRODUCTION

The quasi-momentum Brillouin zones and allowed energy bands of electrons in homogeneous starting materials are split in semiconductor superlattices (SLs) into a number of relatively narrow (10^5–10^7 cm^{-1}) Brillouin minizones and narrow (10^{-3}–10^{-1} eV) allowed and forbidden energy minibands. Due to the small size of the Brillouin minizones, the Bragg reflections of electrons from the SL boundaries manifest themselves clearly in the electrical characteristics of SLs, even in comparatively low electric fields (10^2–10^4 V/cm). In static fields, these reflections give rise to periodic Bloch oscillations (BOs) with reasonably high frequencies [1] and to corresponding Wannier–Stark ladders of energy levels [2]. For example, in an SL with the period d = 100 Å and the miniband width Δ = 20 meV that is in a static field E_C = 4 kV/cm, the BO frequency $f_C \equiv \Omega_C/2\pi \equiv eE_Cd/2\pi\hbar \approx 1$ THz, the amplitude of the electron-coordinate oscillations $Z_C \approx 10^{-5}$ cm $\gg d$, and the spacing between the Wannier–Stark levels $\hbar\Omega_C \approx 4$ meV $\ll \Delta$. We will refer to oscillations of electrons in an alternating electric field as Bloch oscillations in a harmonic field (BOHFs) in order to differentiate these oscillations from conventional BOs. In periodic electric fields (without a static component), BOHFs are periodic along with the field period. In a field that includes constant and harmonic components with the incommensurable frequencies Ω_C and ω ($n_1\Omega_C \neq n_2\omega$, where n_1 and n_2 are the integers that do not have a common multiplier), BOHFs are not periodic. In the case of commensurable frequencies ($n_1\Omega_C = n_2\omega$), the BOHFs are again periodic, but now they have the period $2n_1\pi/\omega$, which is n_1 times larger than the field period. A similar situation arises in a biharmonic field.

The Bragg reflections represent (in the presence of electron scattering) the main origin of static and high-frequency (dynamic) negative differential conductivity (NDC) in SLs. The existence of BOs, BOHFs, and NDC makes the idea of using semiconductor SLs for the design of a terahertz Bloch oscillator very attractive. This study is especially concerned with the possibility of realizing this idea. The paper is structured in the following way: In Section 2, we discuss the main distinctive properties of BOs and BOHFs and formulate the methods for using these oscillations to generate terahertz radiation. In Section 3, we derive the main expressions for the electrical transport and heating of the SL electrons for an arbitrary dispersion relation in strong alternating fields. In Section 4, we study the transient currents and heating of electrons in an SL when a static electric field is abruptly switched on. In Section 5, we study the current oscillations in a periodic field of a meander type and discuss the effect of heating the electrons with an electric field on the amplitude of current oscillations. In Section 6, we study the generation of current using periodic pulsed fields with an off-duty factor that ensures the thermalization of electrons heated by an electric field. In Section 7, we study the dependences of the dynamic differential conductivity in a SL on the dispersion relation in a miniband and the characteristics of electron scattering in SLs. In Section 8, we formulate the main results of this study.

2. PROPERTIES OF BLOCH OSCILLATIONS AND BLOCH OSCILLATIONS IN A HARMONIC FIELD IN A SUPERLATTICE

The properties of BOs and BOHFs are quite different from those of a conventional oscillator; a BO and a BOHF also differ appreciably from one other. When

studying these oscillations, we will use (for simplicity) the additive dispersion relation

$$\varepsilon(\mathbf{k}) = \varepsilon_3(k_3) + \varepsilon_\perp(k_\perp), \quad \varepsilon_\perp(k_\perp) = \frac{\hbar^2 k_\perp^2}{2m}, \qquad (1)$$

where $\varepsilon(\mathbf{k})$ and $\mathbf{k}$ are the energy and the quasi-wave vector of electrons, respectively; $\varepsilon_3(k_3)$ and k_3 are the energy and wave-vector components that are longitudinal with respect to the SL axis; $\varepsilon_\perp(k_\perp)$ and $k_\perp$ are the corresponding transverse components; and m is the effective transverse electron mass. We represent the longitudinal energy $\varepsilon_3(k_3)$ in the form of the Fourier series (in the form of a combination of partial sinusoidal minibands) as

$$\varepsilon_3(k_3) = \frac{1}{2}\sum_{n=1}^{N} \Delta_n[1 - \cos(nk_3 d)], \qquad (2)$$

where Δ_n is the width of a partial sinusoidal miniband. This width can be both positive and negative. We disregard the electron spin; as a result, the dispersion relation is symmetric with respect to k_3. In (2), N is an integer. We assume that the electric field is directed along the SL axis. In what follows, we drop the subscript 3 from the longitudinal energy only if this does not lead to confusion.

We consider the BOs first. It is well known that, in a static field E_C with an arbitrary magnitude, an electron with an arbitrary initial quasi-momentum is localized in the coordinate space in the direction of the field and executes periodic oscillations that are described in terms of the velocity

$$V(k_0, t_0, t) = \frac{1}{\hbar}\frac{\partial \varepsilon(k_3)}{\partial k_3} = \sum_{n=1}^{N} V_n^m \sin[n(k_0 d + \Omega_C(t - t_0))], \qquad (3)$$

where $\mathbf{k}_0$ is the quasi-wave vector of electron at the initial point in time t_0, and $V_n^m = \Delta_n d/2\hbar$ is the highest (in magnitude) partial velocity of the electron (this velocity can exceed the highest velocity in the miniband). It is worth noting that the BO frequency $\Omega_C = eE_C d/\hbar$ is independent of the dispersion relation; rather, this frequency is only completely defined by the electric-field strength and the SL period. At the same time, the velocity amplitude and the shape of BOs (spectrum in the units of Ω_C) are completely governed by the dispersion relation for electrons and are independent of the electric-field strength. In the general case, the BOs are anharmonic. They are harmonic only in a sinusoidal miniband. The amplitudes of the BO harmonics are also independent of the initial conditions. The initial quasi-momentum governs only the initial phase of BOs.

The BO energy (the time-averaged kinetic energy of electrons) is not affected by collisions; rather, only the phase and centroid of the oscillations change, which leads to the drift of electrons, i.e., to a static current. When the field is switched off, the electron oscillations cease immediately; and when the field is varied, the frequency of the oscillations changes. The existence of BOs and the corresponding Wannier–Stark levels is strongly supported by the results of a number of studies [3].

We now consider the properties of BOHFs. For simplicity, we restrict our consideration to the case of a harmonic miniband. Let an electron in an SL be subjected to a multifrequency field

$$E(t) = E_C + \sum_{\alpha=1}^{N} E_\alpha \cos(\omega_\alpha t - \delta_\alpha) \qquad (4)$$

that contains a constant component E_C and N harmonics with arbitrary frequencies ω_α and initial phases δ_α. In this field, an electron executes the oscillations that are described in terms of the velocity

$$V(k_0, t_0, t) = V_m \sin\left\{k_0 d + \Omega_C(t - t_0) + \sum_{\alpha=1}^{N} g_\alpha[\sin(\omega_\alpha t - \delta_\alpha) - \sin(\omega_\alpha t_0 - \delta_\alpha)]\right\} = V_m[C_S(k_0, t_0)\Psi_S(t) + C_A(k_0, t_0)\Psi_A(t)], \qquad (5)$$

where

$$\Psi_S(t) = \cos\left[\Omega_C t + \sum_{\alpha=1}^{N} g_\alpha \sin(\omega_\alpha t - \delta_\alpha)\right], \quad \Psi_A(t) = \sin\left[\Omega_C t + \sum_{\alpha=1}^{N} g_\alpha \sin(\omega_\alpha t - \delta_\alpha)\right], \qquad (6)$$

$$C_S^2(k_0, t_0) + C_A^2(k_0, t_0) = 1, \quad \Psi_S^2(t) + \Psi_A^2(t) = 1, \quad g_\alpha = eE_\alpha d/\hbar\omega_\alpha. \qquad (7)$$

Here, $\Psi_S(t)$ and $\Psi_A(t)$ are the wave-velocity packets that have a different (but independent of the initial conditions) symmetry and spectrum, and $C_S(k_0, t_0)$ and $C_A(k_0, t_0)$ are the amplitudes of these wave packets. The fact that a BOHF can be separated into two "orthogonal" wave packets gives rise to a similarity between the behavior of an SL and the behavior of a two-level system.

In the case of a purely harmonic field

$$E(t) = E\cos\omega t,$$

we use expressions (5) and (6) to obtain

$$\Psi_S(t) = \cos(g\sin\omega t) = J_0(g) + 2\sum_{n=1}^{\infty} J_{2n}(g)\cos 2n\omega t, \quad (8)$$

$$\Psi_A(t) = \sin(g\sin\omega t) = 2\sum_{n=1}^{\infty} J_{2n-1}(g)\sin[(2n-1)\omega t],$$

$$C_S(k_0, t_0) = \sin(k_0 d - g\sin\omega t_0), \quad (9)$$

$$C_A(k_0, t_0) = \cos(k_0 d - g\sin\omega t_0).$$

Here, $J_n(g)$ are the Bessel functions; i.e., the functions $\Psi_S(t)$ contain only the even harmonics of the field, whereas $\Psi_A(t)$ contain only the odd harmonics. We list below the properties of BOHFs that differentiate them from those of BOs for this important case:

(i) The motion of an electron (irrespective of its dispersion relation) in the quasi-momentum space is periodic with the period coinciding with that of the field. The Bragg reflections from the minizone boundaries do not give rise to a specific oscillation period (as in the case of a static field); rather, these reflections modulate the electron oscillations deeply during their period [4]. The width of the corresponding quasi-energy minibands is also modulated [5]. As a result, only the harmonics with frequencies that are multiples of the field frequency are present in the BOHF spectrum. In addition, the dependences of the amplitudes of these harmonics on the field amplitude are highly nonmonotonic. At large amplitudes of the field ($eEd \gg \hbar\omega$), the BOHFs contain harmonics of a very high order ($n > eEd/\hbar\omega$), which is a direct consequence of the large number of Bragg reflections during the field period. For example, the nth ($n \gg 1$) harmonic of BOHFs, which is proportional to $J_n(eE_1 d/\hbar\omega_1)$, is largest in the field $E \approx n\hbar\omega/ed$. The experimentally observed electromagnetic transparency of SLs is a particular manifestation of the nonmonotonic dependence of the BOHF spectrum on the field amplitude [4, 6].

(ii) Localization of electrons in the coordinate space (vanishing of the constant electron-velocity component irrespective of the initial electron momentum) occurs only at discrete values of a dimensionless field amplitude that are specified by zeros of the zeroth-order Bessel function $J_0(eEd/\hbar\omega) = 0$. This phenomenon has come to be known as the "dynamic localization of an electron" [7]. The finiteness of the electron motion leads to the collapse of the electron's quasi-energy minibands [5]; i.e., the quasi-energy electron spectrum in a harmonic field (in contrast to what happens in a static field) becomes discrete only at certain discrete values of the field relative amplitude $g = eEd/\hbar\omega$.

(iii) The initial momentum $\mathbf{k}_0$ does not control the BOHF phase; rather, it controls the amplitudes of the corresponding wave packets and, consequently, in particular, the time-averaged energy and velocity of electrons. The phases of the BOHF harmonics are specified (to within π) by the field phase. Collisions affect the wave-packet amplitudes $C_{S,A}(\mathbf{k}_0, t)$ (including the sign of these amplitudes), the mean kinetic energy, and the BOHF centroid. At $\omega\tau \gg 1$, a BOHF can be considered as a long-lived quasiparticle (spin) with two vibrational degrees of freedom.

If an SL is in a field

$$E(t) = E_C + E\cos\omega t$$

that includes a static component and a single harmonic component, the electron velocity is defined by the relation

$$V(\mathbf{k}_0, t) = V_m \sum_{n=-\infty}^{\infty} J_n(g) \quad (10)$$

$$\times \sin[\mathbf{k}_0 d + \Omega_C(t - t_0) + n\omega t - g\sin\omega t_0].$$

It can be seen from (10) that the shift of the BOHF spectrum induced by a static field is equal to the Bloch frequency Ω_C with the amplitudes of the harmonics remaining intact (here, for clearer presentation, we consider the positive and negative frequencies as not being equivalent). This shift can also be considered as the amplitude modulation of BOHFs by Bloch oscillations in a harmonic field. At an arbitrary E_C, there is no periodicity in BOHFs and the BOHF spectrum includes only the harmonics with incommensurable frequencies $\Omega_C \pm n\omega$. However, due to the fact that a static field does not exhibit a specific phase, the Stark frequency shift disappears in a constant microscopic current and acquires a random phase as a result of collisions (amplitude modulation with a random phase). This shift can be observed only in transient characteristics. In the case of the nonlinear Stark resonance ($n_1\Omega_C = n_2\omega$), the BOHFs are periodic with the period $2n_1\pi/\omega$ (this period is larger by n_1 than that of the field). However, the collisions destroy this periodicity as well, and, as a result, only the harmonics that are multiples of the field frequency remain in the steady-state current. Nevertheless, the aforementioned resonances manifest themselves in the special features of the SL conductivity [8].

The above-listed properties of BOs and BOHFs suggest the following methods for using an SL to generate terahertz radiation:

(i) The use of high-Q BOs and BOHFs ($\Omega_C, \omega \gg \tau^{-1}$). Excitation with pulsed fields (or accomplishment of the quasi-ballistic transport in short SLs).

(ii) The use of low-Q BOs and BOHFs. The use of the dynamic NDC.

(iii) The use of nonmonotonic and highly nonlinear conductivity for efficient multiplication or mixing of frequencies in the cases of both the high-Q and low-Q BOs and BOHFs.

In this paper, we discuss the first two methods.

3. THE ELECTRON TRANSPORT. GENERAL RELATIONS

Let us study the manifestation of BOs and BOHFs in the electrical characteristics of SLs. We use the Boltzmann equation in the approximation of the constant relaxation time τ; thus, we have

$$\frac{\partial f(\mathbf{k}, t)}{\partial t} + \frac{eE(t)}{\hbar}\frac{\partial f(\mathbf{k}, t)}{\partial \mathbf{k}} = -\frac{f(\mathbf{k}, t) - f_0(\mathbf{k})}{\tau},$$
$$f(\mathbf{k}, t_0) = f_0(\mathbf{k}), \tag{11}$$

where $f(\mathbf{k}, t)$ and $f_0(\mathbf{k})$ are the field-perturbed and equilibrium distributions of electrons and t_0 is the point in time when the electric field is switched on. We use the periodicity in the $\mathbf{k}$ space to represent the distribution function for electrons in the form of the following Fourier series:

$$f(\mathbf{k}, t) = \sum_{\nu = -\infty}^{\infty} F_\nu(k_\perp)\exp(i\nu k_3 d)\Phi_\nu(t). \tag{12}$$

Here,

$$F_\nu(k_\perp) = \frac{d}{2\pi}\int_{-\pi/d}^{\pi/d} f_0(\mathbf{k})\exp(-i\nu k_3 d)dk_3. \tag{13}$$

According to expressions (11)–(13), the multicomponent distribution function (in the ν space) $\Phi_\nu(t)$ satisfies a kinetic equation

$$\tau\frac{d\Phi_\nu(t)}{dt} + [1 + i\nu\tau\Omega(t)]\Phi_\nu(t) = 1,$$
$$\Omega(t) = \frac{edE(t)}{\hbar} \tag{14}$$

with the initial conditions

$$\Phi_\nu(t_0) = 1. \tag{15}$$

The solution of this equation is given by

$$\Phi_{\nu(t)} = \left[\exp\left(-\frac{t - t_0}{\tau}\right)\Psi_\nu^*(t_0) + \int_{t_0}^{t}\exp\left(-\frac{t - t_1}{\tau}\right)\Psi_\nu^*(t_1)\frac{dt_1}{\tau}\right]\Psi_\nu(t), \tag{16}$$

where

$$\Psi_\nu(t) = \exp\left(-i\nu\int_0^t \Omega(t_1)dt_1\right) = [\Psi_S(t) - i\Psi_A(t)]^\nu \tag{17}$$

is the BOHF eigenfunction that represents the solution of the kinetic equation (14) with the collision integral and describes the dynamic (i.e., collisionless) modulation of the distribution function of electrons by the field. The functions $\Psi_{S,A}(t)$ are defined by expressions (6).

It is easy to show that the partial current and the mean electron energy are related to the functions $\Phi_\nu(t)$ by the expressions

$$j_\nu(t) = j_0\mathrm{Im}\Phi_\nu(t), \tag{18}$$

$$\varepsilon_\nu(t) = \langle\varepsilon_\nu\rangle_0 + \left(\frac{\Delta_\nu}{2} - \langle\varepsilon_\nu\rangle_0\right)[1 - \mathrm{Re}\Phi_\nu(t)], \tag{19}$$

where

$$j_{0\nu} = \frac{\nu\Delta_\nu ed}{\hbar}\int f_0(\mathbf{k})\cos(\nu k_3 d)\frac{d^3k}{(2\pi)^3} = \frac{end}{\hbar}\left(\frac{\Delta_\nu}{2} - \langle\varepsilon_\nu\rangle_0\right), \tag{20}$$

$\langle\varepsilon_\nu\rangle_0$ and $\varepsilon_\nu(t)$ are the mean partial equilibrium and nonequilibrium electron energies, respectively; and n is the electron concentration. Consequently, the current and relative heating of electrons in an SL with an arbitrary dispersion relation (2) in an arbitrary electric field $E(t)$ are defined by the following expressions:

$$j(t) = \sum_{\nu = 1}^{N} j_\nu(t), \tag{21}$$

$$B(t) \equiv \frac{\varepsilon(t) - \langle\varepsilon\rangle_0}{\frac{\Delta}{2} - \langle\varepsilon\rangle_0} = \sum_{\nu = 1}^{N}\frac{\frac{\Delta_\nu}{2} - \langle\varepsilon_\nu\rangle_0}{\frac{\Delta}{2} - \langle\varepsilon\rangle_0}B_\nu(t). \tag{22}$$

Here,

$$j_\nu(t) = j_{\nu 0}\left\{\exp\left(-\frac{t - t_0}{\tau}\right)\sin\left[\nu\int_{t_0}^{t}\Omega(t_1)dt_1\right] + \int_{t_0}^{t}\frac{dt_1}{\tau}\exp\left(-\frac{t - t_1}{\tau}\right)\sin\left[\nu\int_{t_1}^{t}\Omega(t_2)dt_2\right]\right\}, \tag{23}$$

$$B_\nu(t) \equiv \frac{\varepsilon_\nu(t) - \langle\varepsilon_\nu\rangle_0}{\frac{\Delta_\nu}{2} - \langle\varepsilon_\nu\rangle_0} = 1 - \exp\left(-\frac{t - t_0}{\tau}\right)\cos\left[\nu\int_{t_0}^{t}\Omega(t_1)dt_1\right] - \int_{t_0}^{t}\frac{dt_1}{\tau}\exp\left(-\frac{t - t_1}{\tau}\right)\cos\left[\nu\int_{t_1}^{t}\Omega(t_2)dt_2\right], \tag{24}$$

and $\langle\varepsilon\rangle_0$ and $\varepsilon(t)$ are the mean equilibrium and nonequilibrium electron energies.

4. STATIC CURRENT–VOLTAGE CHARACTERISTIC: TRANSIENT PROCESSES

The Bragg reflections of electrons from the boundaries of the Brillouin minizone represent the main cause of the presence of NDC in the SL [9, 10]. According to (21)–(24), the corresponding current–voltage (*I–V*) characteristics and the heating of electrons in a static electric field E_C are defined by the expressions

$$j_C = \sum_{\nu=1}^{N} j_{0\nu}\frac{\nu\Omega_C\tau}{1+(\nu\Omega_C\tau)^2}, \tag{25}$$

$$\langle\varepsilon\rangle - \langle\varepsilon\rangle_0 = \sum_{\nu=1}^{N}\left[\frac{\Delta_\nu}{2} - \langle\varepsilon_\nu\rangle_0\right]\frac{(\nu\Omega_C\tau)^2}{1+(\nu\Omega_C\tau)^2} \equiv \left(\frac{\Delta}{2} - \langle\varepsilon\rangle_0\right)B(E_C). \tag{26}$$

In an SL with a harmonic minizone ($N = 1$), electrical current attains the largest value $j_0/2$ in a field $E_C = E^*$, where $E^* = \hbar/ed\tau$ is the effective field such that an electron subjected to it passes through the entire Brillouin minizone in time $2\pi\tau$. The effect of the dispersion relation for electrons on the shape of the *I–V* characteristic was discussed by Romanov [10]. It is worth noting that the electrical current tends to zero in a high electric field, while the mean electron energy tends to the large constant value $\Delta/2$ ($B(E_C) \longrightarrow 1$) that corresponds to the uniform distribution of electrons within the minizone; i.e., to an intense heating of electrons in a field that is close to zero.

The expression for the static *I–V* characteristic can be used only if the following conditions for a slow variation in the field are satisfied:

$$\omega\tau \ll 1, \quad \tau dE(t)/dt \ll E^*. \tag{27}$$

The second condition in (27) is the most important one for this consideration. If this condition is not satisfied (for example, in a situation where the field is changed abruptly), transient coherent electron oscillations that generate macroscopic currents can appear in SLs.

We now consider the evolution of both the current and the mean electron energy when the field is abruptly switched on $E(t) = E_C\theta(t)$, where $\theta(t)$ is the unit-step function. Using formulas (21)–(24), we obtain

$$j(t) = \sum_{\nu=1}^{\infty} j_{0\nu}\frac{\nu\Omega_C\tau}{1+(\nu\Omega_C\tau)^2} \times\left[1 - \exp\left(-\frac{t}{\tau}\right)(\cos\nu\Omega_C t - \nu\Omega_C\tau\sin\nu\Omega_C t)\right], \tag{28}$$

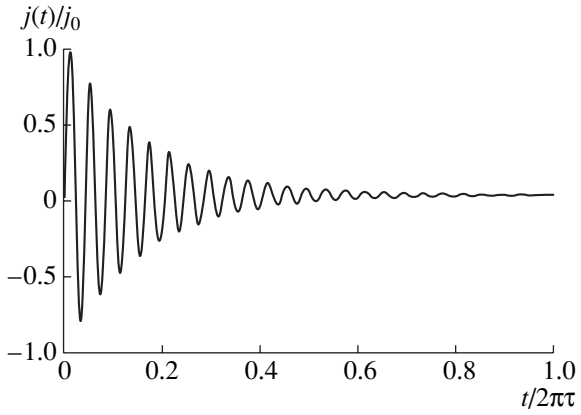

Fig. 1. Oscilloscope patterns of the current in a superlattice when the static field with $\Omega_C\tau = 25$ was abruptly switched on.

$$B_\nu(t) = \sum_{\nu=1}^{N}\frac{(\nu\Omega_C\tau)}{1+(\nu\Omega_C\tau)^2} \times\left[\nu\Omega_C\tau - \exp\left(-\frac{t}{\tau}\right)(\nu\Omega_C\tau\cos\nu\Omega_C t + \sin\nu\Omega_C t)\right]. \tag{29}$$

In Fig. 1, we show the corresponding oscilloscope pattern for a current in an SL with a sinusoidal minizone ($N = 1$) residing in a static field with $\Omega_C\tau = 25$. We should call attention to the fact that $\max[j(t)/j_0] = 1$, whereas $\max(j_C/j_0) = 0.5$ for a static current. The mean electron energy behaves in a similar way: $\max[B(t)] \approx 2$, whereas the static value $B(E_C) < 1$. The energies $\varepsilon(t) = \langle\varepsilon\rangle_0$, $\Delta/2$, and $\Delta - \langle\varepsilon\rangle_0$ correspond to a situation where $B(t) = 0$, 1, and 2. At $t > \pi\tau$, a steady-state distribution of electrons is established in the SL, so that the electric current and the mean electron energy attain values that correspond to the static *I–V* characteristic (25). However, in spite of a small steady-state current, the electrons remain highly heated ($B(t) \longrightarrow 1$). It is noteworthy that the current in the SL is small due exactly to the high degree to which the electrons are heated. We note that the dispersion relation for electrons in the minizone can be deduced from the spectrum of current oscillations in the transient process.

5. OSCILLATIONS OF CURRENT AND HEATING OF ELECTRONS IN THE HARMONIC AND MEANDER-LIKE FIELDS

It would seem that, in order to obtain the efficient generation of radiation-based BOHFs, one can use the harmonic or meander-like fields with a large amplitude at $\max[\Omega(t)\tau] \gg 1$ and the period $T \approx 2\pi\tau$. In Fig. 2, we show the corresponding oscilloscope patterns of the current and mean electron energy in a meander-like field given by

$$E(t) = E_C\theta(t)\tanh(10\sin\omega t) \tag{30}$$

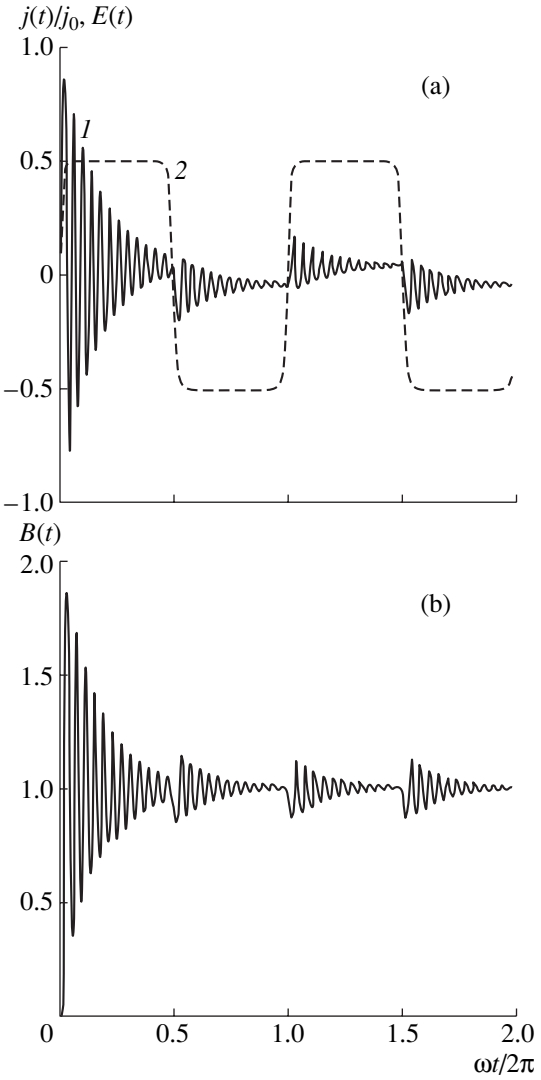

Fig. 2. Oscilloscope patterns of (a) the current and (b) the mean electron energy in a meander-like field with $\Omega_C\tau = 25$ and the period $T = 2\pi\tau$ after this field was switched on abruptly. Curve *1* represents the dimensionless current and curve *2* represents the dimensionless electric field.

at $\omega\tau = 1$ and $\Omega_C\tau = 25$. These patterns were calculated using formulas (23) and (24). The corresponding oscilloscope patterns for a harmonic field have the same shape as well. It can be seen from Fig. 2 that the amplitude of the current oscillations is large only during the first half-period; this amplitude then decreases abruptly (by a factor of 5 in the example under consideration). This decrease is caused by a pronounced heating of the electron gas and by the fact that this gas has no time to cool between the field spikes. As a result of the narrowness of the Brillouin minizone in the SL, a highly heated electron gas in the SL gives rise to low currents in any fields where there is no interminizone tunneling. This circumstance represents a disadvantage of an SL in comparison with a bulk semiconductor. At the same time, we see an advantage of SLs, since the intraminizone current is limited by the value of j_0, which increases the resistance of SLs to high fields. Thus, heating the electron gas detrimentally affects the emission characteristics of SLs.

Calculations show that electron gas cools in a time $\sim\pi\tau$ after the field has been switched off (this is also evident from physical considerations). However, it is useful to bear in mind that, here, the role of τ is played by the energy-relaxation time that usually exceeds the velocity-relaxation time. In addition, the velocity- and energy-relaxation times in SLs without an electric field can be much shorter than those in a strong field. In particular, such a situation takes place in an SL composed of an ensemble of quantum dots [11]. Therefore, the cooling of electron gas in an SL can occur in a shorter time than the electron-gas heating and the current-oscillation damping that are related to the BOs and BOHFs.

6. GENERATION OF CURRENT OSCILLATIONS BY PULSED FIELDS

The results described in Section 5 make it possible to hope that the BOs and BOHFs can be used to generate terahertz radiation in periodic pulsed electric fields with an off-duty factor that ensures the thermalization of electrons. In order to verify whether this possibility could be realized, we studied the evolution of the current and the mean electron energy in periodic fields of the three following types:

(i) A field generated by monopolar rectangular pulses (a meander clipped from below) and represented as

$$E(t) = (E_C/2)[1 + \tanh(10\sin\omega t)]. \quad (31)$$

(ii) A field generated by a sine function clipped from below and described as

$$E(t) = (E_c/2)[1 + \tanh(10\sin\omega t)]\sin\omega t. \quad (32)$$

(iii) A field generated by an uplifted sine function and represented as

$$E(t) = (E_C/2)(1 + \sin\omega t). \quad (33)$$

In Fig. 3, we show the oscilloscope patterns of the current, electron energy, and the current spectrum in a periodic field (31) with $\Omega_C/\omega = 25$ and $\omega\tau = 1$. In this case, the alternating current has a large amplitude (as in the first half-period in Fig. 2) since the electrons have time to thermalize before the next field spike. As should be expected, the spectral current lines are most intense at the harmonics $n_0 \approx \Omega_C/\omega$. In the field given by (32), the alternating current is of the same order of magnitude as in the previous case but has a spectrum that is almost homogeneous until the harmonic n_0; however, as soon as the value of n_0 is exceeded, the spectrum is cut off abruptly. In the field given by (33), the alternating cur-

rents are small since electrons have no time to thermalize in a time during which the field in the SL is low, i.e., when $|E(t)| < E^*$. It is worth noting that the period of BOHFs exceeds that of the field by a factor of 2 in the example under consideration.

Thus, an SL with high-Q BOs and BOHFs can be used for terahertz generation in periodic pulsed fields with an off-duty factor that ensures the thermalization of the electrons heated by the field. A pulsed field can be approximated by a combination of the static and biharmonic fields (field (4) with $N = 2$, $E_2 = E_1/3$, $\delta_1 = 0$, and $\delta_2 = \pi$). Taking into account the aforementioned difference between the relaxation times of the electron distribution in the presence of a high field and without a field, we may state that the interval between pulses in periodic pulsed fields can amount to a small fraction of the corresponding period.

7. A BLOCH OSCILLATOR BASED ON THE NEGATIVE DIFFERENTIAL CONDUCTIVITY IN A SUPERLATTICE

The Bragg reflections represent the main cause of the existence of not only the static (low-frequency) [9, 10] but also dynamic (high-frequency) [12] NDC in an SL. Gigahertz (up to 150 GHz) Gunn oscillators have been already developed on the basis of static NDC in SLs [13]. However, an oscillator based directly on BOs have not been produced yet.

In our opinion, the main cause of the failures in the design of a Bloch oscillator is related to the use of nonoptimized SL structures. Indeed, SLs with a sinusoidal minizone ($N = 1$ in formula (2)), where the BOs are harmonic, are typically studied. In these SLs, the static NDC arises in fields with the Bloch frequency $\Omega_C > \tau^{-1}$ (see (25)), whereas the dynamic NDC is observed at the frequency ω in a field with $\Omega_C > \sqrt{\omega^2 + \tau^{-2}}$ [12]; i.e., the dynamic NDC appears only in the portions of the *I–V* characteristics where the static NDC is observed. As a result, the generation of terahertz oscillations in the SL under consideration is suppressed by the development of a domain instability with a relatively low frequency (the Gunn effect) [14]. In order to design a Bloch oscillator, one needs an SL that exhibits a high-frequency NDC in the portions of the *I–V* characteristics where positive static differential conductivity is observed. In order to gain insight into this method of designing a Bloch oscillator, we studied (see, also, [15, 16]) the dependences of the static and dynamic differential conductivities in an SL on both the dispersion relation in a minizone and the characteristics of electron scattering in the SLs. As the test approximation, we

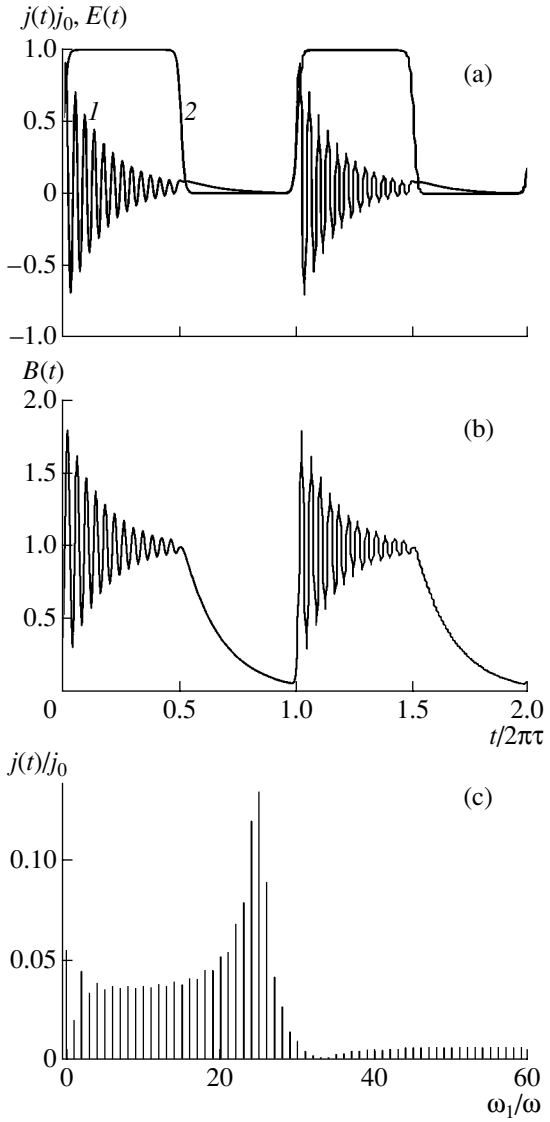

Fig. 3. Oscilloscope patterns of (a) the current, (b) the electron energy, and (c) the spectrum of current in a periodic pulsed electric field (31) with $\Omega_C/\omega = 25$ and $\omega\tau = 1$. Curve *1* represents the dimensionless current and curve *2* represents the dimensionless electric field; ω_1 denotes the current-harmonic frequency.

used the following "superparabolic" (of course, idealized) dispersion relation:

$$\varepsilon_3(k_3) = \frac{\hbar^2}{2} \times \begin{cases} \dfrac{k_3^2}{m_1}, & 0 < |k_3| < k_i, \\ \dfrac{k_3^2}{m_2} - 2k_i\left(\dfrac{1}{m_2} - \dfrac{1}{m_1}\right)\left(|k_3| - \dfrac{k_i}{2}\right), & k_i < |k_3| < \dfrac{\pi}{d}. \end{cases} \quad (34)$$

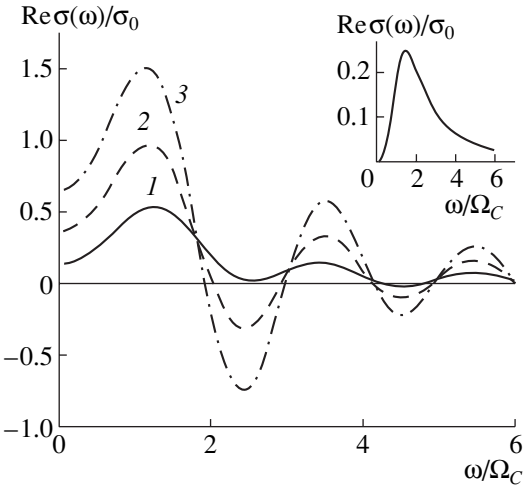

Fig. 4. Dynamic differential conductivities of superlattices with sinusoidal (in the inset) and "superquadratic" minibands (with $\beta = 0.5$ and $\eta =$ (*1*) 1, (*2*) 5, and (*3*) 10) at $\alpha = 0$ in a field with $\Omega_C\tau = 1$.

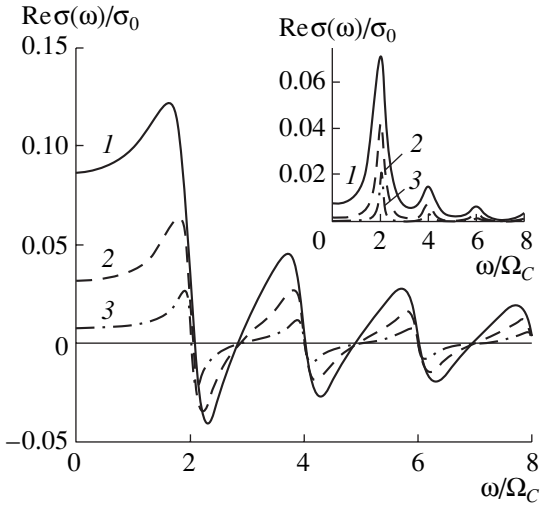

Fig. 5. Dynamic differential conductivities of superlattices with sinusoidal (in the inset) and parabolic minibands for one-sided streaming ($\alpha = 1$) in the fields with $\Omega_C\tau =$ (*1*) 3, (*2*) 5, and (*3*) 10.

This relation is composed of two parabolic functions joined at the points $k_3 = \pm k_i$ with $0 < k_i < \pi/d$. At $m_2 = m_1$ or $k_i = 0$ (or π/d), relation (34) transforms into a parabolic dispersion relation that is cut off at the boundaries of the Brillouin zone; in addition, it satisfactorily approximates the sinusoidal dispersion relation at $m_2 = -m_1 < 0$ and $k_i = \pi/2d$. The BOs are anharmonic for this dispersion relation. The characteristics of anharmonicity depend on the position of the point $\beta \equiv k_i d$, where the corresponding functions are joined, and on the mass ratio $\eta \equiv m_1/m_2$. The minizone width was chosen to be approximately equal to the optical-phonon energy. The probability of emission of this phonon at the minizone boundary was assumed to be constant and equal to α ($0 \le \alpha \le 1$). Whether the single-sided ($\alpha = 1$) or two-sided ($0 < \alpha < 1$) streaming is accomplished in the SL, depends on the value of α [15, 16].

The studies showed the following:

(i) It is possible to locate the ranges of the static and dynamic NDC in SLs in different regions of a static electric field by introducing the anharmonicity in the BOs. In this case, the promising SLs are those with minizones where, mostly, the effective electron mass is positive and decreases as the electron energy increases (the "anti-Gunn" variant). In these SLs, the region of static NDC shifts (in comparison to an SL with a sinusoidal minizone) to higher fields; simultaneously, the region of the dynamic NDC shifts to lower fields. This circumstance makes it possible to detune from the competing low-frequency domain instability under the conditions of the generation of terahertz radiation. As an example, Fig. 4 shows the dynamic differential conductivities of an SL with sinusoidal and superparabolic minizones in the absence of scattering by optical phonons ($\alpha = 0$).

(ii) In an SL with the miniband width on the order of the optical-phonon energy, a double resonance at even-numbered harmonics of BOs appears (since the time required for an electron to acquire optical-phonon energy amounts to about half of the time needed by an electron to traverse the Brillouin minizone); at the same time, the low-frequency NDC can be absent in the entire range of static fields. The aforementioned type of SLs with large values of η is preferential in this case as well (in order to increase the magnitude of the high-frequency NDC). In Fig. 5, we show the dynamic differential conductivities of an SL with the sinusoidal and parabolic minizones when intense scattering of electrons by optical phonons occurs ($\alpha = 1$). It can be seen that the dynamic NDC is not observed in an SL with a sinusoidal minizone; in contrast, this NDC is quite pronounced in an SL with a parabolic minizone. Studies show that the presence of regions with negative effective mass of charge carriers in the minizone detrimentally affects the magnitude of the high-frequency NDC at large values of α.

(iii) In order to obtain large values of the high-frequency NDC, the BOs should not necessarily have a high Q-factor ($\omega \approx \Omega_C \approx \tau^{-1}$); i.e., there is no need for this in SLs with a very high purity.

The specific minizones we suggest can be implemented in electron SLs with a complex unit cell and in the hole SLs with a complex valence band of the initial material.

8. CONCLUSIONS

The above-reported results of studies make it possible to draw the following conclusions:

(i) The superlattices (SLs) with high-Q Bloch oscillations (BOs) and BOs in a harmonic field can be used

to generate terahertz radiation under excitation by high pulsed electric fields with an off-duty factor that ensures the thermalization of electrons.

(ii) A terahertz oscillator with the frequency tuned continuously by an electric field can be designed on the basis of anharmonic BOs in semiconductor SLs. To this end, it is reasonable to use an SL whose minizone has the special characteristics where, largely, the effective mass of the charge carrier (electron or hole) is positive and decreases as the carrier energy increases. This circumstance makes it possible to eliminate the development of undesirable domain instability (the Gunn effect) under the conditions of the generation of terahertz radiation.

In order to produce a terahertz oscillator, one can also use the following objects:

(I) The SLs that include two closely spaced (or partially overlapping) electron (hole) minibands the upper of which is much wider than the lower one, exhibits a smaller effective electron (hole) mass, so that the emission of an optical phonon occurs at the top of the upper miniband. The impurity miniband in which the mobility of electrons (holes) is relatively low can also play the role of the lower miniband.

(II) Where there are individual *p*-type layers based on a semiconductor with a rigid "phonon roof" (in conditions of longitudinal transport), there are two-dimensional subbands in which the effective hole mass decreases as the hole energy increases [17]. In this case, the initiation of dynamic negative differential conductivity is caused by the same mechanisms as in the bulk semiconductors [18], i.e., by streaming (but with a lower dimensionality) and self-modulation of the electron distribution in the two-dimensional quasi-momentum space.

(III) Double quantum wells and dots affected resonantly by harmonic fields. In this case, the Rabi frequency plays the role of the Bloch frequency (i.e., we are dealing with the conversion of infrared radiation to terahertz radiation).

ACKNOWLEDGMENTS

This study was supported by the Russian Foundation for Basic Research (project no. 04-02-17154) and the program "Low-Dimensional Quantum Structures" of the Russian Academy of Sciences and the Ministry of Industry, Science, and Technology of the Russian Federation.

REFERENCES

1. F. Bloch, Z. Phys. **52**, 555 (1928); C. Zener, Proc. R. Soc. London, Ser. A **145**, 523 (1934).
2. G. H. Wannier, Phys. Rev. **117**, 432 (1960); Rev. Mod. Phys. **34**, 645 (1962).
3. J. Feldmann, K. Leo, J. Shah, *et al.*, Phys. Rev. B **46**, 7252 (1992); M. Sudzius, V. G. Lyssenko, F. Löser, *et al.*, Phys. Rev. B **57**, R12693 (1998); F. Löser, Y. A. Kosevich, K. Köhler, and K. Leo, Phys. Rev. B **61**, R13373 (2000).
4. Yu. A. Romanov and Yu. Yu. Romanova, Fiz. Tverd. Tela (St. Petersburg) **43**, 520 (2001) [Phys. Solid State **43**, 539 (2001)].
5. M. Holthaus, Z. Phys. B **89**, 251 (1992); Phys. Rev. Lett. **69**, 351 (1992); M. Holthaus and D. Hone, Phys. Rev. B **47**, 6499 (1993); Phys. Rev. B **49**, 16605 (1994).
6. M. C. Wanke, A. G. Markelz, K. Unterrainer, *et al.*, in *Physics of Semiconductors*, Ed. by N. Scheffter and R. Zimmerman (World Sci., Singapore, 1996), p. 1791.
7. O. N. Dunlap and V. M. Kenkre, Phys. Rev. B **34**, 3625 (1986); Phys. Lett. A **127**, 438 (1988).
8. Yu. A. Romanov and Yu. Yu. Romanova, Zh. Éksp. Teor. Fiz. **118**, 1193 (2000) [JETP **91**, 1033 (2000)].
9. V. A. Yakovlev, Fiz. Tverd. Tela (Leningrad) **3**, 1983 (1961) [Sov. Phys. Solid State **3**, 1442 (1961)].
10. Yu. A. Romanov, Fiz. Tverd. Tela (St. Petersburg) **45**, 529 (2003) [Phys. Solid State **45**, 559 (2003)].
11. I. A. Dmitriev and R. A. Suris, Fiz. Tekh. Poluprovodn. (St. Petersburg) **36**, 1449 (2002) [Semiconductors **36**, 1364 (2002)].
12. S. A. Ktitorov, G. S. Simin, and V. Ya. Sindalovskiĭ, Fiz. Tverd. Tela (Leningrad) **13**, 2230 (1971) [Sov. Phys. Solid State **13**, 1872 (1971)].
13. E. Schomburg, R. Scheuerer, S. Brandl, *et al.*, Electron. Lett. **35**, 12 (1999).
14. H. Kroemer, cond-mat/0007482; cond-mat/0009311.
15. Yu. A. Romanov, L. G. Mourokh, and N. J. M. Horing, J. Appl. Phys. **93**, 4696 (2003).
16. Yu. A. Romanov and Yu. Yu. Romanova, Fiz. Tverd. Tela (St. Petersburg) **46**, 162 (2004) [Phys. Solid State **46**, 164 (2004)].
17. Y. C. Chang and R. B. James, Phys. Rev. B **39**, 12672 (1989).
18. A. A. Andronov and V. A. Kozlov, Pis'ma Zh. Éksp. Teor. Fiz. **17**, 124 (1973) [JETP Lett. **17**, 87 (1973)]; L. E. Vorob'ev, S. N. Danilov, V. N. Tulupenko, and D. A. Firsov, Pis'ma Zh. Éksp. Teor. Fiz. **73**, 253 (2001) [JETP Lett. **73**, 219 (2001)].

Translated by A. Spitsyn

Semiconductors, Vol. 39, No. 1, 2005, pp. 156–159. Translated from Fizika i Tekhnika Poluprovodnikov, Vol. 39, No. 1, 2005, pp. 171–174.

PHYSICS OF SEMICONDUCTOR DEVICES

The Mode Competition, Instability, and Second Harmonic Generation in Dual-Frequency InGaAs/GaAs/InGaP Lasers

V. Ya. Aleshkin*^, B. N. Zvonkov, S. M. Nekorkin**, and Vl. V. Kocharovsky*****

**Institute for Physics of Microstructures, Russian Academy of Sciences, Nizhni Novgorod, 603950 Russia*

^e-mail: Aleshkin@ipm.sci-nnov.ru

***Physicotechnical Research Institute at Lobachevsky State University, Nizhni Novgorod, 603600 Russia*

****Institute of Applied Physics, Russian Academy of Sciences, Nizhni Novgorod, 603950 Russia*

Submitted June 1, 2004; accepted for publication June 16, 2004

Abstract—InGaAs/GaAs/InGaP-based heterolasers with asymmetrically grown quantum wells of two types are developed. For the first time, dual-wavelength operation and second-harmonic generation are realized in these lasers over a wide range of injection currents: from 0.2 A in CW mode up to 10 A in injection with 200-ns-long pulses. Previously unknown special features of such a generation are experimentally revealed and interpreted in terms of the competition and coexistence of various short- and long-wavelength modes, including the "whispering-gallery" modes. *© 2005 Pleiades Publishing, Inc.*

We investigate the stimulated dual-wavelength operation at wavelengths of about 1 μm and the second harmonic generation in injection lasers based on InGaAs/GaAs/InGaP structures with 9-nm-wide quantum wells of two types, which differ in indium concentration by about 10%. For the structures with a 0.1×0.25 mm^2 active region, the dual-wavelength (with a frequency difference of 2.5%) operation is observed at temperatures from 4 to 33°C at a wide range of injection currents: 0.2 A at a constant drive and 10 A at excitation with 200-ns pulses.

For comparison, note that, in early experiments [1–3], dual-wavelength operation in heterolasers was only attained within a narrow range of injection currents, of several percent, above the lasing threshold. An important point concerning the structure of our laser is the asymmetric position of the quantum wells. The two wells providing for the shorter wavelength mode are separated by a 24-nm-wide *i*-GaAs barrier and located almost at the midplane of the waveguide layer, and the third quantum well, responsible for the longer wavelength mode, is shifted from the midplane of the waveguide layer by about 1/7 of its thickness (Fig. 1). The laser waveguide was a standard structure consisting of a central 0.84-μm-thick *i*-GaAs layer and two 0.6-μm-thick wall layers made from *n*- and *p*-InGaP doped at a level of 5×10^{17} cm^{-3}. The lasing lines differed by ~30 meV, depending on temperature and the injection current. For a description of various schemes of dual-wavelength lasers, see [4–6] and the references therein.

Since the waveguide dispersion and the dispersion of the absorption in a heterostructure can hardly cause an appreciable suppression of the TE modes at frequencies differing by 2.5%, it is reasonable to expect that, in similar injection conditions, the threshold for lasing at the two short-wavelength wells is lower than that at the long-wavelength well. This behavior is understandable because, though the latter presents an additional absorbing element for the short-wavelength generation, its coupling to the TE_0 and TE_2 modes is weaker than that of the short-wavelength wells in the central position.

The spectral characteristics of the radiation measured using an MDR-24 grating monochromator at temperatures between 4 and 33°C (Fig. 2) were in line with our expectations. Indeed, an increase in the injection current first gave rise to the stimulated emission of radiation at a higher frequency (at currents between 0.15 and 0.2 A) and, then, to the simultaneous generation of TE modes at both frequencies. The latter phenomenon appeared at a current that exceeded the high-frequency lasing threshold by 1.3–3 times (depending on a particular specimen and temperature). An example of this can be seen in Fig. 3.

Within a narrow range of currents corresponding to the onset of the two-frequency operation, we observed instability, which caused a change in both the spectral power of the lasing and the radiation pattern over time. At a further increase in the injection current, stable lasing at both frequencies was observed up to the currents that destroyed the structure.

The luminance–current characteristics measured for the sum power of lasing differ radically from those typical of single-frequency oscillation in conventional heterolasers. Immediately after the onset of the dual-wavelength operation, the total power abruptly drops by almost half (Fig. 3) and, then, remains nearly constant as the injection current increases (large nonradiative

1063-7826/05/3901-0156$26.00 © 2005 Pleiades Publishing, Inc.

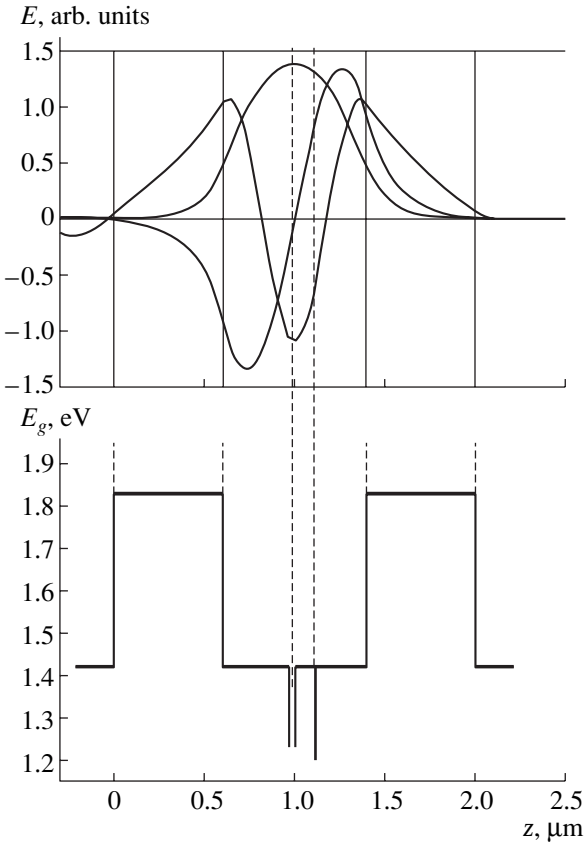

Fig. 1. The profiles of transverse $TE_{0,1,2}$ modes (E) and the energy-band diagram (E_g) along the direction of growth z for the two-color InGaAs/GaAs/InGaP structure.

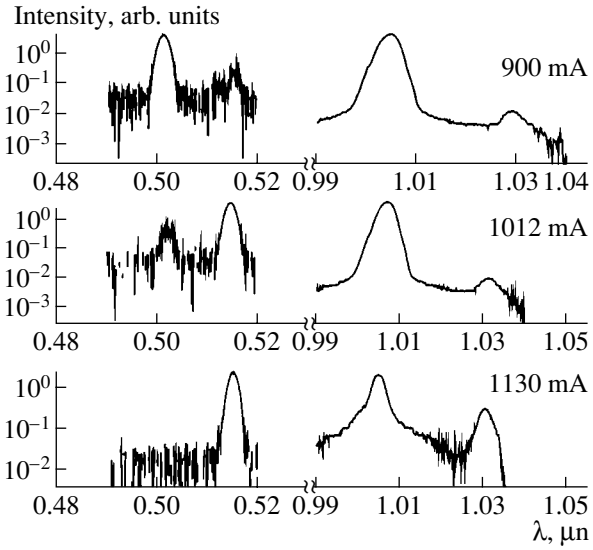

Fig. 2. Typical spectra of continuous two-color lasing accompanied by second harmonics in a 0.25-mm-long structure at room temperature. The injection currents are indicated. Because of the narrow angular aperture of the detector, the intensity at the longer wavelength 1.03 μm, which features a wider directivity pattern (see Fig. 4), seems lower.

losses), though the ratio of powers at the two frequencies changes appreciably. The critical current corresponding to the drop substantially decreased at lower temperatures.

The directivity pattern of the short-wavelength radiation exhibits a typical shape, while the long-wavelength radiation pattern is found to be considerably broadened in the *p–n* junction plane (Figs. 4, 5). The latter circumstance can be explained if we assume that the so-called "whispering-gallery" modes (related to the total internal reflection from the boundaries of the active region) contribute to the long-wavelength field but not to the short-wavelength field, although the short-wavelength field is nonuniform over the *p–n* junction plane. In particular, the weak influence of the injection current on the output power after the transition to the two-frequency operation can be attributed to a high absorption of short-wavelength radiation in the long-wavelength well; in turn, the emission from the long-wavelength well is strongly absorbed (as are the whispering-gallery modes) in the lateral parts of the heterostructure, which are beyond the reach of the injection current. The lateral reflections of the long-wavelength field that are required for the formation of the whispering-gallery modes are most likely to occur near the edges of the upper metallic strip contact rather than at the lateral facets of the laser. This behavior is caused by the presence of a step in the charge-carrier concentration at the aforementioned edges (plasma and thermal effects) and by the partial etching of the upper waveguide layer in these regions during the production of the laser (a step in the dielectric properties of the waveguide).

We also measured the spectra and the radiation patterns of the double frequencies that appear due to the second-order lattice nonlinearity in a thin (0.1 μm) GaAs layer in the vicinity of the output edges. It transpired that both the second harmonics are TM polarized and had nearly the same parameters; however, the intensity of the long-wavelength harmonic grows while that of the short-wavelength harmonic drops as the injection current increases (Fig. 2). The ratio between the intensities of these harmonics and the ratio of the corresponding lasing thresholds depend heavily not only on the laser length but also on the temperature and position of the injection stripe relative the edges of the structure. No lasing at the sum frequency was observed, which apparently indicates that the regions of short- and long-wavelength mode generation are separated spatially (the corresponding fields overlap only slightly at the output end face of the laser).

Our interpretation of the lasing operation modes is essentially based on the assumption that the long-wavelength radiation is represented by whispering-gallery modes and the short-wavelength radiation consists of the conventional modes of a wide (100 μm) waveguide.

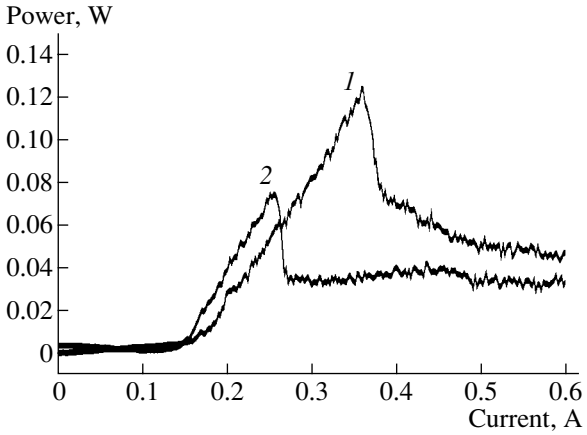

Fig. 3. The luminance–current characteristics of a 0.25-mm-long diode laser with a continuous injection mode at (*1*) 33 and (*2*) 10°C. The smooth sections of linear growth correspond to one-frequency lasing. The threshold drop of the total output power indicates the onset of the two-frequency operation with its power almost independent of the injection current.

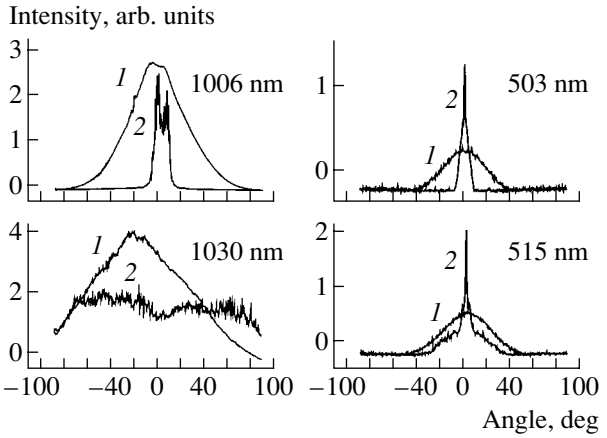

Fig. 4. End view of the radiation patterns in a plane that is (*1*) perpendicular and (*2*) parallel to the quantum wells for a 0.25 μm-long laser with continuous injection at 1.01 A, at room temperature, λ = 1030 nm. A 20-degree shift and the asymmetry of the long-wavelength curve (*1*) is probably related to the distortion of the TE_0 mode in the presence of the TE_1 mode.

The latter modes are highly nonuniform in the quantum-well plane, which is mostly due to the filamentation of the injection in narrow (~10 μm) channels rather than being a result of the wide waveguide. This assumption is supported by the results from studying the field at the output end face of laser [7] by means of scanning near-field microscopy using the spectral separation of short- and long-wavelength modes. Along with the conventional optical microscopy data, these results also indicate that the short-wavelength radiation at the output face of the laser forms a number of bright spots that have a transverse structure typical of the TE_0 mode (possibly, with a slight addition of the TE_2 mode). The long-wavelength radiation also forms a number of spots at the output face of the laser, but they are generally shifted with respect to the short-wavelength spots and probably have a small-scale structure, with a characteristic size being as small as ~1 μm. The evidence for this last fact is provided by the wide radiation pattern at the fundamental frequency and by the pedestal underlying the second-harmonic peak (Fig. 4, λ = 1030 and 515 nm, curves *2*), which can be attributed to the whispering-gallery modes and the multimode structure of the long-wavelength radiation in the plane of the quantum wells. It is interesting that the relative fractions of the transverse TE_0, TE_1, and TE_2 modes of the long-wavelength radiation depend on the injection current and the position at the output face of the laser. The amplitudes of higher harmonics can be comparable to that of the fundamental mode [7].

In general, the evolution of the lasing operation modes as the injection current increases can be conceived as follows: The process of exceeding the short-wavelength threshold is hindered by filamentation; i.e., the injection current flows along separate channels, thus, forming a number of traces of stimulated amplification (at two short-wavelength wells), which almost directly connect the output end faces of laser. The generation of short-wavelength whispering-gallery modes, where the beams are far from the normal orientation to the laser faces, is excluded because of the absorption in between the current channels. In relation to the long-wavelength radiation, the corresponding threshold for the traces mentioned above is not attained when the injection considerably exceeds the short-wavelength threshold, since the long-wavelength well is only one

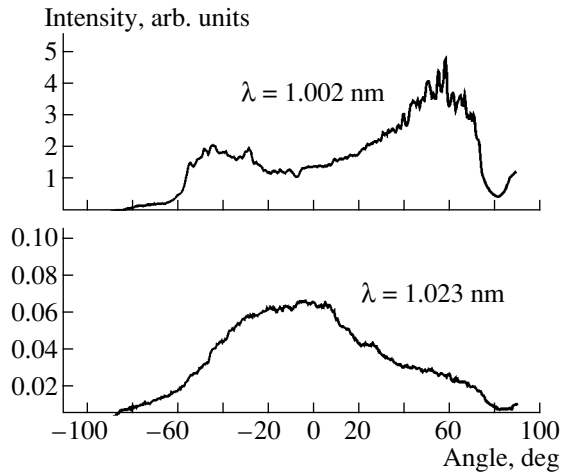

Fig. 5. A lateral view of the radiation patterns in the plane that is perpendicular to the quantum wells for a 0.25 μm-long laser with continuous injection at 1.34 A, at room temperature. The wide angular spectrum indicates that the higher TE modes in the low-pumped part of the structure features lower absorption than the fundamental TE_0 mode that can even transform into the higher modes because of the nonideality of the waveguide.

and occupies an off-center position in the waveguide. However, as soon as the short-wavelength power becomes sufficient to make the long-wavelength well transparent and to enhance the inversion level (an additional optical pump, including the space in between the current channels), the whispering-gallery modes appear. The Q-factor of these modes increases with the injection current, which is, in particular, due to an increase in the reflections as a result of the plasma–thermal effects of refraction at the active region boundaries (and the edge of the current channels), and appears to exceed the Q-factor of ordinary modes, which pass preferentially via the current channels. According to the experiment, no whispering-gallery modes appear in lasers with the length of the active region between 0.5 and 1 mm. This behavior is caused by the fact that a total internal reflection from the end faces of a heterolaser with the constant width of the active region at 0.1 mm cannot be attained. However, for the complete substantiation and detailed clarification of the scenario suggested above, further investigation is required using both experimental and theoretical methods.

ACKNOWLEDGMENTS

This study was supported in part by the Russian Foundation for Basic Research, project nos. 02-02-17536, 04-02-17432, and 02-02-81036; the Presidential Grant for the State Support of Leading Scientific Schools in the Russian Federation, NSh-1744.2003.2; and the International Science and Technology Center, project no. 2293.

REFERENCES

1. Y. Tokuda, N. Tsukada, K. Fujiwara, *et al.*, Appl. Phys. Lett. **49**, 1629 (1986).
2. S. Ikeda and A. Shimizu, Appl. Phys. Lett. **59**, 504 (1991).
3. T. R. Chen, Y. Zhuang, Y. J. Xu, *et al.*, Appl. Phys. Lett. **60**, 2954 (1992).
4. V. Ya. Aleshkin, V. I. Gavrilenko, S. V. Morozov, *et al.*, in *Nanophotonics: Proceedings of Meeting*, Ed. by Z. F. Krasil'nik (Inst. Fiziki Mikrostruktur Ross. Akad. Nauk, Nizhni Novgorod, 2003), Vol. 2, p. 315.
5. N. V. Baĭdus', A. A. Biryukov, B. N. Zvonkov, *et al.*, Fiz. Tekh. Poluprovodn. (St. Petersburg) **38**, 366 (2004) [Semiconductors **38**, 352 (2004)].
6. A. A. Belyanin, D. Deppe, V. V. Kocharovskiĭ, *et al.*, Usp. Fiz. Nauk **173**, 1015 (2003) [Phys. Usp. **46**, 986 (2003)].
7. D. O. Filatov, G. A. Maximov, V. P. Mishkin, *et al.*, in *Proceedings of International Workshop on Scanning Probe Microscopy*, Ed. by S. V. Gaponov (Inst. Phys. Microstruct. Russ. Acad. Sci., Nizhni Novgorod, 2004).

Translated by A. Sidorova

Semiconductors, Vol. 39, No. 1, 2005, pp. 17–21. Translated from Fizika i Tekhnika Poluprovodnikov, Vol. 39, No. 1, 2005, pp. 25–29.

LOW-DIMENSIONAL SYSTEMS

Effect of an Interfacial Oxide Layer on the Electroluminescence Efficiency of Metal–Quantum-Confined Semiconductor Heterostructures

N. V. Baĭdus'^, P. B. Demina, M. V. Dorokhin, B. N. Zvonkov, E. I. Malysheva, and E. A. Uskova^

Physicotechnical Research Institute at Lobachevsky State University, pr. Gagarina 23, Nizhni Novgorod, 603950 Russia

^e-mail: usk@nifti.unn.ru

Submitted June 1, 2004; accepted for publication June 14, 2004

Abstract—The effect of different surface treatments of GaAs/In(Ga)As/GaAs quantum-confined heterostructures on the electroluminescence efficiency of Schottky diodes based on these structures is investigated. It is ascertained that the largest increase in electroluminescence intensity is observed when the surface is treated in CCl_4 at 580°C with subsequent anodic oxidation. It is shown that the interfacial tunnel-thin anodic oxide plays an important role in the injection of minority carriers from the metal into gallium arsenide. The electroluminescence efficiency depends strongly on the anodic-oxide thickness. © *2005 Pleiades Publishing, Inc.*

1. INTRODUCTION

At present, GaAs/In(Ga)As/GaAs quantum-confined heterostructures are used to generate spontaneous emission. Along with anisotype heterostructures [1, 2], Schottky barrier heterostructures are also used [3, 4]. Formation of a layer of In(Ga)As quantum dots (QDs) near the heterostructure surface under a thin (≤30 nm) cap layer of complex composition (InGaAs + GaAs) made it possible to advance to the emission range 1.3–1.55 μm, which is important for fiber optics. At a cap-layer thickness of 12 nm, electroluminescence (EL) at a wavelength of 1.57 μm at 300 K was detected for quantum-confined heterostructures with a Schottky barrier [5].

A distinctive property of a Schottky barrier (as compared to a *p*–*n* junction) is low ($\leq 10^{-4}$) injection of minority carriers [6] into the semiconductor, which is unfavorable for efficient radiative recombination. The purpose of this study is to increase the quantum efficiency of Schottky diodes using different treatments of the surface of quantum-confined heterostructures both during and after epitaxial growth (before barrier formation). Based on the results obtained, the role of anodic oxide in the injection of minority carriers from the metal into the semiconductor in Schottky barrier heterostructures is considered.

2. EXPERIMENTAL

The heterostructures were grown by hydride-metal–organic vapor phase epitaxy at atmospheric pressure on n^+- and p^+-GaAs(100) substrates. A layer of InAs QDs was formed on a buffer layer with a thickness of ~0.5 μm at a temperature of 520°C and doped with bismuth to improve the homogeneity of the layer parameters [7]. In some samples, as in [4, 5], the cap layer has a complex composition: a 2-nm $In_{0.2}Ga_{0.8}As$ quantum well (QW) coated by a thin GaAs layer is adjacent directly to the QDs. The other part of the quantum-confined heterostructure contains only an InGaAs QW (the growth temperature for QWs is 650°C) or a layer of InAs QDs under a coating GaAs layer. The thickness of the cap layer was varied from 10 to 400 nm. For comparison, 400-nm *n*-GaAs epitaxial layers were also grown at 520 or 580°C.

The following surface treatments were used: in situ exposure of the In(Ga)As surface to a flux of carbon tetrachloride and anodic oxidation of the GaAs cap layer before the metal deposition. Anodic oxidation was performed in an electrolyte (3% solution of tartaric acid in ethylene glycol) in the static-voltage mode at voltages from 0.2 to 9 V. The oxidation of the *n*-type samples was performed under illumination.

The growth surface was treated in a flux of CCl_4 at 520 or 580°C. Then, a cap GaAs layer was grown at the same temperature. As we have shown earlier [2], exposure of the growth surface to CCl_4 either changes the composition of the cap layer due to the formation of an acceptor carbon δ layer (520°C) or improves the morphology of QDs and the GaAs cap (580°C) due to the removal of large dislocated clusters. The role of the carbon δ layer in the increase in the EL efficiency was considered in [4]. In this study, we restrict our consideration mainly to structures treated in CCl_4 at 580°C. Following the technique of cluster etching we developed, a thin (~10 nm) GaAs layer was first grown on the layer of In(Ga)As QDs at the QD growth temperature; then,

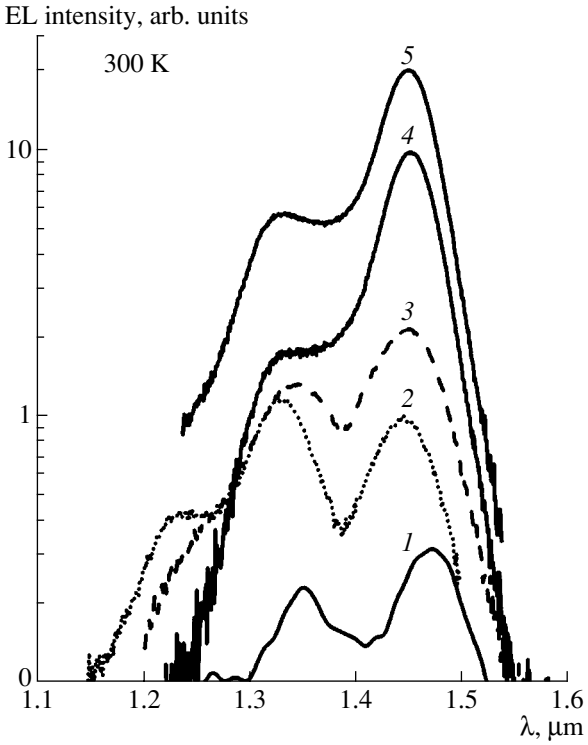

Fig. 1. EL spectra of QD heterostructures based on n^+-GaAs with a Au barrier. The injection current is 30 mA. Samples: (*1*) with no treatment, (*2*) with a carbon δ layer, (*3*) with a carbon δ layer and anodic oxide, (*4*) after treatment in CCl_4 at 580°C, and (*5*) after treatment in CCl_4 at 580°C and with anodic oxide.

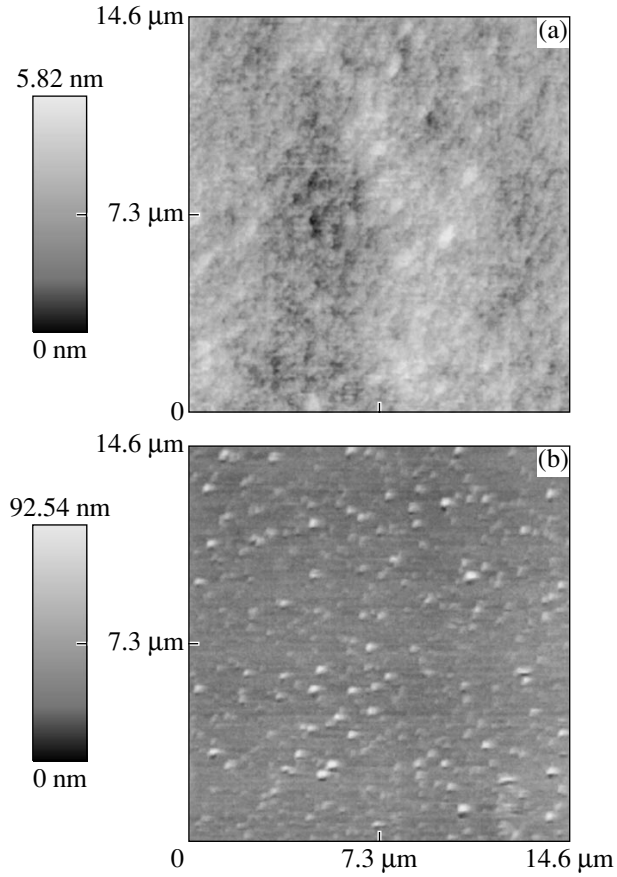

Fig. 2. Surface topography of the GaAs/InGaAs/GaAs structures: (a) the sample treated in CCl_4 at 580°C and (b) the reference sample.

the substrate temperature was increased to 580°C for ~300 s; and, at the end of the heating cycle, carbon tetrachloride was fed into the reactor. After treatment of a quantum-confined heterostructure in CCl_4 for a few seconds, a GaAs cap layer was grown. Structures that were not subjected to any treatment served as reference ones.

Schottky barriers were formed by deposition of metals (Au or Al) using thermal evaporation in vacuum through a mask with 500-μm holes. In most quantum-confined heterostructures under study, the native oxide was not etched from the GaAs surface, in view of the small thickness of the cap layer. The back ohmic contact was formed using an InGa paste or by spark alloying of a Sn foil.

The effect of treatments was estimated by changes in the photoluminescence (PL) and injection (forward-bias) EL spectra and the parameters of the current–voltage (*I–V*) and capacitance–voltage (*C–V*) diode characteristics. The measurements were performed at 77 and 300 K. When measuring the PL and EL spectra, the radiation was collected from the front and back surfaces of the samples, respectively. The surface topography was analyzed by scanning probe microscopy (SPM).

3. RESULTS AND DISCUSSION

The effect of different treatments of the surfaces of quantum-confined heterostructures on the EL intensity I_{EL} is well pronounced in Fig. 1, where the EL spectra of quantum-confined heterostructures with a combined cap layer measured at room temperature are shown. The thickness of the GaAs cap layer in these samples is 20 nm. It can be seen that treatment of each type increases the integral EL intensity. Note that anodic oxidation of the samples treated in carbon tetrachloride leads to an additional increase in the EL intensity (compare curves *2* and *3* and *4* and *5* in Fig. 1). The largest increase in I_{EL} is observed after treatment in CCl_4 at 580°C with subsequent anodic oxidation (Fig. 1, curve *5*). This can be explained as follows.

High-temperature treatment of the structures in CCl_4, according to the SPM data, decreases the density of clusters by a factor of eight to ten (to $(2–3) \times 10^7$ cm^{-2}). The lateral sizes of the clusters increase significantly (from 250 to 700 nm), and their height decreases from ~150 to 5 nm (Fig. 2). After the anodic oxidation, the surfaces of all heterostructures become even more smooth. For example, in structures treated in CCl_4 at 520°C, the height of asperities after the oxidation

decreases by a factor of two to three and is equal to ~20 nm. During anodic oxidation, a layer of gallium arsenide with a thickness of about two-thirds of the anodic oxide thickness is spent [8]. Hence, the initial surface defects are removed and, as a result, the density of nonradiative recombination centers at the new interface between the anodic oxide and GaAs decreases.

In order to determine the role of anodic oxide in the EL mechanism, we measured the dependences of the integral EL intensity on the oxide thickness d_{ox} for structures of different types. The results are shown in Fig. 3. For comparative analysis, we used samples with the simplest composition: *n*-GaAs epitaxial layers (curves *1* and *2*) and quantum-confined heterostructures with only a QW (curves *3* and *4*) or QDs (curve *5*) coated with a fairly thick GaAs layer. The thickness of the cap layer on the QW and the QD layer is 400 and 100 nm, respectively. All dependences in Fig. 3 were measured at 77 K, with an exception made for curve *5* (300 K).

Note that the values of U_{ox}—the voltage at which oxidation occurs—rather than d_{ox} are plotted on the abscissa axis in Fig. 3. The reason is the difficulties we met in determining the thickness of thin (5–10 nm) anodic oxide layers, especially in quantum-confined heterostructures. Generally, when single crystals or epitaxial structures are oxidized, d_{ox} is calculated from the value of U_{ox} by multiplying the latter by the anodic-oxidation constant (~1.7 nm/V) [9]. However, as will be shown below, the anodic oxidation of quantum-confined heterostructures is a specific process and, obviously, it is incorrect to apply the above-described calculation technique to such structures. In order to determine the oxide thickness by the *C–V* method, especially in GaAs-based quantum-confined heterostructures, it is necessary to carry out special low-frequency measurements. In addition, the relative permittivity of GaAs anodic oxide depends strongly on the type of the electrolyte, and the spread of this parameter is rather large [9]. As a result, the values of d_{ox} calculated from the capacitance measurements may differ by a factor of two to three, depending on the chosen value of oxide permittivity. Direct measurement of d_{ox} by SPM at such thicknesses gives a large error because of the oxide inhomogeneity. When analyzing the results, we assumed that d_{ox} is proportional to U_{ox} and that the anodic oxide thickness increases with increasing oxidation voltage.

It can be seen from Fig. 3 that, for structures of all types, the dependence of the integral intensity $I_{EL}(U_{ox})$ is a nonmonotonic function peaked at different values of U_{ox} for epitaxial structures and quantum-confined heterostructures. However, for each specific type of structure, a maximum of I_{EL} is observed at the same value of U_{ox}: at 3 V for epitaxial layers (curves *1*, *2*) and at 6–7 V for quantum-confined heterostructures (curves *3*–*5*). At low oxidation voltages (U_{ox} < 2–3 V), the integrated EL intensity of structures with a QW

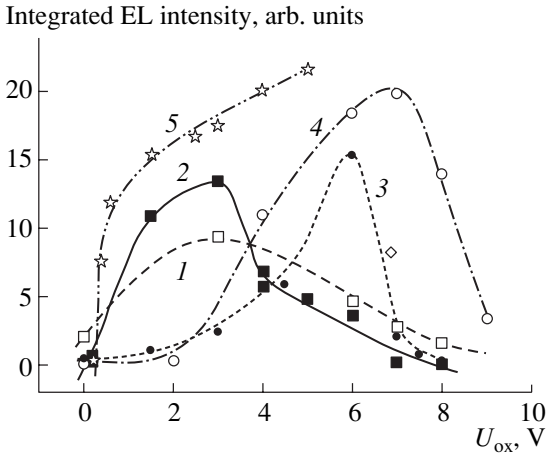

Fig. 3. Dependences of the integral EL intensity on the oxidation voltage for (*1*, *2*) the structures with GaAs epitaxial layers and (*3*, *4*) QW and (*5*) QD heterostructures: (*1*) the epitaxial layer grown at 520°C, (*2*) the epitaxial layer grown at 580°C, (*3*, *5*) the *n*-type quantum-confined heterostructures, and (*4*) the *p*-type quantum-confined heterostructure. The values of the EL intensity of epitaxial layers are increased by a factor of 15.

increases insignificantly with increasing U_{ox} (curves *3* and *4*), whereas, in the epitaxial layers, it is highest at the same values of U_{ox}. Apparently, the reason is that the time mechanism of formation of an anodic oxide in quantum-confined heterostructures, which have a potential barrier at the interface, differs from that for GaAs epitaxial layers. In heterostructures containing only QDs, a highly nonuniform oxidation front is observed. The values of I_{EL} at the same values of U_{ox}, especially for the *p*-type samples (not shown in Fig. 3) have a large spread, which confirms the more complex character of anodic oxidation of quantum-confined heterostructures.

Comparison of curves *1* and *2* in Fig. 3 shows that the EL intensity of the GaAs epitaxial layer grown at 580°C exceeds that of the GaAs layer grown at a lower temperature by approximately a factor of 1.5. The most likely reason is that the GaAs layer grown at the higher temperature has a smaller density of growth defects, which form nonradiative recombination centers. It can also be seen from Fig. 3 that the EL intensity of quantum-confined heterostructures exceeds that of the epitaxial layers by a factor of 15–20 and the heterostructures grown on p^+ substrates have higher values of I_{EL} as compared with the *n*-type structures.

The injection EL data for the GaAs/In(Ga)As/GaAs structures are in agreement with the measurements of the forward portion of the *I–V* characteristic. At small values of U_{ox}, the latter follows an exponential dependence, which is typical of Schottky barriers. The effective height of the Schottky barrier φ_b^* and the ideality factor *n* were calculated by a conventional method [6].

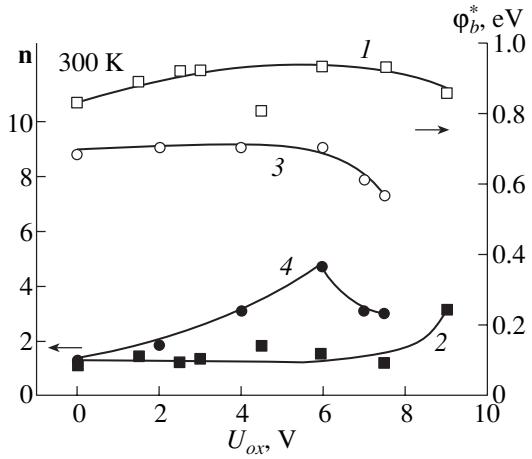

Fig. 4. Dependences of the (*1*, *3*) effective height of the Schottky barrier and (*2*, *4*) the ideality factor of the QW structures on the oxide thickness: (*1*, *2*) *n*-type (Au) and (*3*, *4*) *p*-type (Al) structures. The measurement temperature is 300 K.

The formation of an anodic oxide in QW heterostructures leads to an increase in the effective height of the Schottky barrier both at room temperature and at 77 K. Then, with an increase in U_{ox} from 1.5 to 6–7 V, the value of φ_b^* at 300 K almost does not change and is equal to 0.91 ± 0.02 and 0.7 ± 0.01 eV for the *n*- and *p*-type samples, respectively. With a further increase in U_{ox}, the measured barrier height decreases (Fig. 4, curves *1* and *3*).

The behavior of the parameter **n** at room temperature is different for the *n*- and *p*-type structures (Fig. 4, curves *2* and *4*). In the *n*-type quantum-confined heterostructures, the ideality factor ranges from 1.2 to 1.5, increasing significantly (**n** > 2) only for a structure with a very thick anodic oxide at $U_{ox} = 9$ (curve *2*). For the *p*-type structures, the values of **n** are much larger than for the *n*-GaAs/In(Ga)As structures. With an increase in U_{ox} (≥2 V), **n** increases by a factor of 2–2.5. The latter circumstance indicates that, with an increase in the anodic-oxide thickness, the mechanism of thermionic emission of carriers ceases to be dominant in these structures at much smaller values of d_{ox} than in *n*-type quantum-confined heterostructures. (The change in the mechanism of carrier injection must be taken into account when calculating the parameters of *I–V* characteristics, which is planned to be done in future investigations.) At liquid-nitrogen temperatures, the slope of *I–V* characteristics decreases with increasing oxide thickness.

Note that, in the QD structures, in view of the large spread of d_{ox}, the parameters of the *I–V* characteristics can be calculated only for samples with thin anodic oxides; however, their parameters change similarly with increasing U_{ox}.

Obviously, the different behavior of the parameters of the *I–V* characteristics of the *n*- and *p*-type quantum-confined heterostructures with increasing d_{ox} is related to the oxide properties. According to the data of [10], anodic oxidation of *n*-GaAs leads to the accumulation of a constant negative charge near the external surface of the oxide, which is sufficient to form an inversion layer on the GaAs surface. The buried *p*-type layer near the interface with the metal layer in *n*-type quantum-confined heterostructures increases the Schottky barrier height and improves its quality. Simultaneously, the buried *p*-type layer increases the hole density necessary for the EL excitation. In the *p*-type structures, no inversion layer should be formed and the parameter **n** gradually increases with increasing oxide thickness. The voltage drop across the oxide layer increases as well. The latter circumstance, according to the model proposed in [11, 12], shifts the Fermi level in the metal to the top of the valence band of *n*-GaAs (or to the bottom of the conduction band of *p*-GaAs for the *p*-type structures). As a result, the injection of minority carriers into the semiconductor (and, accordingly, the EL efficiency) increases. Until the oxide is tunnel-transparent for charge carriers, the intensity I_{EL} increases; as soon as the oxide ceases to be transparent, the EL efficiency decreases, which is confirmed by comparison of the results shown in Figs. 3 and 4.

4. CONCLUSIONS

Methods for treating GaAs/In(Ga)As/GaAs quantum-confined heterostructures in order to increase the EL efficiency are described. The largest increase in I_{EL} is observed when the heterostructure surface is exposed to CCl_4 at 580°C with subsequent anodic oxidation. The presence of an interfacial tunnel-thin anodic oxide plays an important role in providing injection of minority carriers from the metal forming the Schottky barrier into gallium arsenide. The EL efficiency depends strongly on the oxide thickness.

ACKNOWLEDGMENTS

We are grateful to S.V. Tikhov for his helpful participation in the discussion of the results.

This study was supported by the program of the Ministry of Education of the Russian Federation "Higher School Research on the Priority Lines of Science and Technology," project no. 05.01.048.

REFERENCES

1. A. E. Zhukov, B. V. Volovik, S. S. Mikhrin, *et al.*, Pis'ma Zh. Tekh. Fiz. **27** (17), 51 (2001) [Tech. Phys. Lett. **27**, 734 (2001)].
2. N. V. Baĭdus', A. A. Biryukov, Yu. A. Danilov, *et al.*, Izv. Ross. Akad. Nauk, Ser. Fiz. **67** (2), 208 (2003).

3. A. Babinski, P. Witczak, A. Twardowski, and J. M. Baranowski, Appl. Phys. Lett. **78**, 3992 (2001).
4. N. V. Baĭdus', B. N. Zvonkov, P. B. Mokeeva, *et al.*, Izv. Ross. Akad. Nauk, Ser. Fiz. **68** (1), 251 (2004).
5. N. V. Baidus, B. N. Zvonkov, P. B. Mokeeva, *et al.*, Semicond. Sci. Technol. **19**, S469 (2004).
6. E. H. Rhoderick, *Metal–Semiconductor Contacts* (Clarendon Press, Oxford, 1978; Radio i Svyaz', Moscow, 1982).
7. B. N. Zvonkov, I. A. Karpovich, N. V. Baidus, *et al.*, Nanotechnology **11**, 221 (2000).
8. É. V. Buts and L. I. Vozmilova, in *Electron Technique*, Ser.: *Semiconducting Materials* (TsNII Élektronika, Moscow, 1976), No. 1 (103), p. 109 [in Russian].
9. I. N. Sorokin, V. Z. Petrova, Yu. D. Chistyakov, *et al.*, in *Foreing Electron Technique* (TsNII Élektronika, Moscow, 1979), No. 14 (209) [in Russian].
10. S. V. Tikhov, B. I. Bednyĭ, I. A. Karpovich, and V. V. Martynov, Mikroélektronika **10**, 250 (1981).
11. H. C. Gard and E. H. Rhoderick, Solid-State Electron. **16**, 365 (1973).
12. N. V. Baĭdus', P. B. Demina, M. V. Dorokhin, *et al.*, in *Proceedings of Meeting on Nanophotonics* (Nizhni Novgorod, 2004), p. 170.

Translated by Yu. Sin'kov

Semiconductors, Vol. 39, No. 1, 2005, pp. 22–26. Translated from Fizika i Tekhnika Poluprovodnikov, Vol. 39, No. 1, 2005, pp. 30–34.

LOW-DIMENSIONAL SYSTEMS

Spectra of Persistent Photoconductivity in InAs/AlSb Quantum-Well Heterostructures

V. Ya. Aleshkin*, V. I. Gavrilenko*^, D. M. Gaponova*, A. V. Ikonnikov*, K. V. Marem'yanin*, S. V. Morozov*, Yu. G. Sadofyev, S. R. Johnson**, and Y.-H. Zhang****

**Institute for Physics of Microstructures, Russian Academy of Sciences, Nizhni Novgorod, 603950 Russia*

^e-mail: gavr@ipm.sci-nnov.ru

***Department of Electrical Engineering and Center for Solid State Electronic Research, Arizona State University, Tempe, AZ 85287 USA*

Submitted June 1, 2004; accepted for publication June 14, 2004

Abstract—Persistent photoconductivity at $T = 4.2$ K in AlSb/InAs/AlSb heterostructures with two-dimensional (2D) electron gas in InAs quantum wells is studied. Under illumination by IR radiation ($\hbar\omega = 0.6$–1.2 eV), positive persistent photoconductivity related to the photoionization of deep-level donors is observed. At shorter wavelengths, negative persistent photoconductivity is observed that originates from band-to-band generation of electron–hole pairs with subsequent separation of electrons and holes by the built-in electric field, capture of electrons by ionized donors, and recombination of holes with 2D electrons in InAs. It is found that a sharp drop in the negative photoconductivity takes place at $\hbar\omega > 3.1$ eV, which can be attributed to the appearance of a new channel for photoionization of deep-level donors in AlSb via electron transitions to the next energy band above the conduction band. © *2005 Pleiades Publishing, Inc.*

1. INTRODUCTION

Quantum-confinement heterostructures based on InAs are promising for the fabrication of high-frequency transistors, resonant-tunneling diodes, devices for midinfrared optoelectronics, and spintronics. A large number of studies have been devoted to the InAs/AlSb heterosystem. The latter exhibits a large value of the conduction-band offset at the heterointerface (equal to 1.35 eV) and high mobility of electrons in InAs quantum wells (QWs) (as high as 9×10^5 cm^2/(V s) at $T = 4.2$ K) and $n_s \approx 10^{12}$ cm^{-2} [1]. The electrons are present even in the QWs of nominally undoped structures [2]; these electrons can be supplied by deep-level donors in an AlSb or surface donors in GaSb cap layer [3–10]. One of the specific features of this heterosystem is bipolar behavior of the persistent photoconductivity (PPC) at low temperatures [2]. When the heterostructures are exposed to IR radiation, positive PPC (PPPC) is observed [11, 12]. This behavior is attributed to the photoexcitation of deep-level donor centers in AlSb barrier layers followed by the capture of photogenerated electrons in InAs QWs: the density of two-dimensional (2D) electrons increases and remains unchanged for many hours until the sample temperature is raised. When the heterostructures are exposed to visible light, negative PPC (NPPC) is observed [2, 10–12]. This behavior is attributed to band-to-band excitation of electron–hole pairs with subsequent separation of electrons and holes by the built-in electric field, capture of electrons by ionized donors, and recombination of holes with 2D electrons in InAs QWs.

Until now, there has been only one publication devoted to the study of the PPC spectra in InAs/AlSb heterostructures [11]; the measurements were carried out in the spectral range $\hbar\omega = 1$–3 eV using undoped samples. In this paper, we report the results of measurements of the PPC spectra both in undoped and selectively doped InAs/AlSb heterostructures over a wider range of photon energies (0.6–6 eV). The goal of this study was to search for new spectral features that may help to gain insight into the origin of 2D electron gas in nominally undoped structures.

2. EXPERIMENTAL

The heterostructures under study were grown by molecular-beam epitaxy [1, 13]. On a semi-insulating GaAs(100) substrate, a composite buffer consisting of a 2.4-μm-thick metamorphic AlSb or GaSb layer and a ten-period GaSb(2.5 nm)/AlSb(2.5 nm) superlattice was grown. The active region included a bottom AlSb barrier of thickness 12–40 nm, a 15-nm-thick InAs QW, a top AlSb or $Al_{0.8}Ga_{0.2}Sb$ barrier of thickness 30–40 nm, and a 6-nm-thick GaSb cap layer. In selectively doped structures, two δ layers of Te were introduced in AlSb barriers 15 nm from the QW. Shutters were opened and closed in a sequence that ensured formation of In–Sb chemical bonds at both QW interfaces [14]. The concentration and mobility of 2D electrons at $T = 4.2$ K were determined from the measurements of the Hall effect and Shubnikov–de Haas oscillations. The parameters of the samples are listed in the table.

The PPC spectra were recorded using an MDR-23 grating monochromator (Fig. 1). A quartz incandescent lamp was used as the radiation source, and the higher-order diffraction peaks were cut off by standard filters. At the monochromator output, radiation with a photon energy from 0.6 to 4 eV (the spectral range was extended to 6 eV in measurements with sample B824) was coupled to an optical fiber and delivered to the sample held within a helium storage Dewar vessel. The samples had the shape of a rectangular platelet with a typical area of 4×4 mm^2, and two stripe In contacts were deposited at the edges (at a distance of about 3 mm). The photoconductivity spectra were recorded in two different modes: (i) each data point was taken after switching off the illumination, consecutive measurements being made step by step starting with the long-wavelength part of the spectrum; and (ii) measurements were performed under continuous illumination with monochromatic radiation with the wavelength slowly scanned starting from the short-wavelength part of the spectrum. The typical time of a spectral recording was several tens of minutes.

3. RESULTS AND DISCUSSION

Photoconductivity spectra for nominally undoped heterostructures A839, A856, and B824 are shown in Fig. 2. One can see that, for these samples, the photoconductivity spectra obtained by the two methods described above (shown by dots and solid lines, respectively) agree well with each other. This means that *persistent photoconductivity* was measured in both modes,

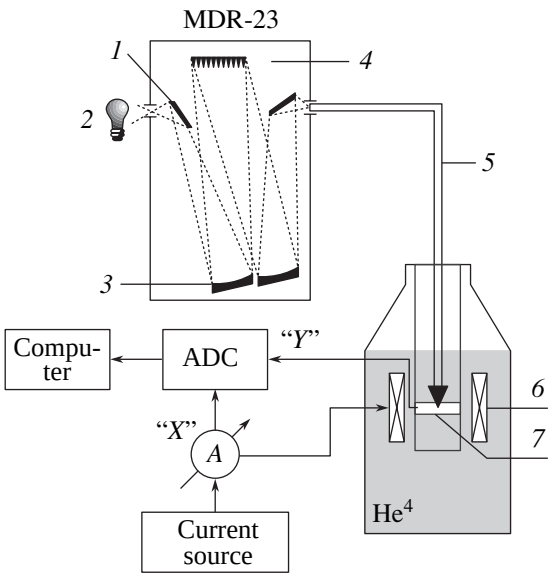

Fig. 1. The block diagram of the setup for measuring the persistent photoconductivity under exposure of the sample to light with different wavelengths: (*1*) rotating mirror, (*2*) quartz incandescent lamp, (*3*) spherical mirror, (*4*) diffraction grating, (*5*) optical waveguide, (*6*) superconducting solenoid, and (*7*) sample under study.

Parameters of the samples under study at $T = 4.2$ K

Sample	Buffer	Top barrier	n_s, 10^{12} cm^{-2}	μ, 10^5 cm^2 V^{-1} s^{-1}
A856	AlSb	$Al_{0.8}Ga_{0.2}Sb$	0.65	3.9
A839	AlSb	AlSb	0.68	2.5
B824	GaSb	AlSb	0.95	4.4
B1445	AlSb	AlSb	2.4	1.0
B1444	AlSb	AlSb	3.2	0.63

i.e., the effect introduced by constant illumination in the case of continuous recording of the spectral curves is insignificant. For comparison, the photoconductivity spectrum of a similar AlSb/InAs/AlSb sample (with an InAs QW width equal to 12 nm) taken from [11] is also shown in Fig. 2. In agreement with the results obtained in [11], we observed PPPC in the long-wavelength part of the spectrum, beginning from the lowest photon energy involved in our measurements ($\hbar\omega = 0.62$ eV). At $\hbar\omega > 1.1$ eV, the sample resistance increases and PPPC is changed to NPPC; simultaneously, the slope of the spectral dependences increases. In all three samples, several characteristic local maxima of NPPC are observed at $\hbar\omega > 2.1$ eV and a sharp drop of the resistance takes place at $\hbar\omega > 3.1$ eV. For sample B824, the measurement range was extended to 6 eV; beginning with 5 eV, a weak gradual increase in NPPC was

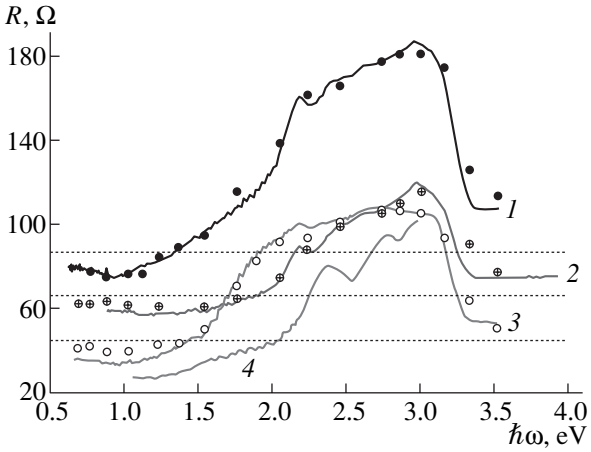

Fig. 2. Photoconductivity spectra of nominally undoped InAs/AlSb heterostructures (curves *1*–*3*). Solid lines correspond to the data recorded under constant illumination with radiation the wavelength of which is continuously scanned from higher to lower photon energies; dots correspond to the values of the resistance recorded after switching illumination off at each point, consecutive data points being taken from lower to higher photon energies. Horizontal dotted lines indicate the values of the dark resistance for each sample (measured after cooling but before the illumination was switched on for the first time). Curves *1*, *2*, and *3* correspond to samples A839, B824, and A856, respectively. Curve *4* represents the photoconductivity spectrum of sample B from [11] (in arbitrary units).

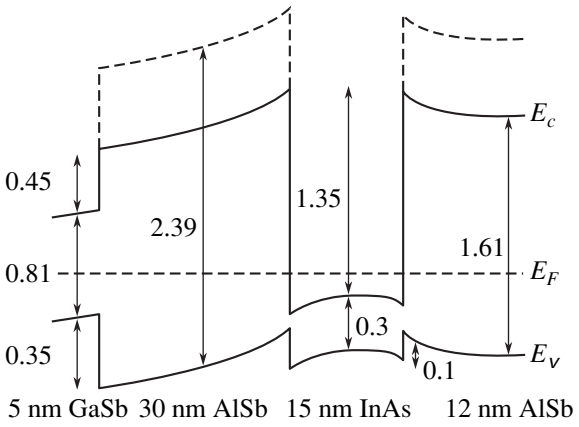

Fig. 3. Energy-band diagram for nominally undoped InAs/AlSb samples. The 2D electron gas appears in the InAs quantum well due to ionization of donors at the surface of the GaSb cap layer and deep-level donors in AlSb barriers, which leads to the formation of the built-in electric field. The dashed line shows the profile for the edge of the Γ valley in the conduction band of AlSb. Arrows indicate energies in eV.

observed. The measurements reported in [11] were carried out in the range of photon energies up to 3 eV, and resistance drop in the ultraviolet region was not observed.

It should be noted that the composition of the thick metamorphic barrier, either GaSb (sample B824) or AlSb (sample A839), has virtually no effect on the photoconductivity spectra. At the same time, the use of $Al_{0.8}Ga_{0.2}Sb$ (A856) alloy as the top barrier results in a shift of the high-slope region in the resistance spectral curve to lower photon energies; meanwhile, the positions of most of the spectral features (in particular, the local resistance peak at $\hbar\omega \approx 2.2$ eV and the sharp drop at $\hbar\omega > 3.1$ eV) remain unchanged.

The energy-band diagram of the active region of a nominally undoped heterostructure with 2D electron gas in the InAs QW is shown in Fig. 3. Following [11], we relate the PPPC observed in the long-wavelength region to the photoinization of deep-level donors and accumulation of electrons in the QW. The nature of the deep donor states needs further investigation. PPPC takes place at energies ($\hbar\omega \geq 0.62$ eV) lower than the distance from the Fermi level (which is located about 100 meV above the bottom of the InAs conduction band) to the edge of the conduction band in AlSb. The corresponding transitions can occur between neutral donors (i.e., donors with levels below the Fermi level) in the bulk of the AlSb barrier layers and higher electron quantum-confinement subbands in the InAs QW (note that the wave functions of these subbands penetrate much more deeply into the barrier than the wave function of the ground subband). The electrons excited into the QW relax rapidly to the states of the ground subband, and their transitions back to the ionized donor centers are inhibited due to high confinement of the ground-subband wave function.

Again following [11], we believe that the NPPC observed upon increasing the photon energy originates from band-to-band excitation of electron–hole pairs with subsequent separation of the charge carriers by the built-in electric field and capture of holes into the QW, where they recombine with the 2D electrons. As the photon energy is increased, the electron–hole pairs are first generated in the GaSb cap layer. The threshold photon energy for the NPPC should exceed the sum of the indirect band gap of GaSb ($\varepsilon_L \approx 0.82$ eV [15]) and the valence-band offset at the interface between the cap layer and the top barrier (0.35 eV for AlSb, see Fig. 3). Another channel of the hole injection into the barrier opens when the energy of the light holes generated by direct band-to-band optical transitions in GaSb exceeds the valence-band offset at the GaSb/AlSb interface. Since the effective masses of the electrons in the Γ valley and the light holes are close to each other, the corresponding photon energy is equal to the sum of the direct band gap $\varepsilon_\Gamma \approx 0.81$ eV and the doubled value of the valence-band offset, which yields ~1.5 eV. With further increase in the photon energy, excitation of electron–hole pairs through the indirect band gap of AlSb sets in for $\hbar\omega > \varepsilon_X = 1.61$ eV (see Fig. 3). Finally, at $\hbar\omega = 2.39$ eV, direct optical transitions of electrons from the valence band to the Γ valley of the AlSb conduction band are expected to set in. If the top barrier is made of $Al_{0.8}Ga_{0.2}Sb$, which has a narrower band gap, all threshold energies in the NPPC spectra should decrease, and exactly this is the case for sample A856 (see Fig. 2).

In the photon energy range from 1.4 to 2.1 eV, oscillations in the spectral dependences of the resistance were observed for all three samples investigated (see Fig. 4). In samples A839 and B824, both of which have barriers composed of AlSb, these oscillations have the same period and phase. For these structures, the period equals about 50 meV in the long-wavelength region and 40 meV in the short-wavelength region. For sample A856, which has an $Al_{0.8}Ga_{0.2}Sb$ top barrier with a narrower gap, the oscillation period varies from 48 to 35 meV. Similar oscillatory behavior was observed for one of the samples in [11]; however, in that case, the oscillation period varied from 80 meV in the long-wavelength region to 50 meV in the short-wavelength region. It was suggested in [11] that the oscillations are related to the emission of longitudinal $\hbar\omega_{LO}$ optical phonons by light holes generated via direct optical transitions in the GaSb layer and injected into the AlSb. In such a case, the period of oscillations should be equal to approximately twice the optical-phonon energy in AlSb (since the effective masses of electrons and light holes are approximately the same); thus, we obtain about 80 meV, which corresponds to the value of the oscillation period for the long-wavelength region obtained experimentally in [11]. Then, it is reasonable to relate the reduction of the oscillation period to

50 meV in the short-wavelength region to the increase in the electron effective mass due to the nonparabolicity of the dispersion relation. In this study, however, significantly smaller oscillation periods are observed, which indicates that the nature of the oscillations is different. It is possible that they are related to the band-to-band excitation of electrons into higher subbands in the InAs QW with subsequent electron capture by ionized deep-level donor centers in the barrier layers.

It should be noted that, for all the structures under study, the threshold of the sharp increase in NPPC appears at photon energies considerably lower than the value of the Γ-point band gap in the barrier layers (in AlSb, ε_Γ = 2.39 eV [15]; in $Al_{0.8}Ga_{0.2}Sb$ grown on an AlSb buffer, according to our estimates, taking into account the elastic strain, ε_Γ = 2.06 eV) (see Fig. 2). Thus, it may be assumed that this threshold is related to the excitation of electrons from the valence band to some comparatively shallow donor states below the Γ valley of AlSb, from which they rapidly relax into the lower *X* valley and then drift in the electric field away from the QW to become captured by deep-level donor centers; meanwhile, holes drift toward the QW and recombine with 2D electrons. The distinctive peak of NPPC at $\hbar\omega$ = 2.2 eV is most probably related to the presence of some specific donor centers in the structures under study; these centers appear to have been absent in the samples studied in [11]. This peak was observed in the structures with the top barrier composed of either AlSb (samples A839 and B824) or $Al_{0.8}Ga_{0.2}Sb$ (sample A856); in the latter case, apparently, the peak is related to similar optical transitions in the bottom AlSb barrier.

A sharp drop in NPPC at $\hbar\omega$ > 3.1 eV is indicative of the appearance of a new mechanism for electron generation. It is important to stress that, despite the photon energies being high, this effect cannot be attributed to the appearance of a new channel for band-to-band electron–hole transitions, since we relate the NPPC effect itself to band-to-band transitions—or, more precisely, to the generation of holes and their subsequent recombination with the 2D electrons. We assume that the observed drop in the NPPC originates from the appearance of a new channel for photoionization of neutral (i.e., lying below the Fermi level) deep-level donor centers, which is related to the excitation of electrons to the next energy band above the conduction band. Electroreflectance data [16] indicate that the energy gap between the conduction band and the next above-lying band at the Γ point in AlSb equals $\Delta_{\Gamma7-\Gamma6}$ = 1.5 eV. Theoretical calculations [17] predict that the energy minimum in that band occurs in the side valley located along the [100] direction and that the bottom of this valley is 0.5 eV lower than the energy at the Γ point. Taking into account that, in the structures under consideration, the Fermi level is shifted by approximately 0.3 eV from the top of the AlSb valence band, the threshold energy for the transitions from the donor states located below the Fermi level can be estimated to be 3.1 eV, which agrees

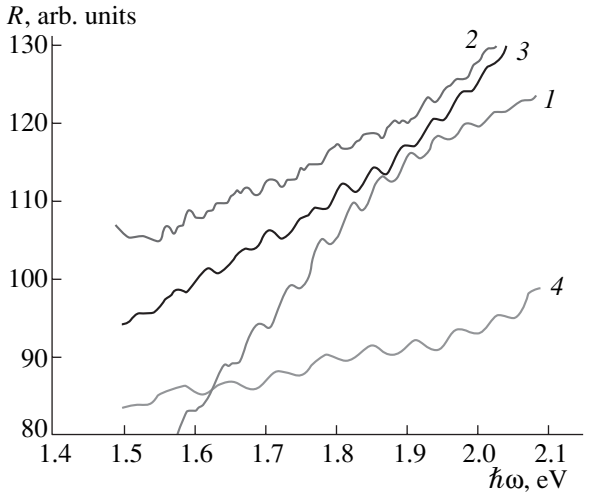

Fig. 4. The photoconductivity spectra of nominally undoped InAs/AlSb heterostructures on an expanded scale (cf. Fig. 2). Curves *1*, *2*, and *3* correspond to samples A839, B824, and A856, respectively. Curve *4* represents the photoconductivity spectrum of sample B from [11].

well with the photon energy corresponding to the occurrence of the sharp drop in NPPC. It should be noted that, for sample A856 with an $Al_{0.8}Ga_{0.2}Sb$ top barrier, the increase in NPPC ceases at $\hbar\omega$ = 2.75 eV; this behavior may be related to the onset of photoionization of neutral deep-level donors in the top barrier via electron transitions into the next energy band above the conduction band. In a structure with asymmetric barriers, this process of electron generation competes, within a certain range of photon energies, with the continuing generation of electron–hole pairs in the lower barrier, which results in a gradual reduction of NPPC at $\hbar\omega$ = 2.75–3.15 eV (see Fig. 2, curve *3*). At $\hbar\omega$ = 3.15 eV, the above-described process of ionization of neutral deep-level donors in the bottom AlSb barrier becomes effective, which results in bending of the spectral curve and a sharp drop in NPPC.

In conclusion, let us briefly discuss the photoconductivity spectra of samples B1444 and B1445 doped selectively with Te (Fig. 5). Here, unlike the spectra of nominally undoped structures, a well-defined peak of positive photoconductivity can be observed in the vicinity of 1 eV. For structure B1445 with a lower doping level, a band of negative photoconductivity in the high-photon-energy region is still present. For this sample, there is a clear difference between the results obtained in the point-by-point and the continuous-scanning modes (see dots and solid line in Fig. 5, curve *1*), and we observed that, after the illumination was turned off, a fairly rapid relaxation (on the scale of tens of seconds) of negative photoconductivity to a lower stationary value took place. In the spectrum of sample B1444 with a higher doping level, a characteristic increase in the resistance in the short-wavelength region of the spectrum is also observed; however, this increase is

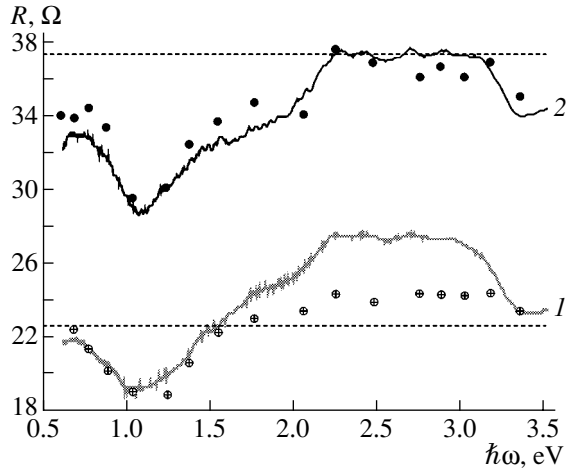

Fig. 5. Photoconductivity spectra of selectively doped InAs/AlSb heterostructures. Solid lines correspond to the data recorded under constant illumination with the radiation whose wavelength is continuously scanned from higher to lower photon energies; dots correspond to the values of the resistance that remain after switching illumination off at each point, consecutive data points being taken from lower to higher photon energies. Horizontal dotted lines indicate the values of the dark resistance for each sample (measured after cooling but before the illumination was switched on for the first time). Curves *1* and *2* correspond to samples B1445 and B1444, respectively.

insufficient to overcome the general trend (which holds for all wavelengths) toward the reduction in the resistance upon the sample illumination.

Comparing the spectra shown in Figs. 2 and 5, one can see that all the features characteristic of the photoconductivity in nominally undoped samples also manifest themselves in structures with selective doping. However, in the latter case, the relative contribution of the photoionization of deep-level centers, leading to PPPC, is considerably greater. Apparently, apart from the formation of shallow donor levels [18], doping AlSb with Te impurity may result in the appearance of deep donor levels that lie below the Fermi level. It is possible that it is ionization of these donors that is responsible for the PPPC peak at $\hbar\omega = 1$ eV (see Fig. 5). If the concentration of Te is high (sample B1444), photoionization of deep-level centers is dominant for all photon energies and NPPC is not observed.

REFERENCES

1. C. Nguyen, B. Brar, C. R. Bolognesi, *et al.*, J. Electron. Mater. **22**, 255 (1993).
2. G. Tuttle, H. Kroemer, and J. H. English, J. Appl. Phys. **65**, 5239 (1989).
3. C. Nguyen, B. Brar, H. Kroemer, and J. H. English, Appl. Phys. Lett. **60**, 1854 (1992).
4. S. Ideshita, A. Furukawa, Y. Mochizuki, and M. Mizuta, Appl. Phys. Lett. **60**, 2549 (1992).
5. J. D. Dow, J. Shen, and S. Y. Ren, Superlattices Microstruct. **13**, 405 (1993).
6. D. J. Chadi, Phys. Rev. B **47**, 13478 (1993).
7. J. Shen, J. D. Dow, S. Yu. Ren, *et al.*, J. Appl. Phys. **73**, 8313 (1993).
8. J. Shen, H. Goronkin, J. D. Dow, and S. Y. Ren, J. Appl. Phys. **77**, 1576 (1995).
9. A. Furukawa and S. Ideshita, J. Appl. Phys. **75**, 5012 (1994).
10. I. Lo, W. C. Mitchell, M. O. Manasreh, *et al.*, Appl. Phys. Lett. **60**, 751 (1992).
11. Ch. Gauer, J. Scriba, A. Wixforth, *et al.*, Semicond. Sci. Technol. **8**, S137 (1993).
12. C. Gauer, J. Scriba, A. Wixforth, *et al.*, Semicond. Sci. Technol. **9**, 1580 (1994).
13. Yu. G. Sadofyev, A. Ramamoorthy, B. Naser, *et al.*, Appl. Phys. Lett. **81**, 1833 (2002).
14. G. Tuttle, H. Kroemer, and J. H. English, J. Appl. Phys. **67**, 3032 (1990).
15. I. Vufgaftman, J. R. Meyer, and L. R. Ram-Mohan, J. Appl. Phys. **89**, 5815 (2001).
16. M. Cardona, F. H. Pollak, and K. L. Shaklee, Phys. Rev. Lett. **16**, 644 (1966).
17. M. L. Cohen and T. K. Bergstresser, Phys. Rev. **141**, 789 (1966).
18. A. Nakagawa, J. J. Pekarik, H. Kroemer, and J. H. English, Appl. Phys. Lett. **57**, 1551 (1990).

Translated by M. Skorikov

Semiconductors, Vol. 39, No. 1, 2005, pp. 27–29. Translated from Fizika i Tekhnika Poluprovodnikov, Vol. 39, No. 1, 2005, pp. 35–37.

LOW-DIMENSIONAL SYSTEMS

Long-Time Photoluminescence Kinetics of InAs/AlAs Quantum Dots in a Magnetic Field

T. S. Shamirzaev^, A. M. Gilinskiĭ, A. K. Bakarov, A. I. Toropov, S. A. Figurenko, and K. S. Zhuravlev

Institute of Semiconductor Physics, Siberian Division, Russian Academy of Sciences, pr. Akademika Lavrent'eva 13, Novosibirsk, 630090 Russia

^e-mail: timur@thermo.isp.nsc.ru

Submitted June 1, 2004; accepted for publication June 14, 2004

Abstract—The influence of a magnetic field on the low-temperature photoluminescence (PL) kinetics of InAs/AlAs quantum dots is studied. It is found that the PL decay becomes faster upon application of the magnetic field. The results obtained are explained in the context of a model that considers the fine structure of exciton levels and their Zeeman splitting in the magnetic field. *© 2005 Pleiades Publishing, Inc.*

1. INTRODUCTION

It is well known that the radiative-recombination lifetime for excitons in self-organized InAs quantum dots (QDs) that are embedded in a GaAs matrix is several nanoseconds [1]. However, it has recently been shown that the recombination dynamics of excitons in a system of InAs QDs formed in an AlAs matrix is quite different, and also that transient photoluminescence (PL) of direct-gap InAs/AlAs QDs exhibits long (millisecond-scale) nonexponential decay [2, 3]. We assumed that this unexpectedly long PL decay is caused by the exchange splitting of excitonic states in small-size QDs [2].

To check this assumption, we examined, in this study, the influence of a magnetic field on the duration of the PL decay in InAs/AlAs QDs. We established that the modification of the energy structure of QD exciton levels by the magnetic field results in a faster decay of the excitonic PL. The results obtained can be understood in the context of a model that takes into account the exchange and Zeeman splitting of the exciton levels in a QD held in a magnetic field [2].

2. EXPERIMENTAL

Heterostructures with self-organized InAs QDs embedded in an AlAs matrix were grown on semi-insulating GaAs (100) substrates by molecular-beam epitaxy in a Riber 32P system. The samples contained five layers of InAs QDs separated by 8-nm-thick AlAs layers. The amount of InAs deposited during the growth of each QD layer was equivalent to 2.7 monolayers of the material. The layers with QDs were grown at 500°C. The growth process was described in detail in [2].

The PL was excited by rectangular pulses from a semiconductor laser with $\hbar\omega$ = 1.82 eV. The peak power density on the sample surface was 5 W/cm^2. The recombination radiation was analyzed using a grating monochromator and detected by a cooled photomultiplier operated in the time-correlated single-photon counting mode. Measurements of the PL kinetics were carried out at liquid-helium temperature. The sample was placed in an Oxford optical cryostat with a superconducting solenoid making it possible to apply a magnetic field up to 6 T.

3. RECOMBINATION MODEL

An exciton represents a system of two paired spins (±1/2 for the electron and ±3/2 for the heavy hole), and its ground state is eightfold degenerate. In QDs formed of materials with zinc-blende crystal lattice symmetry, this degeneracy is lifted due to the exchange interaction and deviation of the dot shape from an ideal sphere [3]. In a spherical QD, exchange interaction leads to a splitting of the ground exciton level into two levels with different values of the total angular momentum: the lower (fivefold degenerate) optically inactive level with $J = 2$ is characterized by a long lifetime τ_T, and the higher (threefold degenerate) optically active level with $J = 1$ is characterized by a short radiative lifetime τ_C. Deviation of the QD shape from a sphere leads to a further lift of the degeneracy already partially lifted by the exchange interaction. In an asymmetric dot, the eightfold degenerate ground level of the exciton splits into five levels characterized by different values of the angular momentum component m [3]: one level with $m = \pm 2$ (ε_2), two levels with $m = \pm 1$ (ε_1^L and ε_1^U), and two levels with $m = 0$ (ε_0^L and ε_0^U). The order in which levels with different values of m are arranged on the energy scale

1063-7826/05/3901-0027$26.00

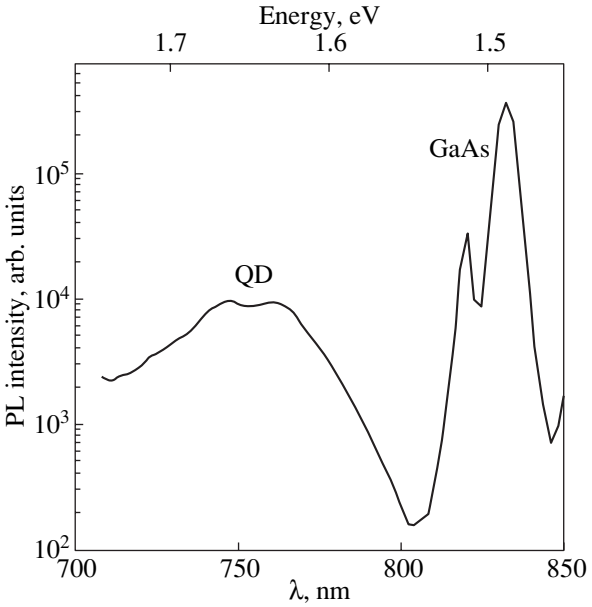

Fig. 1. The photoluminescence spectrum of a structure with InAs quantum dots embedded in an AlAs matrix. The spectrum was recorded at $T = 5$ K.

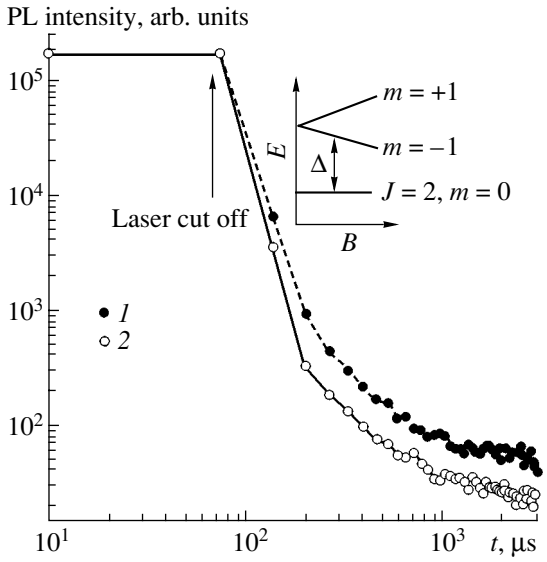

Fig. 2. Kinetics of the photoluminescence of InAs/AlAs quantum dots at $T = 4.2$ K in a magnetic field $B = (1)$ 0 and (2) 5 T.

depends on the shape of the QD; however, the lowest state is always optically inactive. The data from transmission electron microscopy [4] indicate that the shape of the QDs under study can be well approximated by an oblate spheroid. For a dot of this shape, the lowest energy level is the singlet ε_0^L with $m = 0$, and the nearest optically active level is the doubly degenerate ε_1^L with $m = \pm 1$ [3].

In bulk semiconductor materials and QDs of large size, the energy spacing Δ between the optically inactive and optically active states is smaller than kT even at liquid-helium temperature [5]; thus, the kinetics of the excitonic PL is characterized by τ_C. However, for excitons strongly confined in small-size QDs embedded in a wide-gap matrix (the case of InAs QDs in an AlAs matrix), the magnitude of splitting Δ becomes larger than the thermal energy kT at liquid-helium temperature. Thus, in small QDs, in the absence of competing channels for the charge-carrier recombination, the exciton radiative-recombination lifetime is determined mainly by the value of τ_T.

When a magnetic field is applied to a QD, Zeeman splitting of the exciton states degenerate with respect to the angular-momentum component m takes place. The expected behavior of the exciton energy levels in the QDs under study is shown in the inset in Fig. 2. The energy of the lowest level is independent of the field, because the angular-momentum component of this state equals zero. The optically active state splits in the magnetic field, which should result in a reduction of the energy gap Δ; thus, the kinetics of the PL decay should become faster due to an increase in the population of the optically active excited state.

4. EXPERIMENTAL RESULTS AND CONCLUSIONS

The spectrum of the low-temperature PL of a structure with InAs QDs in an AlAs matrix is shown in Fig. 1. The spectral lines at 1.515 and 1.490 eV originate, respectively, from excitonic recombination and band-to-acceptor transitions in the GaAs substrate, and the line at 1.65 eV is related to the radiative recombination of excitons in the QDs. Kinetic curves for the integrated PL from InAs QDs in an AlAs matrix, recorded at 4.2 K in magnetic fields of $B = 0$ and 5 T, are shown in Fig. 2 (curves *1* and *2*, respectively). We can see that, in agreement with our previous data reported in [2], the decay kinetics in a zero magnetic field is nonexponential and, thus, cannot be described by a characteristic lifetime. The duration of the PL decay is several milliseconds. When a magnetic field is applied, the decay kinetics becomes faster, as was expected in the context of the suggested model of exciton recombination in the QDs under study.

Thus, the effect of a magnetic field on the kinetics of photoluminescence (PL) of InAs QDs embedded in an AlAs matrix is studied. It is found that the PL decay becomes faster in the field of 5 T. The results obtained are explained in the context of a model that takes into account the exchange and Zeeman splitting of the exciton levels in a QD held in a magnetic field.

ACKNOWLEDGMENTS

This study was supported in part by the Volkswagen Foundation (grant no. I/76 837); the Russian Foundation for Basic Research (project no. 04-02-16653); and the Ministry of Industry, Science, and Technologies of the Russian Federation.

REFERENCES

1. R. Heitz, A. Kalburge, Q. Xie, *et al.*, Phys. Rev. B **57**, 9050 (1998).
2. T. S. Shamirzaev, A. M. Gilinsky, A. I. Toropov, *et al.*, Pis'ma Zh. Éksp. Teor. Fiz. **77**, 459 (2003) [JETP Lett. **77**, 389 (2003)].
3. Al. L. Efros, M. Rosen, M. Kuno, *et al.*, Phys. Rev. B **54**, 4843 (1996).
4. D. A. Tenne, O. R. Bayutova, A. K. Bakarov, *et al.*, Pis'ma Zh. Tekh. Fiz. **28** (13), 44 (2002) [Tech. Phys. Lett. **28**, 554 (2002)].
5. H. Fu, Lin-Wang Wang, and A. Zunger, Phys. Rev. B **59**, 5568 (1999).

Translated by M. Skorikov

Semiconductors, Vol. 39, No. 1, 2005, pp. 30–32. Translated from Fizika i Tekhnika Poluprovodnikov, Vol. 39, No. 1, 2005, pp. 38–40.

LOW-DIMENSIONAL SYSTEMS

Electroluminescent Properties of Heterostructures with GaInNAs Quantum Wells

A. V. Murel'^, V. M. Danil'tsev, Yu. N. Drozdov, D. M. Gaponova, V. I. Shashkin, V. B. Shmagin, and O. I. Khrykin

Institute for the Physics of Microstructures, Russian Academy of Sciences, Nizhni Novgorod, 603950 Russia
^e-mail: murel@ipm.sci-nnov.ru

Submitted June 1, 2004; accepted for publication June 14, 2004

Abstract—GaInNAs quantum wells were grown by metal–organic vapor-phase epitaxy. In order to improve the optical properties, the GaNAs barriers were incorporated on both sides of the quantum well; these barriers compensated the elastic stresses. Characteristics of the optical transitions were assessed from the measurements of photoluminescence and photocurrent. In order to fabricate light-emitting diodes, nonalloyed ohmic contacts based on heavily δ-doped layers were used. Electroluminescence was observed at a wavelength of ~1.2 μm at temperatures of 77 and 300 K; the electroluminescence intensity depended linearly on the injection current if the latter exceeded a certain threshold value. © *2005 Pleiades Publishing, Inc.*

1. INTRODUCTION

Long-wavelength (1.3–1.5 μm) lasers based on GaInNAs and fabricated on GaAs substrates are of interest in the context of using these lasers in optoelectronic communication lines [1, 2]. The GaInNAs semiconductor compound is studied widely as a possible material for the active layer of vertical-cavity surface-emitting lasers (VCSELs) due to the fact that the VCSEL technology based on GaAs is well developed. This technology includes the formation of distributed Bragg reflectors based on the Al(Ga)As/GaAs grating and selective etching of AlAs in order to spatially confine the region where the current flows. At the same time, the emission-efficiency deterioration caused by introduction of nitrogen is believed to be the most serious problem of GaInNAs layers. Therefore, many researchers made all-out efforts to improve the optical quality of this material.

One of the methods for improving the aforementioned quality is the incorporation of tensile-stressed GaNAs barriers on both sides of the GaInNAs quantum well (QW) [3, 4], which ensures a partial compensation of stresses in the QW and makes it possible to form a wider QW that should give rise to a shift of the emission to longer wavelengths. It is assumed that the GaNAs barriers act as sources of nitrogen and suppress the shift to shorter wavelengths due to nitrogen diffusion from the QW at elevated temperatures.

2. EXPERIMENTAL

The structures were grown on either semi-insulating or heavily doped *n*- and *p*-type GaAs substrates using metal–organic vapor-phase epitaxy (MOVPE) at a low (75 Torr) pressure. Trimethylgallium (TMG) and trimethylindium (TMI) were used as sources of the Group-III elements, while 1,1 dimethylhydrazine (DMHy) and arsine (AsH_3) were used as sources of the Group-V elements. The growth temperature was 650°C for GaAs and 500–600°C for Ga(In)–N–As. The schematic representation of the grown structures is shown in Fig. 1a. A GaInNAs QW with a width of 8.5 nm was incorporated into a 0.5-μm-thick undoped GaAs layer; this QW was surrounded on both sides with 6-nm-thick GaNAs layers. Three layers heavily δ-doped with Si and spaced at 3 nm were grown in the vicinity of the surface; these layers were used as nonalloyed ohmic contacts for electron injection. After heterostructure growth was completed, a 20-nm-thick epitaxial aluminum layer was deposited in situ using a organometallic aluminum-containing compound as the source; this layer acted as a metal contact and also protected the gallium arsenide surface from oxidation. In order to ensure a reliable mechanical and electrical contact, we deposited an additional aluminum layer using thermal evaporation of an aluminum charge. The width and composition of QWs were determined from the data of the X-ray diffraction and secondary-ion mass spectrometry (SIMS). The spectra of the X-ray diffraction were measured using a DRON-4 diffractometer with a Ga(400) monochromator and $CuK\alpha_1$ radiation in the vicinity of the (400)GaAs and (440)GaAs reflections. Optical properties of the samples were studied using the analysis of the photoluminescence (PL) and photocurrent spectra. Electroluminescence (EL) was studied for the samples that were obtained by cleaving and had an area of ~1 mm^2. The pumping was attained using a controlled pulsed current generator with the pulse duration of 10 μs and the repetition frequency of 1 kHz. The radiation emerging from the cleaved side surface was detected at temperatures of 80 and 300 K.

1063-7826/05/3901-0030$26.00 © 2005 Pleiades Publishing, Inc.

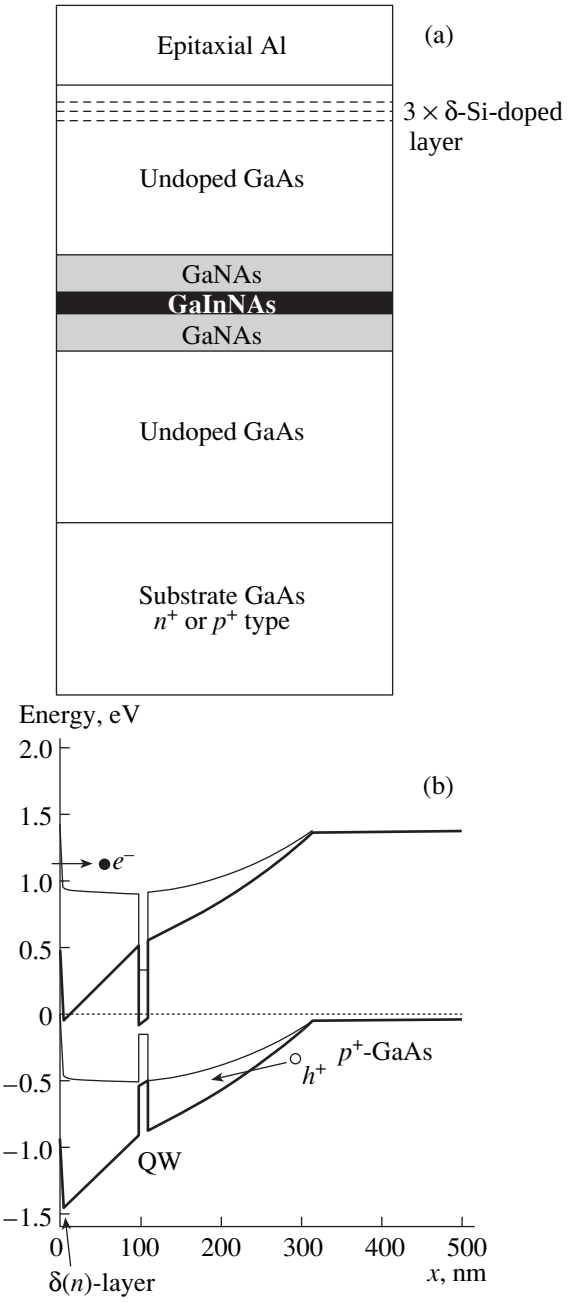

Fig. 1. (a) Schematic representation of the structure containing a GaInNAs quantum well. (b) The energy-band diagram of the structure at the zero bias (the thick solid line) and the forward-bias voltage (the thin solid line).

The assumed energy-band diagram of the light-emitting structure is shown in Fig. 1b for the zero- and forward-bias voltages.

3. RESULTS AND DISCUSSION

The content of nitrogen and indium in quaternary compounds was studied previously [5] in relation to the growth parameters in the course of MOVPE; in this study, we used the results obtained in [5]. The content of nitrogen in the GaNAs barriers was estimated at 2%; the composition of the QW corresponded approximately to $Ga_{0.88}In_{0.12}N_{0.01}As_{0.99}$. In the X-ray diffraction spectra, the peak related to the quaternary-compound layer was located at smaller Bragg angles than that related to GaAs (the lattice constant of GaInNAs is larger than that of GaAs); i.e., the tension as a result of substitution In–Ga is larger than compression as a result of substitution N–As. Therefore, the introduction of barrier layers composed of the GaAsN ternary compound with a reduced lattice constant leads indeed to partial compensation of total elastic strain in the layers and increases the critical thickness for the generation of misfit dislocations.

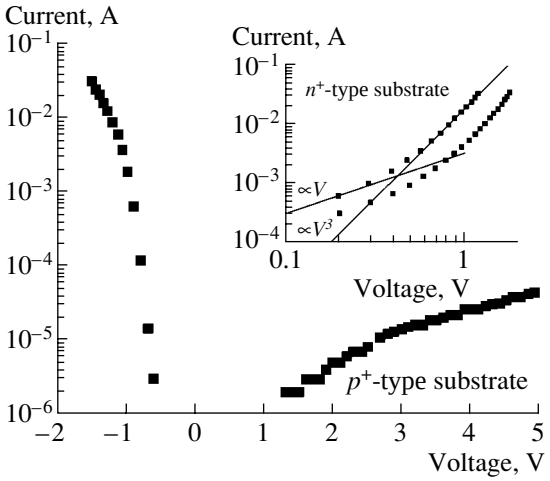

Fig. 2. The current–voltage characteristic of the diode with the GaInNAs quantum well grown on the p^+-type substrate for studying the electroluminescence. The current–voltage characteristic of the same structure grown on the n^+-type substrate is shown in the inset.

The shape of current–voltage (I–V) characteristics of the diodes that were 200 μm in diameter and were formed on the p^+-type substrate was typical of a p^+–n junction (Fig. 2); the nonideality factor was ~2.2 and the series resistance was 10–15 Ω. The capacitance–voltage characteristic measured under a reverse bias voltage indicates that the undoped region is completely depleted. The I–V characteristics of the diodes formed on the n^+-type substrate are shown on the log–log scale in the inset to Fig. 2. The observed initial ohmic portion corresponds to the charge-carrier transport in the n^+–n^-–n^+ structure at low voltages. As the voltage increases, the dependence of current on voltage follows the law $I \propto V^3$ that is characteristic of currents limited by the space charge.

The PL spectrum measured at 80 K includes a band that peaked at a wavelength of 1120 nm and that is related to the basic transition in the QW (Fig. 3). In Fig. 4, we show the spectra of electroluminescence detected from side surface of the cleaved sample at the injection current of 150 mA; a band that peaked at

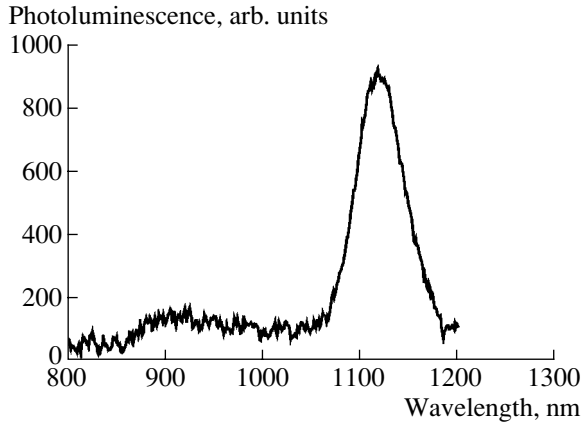

Fig. 3. The photoluminescence spectrum of the structure that contains the GaInNAs quantum well; the spectrum was measured at a temperature of 80 K.

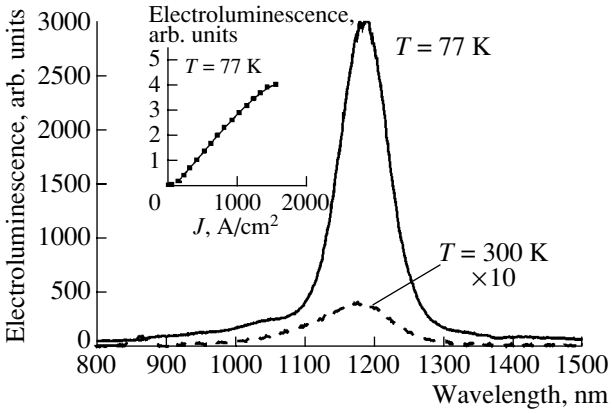

Fig. 4. Electroluminescence spectra of a diode with a GaInNAs quantum well; the spectra were measured at temperatures of 77 and 300 K. The dependence of the electroluminescence intensity on the injection-current density is shown in the inset.

1180 nm is observed in these spectra. The difference between the positions of the peaks in the PL and EL spectra is related to a planar nonuniformity of the samples that is caused by special features of the vapor-phase epitaxy in a horizontal reactor without rotation of the substrates. The EL intensity at 77 K is nearly two orders of magnitude higher than that at room temperature. The output power of electroluminescence depends almost linearly on the injection current (see the inset to Fig. 4).

In order to obtain luminescence at longer wavelengths, one has to increase the content of indium and/or nitrogen in the quantum well for reducing the band gap. This inference implies the development and improvement of the growth technology for quaternary semiconductor compounds and a deeper insight into the processes that occur in the vapor phase and give rise to a profound complex effect on the incorporation of indium and nitrogen into the growing epitaxial film.

4. CONCLUSIONS

The metal–organic vapor-phase epitaxy at temperatures of 500–550°C was used to grow the quantum wells (QWs) of the quaternary GaInNAs compound on the GaAs substrates. In order to improve the optical properties of the structure, the GaNAs barriers that compensated stresses were incorporated on both sides of the QW. We studied the photoelectric properties of fabricated structures. We used a nonalloyed ohmic contact based on heavily δ-doped layers in the structure of the light-emitting diode. Electroluminescence was observed at a wavelength of ~1.2 μm at temperatures of 77 and 300 K; the electroluminescence intensity depended linearly on the injection-current density.

ACKNOWLEDGMENTS

This study was supported by the Russian Foundation for Basic Research (project nos. 03-02-17404 and 04-02-17180) and by the program Physics of Solid-State Nanostructures.

REFERENCES

1. T. Kitatani, M. Kondow, and T. Tanaka, J. Cryst. Growth **221**, 491 (2000).
2. S. Sato, Jpn. J. Appl. Phys., Part 1 **39**, 3403 (2000).
3. E.-M. Pavelescu, T. Jouhti, C. S. Peng, *et al.*, J. Cryst. Growth **241**, 31 (2002).
4. N. Tansu, J.-Y. Yeh, and J. Mawst, Appl. Phys. Lett. **83**, 2512 (2003).
5. A. V. Murel', V. M. Danil'tsev, M. N. Drozdov, *et al.*, Izv. Ross. Akad. Nauk, Ser. Fiz. **68** (1), 87 (2004).

Translated by A. Spitsyn

Semiconductors, Vol. 39, No. 1, 2005, pp. 33–36. Translated from Fizika i Tekhnika Poluprovodnikov, Vol. 39, No. 1, 2005, pp. 41–44.

LOW-DIMENSIONAL SYSTEMS

A Study of Recombination Centers Related to As–Sb Nanoclusters in Low-Temperature Grown Gallium Arsenide

P. N. Brunkov*^, A. A. Gutkin*, Yu. G. Musikhin*, V. V. Chaldyshev*, N. N. Bert*, S. G. Konnikov*, V. V. Preobrazhenskiĭ, M. A. Putyato**, and B. R. Semyagin****

**Ioffe Physicotechnical Institute, Russian Academy of Sciences, St. Petersburg, 194021 Russia*

^e-mail: brunkov@mail.ioffe.ru

***Institute of Semiconductor Physics, Siberian Division, Russian Academy of Sciences, Novosibirsk, 630090 Russia*

Submitted June 1, 2004; accepted for publication June 16, 2004

Abstract—Electronic traps in "low-temperature" GaAs (LT-GaAs) grown at 150°C were studied. The As–Sb clusters appearing in this material after annealing were located in a plane that contained a single Sb monolayer formed during growth. The diameter of the clusters was as large as 20 nm. For the purpose of measurement, Au–*n*-GaAs Schottky barriers were used, in which, for certain bias voltages, the space charge region enclosed the narrow LT-GaAs layer containing the plane of clusters. The bias-voltage dependence of the structure capacitance indicates that the majority of the electrons in this layer are captured by traps, whose energy level lies ~0.5 eV below the bottom of the conduction band. The energy density of states at this energy is 10^{14} cm^{-2} eV^{-1}, which sharply decreases towards the midgap. The existence of traps with activation energies of ~0.5 eV for the thermal emission of electrons is confirmed by deep-level transient spectroscopy. The magnitude of the electron-capture cross section determined by this method is in the range 5×10^{-14}–1×10^{-12} cm^2. It is assumed that traps of this type are related to large As–Sb clusters. © *2005 Pleiades Publishing, Inc.*

1. INTRODUCTION

It is well known [1–3] that gallium arsenide grown by molecular beam epitaxy at low temperatures (LT-GaAs) and subjected to annealing at temperatures exceeding 500°C contains nanosized arsenic clusters. The size and concentration of these clusters depend on the growth and annealing conditions. Some studies [3–5] indicate that these clusters affect resistivity and free-carrier lifetime. The values of these parameters are particularly important for the application of LT-GaAs in microelectronic and optoelectronic devices; however, the relation of As clusters to the parameters of electronic traps observed in LT-GaAs has barely been investigated. In [6], it was found that As clusters 6–8 nm in diameter introduce a new trap with an activation energy for electron thermal emission of about 0.5 eV, but this trap was not observed in LT-GaAs containing clusters with sizes smaller than 3 nm. Our aim was to further study the traps in LT-GaAs with relatively large As–Sb clusters. It is worth noting that the formation conditions and the size of the clusters in our samples differed from those reported in [6].

2. EXPERIMENTAL

The samples under study were grown on n^+-GaAs substrates using molecular-beam epitaxy in a two-chamber Katun setup. The samples contained a LT-GaAs layer grown at 150°C, which was located between two *n*-GaAs layers grown at 580°C that had a thickness of about 0.4 μm and electron concentration of ~2.5×10^{16} cm^{-3}. The thickness of the LT-GaAs layer was 40 nm. In order to narrow the region containing the clusters, a Sb monolayer was introduced into the midplane of the LT-GaAs layer during epitaxial growth. In the plane of the Sb monolayer, As–Sb clusters were formed by the annealing that accompanied the growth of the top *n*-GaAs layer [7]. Transmission electron microscopy (TEM) studies showed that our structure contained clusters about 4–7 nm in diameter as well as particularly large clusters with sizes up to 22 nm (Fig. 1). The total concentration of these clusters was (3–4) × 10^{10} cm^{-2}. As we were using the TEM technique, we were unable detect clusters with sizes smaller than 3 nm. For the chosen growth conditions and thickness of the LT-GaAs layer, the calculated concentration

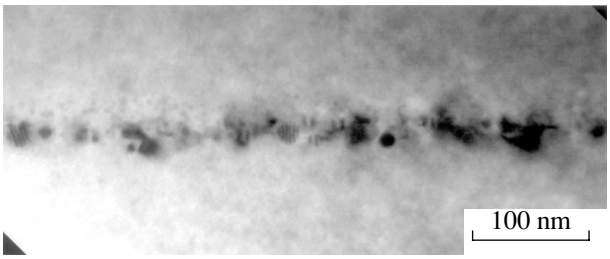

Fig. 1. A bright-field TEM image (**g** = 220) of a cross section of the structure in the region of the GaAs layer grown at a low temperature.

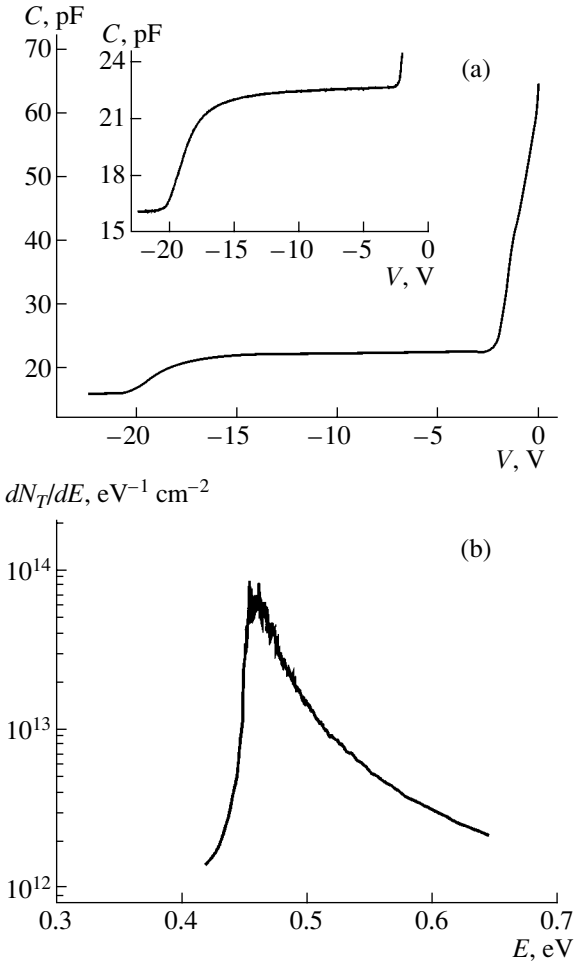

Fig. 2. (a) Capacitance–voltage (*C–V*) curves for the structure at $T = 270$ K. In the inset, a portion of the *C–V* characteristic, where the capacitance is quasi-constant, is shown on an enlarged scale. (b) The energy density of deep states dN_T/dE obtained from the *C–V* characteristic using expressions (1) and (2).

and characteristic cluster size were 3×10^{10} cm^{-2} and 12 nm, respectively [7].

To study traps using a capacitance technique, Schottky barriers were formed by depositing Au on the sample surface through an aperture in the mask. The contact area S was $\sim 1.1 \times 10^{-3}$ cm^2. An AuGe alloy fired at a temperature of 400°C was used as an ohmic contact to the n^+ substrate.

For deep-level transient spectroscopy (DLTS), we used the setup described in [6]. In the DLTS experiments, the small width of the layer containing clusters allowed us to avoid any difficulties related to the presence of a large number of recharged traps [6] and, moreover, to study the distribution of trap energies by analyzing the dependence of the high-frequency barrier capacitance C on the bias voltage V. This dependence was measured at a frequency of 1 MHz using a Boonton 72B capacitance bridge. The constant bias voltage was changed in steps of 15 mV, and the time during which the sample was maintained at each bias was 2.5 s.

3. RESULTS AND DISCUSSION

The high-frequency capacitance C as a function of the reverse bias V is shown in Fig. 2a. In equilibrium at zero bias, the layer of nanoclusters is negatively charged due to electron capture and is surrounded on both sides by regions of space charge formed by ionized shallow donors [8]. The space charge layer at the rectifying Au–*n*-GaAs contact expands with reverse bias and, at $V \approx -1$ V, as this layer touches one of these regions, the capacitance sharply decreases (Fig. 2a) [8]. Therefore, using the magnitude of the capacitance "jump" in this region, one can estimate the total thickness ($2L$) of the cluster layer and the two adjacent space-charge regions as approximately 0.3 μm. The capacitance corresponding to the beginning of the jump determines the width of the space charge layer w^* in the Au–*n*-GaAs barrier at which this layer touches the space-charge region in the vicinity of the clusters. Then, the distance x_1 from the central plane of the cluster layer to the sample surface is given by the sum $x_1 = w^* + L$ and is equal to ~0.4 μm in our samples.

In the region of $C(V)$ dependence that follows the sharp drop mentioned above, the capacitance weakly decreases as the reverse bias increases (Fig. 2a). In this region, an increase in the negative charge in the metal electrode of the Schottky barrier is compensated for by an increase in the total positive charge of the semiconductor, due to a decreasing number of electrons trapped in the layer of clusters located in the space charge layer. An insignificant decrease in the capacitance in this region of the $C(V)$ curve (see the inset in Fig. 2a), in addition to the large width of this region, indicate that the majority of electrons are accumulated at the levels with closely spaced energies in a thin layer. Since, in our samples, these levels lie in the upper half of the GaAs band gap, we may assume that, at a reverse bias, the position of the quasi-Fermi level that determines the stationary level occupancy coincides with the position of the Fermi level in the neutral *n*-GaAs region that is located beyond the space charge layer. Such a circumstance is preserved until the quasi-Fermi level approaches the midgap in the layer of nanoclusters. Therefore, a small decrease in the capacitance accompanied by an increasing reverse bias on the plateau of the $C(V)$ dependence and beyond this region is caused by the increase in the width of the space charge layer that produces a lowering of the quasi-Fermi level in the layer of clusters sufficient for the compensation of the charge in the metal electrode.

By solving the Poisson equation for the structure considered in the approximation of a stepped function of deep level occupation and a vanishingly thin layer of clusters, we can determine the energy density of deep states dN_T/dE in the plane of clusters from the

C–V characteristic. In the CGSE system of units, we have

$$\frac{dN_T}{dE} = \frac{\varepsilon}{4\pi x_1 q^2}\left[\frac{SqN_d}{C^2(V)}\left(\frac{\varepsilon S}{4\pi C(V)} - x_1\right)\right]^{-1} \times \left[\left|\frac{dV}{dC}\right| + \frac{SqN_d x_1}{C^2(V)}\right], \quad (1)$$

where N_d is the concentration of uncompensated shallow donors in n-GaAs, q is the elementary charge, and ε is the permittivity. The energy E is measured from the bottom of the conduction band and increases in the GaAs band gap.

Expression (1) yields dN_T/dE at an energy corresponding to the quasi-Fermi level at the voltage V. To obtain the energy dependence of dN_T/dE, it is necessary to use the relation

$$E = (2\pi/\varepsilon)q^2 N_d[\varepsilon S/(4\pi C(V)) - x_1]^2 + E_F, \quad (2)$$

where E_F is the distance from the Fermi level to the bottom of the conduction band in neutral n-GaAs.

By numerically solving the neutrality equation for n-GaAs making an allowance for a low degree of compensation, at T = 270 K and $N_d = 2.5 \times 10^{16}$ cm^{-3}, we obtain E_F = 0.060–0.065 eV below the bottom of the GaAs conduction band. Figure 2b shows the energy dependence of the energy density of deep states dN_T/dE in the LT-GaAs layer as calculated from the C–V characteristic (Fig. 2a) using expressions (1) and (2). The density of states dN_T/dE has a pronounced maximum of about 10^{14} eV^{-1} cm^{-2} at the energy $E \approx 0.46$ eV and drops by approximately two orders of magnitude when approaching the GaAs midgap. A sharp decrease in the density of states dN_T/dE on the side of low energies (Fig. 2b) may be due to the fact that, in the above model, the contribution of the change in the charge of the top GaAs layer to the differential capacitance is disregarded; however, this contribution can be important at low reverse-bias voltages. An estimation of the total number of electrons in deep states in the layer of clusters is calculated using the length of the plateau region of the C–V characteristic and value of the capacitance in this region and yields $\sim 2 \times 10^{12}$ cm^{-2}, consistent with the density of states dN_T/dE plotted in Fig. 2b.

In the DLTS spectrum, for our samples, a single electronic trap was found. To prevent the recharging of numerous traps in the LT-GaAs layer [6] and to probe the traps lying in a narrow energy range, we used a low-amplitude filling pulse of V_p = 1 V. It appeared that in the low-temperature region (210–230 K), where the DLTS peak shifts to higher temperatures as the emission-rate window of the two-strobe integrator is increased, an anomalously strong increase in the peak amplitude was observed. This effect is related to the existence of a potential barrier, which prevents the electrons from penetrating into the LT-GaAs layer during the filling pulse. Therefore, at the low temperatures at the end of the filling pulse, the degree of trap filling appears to be below the steady-state value and increases with the temperature. This circumstance affects both the amplitude and the position of the peak in the DLTS spectrum and distorts the Arrhenius plot (see Fig. 3). Thus, in order to determine the trap parameters, we used DLTS spectra measured at temperatures above 260 K, which corresponded to the window of emission rates of the two-strobe integrator of 400–1600 s^{-1}, where the amplitude of the capacitance relaxation stopped varying in relation to the increasing temperature, i.e., the trap occupancy in the LT-GaAs layer at the end of the filling pulse always attained a steady-state value. A change in the gate voltage V from –4 to –3.1 V produced barrier lowering and a decrease in the bending of the Arrhenius plot (Fig. 3). The high-temperature portion of the Arrhenius plot corresponds to activation energies in the range 0.48–0.60 eV with capture cross sections from 5×10^{-14} cm^2 to 1×10^{-12} cm^2. The activation energies agree satisfactorily with the data obtained from the analysis of the $C(V)$ dependence (Fig. 2b).

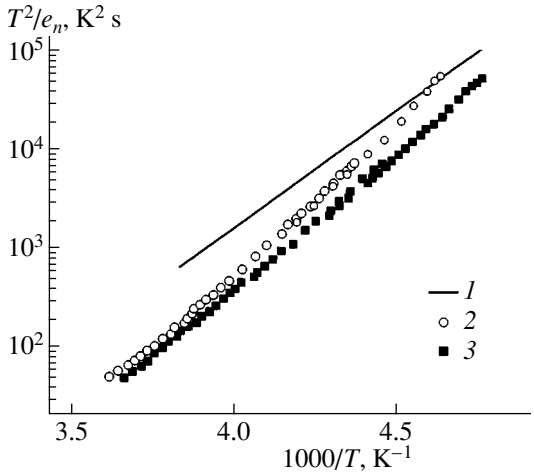

Fig. 3. The Arrhenius plots for electronic traps in a layer of GaAs grown at a low temperature. (*1*) A $Q2$ trap [6]; (*2*, *3*) the results of this study (*2*) at a bias voltage of V = –4 V and (*3*) at a bias voltage of V = –3.1 V.

As can be seen in Fig. 3, the electron emission rates for the trap under study are rather close to the parameters of the $Q2$ trap detected by Brunkov *et al.* [6] in the samples that had a LT-GaAs layer where the average As cluster size formed without introducing Sb atoms was about 6–8 nm. This fact confirms the assumption [6] that the appearance of an electronic trap with an activation energy of ~0.5 eV and a large capture cross section is related to the formation of large clusters in the LT-GaAs layers. A slight difference in relation to the capture cross sections and activation energies between the $Q2$ trap and the trap considered in this study could

be caused by the difference in cluster size and composition and, in part, by an error in determining the trap parameters.

ACKNOWLEDGMENTS

This study was supported by the Russian Foundation for Basic Research, project no. 03-02-16607.

REFERENCES

1. M. R. Melloch, K. Mahaligam, N. Otsuka, *et al.*, J. Cryst. Growth **111**, 39 (1991).
2. N. A. Bert, A. I. Veĭnger, M. D. Vilisova, *et al.*, Fiz. Tverd. Tela (St. Petersburg) **35**, 2609 (1993) [Phys. Solid State **35**, 1289 (1993)].
3. T.-C. Lin and T. Okumura, Jpn. J. Appl. Phys. **35**, 1630 (1996).
4. H. Ruda and A. Shik, Phys. Rev. B **63**, 085203 (2001).
5. P. A. Loukakos, C. Kalpouzos, I. E. Perakis, *et al.*, Appl. Phys. Lett. **79**, 2883 (2001).
6. P. N. Brunkov, A. A. Gutkin, A. K. Moiseenko, *et al.*, Fiz. Tekh. Poluprovodn. (St. Petersburg) **38**, 401 (2004) [Semiconductors **38**, 387 (2004)].
7. V. V. Chaldyshev, Mater. Sci. Eng. B **88**, 195 (2002).
8. P. N. Brunkov, V. V. Chaldyshev, N. A. Bert, *et al.*, Fiz. Tekh. Poluprovodn. (St. Petersburg) **32**, 1170 (1998) [Semiconductors **32**, 1044 (1998)].

Translated by I. Zvyagin

Semiconductors, Vol. 39, No. 1, 2005, pp. 37–40. Translated from Fizika i Tekhnika Poluprovodnikov, Vol. 39, No. 1, 2005, pp. 45–48.

LOW-DIMENSIONAL SYSTEMS

Effect of the Electrochemical Modification of a Thin Ga(In)As Cap Layer on the Energy Spectrum of InAs/GaAs Quantum Dots

I. A. Karpovich^, A. V. Zdoroveishchev, S. V. Tikhov, P. B. Demina, and O. E. Khapugin

Lobachevsky State University, pr. Gagarina 23, Nizhni Novgorod, 603950 Russia

^e-mail: fdp@phys.unn.ru

Submitted June 1, 2004; accepted for publication June 16, 2004

Abstract—It was shown that the selective etching and anodic oxidation of a thin Ga(In)As cap layer makes it possible to decrease the ground-state transition energy in InAs/GaAs quantum dots from ~0.9 to ~0.7 eV due to the resulting partial stress relaxation. Similar processing of surface quantum dots leads to a decrease in the quantum-dot height that increases the transition energy. *© 2005 Pleiades Publishing, Inc.*

1. INTRODUCTION

The energy spectrum of self-assembled InAs quantum dots (QDs) in the GaAs matrix that have thin cap layers (thinner than ~30 nm) becomes sensitive to this layer's thickness and the chemical composition. This sensitivity is mainly caused by the dependence of the spectrum on the elastic-stress field existing in QDs. The field is governed by the parameters of the layer [1–4]. This circumstance offers a fresh opportunity to control the QD spectrum. The cap-layer parameters, as a rule, are set during its growth at high temperatures. In this case, as well as changes in QD elastic stresses, changes in other factors affecting the QD energy spectrum can occur, in particular, a change in the QD morphology, which is associated with diffusion. Of theoretical and practical interest is the opportunity to control the QD spectrum at low temperatures after the growth of the structure. Such control allows a more definite separation of the influence of individual factors, particularly the elastic stresses, on the energy spectrum and electronic properties of QD heterostructures and can be used to fine tune the spectrum. In this study, we use photoelectric and photoluminescence spectroscopy, and atomic-force microscopy (AFM) to analyze the possibility of controlling the QD spectrum by an electrochemical modification (selective chemical etching and anodic oxidation) both of a cap layer and QDs grown on the structure surface.

2. EXPERIMENTAL

InAs/GaAs QD heterostructures (QDHs) were grown on a (100) surface of semi-insulating GaAs using metal–organic chemical vapor deposition (MOCVD) at atmospheric pressure. A buffer *n*-GaAs layer 0.6 μm thick and with an electron concentration of $\sim 5 \times 10^{16}$ cm^{-3} was grown at a temperature of 650°C; the temperature was then decreased to 520°C and an InAs QD layer (five monolayers) was deposited. To improve the InAs QD layer's homogeneity, it was doped with bismuth during the deposition [5]. The structures with a QD layer were coated with a homogeneous GaAs layer 3–30 nm thick, a double cap layer consisting of an $In_{0.3}Ga_{0.7}As$ quantum well (QW) layer 2 nm thick and a top GaAs layer, and a structure without a cap layer (i.e., structures with surface QDs (SQDs) were also grown).

The structures were etched in a selective etchant, i.e., a (0.8 M $K_3[Fe(CN)_6]$ + 0.3 M KOH) : H_2O 1 : 5 solution mixed with glycerin at a ratio of 1 : 2. The etchant exhibits a low etch rate of InAs (~0.1 nm/min) and a relatively high etch rate of GaAs (~10 nm/min) [6]. Anodic oxidation of the structures was carried out in a mixture of 3% solution of tartaric acid with ethylene glycol (1 : 1) at a static voltage.

The spectra of the photovoltage at the interface between the semiconductor and liquid electrolyte (PVSE) were measured at 300 K using the method described in [7]. To eliminate the effect of the light absorption in the electrolyte (1M KCl solution) on the spectra, the structures were illuminated through the substrate, which caused a spectrum cutoff in the GaAs fundamental-absorption region. The photoluminescence (PL) spectra were measured at 77 K during photoexcitation by an He–Ne laser beam with an intensity of up to 100 W/cm^2.

3. RESULTS AND DISCUSSION

Figure 1 shows the PVSE spectra of structures with a combined QW/QD layer, a single QD layer, or an SQD layer (curves *1*, *5*, *8*, respectively). We should note that all the structures were grown under the same conditions before the final operations of the QW layer and GaAs cap layer deposition. The formation of the combined QW/QD layer in the QDH that has a double GaAs/InGaAs cap layer results in a red shift of the energy E_0(QD) of the ground-state transition in InAs QDs. This is due to a partial elastic-stress relaxation

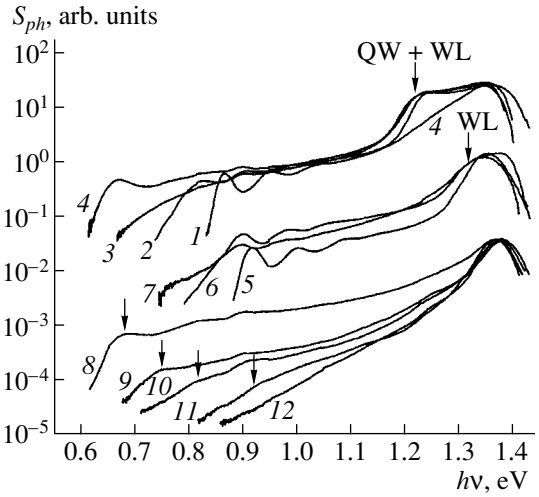

Fig. 1. The evolution of the PVSE spectra during selective etching of the QDH with a combined QW/QD layer (*1–4*), a single QD layer (*5–7*), and surface QDs (*8–12*). The etching time is (*1*, *5*, *8*) 0 s, (*2*, *6*) 240 s, (*3*, *7*) 360 s, (*4*) 480 s, (*9*) 30 s, (*10*) 60 s, (*11*) 270 s, and (*12*) 540 s. The thickness of the cap GaAs layer is 30 nm.

caused by a decrease in the lattice mismatch at the InGaAs/InAs interface [3, 4]. In the structures with a double cap layer instead a homogeneous layer, the energy E_0(QD) was lowered from 0.92 (curve *5*) to 0.87 eV (curve *1*). In this case, the energy of the ground-state transition in the $In_{0.3}Ga_{0.7}As$ QW also decreases from 1.37 (in the structure with a single QW) to 1.23 eV in the WQ/QD layer (curve *1*) due to the formation of a hybrid quantum well, QW + WL (InAs wetting layer), between QDs [4]. The absence of cap layer results in the elastic-stress relaxation in SQDs decreasing E_0(QD) to ~0.68 eV (curve *8*). According to the AFM data, SQDs had an average height of ~6 nm, a lateral size of ~40 nm, and a surface concentration of $\sim 10^{10}$ cm^{-2}.

3.1. Selective Etching of the Cap Layer and SQDs

Figure 1 shows the PVSE spectra evolution during step etching of the QDH surface. Selective etching of the GaAs cap layer is nonuniform and forms a hilly surface where the roughness height exceeds the QD height. However, when the etch front reaches the QD layer, the etching surface is smoothed for a short period and only clusters, i.e., QDs, emerge on the wetting InAs layer and above the surface [6]. The stress relaxation in the QD from the decrease in the effective thickness of the GaAs cap layer results in the red shift of the spectrum, i.e., in a decrease in E_0(QD). As the GaAs cap layer is completely etched off, E_0(QD) reaches its lowest point. If the etching is continued, E_0(QD) begins to increase because of the etching of the QDs themselves. For the structure with a combined QW/QD layer, the lowest E_0(QD) is close to the initial value for SQDs (curves *4*, *8*). However, such a low value is not usually attained in a structure with a single QD layer (curve *7*). We believe that this behavior is mainly caused by the etching of the tops of clusters (QDs in the latter case) that are not coated by the QW layer. At this stage, AFM reveals QDs, whose sizes and surface densities are close to the corresponding parameters for SQDs [6]. It is noteworthy that the largest nonuniformity in the energy distribution of QDs takes place at the etching stage immediately preceding the complete removal of the GaAs cap layer (curve *3*). Apparently, this observation is indicative of the inhomogeneity of the residual coating of individual QDs. Let us consider the spectrum evolution after attaining the lowest E_0(QD) by using the example of the etching of a SQD structure, which was studied in more detail.

Electrochemical modification of InAs/GaAs SQDs is of interest due to the feasibility of establishing a direct relation between their electronic properties and the morphology determined from the data of scanning probe microscopy. SQDs differ from QDs incorporated into the matrix in relation to fields of elastic stresses and potential well shapes and, hence, by energy spectra (Fig. 1, curve *8*).

During step etching of SQDs, their lateral size varied slightly, but their height decreased, which, as expected, caused a blue shift of the PVSE spectra (Fig. 1, curves *9–12*). This shift was accompanied by a decrease in photosensitivity in the SQD absorption region. Since no significant decrease in the QD surface density was observed at the initial stages of etching, the photosensitivity decrease seems to be associated with an increase in the recombination rate on the etched QD surface. As SQDs and QDs incorporated in the matrix are completely etched off, the photosensitivity of all the structures in the region of $h\nu < 1.4$ eV is controlled by surface states and takes on the form of curve *12* [7].

The arrows in curves *8–11* indicate the values of E_0(QD), determined from PL spectra at 77 K, taking into account the temperature shift. They are consistent with the photoelectric spectroscopy data. Histograms of the height distribution of SQDs at various etching stages were used to determine the average QD height h. The dependence of the transition energy E_0(QD) on h is shown in Fig. 2 (curve *1*). After SQD etching for 270 s, it is difficult to distinguish between QDs and other surface irregularities in AFM images of the etched surface or to construct the histogram of the height distribution of QDs. However, the PL peak from QDs is quite pronounced in the PVSE and especially in PL spectra. The lowest height of etched QDs is ~ 1.75 nm (curve *1*) and was determined by an extrapolation of the dependence $E_0(\text{QD}, h) = 1.04 - 0.06h$ obtained at large values of h, where the height h and E_0(QD) are given in nanometers and electronvolts.

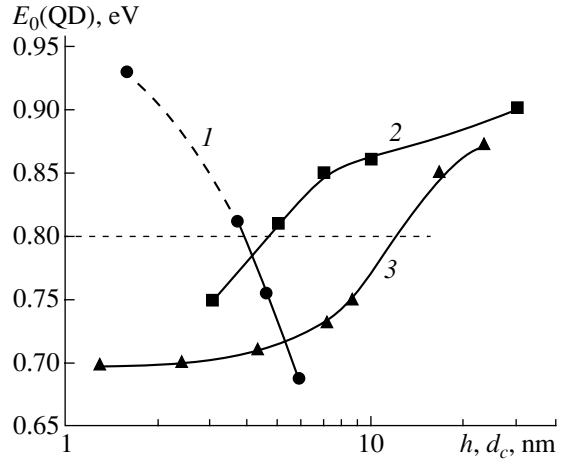

Fig. 2. The dependence of the energy E_0(QD) of the ground-state transition on (*1*) the QD height h and the cap GaAs layer thickness d_c in (*2*) unoxidized structures and (*3*) anodic-oxidized structures.

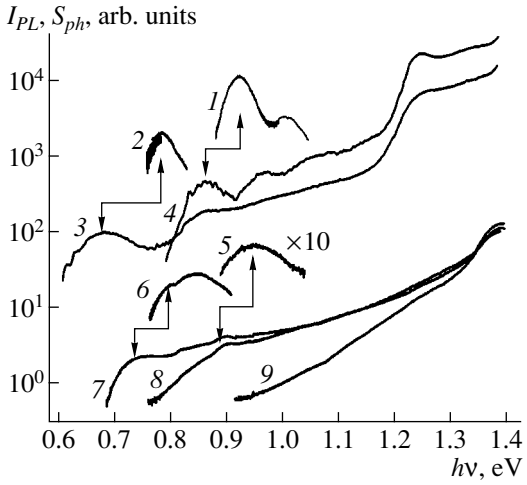

Fig. 3. The influence of the anodic oxidation of the QDH surface on the PL spectra at 77 K and on the PVSE spectra at 300 K for (*1–4*) the structure with a combined QW/QD layer (a cap GaAs layer is 7 nm) are, respectively, (*1*, *4*) the PL and PVSE spectra before oxidation and (*2*, *3*) the same after anodic oxidation at a voltage of 2 V. (*5–9*) The structure with SQDs: (*6*, *7*) the PL and PVSE spectra, respectively, before oxidation; (*5*, *8*) the same after anodic oxidation at a voltage of 0.5 V; and (*9*) the PVSE spectrum after anodic oxidation at a voltage of 1 V.

3.2. Anodic Oxidation of the GaAs cap layer and SQDs

A similar red shift of E_0(QD) is observed for the anodic oxidation of a thin cap layer. Figure 3 shows the effect of anodic oxidation on the PVSE and PL spectra of QDHs with a double cap layer at a GaAs layer thickness of 7 nm (curves *1–4*). The available data [8] on the dependence of the anodic oxide thickness on the anodic oxidation voltage (these data agree with the estimates under discussion) show that a fraction of the GaAs cap layer with a thickness of $\Delta d_c = 1.35V_a$ (nm) is expended to form an anodic oxide at the anodic oxidation voltage V_a (V). After anodic oxidation at a voltage of 2 V, the cap-layer thickness decreased, according to the calculation, from 7 to ~4 nm. In this case, the red shift in the PL and PVSE spectra was larger than 150 meV (curves *2*, *3*). The thin amorphous oxide layer does not induce additional stresses. In particular, this inference is confirmed by the fact that the oxide etching does not change E_0(QD). Therefore, oxidation, as well as etching, reduces the thickness of the epitaxial GaAs cap layer that induces stresses in QDs. After anodic oxidation at 5 V, which should result in complete oxidation of the cap layer and the QDs themselves, the photosensitivity in the QD and hybrid QW absorption region totally disappeared.

In the QDH with a partially oxidized double cap layer (curve *3*), even lower E_0(QD) than in the SQD structure grown under the same conditions was observed (curve *7*). Comparative measurements of the spectra of oxidized and unoxidized QDHs with various cap layer thicknesses showed the following: At a given thickness of the unoxidized fraction of the GaAs cap layer, a larger shift of E_0(QD) is attained than when overgrowing QDs with the same GaAs cap layer (Fig. 2, curves *2* and *3*). As can be seen in Fig. 2, the transition energy E_0(QD) = 0.8 eV, which corresponds to the transparency window of an optical fiber at a wavelength of 1.55 μm, is attained at a cap layer thickness of 5 nm in unoxidized structures (partial oxidation of the structures in air is disregarded) and 12 nm in oxidized structures. This result, which is of practical importance, suggests that there exists an additional factor in anodic oxidation, which reduces elastic stresses in QDs. We believe that this factor is the drain of Ga and As sublattice vacancies generated during the anodic oxidation of GaAs into the stressed clusters, i.e., QDs (see, e.g., [9, 10]). Elastically compressed InAs clusters form a potential well for such defects and should getter them.

Anodic oxidation of the SQD layer, as well as etching, gives rise to a blue shift of E_0(QD) (curves *5*, *8*). At an anodic oxidation voltage of 1 V, clusters, i.e., SQDs, are apparently completely oxidized, since the PL from SQDs disappears, and the PVSE spectrum takes on a form typical of the actual GaAs surface (curve *9*).

4. CONCLUSIONS

The above-considered results show that the modification of the thin cap layer of QDHs and QDs, which were grown on the structure surface by selective etching and anodic oxidation, is an efficient method for varying the QD energy spectrum in a reasonably wide range. This circumstance can be used to study the dependences of the electronic characteristics of QDs on elastic stresses, confining-barrier heights, and QD sizes. Of practical interest is the fact that the E_0(QD)

variation range, during modification, overlaps both optical-fiber transparency windows.

The relation between the energy spectrum of clusters, i.e., QDs, and their morphology was established by modification of the same QDs. The results also show that the AFM study of QDs buried under the cap layer using selective chemical etching [6] requires some consideration of the possible changes in the morphology of clusters, i.e., QDs, that are associated with their undercutting.

ACKNOWLEDGMENTS

This study was supported by the Russian Foundation for Basic Research (project no. 03-02-17178) and a joint program of the Ministry of Education of the Russian Federation and the CRDF US (BRHE Program REC-001).

REFERENCES

1. H. Saito, K. Nishi, and S. Sugou, Appl. Phys. Lett. **73**, 2742 (1998).
2. S. Fafard, Appl. Phys. Lett. **76**, 2707 (2000).
3. K. Nishi, H. Saito, S. Sugou, and J.-S. Lee, Appl. Phys. Lett. **74**, 1111 (1999).
4. I. A. Karpovich, B. N. Zvonkov, S. B. Levichev, *et al.*, Fiz. Tekh. Poluprovodn. (St. Petersburg) **38**, 448 (2004) [Semiconductors **38**, 431 (2004)].
5. B. N. Zvonkov, I. A. Karpovich, N. V. Baĭdus', *et al.*, Fiz. Tekh. Poluprovodn. (St. Petersburg) **35**, 92 (2001) [Semiconductors **35**, 93 (2001)].
6. I. A. Karpovich, N. V. Baidus, B. N. Zvonkov, *et al.*, Phys. Low-Dimens. Semicond. Struct., Nos. 3–4, 341 (2001).
7. I. A. Karpovich, A. P. Gorshkov, B. N. Zvonkov, *et al.*, Fiz. Tekh. Poluprovodn. (St. Petersburg) **35**, 564 (2001) [Semiconductors **35**, 543 (2001)].
8. É. V. Buts and L. N. Vozmilova, Élektron. Tekh., Ser. 2: Poluprovodn. Prib., No. 1, 100 (1976).
9. S. Hu, J. Appl. Phys. **45**, 1567 (1974).
10. A. F. Vyatkin, F. G. Ital'yantsev, I. V. Konetskiĭ, *et al.*, Poverkhnost, No. 11, 67 (1986).

Translated by A. Kazantsev

Semiconductors, Vol. 39, No. 1, 2005, pp. 4–7. Translated from Fizika i Tekhnika Poluprovodnikov, Vol. 39, No. 1, 2005, pp. 8–12.

ELECTRONIC AND OPTICAL PROPERTIES OF SEMICONDUCTORS

Properties of the GaSb:Mn Layers Deposited from Laser Plasma

Yu. A. Danilov*^, E. S. Demidov*, Yu. N. Drozdov, V. P. Lesnikov***, and V. V. Podol'skiĭ*****

**Nizhni Novgorod State University, pr. Gagarina 23, Nizhni Novgorod, 603950 Russia*

^e-mail: danilov@phys.unn.ru

***Institute for Physics of Microstructures, Russian Academy of Sciences, Nizhni Novgorod, 603950 Russia*

****Physicotechnical Research Institute at Lobachevsky State University, pr. Gagarina 23/3, Nizhni Novgorod, 603950 Russia*

Submitted June 1, 2004; accepted for publication June 16, 2004

Abstract—The X-ray diffraction and electrical and magnetic properties of GaSb:Mn layers deposited on GaAs (100) substrates from a laser plasma in free space are studied. It is shown that the films deposited at 200–440°C are epitaxial mosaic single crystals. Manganese-doped layers (up to ~4 at % Mn) had a hole concentration higher than 1×10^{19} cm^{-3}. Structures with the GaSb:Mn layers grown at 200°C had an anomalous Hall effect. A normal Hall effect was observed for the GaSb:Mn layers grown at 440°C. The exposure of these layers to a laser pulse (wavelength $\lambda = 0.68$ μm, duration 25 ns) caused an increase in the hole concentration and the emergence of the anomalous Hall effect at room temperature. Magnetic ultrahigh-frequency measurements confirmed that the films were ferromagnetic up to 293 K and revealed a magnetism anisotropy. © *2005 Pleiades Publishing, Inc.*

1. INTRODUCTION

Light-emitting structures and photodetectors based on GaSb (the GaSb band gap is 0.725 eV at 300 K) are promising IR-region devices. A number of the parameters of this semiconductor, specifically, the quite high electron and hole mobilities are favorable for extending the application range of GaSb [1]. The potential of GaSb is also promoted by current progress in the growth technology of heteroepitaxial GaSb-containing compositions, including the structures with quantum dots (QDs) and quantum wells (QWs). In addition, as far back as 1974, it was shown that the $Ga_{1-x}Mn_xSb$ alloys possess ferromagnetic properties at room temperature as well as semiconductor properties [2]. It was later found that the magnetic properties of $Ga_{1-x}Mn_xSb$ solid solutions depend on the chosen method of preparation. Thus, $Ga_{1-x}Mn_xSb$ bulk single crystals with x from 0.03 to 0.14 and grown by the Bridgman–Stockbarger method are ferromagnets with a Curie temperature (T_c) of approximately 540 K [3]. The properties of thin (~0.2 μm) $Ga_{1-x}Mn_xSb$ layers grown by molecular-beam epitaxy (MBE) on GaAs(100) substrates are primarily determined by the growth temperature T_g [4]. The layers grown at high T_g (~560°C) contained MnSb clusters. In this case, the magnetic field dependence of magnetization had the shape of a hysteresis loop when measured at room temperature and below. However, the Hall effect was normal, which indicated that ferromagnetic clusters did not affect the charge-carrier transport. The $Ga_{1-x}Mn_xSb$ layers ($x \le 0.04$) grown at $T_g \approx 250$°C had the anomalous Hall effect and negative magnetic resistance at low measurement temperatures. This fact was attributed to the presence of a second (GaMn)Sb ferromagnetic phase, in addition to MnSb, with $T_c \approx 25$ K [5]. It is generally accepted that the exchange interaction between the spins of the Mn atoms in the (III–Mn)–V solid solution is realized via free holes (the Rudermann–Kittel–Kasuya–Ioshida mechanism) [6].

In this study, we used laser plasma deposition (LPD) in free space to grow the Mn-doped GaSb layers. One of the advantages of this method compared with MBE is the relative simplicity of the equipment. The results from an examination of the properties of the LPD-grown $Ga_{1-x}Mn_xSb$ layers are given below.

2. EXPERIMENTAL

To deposit the GaSb films, we used a pulsed Q-switched YAG laser operating at a wavelength of 1.06 μm. We used a rotating combined target that consisted of a wafer of single-crystal undoped GaSb partially covered with high-purity metallic Mn. The trace of the laser evaporation of a material is circular; therefore, the ratio between the arc lengths of sputtered GaSb and Mn determined the doping level of the grown layer. The substrates were semi-insulating GaAs (100) wafers. The deposition temperature was varied in the range $T_g = 200$–440°C.

We carried out the X-ray diffraction study of the structures using a DRON-4 double-crystal diffractometer (Ge (400) monochromator, Cu$K_{\alpha 1}$ radiation). The electrical and magnetotransport characteristics were measured for structures with In contacts in the van der

Pauw geometry at 293 and 77 K. In order to study the magnetic properties of the GaSb:Mn layers, we used a 3-cm ESR spectrometer with a computer-controlled scan of the field of a fast-response magnet. This allowed us to attain a high sensitivity when recording the broad lines of the magnetic resonance. The absorption of microwave power was measured at 77 and 293 K at normal and parallel field orientations relative to the sample plane in magnetic fields as high as 0.45 T.

3. RESULTS AND DISCUSSION

Figure 1 shows the X-ray diffraction spectra of the θ/2θ scanning for the GaSb/GaAs structures obtained at a substrate temperature of 440°C. The spectra of the structure with an undoped GaSb layer (curve *1*) include peaks of the substrate at 2θ = 66.05° (the GaAs(400) reflection) and of the layer at 2θ = 60.740° (the GaSb(400) reflection). Using this value of 2θ, the calculation of the lattice parameter for undoped GaSb yields a_0 = 0.60959 nm, which coincides with the published data [1]. A rocking curve width served as the integrated characteristic of the layer's structural quality. This curve was measured using the angle of the crystal rotation at its full width at a half-maximum of the layer peak (FWHM) when the detector slit was widely opened [7]. The value of FWHM for the undoped GaSb layer is Δω = 0.40°. Consequently, the GaSb layer is a mosaic single-crystal that is epitaxially grown on the GaAs (100) substrate.

Figure 1 (curve *2*) shows the X-ray diffraction spectrum for the structure with an Mn-doped GaSb layer deposited at the same temperature of 440°C. The intensity of the GaSb(400) peak slightly decreased, and the peak itself shifted to somewhat larger angles compared with the undoped layer. It was previously noted that the $Ga_{1-x}Mn_xSb$ alloys in the composition range $0 \le x \le 0.14$ have a zinc-blende structure [3]. Using the formula [8] for the lattice parameter of $Ga_{1-x}Mn_xSb$ $a(x) = a_0 - 0.00528x$ and the average angle value 2θ = 60.765° for the Mn-doped layers grown at T_g = 350–440°C, we estimated the level of Mn doping as $x \approx 0.043$. In all the subsequent experiments in this study, we maintained this level of Mn doping.

As the growth temperature of the GaSb:Mn layer decreased, the value of FWHM increased steadily from 0.4° at T_g = 440°C to 0.45° at T_g = 350°C and to 0.5° at T_g = 300°C. The GaSb(400) peak, although less intense, was observed down to T_g = 200°C. This fact indicates that the quality of the epitaxial GaSb:Mn layer is rather high at deposition temperatures of 200–440°C.

The electrical properties of the structures depend heavily on the growth temperature of the GaSb films. Undoped GaSb layers grown at T_g = 440°C were of a *p*-type conductivity with the hole concentration ~2×10^{18} cm^{-3} and mobility of ~30–40 cm^2/(V s). A decrease in T_g down to 200°C caused an increase in the hole concentration of ~1.6×10^{19} cm^{-3} and a decrease in mobility. In both cases, the undoped GaSb layers had the normal Hall effect; i.e., the Hall resistance R_{xy} varied proportionally to the magnetic field *B* applied normally to the sample plane. Figure 2 (curve *1*) shows the dependence $R_{xy}(B)$ for the structure grown at T_g = 200°C. It is noteworthy that undoped GaSb grown by other methods usually exhibits *p*-type conductivity as well. It is generally believed that the acceptors responsible for such behavior may be antisite defects Ga_{Sb} [1]. The mentioned simultaneous increase in the hole concentration and the degree of structural disordering with a decrease in T_g can be offered as evidence of the defect origin of the *p*-type conductivity in undoped LPD-grown GaSb films.

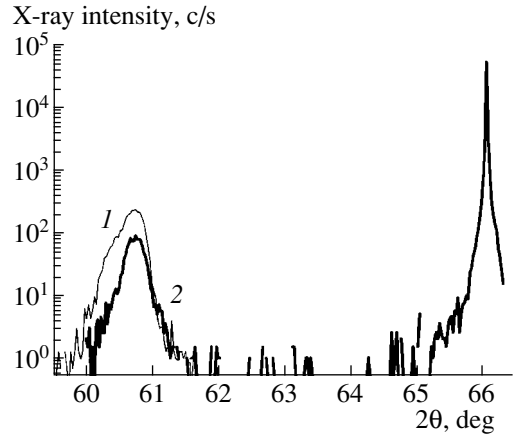

Fig. 1. X-ray diffraction spectra for the GaSb/GaAs structures grown at T_g = 440°C. (*1*) The undoped structure, and (*2*) the Mn-doped structure. Spectrum *1* is restricted to the vicinity of the GaSb(004) peak.

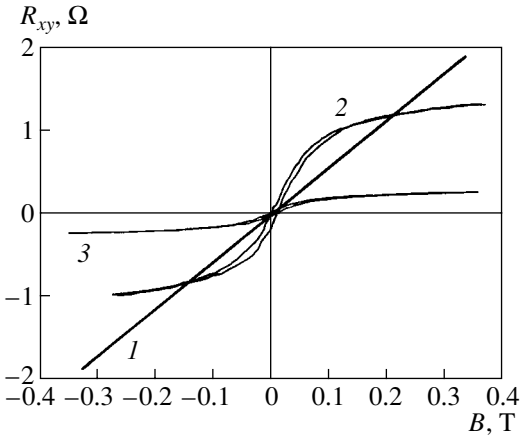

Fig. 2. Hall resistance at room temperature as a function of the applied magnetic field (*1*) for the undoped film and for the GaSb:Mn samples with x = 0.043 (*2*) prior to and (*3*) after laser annealing. The film deposition temperature T_g = 200°C.

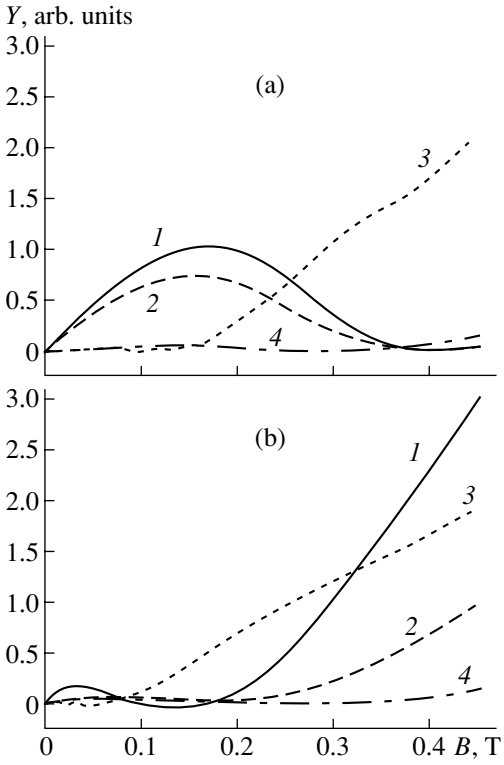

Fig. 3. Absorption Y of the microwave power in relation to the magnetic field for the structures with a GaSb:Mn layer (*1*, *2*) 70 nm thick and (*3*, *4*) 140 nm thick with the magnetic field oriented (*1*, *3*) normally and (*2*, *4*) parallel to the sample plane. The measurement temperature: (a) 293 K and (b) 77 K.

Doping of GaSb layers with Mn during growth at T_g = 200°C leads to the emergence of the anomalous Hall effect at room temperature (Fig. 2, curve *2*). The parameters of the layers in the case of the anomalous Hall effect were calculated by the method described in [9]. The hole concentration at 293 K for the GaSb:Mn layers (T_g = 200°C) was ~1.4×10^{20} cm^{-3}, which is almost an order of magnitude higher than the concentration in the undoped layer. The saturation magnetization M_s was estimated at 5.0×10^4 A/m. At a measurement temperature of 77 K, a broad hysteresis loop emerged in the $R_{xy}(B)$ dependence, and saturation was unattainable in the available range of values of magnetic induction (up to 0.4 T). Therefore, the carrier concentration in this case could not be calculated correctly. Laser annealing of the GaSb:Mn layers (T_g = 200°C) by a pulse with the wavelength λ = 0.68 μm, the pulse duration τ = 25 ns, and the power density $W = 5 \times 10^5$–10^6 W/cm^2 introduced no variations in the anomalous character of the Hall effect (Fig. 2, curve *3*). However, this annealing increased the hole concentration to 5.1×10^{20} cm^{-3}. The saturation magnetization remained unchanged after annealing (5.0×10^4 A/m). The coercive force was weak and equal to ~8.5 mT.

The structures with the GaSb:Mn layers grown at the higher temperature T_g = 440°C had the normal Hall effect both when measured at room temperature and at 77 K. The hole concentration was ~5×10^{19} and ~1.5×10^{19} cm^{-3} at the measurement temperatures 293 and 77 K, respectively. Annealing of the GaSb:Mn structures (T_g = 440°C) by a single laser pulse lead to the emergence of the anomalous Hall effect. As a result of this treatment, the hole concentration in the layers substantially increased, to values of higher than 5×10^{20} cm^{-3}.

The comparison between the electrical properties of undoped and Mn-doped GaSb layers indicates that the doping Mn atoms are acceptors. This fact is consistent with the calculation in [10], according to which the acceptor level "2+/3+" Mn at the Ga site in GaSb should be located 0.6 eV below the valence band top. In this case, the $3d^5$ Mn_s^{2+} (Ga^{3+}) ions in the state $^6S_{5/2}$ introduce the Kohn–Lattinger shallow hydrogen-like acceptor level near the valence band top of GaSb.

For a chosen level of Mn doping, the magnetic properties of the GaSb films, as well as their electrical properties, are governed by the growth temperature. For example, the films grown at T_g = 400°C have $M_s = 1.5 \times 10^5$ A/m and a coercive force of 49 mT; i.e., the films have a higher magnetic hardness than those grown at T_g = 200°C. This estimate was obtained from the curves of the anomalous Hall effect measured at 293 K. The given results indicate that ferromagnetism is observed in the studied GaSb:Mn layers; moreover, in this case, T_c > 293 K.

The measurements using an ESR spectrometer, which were carried out for the samples with the GaSb:Mn layers grown at 440°C, confirmed the ferromagnetism of the structures grown. At the measurement temperatures of 77 and 293 K, we found the strong absorption of microwave radiation characteristic of ferromagnetic resonance (Fig. 3). This absorption depends on the field, temperature, sample orientation, and layer thickness. Unfortunately, the range of the magnetic fields of the ESR spectrometer we used, which were no higher than 0.45 T, provided no way of recording the complete spectrum of the ferromagnetic resonance. We believe that a strong steady increase in the absorption of microwave power as the field increases (see Fig. 3) is caused by the left-hand wing of the ferromagnetic resonance spectrum. The anisotropy of the spectra in Fig. 3 is consistent with a classic formula that represents the effect of demagnetizing factors N on the ferromagnetic resonance frequency [11]:

$$\omega_0^2 = \gamma^2[B_0 + (N_y - N_z)\mu_0 M][B_0 + (N_x - N_z)\mu_0 M],$$

where γ is the magnetomechanical ratio; μ_0 is the magnetic permeability of free space; M is the magnetization; and the demagnetizing factors for the sample plane orientation normal to the field are equal to $N_x = N_y = 0$, $N_z = 1$, and equal to $N_x = N_z = 0$, $N_y = 1$ for the parallel orientation. As the layer thickness increases,

the role of the demagnetizing factor increases. The temperature shift is consistent with the natural broadening of the ferromagnetic resonance lines occurring as the temperature increases. These facts confirm the presence of ferromagnetism in the GaSb:Mn layer up to a measurement temperature of 293 K. A strong intrinsic magnetic field may indicate that the inclusions of the MnSb phase are formed at an average Mn content of ~4 at %. The MnSb phase is ferromagnetic up to $T_c = 587$ K [11]. However, the high crystalline quality of the layers also indicates that a $Ga_{1-x}Mn_xSb$ alloy is formed. According to the data [3], this alloy can be ferromagnetic when T_c is higher than room temperature at $x > 0.03$ and has the same crystal lattice as undoped GaSb.

Figure 3 shows bell-like broad resonance peaks (width $\Delta B \approx 0.22$ T) with effective *g*-factors equal to about two and four, which are characteristic of the normal ESR. These peaks indicate that the Mn distribution in the layers is spatially nonuniform. In this context, we may assume that, along with the $Ga_{1-x}Mn_xSb$ paramagnetic alloy that has small *x* values, two ferromagnetic phases with different T_c are present in the layers grown. These are the $Ga_{1-x}Mn_xSb$ alloy ($x > 0.3$) and the MnSb inclusions. The ESR spectra are attributed to a solid solution of Mn at Ga sites with the configuration $3d^5$ in the $^6S_{5/2}$ state in the spacings between inclusions. The presence of the line with the *g*-factor of ~2 (Fig. 3a, the shoulder in curve *3* at 0.3 T) is indicative of the existence of regions where the ferromagnetic phase makes almost no contribution to the magnetic field added to the external field. Broad ESR lines with the *g*-factor equal to about four (Fig. 3a, curves *1*, *2*, and *4* peaked at 0.17 T) are apparently related to a fraction of single Mn atoms near the ferromagnetic inclusions. Their magnetic field, when added to the external field, induces the low-field ESR shift. Figure 3a shows that ferromagnetic resonance manifests itself at room temperature up to 0.45 T only for a thicker layer, although ESR anisotropy can also be recognized for a structure with a thin layer.

Microwave absorption was studied only in the structures grown at $T_g = 440$°C. Therefore, the conclusion concerning the possible existence of an MnSb phase could not be applied to the films grown at low temperatures ($T_g = 200$°C). The anomalous Hall effect could not be associated with the existence of precipitates [12]. Therefore, it would be logical to assume that the GaSb:Mn films contain both the MnSb inclusions at higher growth temperatures and the $Ga_{1-x}Mn_xSb$ alloy that exhibits ferromagnetic properties at room temperature. The mechanism of ferromagnetism when $T_c >$ 293 K in the LPD-grown GaSb:Mn films is not still completely clear. However, the prospects for their practical application in spintronics devices are assured.

4. CONCLUSIONS

Thus, we showed that it is possible to grow GaSb:Mn epitaxial layers on semi-insulating GaAs substrates using laser plasma deposition. The electrical and magnetic properties of the films depend heavily on the deposition temperature. The GaSb:Mn layers have electrical the properties of a degenerate semiconductor and possess ferromagnetism with a Curie temperature above room temperature.

ACKNOWLEDGMENTS

This study was supported by a Program of the Russian Academy of Sciences “Spin-Dependent Effects in Solids and Spintronics” and by the Russian Foundation for Basic Research, project no. 03-02-16777.

REFERENCES

1. P. S. Dutta, H. L. Bhat, and V. Kumar, J. Appl. Phys. **81**, 5821 (1997).
2. M. I. Aliev, G. I. Safaraliev, A. N. Guliev, *et al.*, Izv. Akad. Nauk SSSR, Neorg. Mater. **10**, 1778 (1974).
3. T. Adhikari and S. Basu, J. Magn. Magn. Mater. **161**, 282 (1996).
4. F. Matsukura, E. Abe, Y. Ohno, and H. Ohno, Appl. Surf. Sci. **159–160**, 265 (2000).
5. F. Matsukura, E. Abe, and H. Ohno, J. Appl. Phys. **87**, 6442 (2000).
6. F. Matsukura, H. Ohno, A. Shen, and Y. Sugawara, Phys. Rev. B **57**, R2037 (1998).
7. D. K. Bowen and B. K. Tanner, *High Resolution X-ray Diffractometry and Topography* (Taylor and Francis, London, 1998; Nauka, St. Petersburg, 2002).
8. S. Basu and T. Adhikari, J. Alloys Compd. **205**, 81 (1994).
9. E. V. Kuchis, *Galvanomagnetic Effects and Methods of Their Studies* (Radio i Svyaz’, Moscow, 1990) [in Russian].
10. E. S. Demidov, Fiz. Tverd. Tela (St. Petersburg) **34**, 37 (1992) [Sov. Phys. Solid State **34**, 18 (1992)].
11. C. Kittel, *Introduction to Solid State Physics*, 5th ed. (Wiley, New York, 1976; Nauka, Moscow, 1978).
12. K. W. Edmonds, R. P. Campion, K.-Y. Wang, *et al.*, J. Appl. Phys. **93**, 6787 (2003).

Translated by N. Korovin

Semiconductors, Vol. 39, No. 1, 2005, pp. 41–43. Translated from Fizika i Tekhnika Poluprovodnikov, Vol. 39, No. 1, 2005, pp. 49–52.

LOW-DIMENSIONAL SYSTEMS

Intersubband Absorption of Light in Heterostructures with Double Tunnel-Coupled GaAs/AlGaAs Quantum Wells

L. E. Vorob'ev*^, V. Yu. Panevin*, N. K. Fedosov*, D. A. Firsov*, V. A. Shalygin*, V. V. Kapaev, S. Hanna***, S. Schmidt***, E. A. Zibik***, and A. Seilmeier*****

**St. Petersburg State Polytechnical University, St. Petersburg, 195251 Russia*

^e-mail: lvor@rphf.spbstu.ru

***Lebedev Physical Institute, Russian Academy of Sciences, Moscow, 117924 Russia*

****Institute of Physics, University of Bayreuth, 95440 Bayreuth, Germany*

Submitted June 1, 2004; accepted for publication June 14, 2004

Abstract—Intersubband absorption of mid-IR light was studied in heterostructures with asymmetrical tunnel-coupled quantum wells in equilibrium conditions and under high-power pumping by picosecond pulses of light. The energy spectrum of electrons in tunnel-coupled quantum wells was found from an analysis of equilibrium and nonequilibrium intersubband absorption spectra. The dynamics of intersubband absorption under high-power optical pumping was studied using the pump-and-probe picosecond technique. The experimental data are compared with the results of calculations based on solving rate equations. The intersubband relaxation times are determined. © *2005 Pleiades Publishing, Inc.*

1. INTRODUCTION

The development of mid-IR (λ = 5–20 μm) lasers is one of the actual problems in modern semiconductor optoelectronics. Mid-IR laser emission has found a variety of scientific and technological applications, such as the detection of chemical components and biological substances, environmental monitoring, molecular spectroscopy, noninvasive medical diagnostics, mineral exploration, etc. Along with the well-known cascade laser [1], the so-called fountain laser [2] emits light this spectral range. The latter operates on intersubband transitions in tunnel-coupled quantum wells (TCQWs) under intraband optical pumping.

However, the population inversion between the excited quantum confinement levels in TCQWs can also be obtained with the use of interband optical or injection current pumping, which is more convenient for industrial applications. The principle of formation of intersubband population inversion in QW structures, which is also applicable to TCQWs, has been discussed in [3]. Now we present the experimental data on optical properties of TCQWs related to intersubband electron transitions. The experiments were performed both under interband optical pumping and in equilibrium conditions at different temperatures.

2. SAMPLES

A structure containing 150 pairs of GaAs/$Al_xGa_{1-x}As$ TCQW was grown for study. QW pairs were separated by 20-nm-thick barriers, which were not transparent to tunneling. The Al content in the solid solution was x = 0.42 in barriers, x = 0 in the first QW, and x = 0.06 in the second. The structure was selectively doped in the central part of the wide barrier, and the surface density of electrons was $N_s = 3 \times 10^{11}$ cm^{-2}. According to calculations, four quantum confinement subbands were present in these TCQWs.

Figure 1 shows the potential profile found by self-consistent solution of the Poisson and Schrödinger equations, calculated electron wave functions, and optical transitions of electrons with the largest optical matrix element. The states with energies $E_{\Gamma 1}$ and $E_{\Gamma 4}$ are genetically related to the first, narrower, QW, whereas the states with energies $E_{\Gamma 2}$ and $E_{\Gamma 3}$ are induced by the second, wider QW. This results, in particular, in that the wave function of the ground state, $\Psi_{\Gamma 1}$, is localized mainly within the narrow well, whereas that of the first excited state, $\Psi_{\Gamma 2}$, is localized within the wide well (see Fig. 1). The values of optical matrix elements $|M_{ik}|^2 = \left|\int \Psi_k^* \hat{p}_z \Psi_i dz\right|^2$, which define the probability of optical transitions between levels i and k, differ strongly. The largest contribution to intersubband absorption is made by the transitions between the closest levels, genetically related to one and the same QW, whereas the transitions between the levels in neighboring wells are significantly weaker: $|M_{14}|^2 \gg |M_{24}|^2$ and $|M_{23}|^2 \gg |M_{13}|^2$.

3. RESULTS AND DISCUSSION

To determine the positions of energy levels in TCQWs, we studied equilibrium spectra of intersubband absorption at different temperatures (Fig. 2). The spectra comprise two distinct absorption bands. The spectral position of these bands allows us to attribute

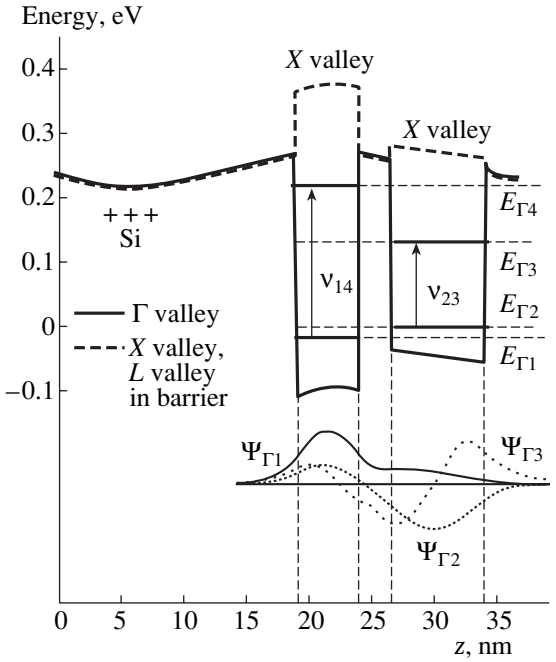

Fig. 1. Energy profile of GaAs/$Al_xGa_{1-x}As$ TCQW structure, electron wave functions, and optical transitions of electrons in a structure.

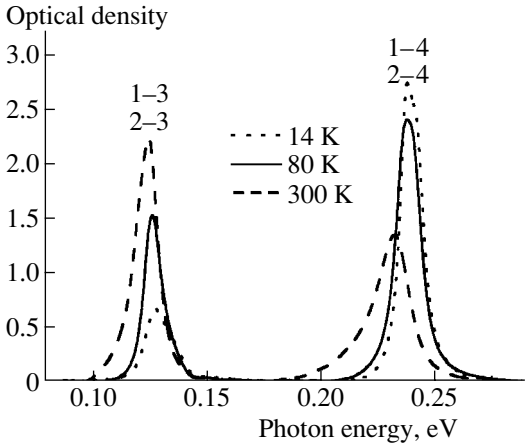

Fig. 2. Experimental equilibrium spectra of intraband absorption in a structure with TCQW.

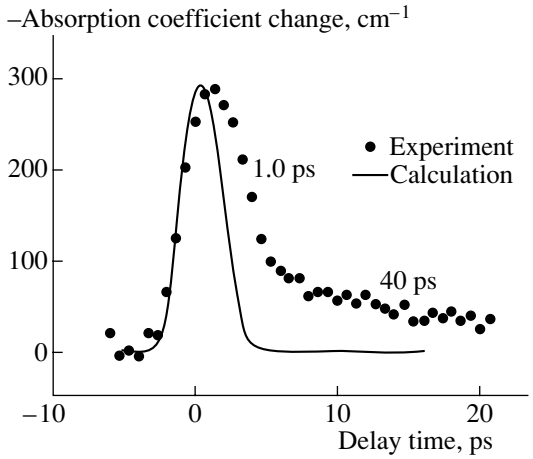

Fig. 3. Variation of the absorption in the long-wavelength band at equal frequencies of light in the pumping and probing pulses ($h\nu_{pump} = h\nu_{probe} = h\nu_{23} = 124$ meV) as function of the delay between the high-power pumping pulse (of about 1 μJ in energy) and the weak probing pulse. The width of pulses 3 ps. $T = 300$ K.

the long-wavelength band to 1–3 and 2–3 transitions in Γ valley, and the short-wavelength one to 1–4 and 2–4 transitions in the same valley, with the peaks related to transitions from levels 1 and 2 merged in each band. This is why the equilibrium absorption spectra do not allow us to determine the energy spacing between levels 1 and 2.

The temperature dependence of the equilibrium intersubband absorption is explained by the redistribution of electrons between the ground ($E_{Γ1}$) and first excited ($E_{Γ2}$) states in a TCQW: as temperature increases, the $E_{Γ2}$ level is filled and the electron density on $E_{Γ1}$ level decreases. The result is that the long-wavelength absorption band, in which transitions 2–3 dominate, is enhanced and, simultaneously, the short-wavelength band, in which transitions 1–4 dominate, fades. The calculated dependences of the absorption coefficients for three temperatures nearly coincide with the experimental spectra.

The energy spacing $E_{Γ2} - E_{Γ1} = h\nu_{12}$ was determined from the investigation of the absorption spectra under high-power intersubband pumping with a photon energy of $h\nu_{pump} = h\nu_{23}$, which ensured the occupation of level 3. This approach allowed us to determine the spectral dependence of absorption associated with transitions 3–4. The experiment was performed in a pulsed mode, the width of the pumping pulse of light was ~2 ps, and the probing pulse ($h\nu_{probe} \approx h\nu_{34}$) was delayed by 1.5 ps in respect to the pumping pulse. The analysis of the spectra obtained yielded an energy spacing of $E_{Γ4} - E_{Γ3} = h\nu_{34}$; this allows an unambiguous determination of the energy spacing between $E_{Γ2}$ and $E_{Γ1}$ levels: $h\nu_{12} = h\nu_{14} - h\nu_{23} - h\nu_{34}$; the obtained value is ~11 meV.

The pump-and-probe picosecond technique was used in studying the dynamics of variation of intersubband absorption under high-power intersubband optical pumping. Different combinations of frequencies of the pumping and probing light were chosen in accordance with the spacing between the subbands. Figure 3 shows the experimental data obtained with equal frequencies of pumping and probing light: $\nu_{pump} = \nu_{probe} = \nu_{23}$. This experiment demonstrates a biexponential character of the absorption evolution with time.

The dynamics of intersubband absorption was calculated based on the system of rate equations, taking into account intersubband electron transitions involv-

ing optical phonons and impurities. Also, the shape of pumping and probing pulses was taken into account. This method allowed us to estimate the intersubband relaxation times, which is necessary for the elucidation of the conditions for the population inversion to be obtained in TCQW. The calculated data are shown in Fig. 3. It is necessary to stress that the model used describes only fast processes associated with intersubband transitions involving LO phonons. A long-term process is possibly associated with electron transitions from the levels related to deep impurities (which are localized within the barrier in the vicinity of the QW interface) to states in the TCQW subbands.

Figure 4 shows how the absorption coefficient for transitions 1–4 varies with the delay time (the frequency of the pumping light pulse was $\nu_{pump} = \nu_{14}$, the probing was done at the same frequency, $\nu_{probe} = \nu_{14}$). The short-term relaxation processes are mainly associated with electron transitions involving optical phonons from subband 4 to 1, with subsequent trapping into Γ subbands. The long-term processes can be attributed to transitions of nonequilibrium electrons from *X* and *L* valleys in the barrier to Γ subbands in QWs. As temperature increases, this process speeds up (the characteristic time decreases from 60 ps at $T = 80$ K to 20 ps at $T = 300$ K), which can be attributed to thermal emission of electrons from *X* and *L* valleys.

Experimentally obtained fast relaxation times for the absorption of light in the long-wavelength (ν_{23}) and short-wavelength (ν_{14}) bands at 300 K were $\tau_{32} = 1$ ps and $\tau_{41} = 1.3$ ps. These times must exceed the times of intersubband electron transitions 3–2 and 4–1.

The calculated times of intersubband electron scattering 3–2 and 4–1, involving optical phonons and impurities, are 0.65 and 1.4 ps, respectively, at room temperature. (According to calculations, the other recombination channels, e.g., 4–3–1, 4–3–2–1, are slower). Owing to the nonparabolicity of the energy spectrum, the main contribution to absorption at these frequencies is made by electrons near the bottom of subbands 2 and 1. Therefore, the relaxation time of absorption is longer than the intersubband scattering time, by approximately the emission time of a cascade of the appropriate number of optical phonons. The emission time for a single phonon in intrasubband scattering of an electron is ~0.1 ps. Finally, we obtain the relaxation time of absorption, $\tau_{32} = 0.95$ ps, for optical transitions between subbands 3 and 2, and $\tau_{41} = 2$ ps for transitions between subbands 4 and 1, which is close to the experimental data presented above.

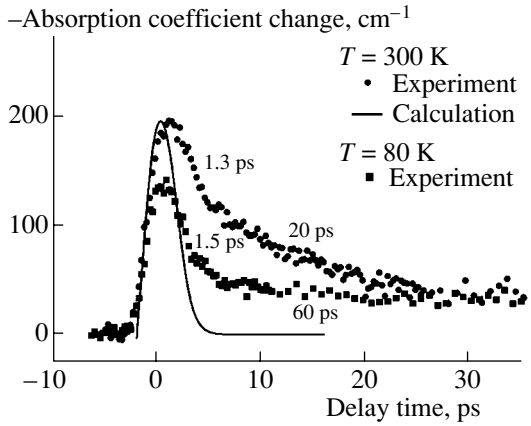

Fig. 4. Variation of the absorption in the short-wavelength band at equal frequencies of light in the pumping and probing pulses ($h\nu_{pump} = h\nu_{probe} = h\nu_{14}$; $h\nu_{14} = 232$ meV at $T = 300$ K, and $h\nu_{14} = 237$ meV at $T = 80$ K) as function of the delay between the high-power pumping pulse (~1 μJ) and the weak probing pulse. The width of pulses 3 ps.

4. CONCLUSIONS

Optical phenomena related to intersubband electron transitions in tunnel-coupled QWs have been studied. The variation of the intersubband absorption as a function of time is of biexponential character. The nature of short- and long-term components of the relaxation curves is explained.

ACKNOWLEDGMENTS

The study was supported by INTAS, Deutsche Forschungsgemeinschaft (German Research Foundation), the International Science and Technology Center, the Russian Foundation for Basic Research, and the Ministry of Education and Science of the Russian Federation.

REFERENCES

1. J. Faist, F. Capasso, D. L. Sivco, *et al.*, Science **264**, 553 (1994).
2. O. Gauthier-Lafaye, P. Boucaud, F. H. Julien, *et al.*, Appl. Phys. Lett. **71**, 3619 (1997).
3. A. Kastalsky, L. E. Vorobjev, D. A. Firsov, *et al.*, IEEE J. Quantum Electron. **37**, 1356 (2001).

Translated by D. Mashovets

Semiconductors, Vol. 39, No. 1, 2005, pp. 44–49. Translated from Fizika i Tekhnika Poluprovodnikov, Vol. 39, No. 1, 2005, pp. 53–58.

LOW-DIMENSIONAL SYSTEMS

Current Oscillations under Lateral Transport in GaAs/InGaAs Quantum Well Heterostructures

A. V. Antonov*, V. I. Gavrilenko*, E. V. Demidov*^, B. N. Zvonkov, and E. A. Uskova****

**Institute for Physics of Microstructures, Russian Academy of Sciences, Nizhni Novgorod, 603950 Russia*

^e-mail: demidov@ipm.sci-nnov.ru

***Physicotechnical Institute, Lobachevsky State University, pr. Gagarina 23/5, Nizhni Novgorod, 603950 Russia*

Submitted June 1, 2004; accepted for publication June 14, 2004

Abstract—The current–voltage (*I–V*) characteristics were measured and the current-pulse oscilloscope patterns were obtained for multilayer *n*-InGaAs/GaAs quantum-well heterostructures and *n*-GaAs epitaxial layers with various doping levels. It is shown that the *I–V* characteristics flatten at low doping levels in fields of 300–400 V/cm. In more heavily doped samples, current oscillations are initiated with a period corresponding to a drift velocity of $(3–3.5) \times 10^5$ cm/s at **E** ∥ [110] and are approximately larger at **E** ∥ [100] by a factor of 1.5. The results obtained are attributed to the formation of, respectively, stationary and moving acoustoelectric domains in the structures. In fields above 1.5 kV/cm, high-frequency Gunn oscillations corresponding to a drift velocity of 1.5×10^7 cm/s were observed. © *2005 Pleiades Publishing, Inc.*

1. INTRODUCTION

The phenomenon of spatial transport of carriers in semiconductor heterostructures with selectively doped barriers (in particular, δ-doped) in a strong lateral (i.e., directed in the well plane) electric field was actively studied in the 1980s (see, e.g., review [1]). Due to heating of carriers by the electric field, they can be carried away from quantum wells into doped barrier layers. As a result, the carrier mobility decreases due to the onset of the mechanism of scattering at ionized impurities, which can cause a decrease in the current, i.e., the formation of *N*-type negative differential conductivity (NDC), as is the case in the Gunn effect in GaAs-type semiconductors (see, e.g., [2]). The *N*-type NDC formation can give rise to electronic instability, in particular, the formation of stationary or mobile domains of strong field. The spatial transport of hot carriers from quantum wells (QWs), where their mobility and effective temperature are rather high, into higher-lying energy states with low mobility, where the effective temperature decreases, can cause population inversion [3–8].

This paper is devoted to the experimental study of electric transport of hot carriers in *n*-InGaAs/GaAs QW heterostructures in strong lateral electric fields. Previously [9–11], flattening of the current-voltage (*I–V*) characteristics and the initiation of current oscillations was observed in such structures at liquid-helium and liquid-nitrogen temperatures in fields of 300–1000 V/cm. This behavior was related to spatial transport of hot carriers and the *N*-NDC arising under these conditions. In this study, we compared the *I–V* characteristics and current-pulse oscilloscope patterns measured in *n*-InGaAs/GaAs QW heterostructures and *n*-GaAs epitaxial films with the published data on GaAs/AlGaAs heterostructures. Based on this comparison, we concluded that the observed oscillations are associated with the development of acoustoelectronic instability in the samples.

Since GaAs is a piezoelectric, a strain caused by a transverse acoustic wave propagating in the [110] direction induces a macroscopic electric field. This results in the intense interaction of electrons moving in the same direction with lattice vibrations. Therefore, as the electron velocity exceeds the propagation velocity of the acoustic wave, electrons begin to actively emit phonons (an analogue of Cherenkov radiation) [12–14].

As an electric field stronger than a certain critical value is turned on along the [110] direction, acoustic waves propagating from the cathode to the anode are amplified in the crystal. As a result, the flux envelope exponentially increases to the anode. Since the acoustic wave causes acoustoelectric current directed opposite to the drift motion of electrons, the voltage drop in the near-anode region increases to retain the total current, and the field decreases in other sample regions. In turn, as the electric field strengthens, the acoustic wave gain increases significantly in this region. Such positive feedback causes the formation of a stationary near-anode electroacoustic domain with strong acoustic and electric fields [12–14], as well as flattening of *I–V* characteristics in strong fields. The pattern of acoustic instability development radically changes under conditions of significant amplification (more than 100 dB/cm). In this mode, the acoustic streaming very rapidly reaches a level of nonlinearity, which results in the formation of a mobile acoustoelectric domain. The latter represents a short (~100 μm) packet of acoustic oscillations moving over the sample with a velocity close to the velocity of sound. If the field was applied in other directions,

Parameters of the studied n-In_xGa_{1-x}/GaAs samples with single and double quantum wells and n-GaAs epitaxial layers (the concentration values correspond to room temperature)

Structure index	x	d_{1QW}, Å	d_{2QW}, Å	Number of periods	Structure thickness, μm	n_s, 10^{11} cm^{-2} (per period)	N_s, 10^{12} cm^{-2} (total)
2987	0.08	200	100	20	2.3	1.1	2.2
3490	0.08	200	100	20	2.3	3.0	6.0
3517	0.08	200	–	20	2.5	3.9	7.8
3518	–	–	–	–	2.5	–	7.0
3628	–	–	–	–	2.4	–	48
3629	–	–	–	–	2.4	–	18.5
3630	–	–	–	–	2.4	–	7.0
3631	–	–	–	–	2.4	–	3.4
3732	0.1	200	–	20	2.5	0.3	0.6
3734	0.1	200	–	20	2.5	2.4	4.8
3735	0.1	200	100	20	2.6	2.0	4.0
4079	0.06	200	–	20	2.6	1.4	2.9
4081	0.06	200	100	20	2.6	2.5	4.9

oblique waves propagating at an angle to the field direction were amplified. Oscillations caused by acoustoelectric domains in GaAs/AlGaAs QW heterostructures were studied in detail in [15]. As the field (applied in the [110] direction) exceeds a critical value, strong current oscillations were observed. The electron drift velocity at the threshold field was 10^6–10^7 cm/s. In layers with nondegenerate carriers, damping oscillations with a frequency corresponding to the drift velocity $\sim 3.5 \times 10^5$ cm/s were observed; this velocity is identical to that of acoustic phonons. Oscillations were most pronounced at liquid-nitrogen temperature. As the temperature increased, the oscillation amplitude decreased and ultimately disappeared at $T = 200$ K. In layers with high electron density, current oscillations were not damped, and their frequency was significantly higher.

2. EXPERIMENTAL

The electric transport of hot carriers was studied in pulsed electric fields. The pulse duration τ of the electric voltage up to 1000 V applied to samples was several microseconds. To prevent the sample from overheating, a low pulse repetition frequency (30–10 Hz) was used. The leading-edge duration of the high-voltage pulse did not exceed 30 ns. The voltage-pulse amplitude could be slowly (for a few minutes) varied from zero to the highest value. The pulse shape and amplitude of the voltage and current through the sample were monitored by observing the signal on the screen of a Tektronix TDS3034B digital oscilloscope with a passband of 350 MHz, used also to store signals in a computer's memory. The measurements were carried out at both room and low temperatures ($T = 77$ and 4.2 K). In the latter cases, a sample holder was mounted in transportable Dewar flasks with liquid nitrogen or helium, respectively.

The samples under study were grown using gas-transport epitaxy on semi-insulating GaAs (001) substrates. The sample parameters are listed in the table. Multilayer n-$In_xGa_{1-x}As$/GaAs heterostructures with single and double QWs were studied, as well as thin n-GaAs epitaxial layers. The heterostructures contained 20 pairs of QWs 200 and 100 Å wide, separated by a GaAs barrier 50 Å thick (or 20 separate QWs 200 Å wide) spaced by 800–900 Å. Narrow wells in samples 2987, 4079, and 4081 were δ-doped with silicon; all the other samples were homogeneously doped. The room-temperature electron mobility depended on the doping level only slightly and was ~4500 cm^2/(V s). Rectangular samples 5×5 mm in size were cut from the structure. Strip ohmic contacts were deposited and fired in on the sample surface, spaced ~3 mm apart.

3. RESULTS AND DISCUSSION

Typical oscilloscope patterns of current pulses in heterostructures with single and double QWs are shown in Figs. 1 and 2. Beginning with a certain threshold value of the applied voltage ($U/l \approx 300$ V/cm), oscillations arise on the current pulse. The initiation of current instability was observed at $T = 4$ and 77 K; however, oscillations did not arise at room temperature. As the spacing between the contacts was decreased threefold (to $l = 1$ mm), the oscillation frequency increased approximately three times. At the same time, the oscillation frequency and the current oscilloscope pattern remained almost unchanged as the sample width decreased. This observation suggests that the oscillation frequency is independent of the sample resistivity (hence, it is related to the sample length, rather than to the external electric circuit). The structures with double QWs and selective doping (2987 and 4081) were

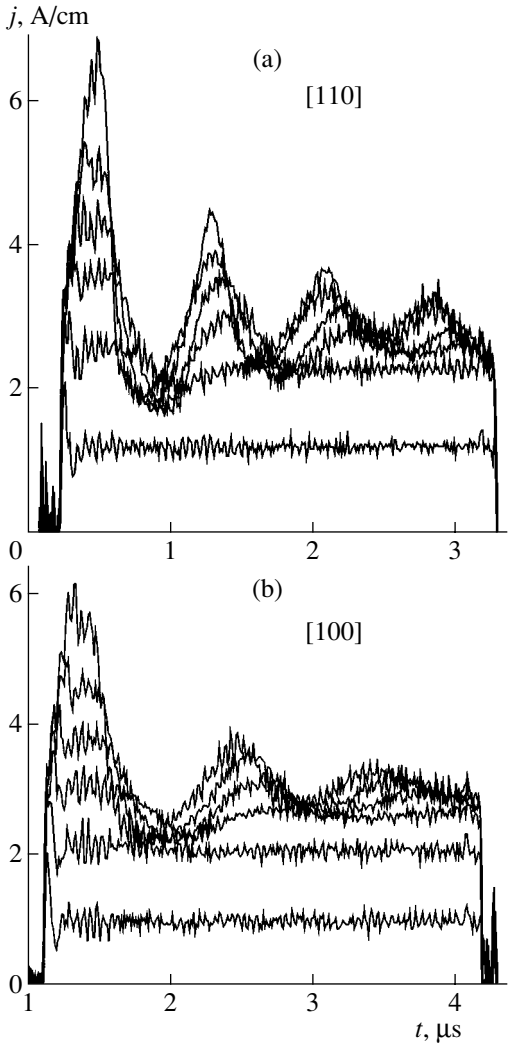

Fig. 1. Current-pulse oscilloscope patterns for sample 3734, measured at (a) **E** || [110] and (b) **E** || [100]; T = 4.2 K, l = 3 mm.

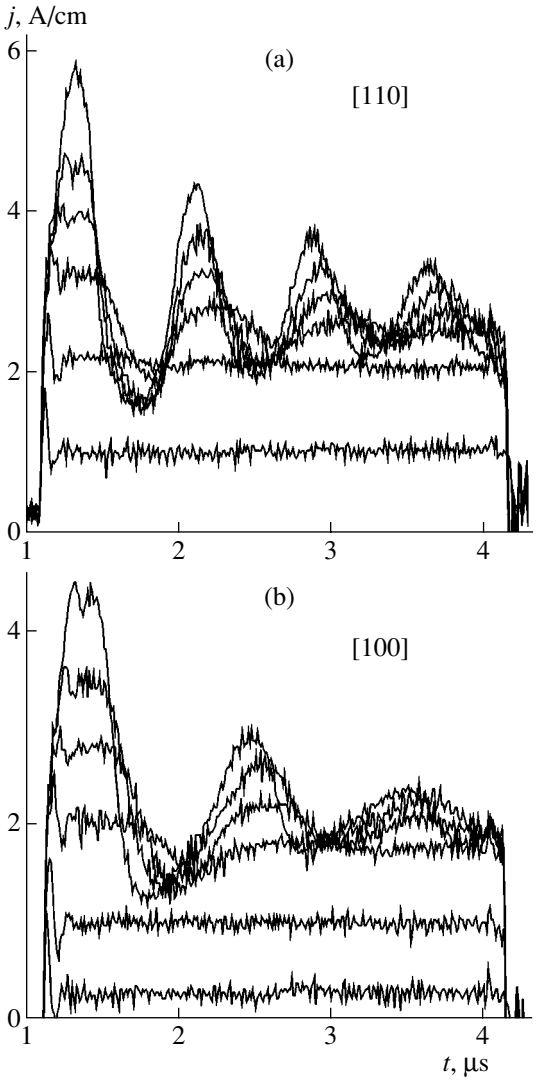

Fig. 2. The same as in Fig.1, but for sample 3735.

"designed" with the purpose to study spatial transport of carriers in strong lateral electric fields. In such heterostructures, the lower level in the narrow (δ-doped) QW is higher by approximately 10 meV than in the wide well, while the Fermi energy is several millielectronvolts.

Thus, most carriers are concentrated in wide wells at low temperatures. As carriers are heated in the electric field, the spatial transport from a wider QW to the higher-lying level in a narrow well (due to scattering at optical phonons) should cause a decrease in the mobility (due to strong impurity scattering in narrow doped QWs) and electron thermalization in narrow wells. A reverse transition appears to be complicated; as a result, the current can decrease and electric instability can develop, which qualitatively agrees with the observed pattern.

Further studies showed that current oscillations are also observed in uniformly doped samples with double QWs (3490, 3735). It was assumed that instabilities under conditions of the spatial transport from wide QWs into narrow QWs are caused by scattering at interface roughness, which should play a larger role in narrower QWs. It is reasonable to assume that the oscillation period is controlled by the time of passage of the domain of the strong electric field through the sample, as in the ordinary Gunn effect, where the domain velocity is equal to the carrier drift velocity. A similar result was also obtained for domain instability in selectively doped GaAs/AlGaAs heterostructures under conditions of spatial transport [1]. In the case under consideration, a drift velocity of about 3×10^6 cm/s corresponds to the instant of instability onset. At the same time, the domain velocity can readily be estimated from the oscillation period, which is approximately 1 μs for a sample 3 mm long. This velocity is as low as 3 ×

10^5 cm/s, i.e., ten times lower than the carrier drift velocity. A similar disagreement also took place for current oscillations observed in *p*-InGaAs/GaAs heterostructures [16], which was inconsistent with the proposed ODP mechanism associated with spatial transport.

In order to gain insight into the conditions of the initiation of the observed current instability, the reference samples that contained separate QWs and uniformly doped *n*-GaAs films (see table) were grown and studied. The *I–V* characteristics and current-pulse oscilloscope patterns of samples with double and single QWs are similar to each other (cf. Figs. 1 and 2). The threshold values of the applied electric field, the current densities corresponding to oscillation onset, and the oscillation periods agree with good accuracy. Thus, the measurements carried out showed that double QWs in the heterostructure has almost no effect on the observed current instability; hence, this instability is not related to spatial transport from wide QWs into narrow QWs. It is noteworthy that current oscillations in multilayer $In_{0.16}Ga_{0.84}As/GaAs$ heterostructures with individual deeper QWs were previously observed in [17].

Sample 3518 is a uniformly doped *n*-GaAs film 2.5 μm thick, which corresponds to the thickness of heterostructures 3490 and 3518 with total carrier concentrations close to that in sample 3490 (see table). In this sample, the current-oscillation dynamics was appreciably different from that in heterostructures. The threshold value of the applied electric field somewhat increased to ≈450 V/cm in comparison with 300 V/cm; however, the threshold current density (hence, the drift velocity) decreased to 1.5 A/cm in comparison with 3–4 A/cm. The oscillation shape significantly changed as well. Instead of weakly damping sinusoidal or spiky oscillations, sample 3518 exhibited a significant "spike" at the leading edge of the current pulse followed by fast-damping oscillations, which is characteristic of the establishment of stationary domain conditions in the ordinary Gunn effect. It follows from the oscilloscope patterns that a pronounced current saturation takes place in strong electric fields, which is also characteristic of static domain conditions. At the same time, the oscillation period remained almost the same as in heterostructures. Since there is no spatial transport in a rather thick epitaxial film, it is clear that current oscillations observed have a radically different origin.

These studies were complemented with electric-transport measurements in a series of epitaxial *n*-GaAs films with various doping levels (sequentially grown samples 3628–3631). As the carrier concentration increased, the static domain conditions in "lightly doped" samples 3631 and 3630 were replaced by conditions of weakly damping oscillations in samples 3629 and 3628.

Apparently, the observed current instabilities can be attributed to the formation of acoustoelectric domains in the samples under study in strong electric fields. As mentioned above, GaAs is a piezoelectric material; hence, the intense interaction of electrons with acoustic phonons takes place. An oscillation period of 1 μs in the samples under study corresponds to a transport velocity of 3.6×10^5 cm/s, which is close to the velocity of propagation of transverse acoustic phonons in the [110] direction. The efficient interaction of electrons with an acoustic wave can take place if this wave induces a longitudinal electric field, i.e., a field directed along the wave propagation. There are only two waves of this type in GaAs and other semiconductors with identical crystal structures: a transverse wave polarized along the [001] crystallographic direction and propagating in the [110] direction and a longitudinal acoustic wave propagating in the [111] direction [17]. In GaAs, the propagation velocity of the above-mentioned TA and LA waves is 3.35×10^5 and 5.4×10^5 cm/s, respectively [18]. In most cases, the TA wave is excited, which interacts more actively with carriers due to a lower velocity. In [15], the initiation of current instabilities in GaAs/AlGaAs heterostructures was observed when the carrier drift velocity was 10^6–10^7 cm/s, i.e., it exceeded by almost ten times the TA wave velocity in the case under consideration.

Thus, by analogy with current instabilities observed in [15], it is reasonable to associate current oscillations we observed in *n*-InGaAs/GaAs QW heterostructures and *n*-GaAs epitaxial films with acoustoelectronic instability. In all the above-described samples, the electric field was applied exactly in the [110] direction, along which GaAs can be easily cleaved, which necessarily prescribed the configuration of samples and strip contacts. To verify the hypotheses of "acoustoelectronic origin" of oscillations, rectangular samples were cleaved in the [110] and [100] directions from heterostructures with single (3732, 3734) and double (3735) QWs (see table). In sample 3732 with a low doping level ($n_s = 3 \times 10^{10}$ cm^{-2} per QW), oscillations were almost not observed. At liquid-helium and liquid-nitrogen temperatures, pronounced flattening in the *I–V* characteristic was observed in this sample, which can be attributed to the formation of a stationary near-anode acoustoelectric domain. As can be seen from Figs. 1 and 2, current oscillations with a period of about 1 μs, corresponding to a transport velocity of 3.5×10^5 cm/s close to the TA wave propagation velocity, were observed in heavier doped heterostructures 3734 and 3735 as the electric field was applied in the [110] direction. However, in the samples cleaved from the same structures in the [100] direction, the oscillation period increased approximately by a factor of 1.5. It is reasonable to explain this increase by the fact that acoustic waves propagating in the [110] direction at an angle of 45° to the electron drift direction are still excited in the crystal at $\mathbf{E} \parallel [100]$, which decelerates the domain velocity by a factor of $\sqrt{2}$ [19, 20].

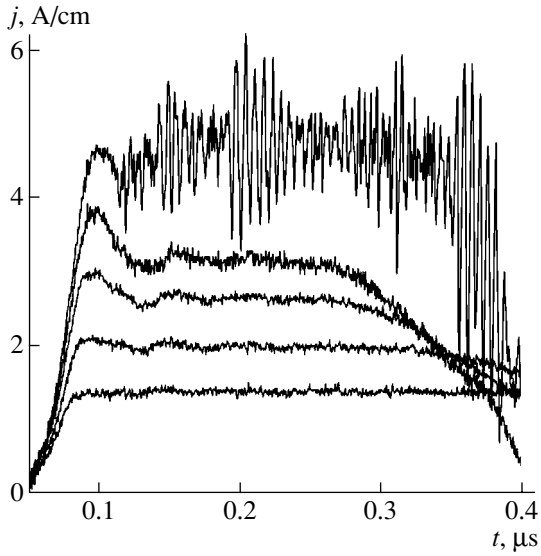

Fig. 3. High- and low-frequency current oscillations measured in sample 4081 at $T = 4.2$ K and $l = 1$ mm.

Apparently, the strong electric field induced in acoustoelectric domains gives rise to surface breakdown of the samples, which does not allow application of a field of several kilovolts per centimeter, which is necessary to implement various mechanisms for generating the inverse distributions of carriers. To diminish the probability of breakdown, we used shorter samples with contacts spaced at 1 mm; the measurements were carried out with shorter pulses with a duration of several tenths of a microsecond. In sample 4081 at $T = 4.2$ K, we observed for the first time current oscillations of two types [21]: low-frequency oscillations associated with the formation of acoustoelectric domains moving in the structure were initiated as usual in fields of about 300 V/cm; in fields of 1.5 kV/cm, high-frequency (~150 MHz) Gunn-type oscillations arose and corresponded to an electron transport velocity of 1.5×10^7 cm/s (Fig. 3). High-frequency oscillations were "modulated" by acoustoelectric oscillations. Simultaneously with the initiation of high-frequency oscillations, intense long-wavelength IR radiation was detected in the structures. At room temperature, acoustoelectric oscillations were not initiated, and only high-frequency oscillations were observed. In sample 4079 with a lower level of doping, mobile acoustoelectric domains were not formed and high-frequency oscillations were observed in strong fields. Rather low values of the applied electric voltage (~1.5 kV/cm at $T = 4.2$ K), at which Gunn oscillations were initiated, can be explained by a nonuniform field distribution in the sample in the presence of a mobile or stationary acoustoelectric domain.

4. CONCLUSIONS

Thus, *I–V* characteristics and current pulse oscilloscope patterns of multilayer *n*-InGaAs/GaAs quantum well heterostructures and *n*-GaAs epitaxial films with various doping levels were measured. It was shown that the *I–V* characteristics flatten at low doping levels ($N_s \approx 6 \times 10^{11}$ cm^{-2} for heterostructures and $N_s \approx 3 \times 10^{12}$ cm^{-2} for GaAs films) at $T = 4.2$ and 77 K in the fields of 300–400 V/cm. In more heavily doped samples under the same conditions, current oscillations are initiated with a period that corresponds to the transport velocity of $(3–3.5) \times 10^5$ cm/s at $\mathbf{E} \parallel [110]$ and a period by a factor of ~1.5 longer at $\mathbf{E} \parallel [100]$. The results obtained are explained by the formation of, respectively, stationary and mobile acoustoelectric domains due to the fact that TA waves propagating along the [110] crystallographic direction are excited by hot electrons. At applied voltages above 1.5 kV/cm, high-frequency oscillations corresponding to an electron transport velocity of 1.5×10^7 cm/s develop in the structures, which is related to the formation of the Gunn domains.

ACKNOWLEDGMENTS

This study was supported by the Russian Foundation for Basic Research (project no. 02-02-16763), the International Science and Technology Center (project no. 2293), the Ministry of Industry, Science, and Technologies of the Russian Federation, and the Federal program Integration.

REFERENCES

1. Z. S. Gribnikov, K. Hess, and G. A. Kozinovsky, J. Appl. Phys. **77**, 1337 (1995).
2. M. Shur, *GaAs Devices and Circuits* (Plenum, New York, 1987; Mir, Moscow, 1991).
3. V. Ya. Aleshkin, A. A. Andronov, A. V. Antonov, *et al.*, Phys. Status Solidi B **204**, 563 (1997).
4. V. Ya. Aleshkin, A. A. Andronov, A. V. Antonov, *et al.*, Physica B (Amsterdam) **249–251**, 971 (1998).
5. V. Ya. Aleshkin, A. A. Andronov, A. V. Antonov, *et al.*, Inst. Phys. Conf. Ser., No. 162, 105 (1999).
6. V. Ya. Aleshkin and A. A. Andronov, Pis'ma Zh. Éksp. Teor. Fiz. **68**, 73 (1998) [JETP Lett. **68**, 78 (1998)].
7. V. Ya. Aleshkin, A. A. Andronov, and A. A. Dubinov, Fiz. Tekh. Poluprovodn. (St. Petersburg) **37**, 224 (2003) [Semiconductors **37**, 215 (2003)].
8. V. Ya. Aleshkin and A. A. Dubinov, Fiz. Tekh. Poluprovodn. (St. Petersburg) **36**, 724 (2002) [Semiconductors **36**, 685 (2002)].
9. V. Ya. Aleshkin, A. A. Andronov, A. V. Antonov, *et al.*, Proc. SPIE **4418**, 192 (2001).
10. R. Kh. Zhukavin, S. G. Pavlov, V. N. Shastin, *et al.*, in *Proceedings of the Conference on Nanophotonics* (Inst. Fiziki Mikrostruktur Ross. Akad. Nauk, Nizhni Novgorod, 2000), p. 157.

11. A. V. Antonov, V. I. Gavrilenko, B. N. Zvonkov, *et al.*, in *Proceedings of the Conference on Nanophotonics* (Inst. Fiziki Mikrostruktur Ross. Akad. Nauk, Nizhni Novgorod, 2002), p. 215.
12. V. M. Rysakov, Usp. Fiz. Nauk **161** (12), 1 (1991) [Sov. Phys. Usp. **34**, 1027 (1991)].
13. V. M. Rysakov, Fiz. Tverd. Tela (St. Petersburg) **39**, 835 (1997) [Phys. Solid State **39**, 741 (1997)].
14. Yu. K. Pozhela, *Plasma and Current Instabilities in Semiconductors* (Nauka, Moscow, 1976) [in Russian].
15. N. Balkan, B. K. Ridley, and J. S. Roberts, Superlattices Microstruct. **5**, 539 (1989).
16. V. Ya. Aleshkin, A. A. Andronov, A. V. Antonov, *et al.*, in *Abstracts of International Symposium on Nanostructures* (St. Petersburg, 1996), p. 443.
17. B. K. Ridley, Semicond. Sci. Technol. **3**, 542 (1988).
18. J. Blakemore, J. Appl. Phys. **53**, R123 (1982).
19. A. V. Antonov, A. V. Gavrilenko, V. I. Gavrilenko, *et al.*, in *Proceedings of Meeting on Nanophotonics* (Inst. Fiziki Mikrostruktur Ross. Akad. Nauk, Nizhni Novgorod, 2003), Vol. 2, p. 215.
20. A. V. Antonov, A. V. Gavrilenko, V. I. Gavrilenko, *et al.*, Izv. Ross. Akad. Nauk, Ser. Fiz. **68** (1), 68 (2004).
21. A. V. Antonov, V. I. Gavrilenko, E. V. Demidov, *et al.*, in *Proceedings of Meeting on Nanophotonics* (Inst. Fiziki Mikrostruktur Ross. Akad. Nauk, Nizhni Novgorod, 2004), p. 195.

Translated by A. Kazantsev

Semiconductors, Vol. 39, No. 1, 2005, pp. 50–53. Translated from Fizika i Tekhnika Poluprovodnikov, Vol. 39, No. 1, 2005, pp. 59–62.

LOW-DIMENSIONAL SYSTEMS

Optical Phenomena in InAs/GaAs Heterostructures with Doped Quantum Dots and Artificial Molecules

L. E. Vorob'ev[1], V. Yu. Panevin[1], N. K. Fedosov[1], D. A. Firsov[1]^, V. A. Shalygin[1], A. A. Andreev[2, 3], Yu. B. Samsonenko[4], A. A. Tonkikh[4], G. E. Cirlin[4], N. V. Kryzhanovskaya[3], V. M. Ustinov[3], S. Hanna[5], A. Seilmeier[5], N. D. Zakharov[6], and P. Werner[6]

[1]St. Petersburg State Polytechnical University, St. Petersburg, 195251 Russia

^e-mail: dmfir@rphf.spbstu.ru

[2]Department of Physics, University of Surrey, Guildford, GU2 7XH, UK

[3]Ioffe Physicotechnical Institute, Russian Academy of Sciences, St. Petersburg, 194021 Russia

[4]Institute for Analytical Instrumentation, Russian Academy of Sciences, St. Petersburg, 198103 Russia

[5]Institute of Physics, University of Bayreuth, Germany

[6]Max Planck Institute of Microstructure Physics, 06120 Halle (Saale), Germany

Submitted June 1, 2004; accepted for publication June 14, 2004

Abstract—Spectra of intraband absorption of polarized mid-IR light were investigated in undoped, *p*-, and *n*-doped InAs/GaAs quantum dots (QDs) covered with an InGaAs layer. Optical matrix elements for intraband electron and hole transitions in QDs have been calculated for different polarizations of light, and a good agreement with the experimental data is obtained. It is shown that the intraband absorption of light by electrons strongly exceeds the absorption by holes. Photoluminescence spectra and TEM images of structures with artificial molecules formed by pairs of QDs were studied. © *2005 Pleiades Publishing, Inc.*

1. INTRODUCTION

The study of intraband optical transitions of carriers in quantum dots (QDs) is important for the design of new optoelectronic devices and for detectors and emitters of mid-IR light. The photoinduced intraband absorption of light in undoped InAs/GaAs QDs and in *n*-type QDs was studied by several authors [1, 2], but the data on the intraband absorption of light in *p*-type QDs and the comparative analysis of absorption in *n*- and *p*-type structures are unavailable. These data are of interest for the development of efficient photodetectors, as well as for the study of the optical loss related to the absorption of light by holes in lasers operating on intraband electron transitions within QDs. In this study, we experimentally and theoretically examined the intraband absorption of IR light in InAs/GaAs QD structures.

Optical properties of structures with artificial molecules constituted by pairs of vertically coupled QDs have been studied in insufficient detail. Meanwhile, structures of this kind have already been suggested as basic elements of the quantum computer [3, 4]. Also, structures with artificial molecules can be used in designing emitters for mid-IR and terahertz ranges; because the energy splitting of the ground state in an artificial molecule is a function of the spacer width, it lies in the range from several to several tens of millielectronvolts. We present our results on growing and studies of InAs/GaAs structures with artificial molecules.

2. SAMPLES AND EXPERIMENTAL PROCEDURE

Optical transitions in QDs were studied in MBE-grown 15-layer InAs/GaAs QD structures. As distinct from standard Stranski–Krastanow procedure, prior to the deposition of GaAs matrix, QDs were overgrown with a thin (5 nm) $In_{0.12}Ga_{0.88}As$ layer. This layer modified the structural and optical properties of QDs. To obtain *n*- and *p*-type conduction, structures were doped with Si or Be, respectively. The doped GaAs layer, 2 nm in thickness, was situated 1.5 nm below the QD layers. The surface density of QDs in a single layer was 3×10^{10} cm^{-2}; the surface density of the dopant was approximately six times larger. The absorption was measured in samples of multipass configuration.

To produce artificial molecules, two InAs/GaAs QD layers separated by a GaAs spacer $d_s = 5$ nm thick were grown on a GaAs substrate. The amount of InAs deposited in the first and second QD layers differed, 4 and 2.5 monolayers, respectively. This method made possible the formation of coupled QDs of the same size. Photoluminescence (PL) and TEM studies of the structures were performed.

3. RESULTS AND DISCUSSION

Figure 1 shows experimental data on intraband absorption of *s*- and *p*-polarized light in QD structures. The spectral features indicated by arrows can be attrib-

uted to intraband transitions of electrons and holes between quantum-confinement levels. The absorption peaks associated with electron transitions are observed in *s*- and *p*-polarizations at 95 and 175 meV, respectively. The absorption peak associated with hole transitions is observed in *s*-polarization at the photon energy of about 96 meV.

In the calculations of the band structure of semiconductor QDs and molecules, we have taken into account the following important factors:

(i) elastic stress in a structure, taking into account the prescribed shape of a QD, distribution of the composition of the material, and presence of a thin wetting layer;

(ii) piezoelectric fields;

(iii) complex structure of the valence band and its modification by elastic strain;

(iv) spin-orbit interaction and nonparabolicity of the conduction band.

A sufficiently good approximation for solution of this problem with the consideration of all the listed factors consists in solving a 3D problem of the linear theory of elasticity and a system of equations in terms of the method of wave function envelopes on the basis of a 8×8 effective Hamiltonian in Kane's model. The solving of this problem for a QD of arbitrary shape involves considerable calculation difficulties. However, a considerable part of the solution of the problem, specifically, the calculation of elastic stress and piezoelectric fields, can be performed analytically for an arbitrary shape of QD, without any simplifying assumptions. The result has the form of Fourier transforms of the stress tensor and piezoelectric potential. To obtain this result, we used the Green function formalism for the linear equation of elasticity [5]. Further, in calculating the band structure it is convenient to use the plane-wave expansion in terms of 8×8 effective Hamiltonian in Kane's model. The application of this method for strained nitride QDs in the wurtzite-type crystal structure is discussed in [6].

In the plane-wave method, the wave function of an electron or a hole localized in a QD is represented as a superposition of spatial wave functions:

$$\mathbf{\Psi}(\mathbf{r}) = \sum_{\mathbf{k},\,\alpha} C_{\mathbf{k},\,\alpha} |\mathbf{k}, \alpha\rangle, \qquad (1)$$

where the plane wave $|\mathbf{k}, \alpha\rangle \propto \exp(i\mathbf{kr})$ is an eigenstate of the 8×8 $\mathbf{k} \cdot \mathbf{p}$ effective Hamiltonian in the generalized Kane's model [7], and α indicates the state of electrons and light, heavy, and spin-split holes (spin included). In (1), the wave function $\mathbf{\Psi}$ and plane wave $|\mathbf{k}, \alpha\rangle$ are eight-component vectors, each component associated with the corresponding Bloch function. Energies of electrons and holes localized in a QD or an artificial molecule, and coefficients $C_{\mathbf{k},\,\alpha}$ were found by numerically solving the problem of eigenvectors and eigenvalues of a large matrix whose elements depend on the Fourier transforms of the shape of QD or artificial molecule and on the distribution of elastic and piezoelectric stresses. As mentioned above, the required Fourier transforms can be found analytically.

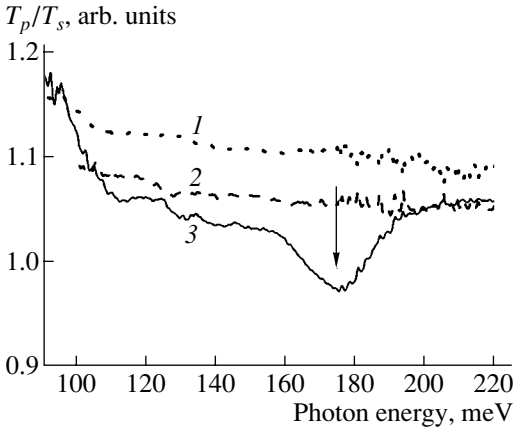

Fig. 1. The ratio between the transmittances of *p*- and *s*-polarized light for samples differing by the doping of QDs: (*1*) *p*-type; (*2*) undoped; (*3*) *n*-type.

In the calculations, we assumed that QDs are in the form of truncated pyramids with the lower base of 16×16 nm^2, upper base 4×4 nm^2, and height 5.5 nm. Figure 2 shows the data calculated with an account for Gaussian broadening of separate transitions.

The spectral position and polarization dependence of the calculated curves in Fig. 2 agree well with the experimental transmission spectra (Fig. 1). In particular, both the calculation and experiment show that the absorption of light by holes is several times weaker than by electrons. In addition, the dependences of the light absorption on polarization and spectral composition of light are different. This result seems favorable for the development of bipolar mid-IR lasers operating on interlevel electron transitions in QDs (see, e.g., [8]). Strong absorption by holes might reduce the optical gain related to intraband electron transitions between the QD levels.

The difference between matrix elements for electrons and holes is related to the fact that the matrix element for QD is defined by two factors: (i) bulk matrix element, built with the wave functions of the bulk crystal and (ii) spatial overlapping of the wave functions of the initial and final states in a QD. The bulk matrix element for electron transitions is several times larger than for holes. In addition, the overlapping of the wave functions between the ground and excited states in a QD (the energies of corresponding intraband transitions exceed 70 meV) is smaller than the overlapping between electron states for the same energy of the intraband transition. Therefore, both these factors lead to a higher cross section of the intraband absorption for electrons.

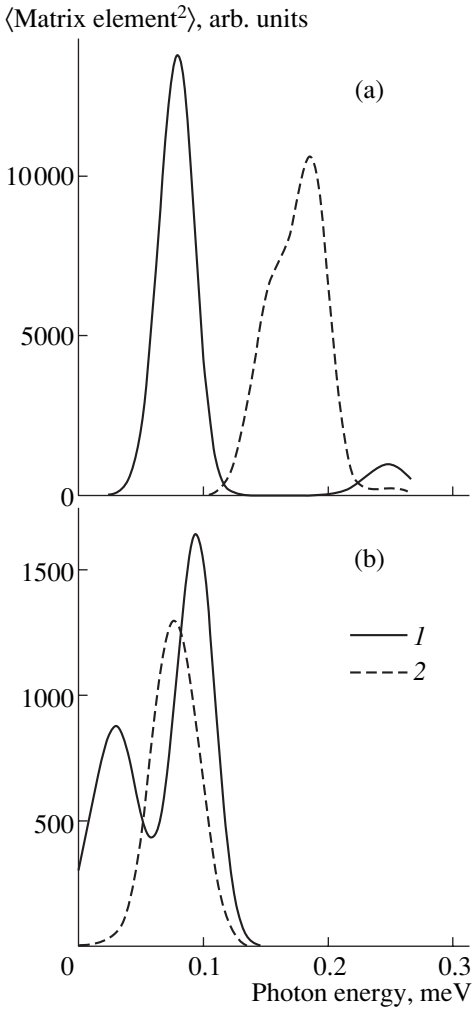

Fig. 2. Calculated optical matrix elements for interlevel transitions. (a) electrons, (b) holes. Light polarization: (*1*) *s*; (*2*) *p*. The broadening of 20 meV was taken into account.

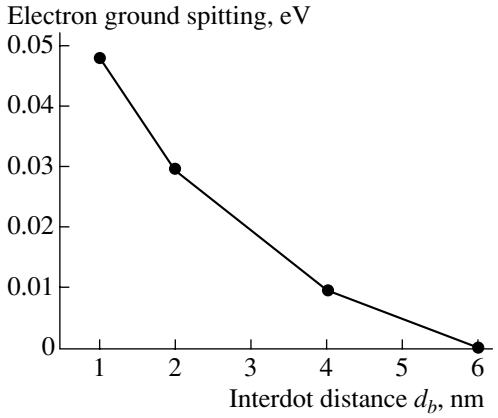

Fig. 3. Calculated energy splitting of the QD ground state as function of the distance d_b between coupled QDs (the spacer thickness $d_s = d_b + h_t$).

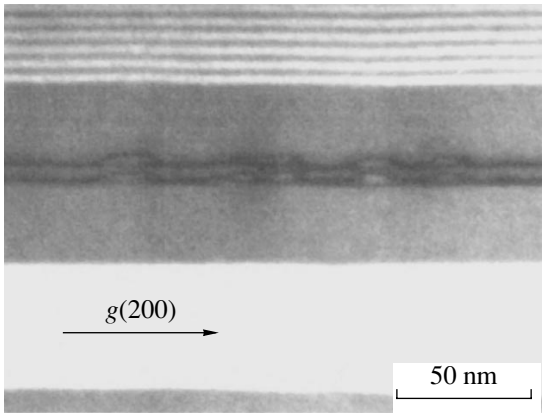

Fig. 4. Cross-sectional TEM image of a structure with two QD layers.

In structures with artificial molecules formed by pairs of vertically coupled QDs, the splitting of the ground level depends on the distance between QDs. Figure 3 shows the calculated energy splitting of the QD ground level. The following parameters of the structure were used in the calculation: QD height h_t = 4 nm, base 13×13 nm^2, upper base 10×10 nm^2, wetting layer thickness 0.5 nm. These parameters agree with TEM images of artificial molecules, one of which is shown in Fig. 4. The study of high-resolution TEM images has shown that the material of the QD has a composition $In_{0.5}Ga_{0.5}As$, which was also used in the calculation.

Figure 5 shows PL spectra recorded in a wide range of pumping intensity. Two peaks can be distinguished, 42 meV apart. Within a considerable range of pumping intensities, the intensities of these peaks coincide; this allows us to attribute these peaks to electron transitions from symmetric and antisymmetric states of an artificial molecule, which are formed upon splitting of the

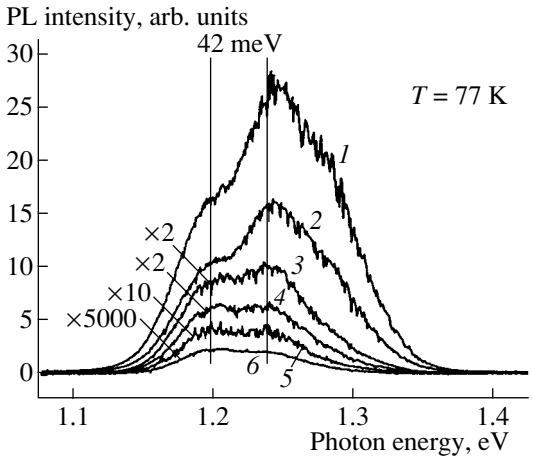

Fig. 5. PL spectra of a structure with artificial molecules for different pumping levels: (*1*) I_0; (*2*) $I_0/2$; (*3*) $I_0/7$; (*4*) $I_0/50$; (*5*) $I_0/500$; and (*6*) $I_0/250000$. Here, I_0 corresponds to 40 mW power of the Ar^+ laser. The splitting of the QD ground state is indicated. The spacer thickness $d_b + h_t = 5$ nm.

QD ground state. Both TEM images and PL spectra demonstrate that our structures contain symmetrical coupled QDs, which form an artificial molecule.

The experimentally obtained splitting of the ground state, 42 meV, agrees well with the calculated value of 46 meV (see Fig. 3, d_b = 1 nm).

4. CONCLUSIONS

We have obtained experimental and theoretical evidence that, in InAs/GaAs QD structures, the intraband absorption of mid-IR light, associated with electron transitions, is several times stronger than the absorption associated with hole transitions. This fact is favorable for the development of mid-IR lasers operating on intraband electron transitions.

Structures with pairs of vertically coupled QDs were grown and studied. PL spectra and TEM images confirm the formation of artificial molecules.

ACKNOWLEDGMENTS

The study was supported by INTAS, the International Science and Technology Center, the Russian Foundation for Basic Research, and the Ministry of Science and Education of Russia. A.A. Andreev also acknowledges the support of EPSRC (Engineering and Physical Sciences Research Council, UK).

REFERENCES

1. S. Sauvage, P. Boucaud, F. H. Julien, *et al.*, J. Appl. Phys. **82**, 3396 (1997).
2. S. Sauvage, P. Boucaud, F. H. Julien, *et al.*, Appl. Phys. Lett. **71**, 2785 (1997).
3. A. Barenco, D. Deutsch, A. Ekert, and R. Jozsa, Phys. Rev. Lett. **74**, 4083 (1995).
4. M. Bayer, P. Hawrylak, K. Hinzer, *et al.*, Science **291**, 451 (2001).
5. A. D. Andreev, J. R. Downes, D. A. Faux, and E. P. O'Reilly, J. Appl. Phys. **86**, 297 (1999).
6. A. D. Andreev and E. P. O'Reilly, Phys. Rev. B **62**, 15851 (2000).
7. T. B. Bahder, Phys. Rev. B **41**, 11992 (1990); Phys. Rev. B **46**, 9913 (1992).
8. A. Kastalsky, L. E. Vorobjev, D. A. Firsov, *et al.*, IEEE J. Quantum Electron. **37**, 1356 (2001).

Translated by D. Mashovets

Semiconductors, Vol. 39, No. 1, 2005, pp. 54–57. Translated from Fizika i Tekhnika Poluprovodnikov, Vol. 39, No. 1, 2005, pp. 63–66.

LOW-DIMENSIONAL SYSTEMS

Calculation of the States of Shallow Donors in Quantum Wells in a Magnetic Field Using Plane Wave Expansion

V. Ya. Aleshkin^ and L. V. Gavrilenko

Institute for Physics of Microstructures, Russian Academy of Sciences, Nizhni Novgorod, 603950 Russia

^e-mail: aleshkin@ipm.sci-nnov.ru

Submitted June 1, 2004; accepted for publication June 14, 2004

Abstract—A nonvariational method for calculating the states of shallow donors in quantum wells in a magnetic field is suggested. The method can be used in a wide range of magnetic fields, starting with zero. The method is based on the expansion of the electron-wave function in a basis of eigenfunctions of the Hamiltonian operator that describes a rectangular quantum well. The results obtained by this method are compared to the experimental data and to the results of calculations using different theoretical methods. The comparison shows that our method describes the observed spectrum of the shallow-donor states in quantum wells in a magnetic field with a higher accuracy than the methods used in the study by Chen *et al.* *© 2005 Pleiades Publishing, Inc.*

1. INTRODUCTION

The results of experimental studies of the states of shallow-level impurities in heterostructures with quantum wells (QWs) in magnetic fields have already been reported for quite a long time. Both variational and nonvariational theoretical methods were used to explain the data obtained [1, 2]. Although variational calculations have recently been used to describe even the excited impurity states (up to $4p_{\pm}$ states) [1], the calculation of the wave functions of these states requires trial functions with a large number of variational parameters. As to nonvariational methods, their accuracy depends heavily on the choice of the basis used for the expansion of the wave function. Thus, if the eigenfunctions of an electron in a magnetic field are chosen as a basis [2], then, for low magnetic fields, one has to take into account many terms of the series in order to accurately describe the localized impurity states. Although an experiment is typically performed in rather high magnetic fields (above 1–2 T), it is useful to know the behavior of energy levels with decreasing magnetic field. The knowledge of this behavior helps to identify the impurity levels and to find out which group they belong to.

In this study, we suggest a method of calculating the donor states in heterostructures with QWs in a magnetic field applied in the direction of heterostructure growth. The method is based on the expansion of the electron wave function in the eigenfunctions of the Hamiltonian operator that describes a rectangular QW using the "plane waves" which do not depend on magnetic field [3]. Such a choice of the basis functions allows one to easily describe the ground and the excited impurity states not only at high, but also at low magnetic fields, down to zero field.

2. CALCULATION METHOD

Without loss of generality, we may assume that the sample under study has a cylindrical form and the z axis is normal to the plane of the QW. The magnetic field directed along the axis of structure growth does not violate the axial symmetry of the problem and, therefore, the projection of the angular momentum onto the z axis $L_z = \hbar m$ is conserved. To find the energy spectrum, we expand the wave functions of impurity states in the eigenfunctions of the Hamiltonian operator in the absence of magnetic field and impurity potential,

$$\Psi_n^m(\rho, \phi, z) = \frac{\exp im\phi}{\sqrt{2\pi}} \sum_{n,k} \sqrt{\frac{\pi}{R}} f_n^m(k) \psi_n(z) J_m(k\rho). \quad (1)$$

Here, ρ and ϕ are the polar coordinates in the plane of the QW; k is the magnitude of the two-dimensional wave vector; R is the radius of the cylindrical sample; $\psi_n(z)$ is the wave function that describes electron motion along the z axis, corresponds to the nth confinement subband, and satisfies the one-dimensional Schrödinger equation without the impurity potential and magnetic field; and $J_m(k\rho)$ is a Bessel function of order m. We note that, in expansion (1), we omit the term corresponding to the contribution of the continuous spectrum. This assumption is valid if the binding energies of the donor states considered are much smaller than the depth of the QW and the states are localized within the well.

In the case of an isotropic parabolic dispersion relation for electrons, the Schrödinger equation for a parti-

1063-7826/05/3901-0054$26.00

cle in the potential of an impurity center in a rectangular QW in a magnetic field has the following form:

$$\hat{H}(\mathbf{r}) = \frac{\hat{\mathbf{p}}^2}{2\mu} + U(z) - \frac{e^2}{\kappa\sqrt{\rho^2 + (z - z_{im})^2}} + V_{\text{chem}} + \frac{e\hbar}{c\mu}H\left(-i\frac{\partial}{\partial\varphi}\right) + \frac{e^2H^2\rho^2}{8\mu c^2}. \quad (2)$$

Here, μ is the electron effective mass, the potential $U(z)$ specifies the energy structure of the QW and depends on the Al content in the $Al_xGa_{1-x}As$ alloy [4], κ is the permittivity, z_{im} is the coordinate of the donor, H is the magnetic field, and V_{chem} is the potential that accounts for the non-Coulomb form of the donor potential at small distances (the so-called chemical shift). The short-range potential V_{chem} was chosen in the form of the screened Coulomb potential

$$V_{\text{chem}} = C\frac{e^2}{\kappa}\frac{\exp(r/l_{\text{D}})}{r} \quad (3)$$

with screening length $l_{\text{D}} = 5$ Å; the constant C was chosen so that the ionization energy of 1s donor states corresponded to the experimental data at one of the values of the magnetic field. Substituting wave function (1) into the Schrödinger equation, we obtain the integro-differential equation for the expansion coefficients,

$$-\frac{e^2H^2}{8\mu c^2}\left(\frac{\partial^2}{\partial k^2} - \frac{1}{k}\frac{\partial}{\partial k} + \frac{1/4 - m^2}{k^2}\right)f_n^m(k) + \left(\varepsilon_n - \varepsilon + \frac{\hbar^2k^2}{2\mu} + \frac{\hbar eHm}{2c\mu}\right)f_n^m(k) - \frac{e^2k}{2R\kappa}\sum_{n'}\int_0^\infty dk' f_{n'}^m(k')I^m(k, n; k', n') = 0. \quad (4)$$

Here, ε is the energy of an electron, ε_n is the energy that corresponds to the bottom of the nth subband, and

$$I^m(k, n; k', n') = \int_0^{2\pi}\cos\theta d\theta \times \int_{-\infty}^{\infty} dz\psi_n^*(z)\psi_{n'}(z)\left[\frac{1}{K}\exp(-|z - z_{im}|K) + \frac{C}{\sqrt{K^2 + 1/l_{\text{D}}^2}}\exp(-|z - z_{im}|\sqrt{K^2 + 1/l_{\text{D}}^2})\right],$$

$$K^2 = k^2 + k'^2 - 2kk'\cos\theta.$$

Equation (4) was solved using the method of finite differences, in which case the derivatives were replaced by ratios of the change in the function to the change in the argument, and the integral with respect to k' was replaced by the sum over a discrete set of k'. Each term in this sum corresponds to the integral over some interval of k'. If this interval is small compared to the characteristic scale of the variation in the integrand, the integral over each of the intervals can be replaced by the product of the interval size and the value of the integrand in this interval. We used an equidistant partition in k' with a step of Δk. In our case, there are two factors that affect the localization radius of the wave function in the plane of the QW: the impurity potential and the magnetic field. Therefore, the partition step should be chosen so that it were much smaller than the inverse Bohr radius r_{B} and the magnetic length l_H, i.e., $\Delta k \ll \min(1/r_{\text{B}}, 1/l_H)$. Furthermore, it is clear that the sum over k may be truncated by replacing the upper infinite summation limit by a finite quantity $k_{\max}$ that satisfies the condition $k_{\max} \gg \max(1/r_{\text{B}}, 1/l_H)$. We also note that a uniform partition in k ($k_i = i\Delta k$), which we used, is almost equivalent to zero boundary conditions at $\rho = R = \pi/\Delta k$. Complete equivalence would be attained if we chose the roots of the Bessel function $J_m(kR)$ as the k points.

The solution of the integro-differential equation (4) is reduced to finding the eigenvalues and eigenvectors of the matrix A^m of dimension $n_{\max}N \times n_{\max}N$, where $n_{\max}$ is the number of confinement subbands in the QW and $N = k_{\max}/\Delta k$,

$$A^m_{n, i; n' j} = \left[-\frac{e^2H}{8\mu c^2}\left(\frac{\delta_{j, i+1} + \delta_{j, i-1} - 2\delta_{j, i}}{\Delta k^2} + \frac{\delta_{j, i+1} - \delta_{j, i-1}}{2i\Delta k^2} + \frac{1 - m^2}{i^2\Delta k^2}\right)\delta_{n, n'}\right] + \left[\left(\varepsilon_n + \frac{\hbar^2\Delta k^2 i^2}{2\mu} + \frac{\hbar eHm}{2c\mu}\right)\delta_{i, j}\delta_{n, n'}\right] + \frac{e^2i(\Delta k)^2}{\pi\kappa}I^m(i\Delta k, n; j\Delta k, n'). \quad (5)$$

However, for $i = j$, the elements of the A^m matrix are singular. To avoid this difficulty, we note that this singularity is integrable in k. Therefore, following [3], we introduce in this case the average value $\bar{A}^m$ by

$$\bar{A}^m_{n, i; n', i} = \frac{1}{\Delta k}\int_{k_j - \Delta k/2}^{k_j + \Delta k/2} A_{n, i; n', j}dk_j. \quad (6)$$

3. RESULTS AND DISCUSSION

To study the accuracy of the method, we calculated the spectrum of impurity states and of the energies of the $1s \longrightarrow np_\pm$ transitions ($n = 2, 3$) for shallow donors in a QW in a magnetic field. The heterostructure param-

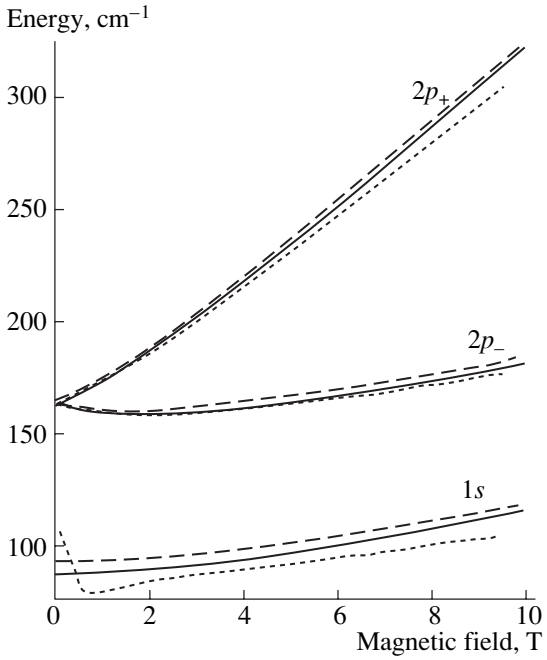

Fig. 1. Energies of the $1s$ and $2p_\pm$ levels for a donor at the center of a $Al_{0.3}Ga_{0.7}As$ quantum well of width d_{QW} = 125 Å in relation to the magnetic field. Solid lines correspond to our calculations; dashed lines, to the variational method [1]; and dotted lines, to the nonvariational method [2].

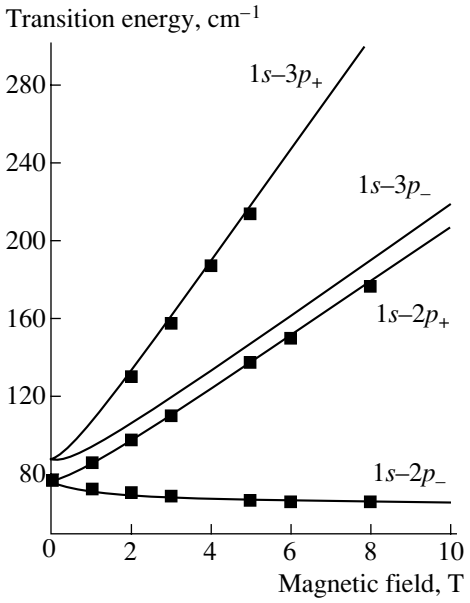

Fig. 2. Magnetic field dependences of the energies of optical $1s \longrightarrow np_\pm$ transitions (n = 2, 3) for the $Al_{0.3}Ga_{0.7}As$ heterostructure with a quantum well of width d_{QW} = 125 Å. Squares correspond to the experimental data and the lines represent the results of the calculations.

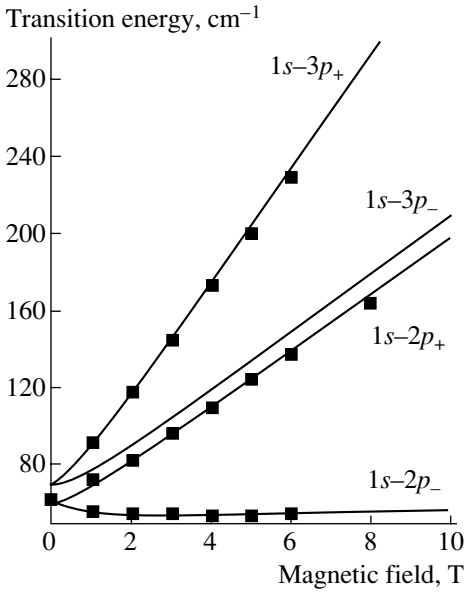

Fig. 3. The same as in Fig. 2, but for the sample with a quantum well of width d_{QW} = 210 Å.

eters were chosen to be the same as in [1, 2], where the experimental results were described. The donor was located at the center of the $Al_{0.3}Ga_{0.7}As$ QW with a width of d_{QW} = 125 or 210 Å. In the first heterostructure, the QW contained three confinement subbands; in the second, the number of subbands was five. If the energy corresponding to the bottom of a subband is much larger than the impurity ionization energy, then this subband affects the formation of impurity states only slightly. Therefore, we considered only three confinement subbands for both types of heterostructures. To ensure sufficient accuracy of calculations, for each subband, a splitting with 1000 points in the k space was used. We set the electron effective mass $\mu = 0.067m_0$ and the permittivity of the material $\kappa = 12.9$.

In Fig. 1, the results of our calculations are compared to the results obtained by the variational [1] and nonvariational methods with a different choice of the basis for the expansion of the wave function and with an electron effective of mass $\mu = 0.069m_0$ [2]. We see that nonvariational methods yield lower energies of the states than the variational calculation. It is known that a variational calculation overestimates the level energies. In addition, the method suggested in [2] describes inadequately the $1s$ state in magnetic fields below 1 T.

In Figs. 2 and 3, the results of the calculation are compared to the experimental data obtained by measuring the absorption spectra for two $Al_{0.3}Ga_{0.7}As$ samples with QWs of different widths [1]. In the impurity absorption spectra in magnetic fields, the optical transitions corresponding to the selection rules $\Delta m = \pm 1$ ($1s \longrightarrow 2p_-$, $1s \longrightarrow 2p_+$, $1s \longrightarrow 3p_-$, $1s \longrightarrow 3p_+$, etc.) are observed. It can be seen in Figs. 2 and 3 that the method suggested in this study yields results that are in good agreement with the experimental values of the transition energies in the entire range of magnetic fields.

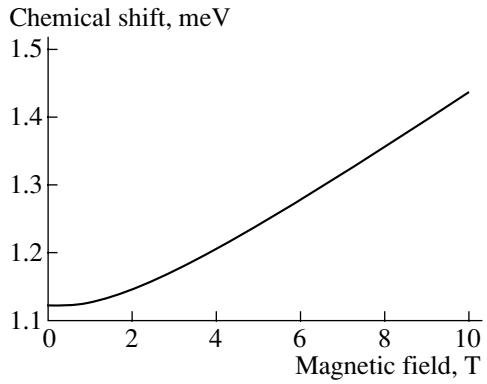

Fig. 4. Magnetic field dependence of the chemical shift for the 1*s* state of an impurity in a QW.

For 1*s* electron states, we took into account the chemical shift, which was about 1 meV. Figure 4 shows that the chemical shift increases with magnetic field. The reason for this behavior is that the electron wave function becomes increasingly localized near the impurity with increasing magnetic field.

ACKNOWLEDGMENTS

This study was supported by the Russian Foundation for Basic Research (project no. 04-02-17178), the International Science and Technology Center (grant no. 2293), the program Universities of Russia (grant UR.01.01.057), and the Ministry of Industry, Science, and Technology of the Russian Federation (contract nos. 40.072.1.1.1173 and 40.031.1.1.1187).

REFERENCES

1. R. Chen, J. P. Cheng, D. L. Lin, *et al.*, J. Phys.: Condens. Matter **7**, 2577 (1995).
2. V. Ya. Aleshkin, D. B. Veksler, and V. I. Gavrilenko, in *Proceedings of Meeting on Nanophotonics* (Inst. Fiziki Mikrostruktur Ross. Akad. Nauk, Nizhni Novgorod, 2000), p. 88.
3. J. P. Loehr and J. Singh, Phys. Rev. B **41**, 3695 (1990).
4. E. H. Li, Physica E (Amsterdam) **5**, 215 (2000).

Translated by I. Zvyagin

Semiconductors, Vol. 39, No. 1, 2005, pp. 58–61. Translated from Fizika i Tekhnika Poluprovodnikov, Vol. 39, No. 1, 2005, pp. 67–70.

LOW-DIMENSIONAL SYSTEMS

The Effect of the Localization in a Quantum Well on the Lifetime of the States of Shallow Impurity Centers

E. E. Orlova*^, P. Harrison, W.-M. Zhang***, and M. P. Halsall*****

**Institute for Physics of Microstructures, Russian Academy of Sciences, Nizhni Novgorod, 603950 Russia*

^e-mail: orlova@ipm.sco-nnov.ru

***School of Electronic and Electrical Engineering, The University of Leeds, LS2 9JT, UK*

****Department of Physics, UMIST, PO BOX 88, Manchester M60 1QD, UK*

Submitted June 1, 2004; accepted for publication June 14, 2004

Abstract—The results of theoretical and experimental studies into the effect of the localization in a quantum well on the lifetime of the states of shallow impurity centers are reported. The transitions between excited impurity states are induced by an interaction with acoustic phonons whose wave vectors exceed the scale of localization of the wave function in the wave-vector space and, therefore, are determined by the asymptotic behavior of the wave function of impurity states at large wave vectors. It is shown that the localization in a quantum well results in a slower decay of the wave functions of the impurity states in the wave vector space and can result in an exponential decrease in the lifetime of impurity states along with the width of the well. The theoretical results are in good agreement with the experimental data on the lifetime of acceptor states in GaAs/AlAs:Be structures.

An interest in nonequilibrium population and lifetimes of shallow impurity states in semiconductors is related to the possibility of generating stimulated radiation using impurity transitions, which has recently been experimentally realized [1, 2]. Semiconductor structures are attractive from the point of view of developing new sources of stimulated radiation using impurity transitions, since the properties of impurity states that remain constant in bulk semiconductors can be changed by varying the parameters of the structures [3]. The lifetimes of impurity states represent a major factor that determines both the possibility of producing a population inversion and a generation threshold for impurity transitions. Here, we report the results of experimental and theoretical studies into the lifetime of excited impurity states in heterostructures with δ-doped quantum wells (QWs).

The experimental study of the relaxation of impurity state electrons in GaAs:Be and GaAs/AlAs:Be structures was performed using a free-electron laser (Dutch FEL) [4, 5]. The structures contained QWs with widths of 20, 15, or 10 nm with δ-doped layers at the center of the well (Fig. 1). For all the samples, the measurements of the absorption of long-wavelength infrared radiation at low temperatures (4 K) showed three main lines of 1*s*–2*p* transitions. The ionization and excitation energies increase as the QW width L decreases, in agreement with the variational calculations for impurity states [3]. The relaxation dynamics for electrons in impurity states was studied using dual (pump–probe) picosecond pulses. A fast decrease in the lifetime of the 2*p* acceptor state along with the decreasing L, from 360 ps in bulk GaAs to 55 ps, was observed in the case of 10 nm QWs (Fig. 2). It is worth noting that the well width L was much greater than the radius of the orbits of impurity states, and the energies of the states changed by no more than 20% in all the investigated structures.

Transitions between lower excited impurity states with relatively large energy separations involve the emission of acoustic phonons whose wave vector exceeds the size of the wave function in the wave-vector space. The probability of these transitions is determined by the short-wavelength asymptotic behavior of the wave functions of impurity states [6], which cannot

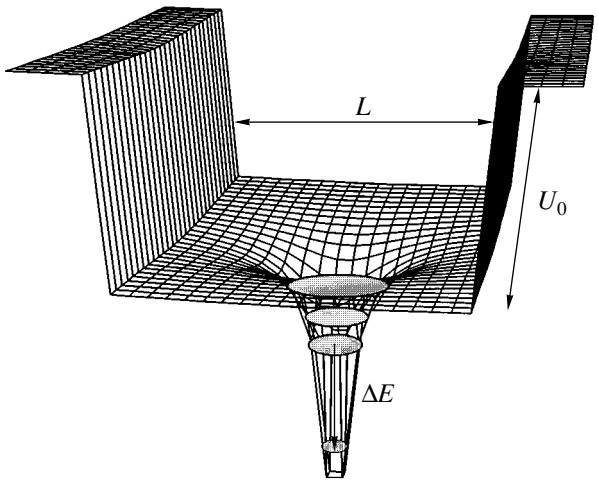

Fig. 1. An energy diagram of impurity transitions in a quantum well.

be obtained by the variational procedure used for calculating the impurity states. The probability of transitions from the hydrogen-like *p*-states in bulk semiconductors decreases as the transition energy ΔE increases to ΔE^{-7} or faster [7]. The energies of impurity transitions increase as well width decreases [3]; however, this increase is not accompanied by a decrease in the transition probability. In contrast, a sharp decrease in the lifetime of impurity states is observed. This decrease is related to a change in the short-wavelength asymptotic behavior of impurity states in QWs.

The state of a hydrogen-like center in a QW is described by the Schrödinger equation in the effective mass approximation

$$\mathbf{T}(\hat{\mathbf{p}})\phi(\mathbf{r}) + U(z)\phi(\mathbf{r}) - \frac{e^2}{\varepsilon r}\phi(\mathbf{r}) = E\phi(\mathbf{r}), \qquad (1)$$

where $\mathbf{T}(\hat{\mathbf{p}})$ is the kinetic-energy operator, ε is the permittivity, and the potential of the QW is $U(z) = -U_0$ for $|z| < L/2$ and $U(z) = 0$ for $|z| > L/2$ (see Fig. 1). To study the short-wavelength asymptotic behavior, it is convenient to use the wave-vector representation,

$$\mathbf{T}(\hbar\mathbf{k})\varphi(\mathbf{k}) - \frac{LU_0}{2\pi}\int\varphi(k_z', \mathbf{k}_\perp)\frac{\sin[(k_z - k_z')L/2]}{(k_z - k_z')L/2}dk_z' - \frac{e^2}{2\pi^2\varepsilon}\int\frac{\varphi(\mathbf{k}')}{|\mathbf{k} - \mathbf{k}'|^2}d\mathbf{k}' = E\varphi(\mathbf{k}), \qquad (2)$$

where $\mathbf{k}_\perp$ is the component of the wave vector normal to the *z* axis. The wave function in the real space is obtained by the Fourier transformation of $\varphi(\mathbf{k})$,

$$\phi(\mathbf{r}) = (2\pi)^{-3/2}\int\varphi(\mathbf{k})\exp(-i\mathbf{k}\mathbf{r})d\mathbf{r}.$$

For large wave vectors, the wave function is a combination of two components,

$$\varphi(\mathbf{k}) = \Phi_w(\mathbf{k}) + \Phi_C(\mathbf{k}). \qquad (3)$$

The second component in (3) is

$$\Phi_C(\mathbf{k}) = \frac{e^2}{2\pi^2\varepsilon\mathbf{T}(\hbar\mathbf{k})}\int\frac{\varphi(\mathbf{k}')}{|\mathbf{k} - \mathbf{k}'|^2}d\mathbf{k}'. \qquad (4)$$

This component is similar to the function obtained in [6] for Coulomb centers in bulk material. The first component in (3) contains the potential of the QW,

$$\Phi_w(\mathbf{k}) = \frac{LU_0}{2\pi\mathbf{T}(\hbar\mathbf{k})}\int\varphi(k_z', \mathbf{k}_\perp)\frac{\sin[(k_z - k_z')L/2]}{(k_z - k_z')L/2}dk_z'. \qquad (5)$$

The behavior of $\Phi_C(\mathbf{k})$ at large *k* can be considered using the Taylor expansion of the quantity $1/|\mathbf{k} - \mathbf{k}'|^2$ in powers of *k*'. According to [6], at large wave vectors, the function $\Phi_C(\mathbf{k})$ decays as $k^{-(n+4)}$, where *n* is the order of the first nonvanishing moment of $\varphi(\mathbf{k})$.

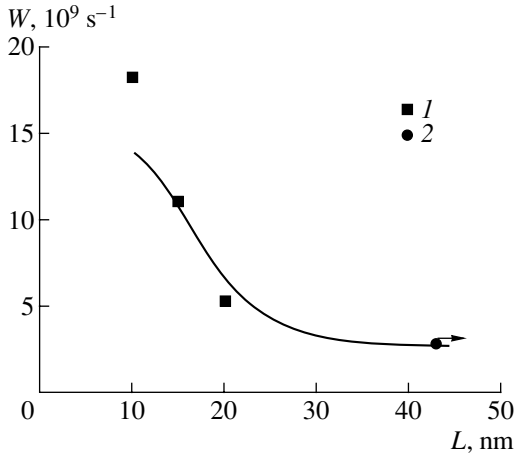

Fig. 2. The dependence of the probability of the $2p_0 \longrightarrow 1s$ transition on the width of the quantum well *L* in GaAs/AlAs structures. The line corresponds to the calculation, and the experimental data is marked (*1*) for the structures and (*2*) for bulk GaAs.

To determine the asymptotic behavior of $\Phi_w(\mathbf{k})$, we retain the first term in the Taylor expansion in expression (5), $1/|k_z - k_z'| \approx 1/k_z$ and assume that $k_z' \ll k_z$. We then obtain

$$\Phi_w(\mathbf{k}) = \frac{U_0}{\pi\mathbf{T}(\hbar\mathbf{k})k_z}\int\varphi(k_z', \mathbf{k}_\perp)\sin[(k_z - k_z')L/2]dk_z'. \qquad (6)$$

Putting the sine in an exponential form and performing the inverse Fourier transformation of $\varphi(k_z', \mathbf{k}_\perp)$, we find

$$\Phi_w(\mathbf{k}) = \frac{\mu U_0}{\sqrt{2\pi^3}\mathbf{T}(\hbar\mathbf{k})k_z}\int\phi(\mathbf{r})|_{z = L/2}\exp(i\mathbf{k}_\perp\mathbf{r}_\perp)d\mathbf{r}_\perp, \qquad (7)$$

where $\mu = \sin(k_zL/2)$ for even-numbered wave functions and $\mu = \cos(k_zL/2)/i$ for odd-numbered wave functions. Since μ oscillates rapidly with varying *L* as $k_z \gg 2/L$, the quantity $|\mu|^2$ can be approximated by its average over the period as $\overline{|\mu|^2} = 1/2$. Thus, at large k_z, the first component of the wave function (3) $\Phi_w(k_z) \propto k_z^{-3}$ also decays more slowly than the second component $\Phi_C(k_z)$. To estimate the contribution of the component Φ_w and its dependence on the well width, we assume that the Bohr radius is much smaller than the well width ($a_B \ll L$) and the difference of the wave functions of impurity states in the well from those of impurity states in a bulk semiconductor is small. Since the bulk impurity wave functions exponentially decrease the further from the center they are, the integrals in (7) also exponentially decrease as the well width increases. In the approxima-

tion of a nondegenerate isotropic band, we obtain the following expression for the 1*s* and $2p_0$ states:

$$\begin{aligned}\Phi_w^{1s}(\mathbf{k}) &= Q^{1s}\sin(k_zL/2)F(\mathbf{k})\\ &\times\exp(-k_\perp^2 a_B L/4 - L/2a_B),\\ \Phi_w^{2p_0}(\mathbf{k}) &= Q^{2p_0}\cos(k_zL/2)LF(\mathbf{k})\\ &\times\exp(-k_\perp^2 a_B L/2 - L/4a_B).\end{aligned} \tag{8}$$

Here,

$$F(\mathbf{k}) = \frac{U_0 a_B L}{(2\pi)^3}\mathbf{T}(\hbar\mathbf{k})k_z;$$

$$Q^{1s} = (2\pi)^{3/2}\phi_{1s}(\mathbf{r}=0),$$

$$Q^{2p_0} = -(2\pi)^{3/2} i\nabla\phi_{2p_0}(\mathbf{r})\Big|_{\mathbf{r}=0}.$$

A slower asymptotic decay of the wave function of impurity states, which is due to the effect of the potential of the QW, can result in an increase in the probability of transitions with an emission of short-wavelength acoustic phonons.

In the approximation of an isotropic phonon dispersion relation, the transition probability between states 1 and 2 with the spontaneous emission of acoustic phonons is given by [8]

$$W_{2\to1} = \frac{1}{16\pi}\frac{C}{l_0}\left(\frac{\Delta E}{mC^2}\right)^3\int\left|M_{1,2}^{\mathbf{q}}\right|^2 d\Omega_q, \tag{9}$$

where the integration is performed with respect to the angles of the vector $\mathbf{q}$, $\hbar Cq = \Delta E$, C is the velocity of sound, m is the effective mass, $l_0 = \pi\hbar^4\rho_c/2m^3E_D^2$ is the characteristic length for acoustic-phonon scattering, ρ_c is the crystal density, and E_D is the deformation-potential constant. The transition matrix element in the wave-vector representation is given by

$$M_{1,2}^{\mathbf{q}} = \int\varphi_2^*(\mathbf{k})\varphi_1(\mathbf{k}+\mathbf{q})d\mathbf{k}. \tag{10}$$

At large $\mathbf{k}$, this matrix element is specified by the contributions of two maxima (near $\mathbf{k} = 0$ and $\mathbf{k} = -\mathbf{q}$), where the slower functions can be expanded in the Taylor series. Thus, we find that the integral in (10) is proportional to the values of the wave function or its derivative at $\mathbf{k} = \mathbf{q}$. The component of the matrix element corresponding to Φ_C is proportional to $q^{-(4+n_1+n_2)}$, where $n_{1,2}$ are the orders of the first nonvanishing moments of the wave function, whereas the contribution of Φ_w is proportional to $q^{-(3+n)}$, where n is the smaller of the numbers n_1 and n_2. For transitions between the states of *s* and *p* types, we have

$$M_{s,p}^{\mathbf{q}} = Q^p\nabla_q\varphi_s(\mathbf{q}) + \varphi_p^*(-\mathbf{q})Q^s. \tag{11}$$

Assuming that Φ_w makes the main contribution to the wave function at $\mathbf{k} = \mathbf{q}$ and taking into account that $L \gg a_B$, q^{-1}, we obtain for the matrix element of the $2p_0 \longrightarrow 1s$ transition,

$$\begin{aligned}M_{1s,2p_0}^{\mathbf{q}} &= \frac{Q^{1s}Q^{2p_0}U_0L^2a_B\cos(q_zL/2)}{(2\pi)^3\mathbf{T}(\hbar\mathbf{q})q_z}\\ &\times\exp(-q_\perp^2La_B/2)\exp(-L/4a_B)\end{aligned} \tag{12}$$

and, for the probability of transition between these states,

$$M_{1s\to2p_0} = \frac{(Q^{1s}Q^{2p_0}U_0)^2a_BL^3}{2^8\pi^6l_0mC^2\hbar q^5}\exp(-L/2a_B). \tag{13}$$

Thus, the transition probability increases exponentially as the well width decreases. Comparing (13) with the results of [6], we see that the short-wavelength asymptotic behavior of the probability of an impurity transition with the emission of acoustic phonons is determined by the potential of the QW if the following condition is satisfied:

$$\left(\frac{U_0}{e^2/\varepsilon a_B}\right)^2 q^2L^3a_B^{-1}e^{-L/2a_B} \gg 3\pi^2 2^6. \tag{14}$$

The typical depth of the QW U_0 is much greater than the ionization energy $E_i \simeq e^2/2\varepsilon a_B$ (in *p*-GaAs/AlAs structures, $U_0 = 460$ meV and $E_i = 28$–35 meV). The phonon wave vectors corresponding to impurity transitions are equal to $q \gg 1/L$ (the energy ΔE corresponding to $q = 1/L$ is smaller than 0.4 meV in the investigated structures). Thus, condition (14) is satisfied for the wide range $L \gg 2a_B$.

According to (11), the contributions of $\Phi_w(q)$ and $\Phi_C(q)$ to the matrix element are additive at $q \gg 1/a_B$. Since the component of the matrix element proportional to $\Phi_w(q)$ oscillates as $\cos(q_zL/2)$, the part of $\left|M_{1s,2p_0}^{\mathbf{q}}\right|^2$ that contains the product of $\Phi_w(q)$ and $\Phi_C(q)$ vanishes after being averaged over the oscillation period $4\pi/q \ll L$. Thus, the contributions to the transition probability containing $\Phi_w(q)$ and $\Phi_C(q)$ are additive. The results of the calculation of the dependence of the probability of the $2p_0 \longrightarrow 1s$ transition on the well width in GaAs/AlAs structures are shown in Fig. 2 together with the experimental data. In the calculations, we used the following values of the parameters: $a_B = 16$ Å, $U_0 = 460$ meV, $m = 0.51m_0$, $C = 4.8\times10^5$ cm/s, and $\varepsilon = 12.9$. The quantity $l_0 = 5.2\times10^{-4}$ cm was obtained from the measurements of the hole mobility in GaAs [9]; $\Delta E = 16$ meV is the energy of the transition from the first excited state to the split-off ground state, which determines the observed relaxation times (this energy varies slowly in the structures under study [10, 11]). The agreement between the results of the calculation and experimental data may be considered as good.

Thus, we experimentally observed and theoretically justified the decrease in the lifetime of impurity states in QWs. This effect is a consequence of a change in the behavior of the wave function of impurity states as $k \longrightarrow \infty$ in QWs, which results in the enhancement of the interaction with short-wavelength acoustic phonons.

ACKNOWLEDGMENTS

This study was supported by the Royal Society/NATO Fellowship, the Russian Foundation for Basic Research (project no. 03-02-16586), and the EPSRC (grant no. GR/N65639/01).

REFERENCES

1. S. G. Pavlov, R. Kh. Zhukavin, E. E. Orlova, *et al.*, Phys. Rev. Lett. **84**, 5220 (2000).
2. M. A. Odnoblyudov, I. N. Yassievich, M. S. Kagan, *et al.*, Phys. Rev. Lett. **83**, 644 (1999).
3. W.-M. Zhang, M. P. Halsall, P. Harmer, *et al.*, J. Appl. Phys. **92**, 6039 (2002).
4. W.-M. Zhang, M. P. Halsall, P. Harmer, *et al.*, Phys. Status Solidi B **235**, 54 (2003).
5. M. P. Halsall, P. Harrison, J.-P. R. Wells, *et al.*, Phys. Rev. B **63**, 155314 (2001).
6. S. V. Meshkov, Fiz. Tverd. Tela (Leningrad) **21**, 1114 (1979) [Sov. Phys. Solid State **21**, 647 (1979)].
7. G. Ascarelly and S. Rodriquez, Phys. Rev. **124**, 1321 (1961).
8. V. N. Abakumov, V. I. Perel, and I. N. Yassievich, *Nonradiative Recombination in Semiconductors* (North-Holland, Amsterdam, 1991).
9. D. E. Hill, J. Appl. Phys. **41**, 1815 (1970).
10. W. T. Masselink, Y.-C. Chang, and H. Morkoç, Phys. Rev. B **32**, 5190 (1985).
11. A. A. Reeder, J.-M. Mercy, and B. D. McCombe, IEEE J. Quantum Electron. **24**, 1690 (1988).

Translated by I. Zvyagin

Semiconductors, Vol. 39, No. 1, 2005, pp. 62–66. Translated from Fizika i Tekhnika Poluprovodnikov, Vol. 39, No. 1, 2005, pp. 71–75.

LOW-DIMENSIONAL SYSTEMS

Cyclotron Resonance in Doped and Undoped InAs/AlSb Heterostructures with Quantum Wells

V. Ya. Aleshkin*, V. I. Gavrilenko*^, A. V. Ikonnikov*, Yu. G. Sadofyev, J. P. Bird**, S. R. Johnson**, and Y.-H. Zhang****

**Institute for the Physics of Microstructures, Russian Academy of Sciences, Nizhni Novgorod, 603950 Russia*
^e-mail: gavr@ipm.sci-nnov.ru
***Department of Electrical Engineering and Center for Solid-State Electronic Research, Arizona State University, Tempe, AZ 85287, USA*

Submitted June 1, 2004; accepted for publication June 14, 2004

Abstract—Backward-wave tubes are used to study the spectra of cyclotron resonance in the range of 150–700 GHz in the AlSb/InAs/AlSb heterostructures with quantum wells and with an electron concentration in a two-dimensional electron gas ranging from 2.7×10^{11} to 8×10^{12} cm^{-2} at 4.2 K. A significant increase in the cyclotron mass (from $0.03m_0$ to $0.06m_0$) is observed as the electron concentration (and, correspondingly, the Fermi energy) increases, which is typical of semiconductors with a nonparabolic dispersion relation. The results obtained are in satisfactory agreement with theoretical calculations of cyclotron masses at the Fermi level in the context of the simplified Kane model. © *2005 Pleiades Publishing, Inc.*

1. INTRODUCTION

Recently, an active interest in heterostructures with InAs/AlSb quantum wells (QWs) was aroused. These QWs exhibit a number of remarkable properties; for example, the QW for electrons is extremely deep (1.3 eV), while the electron mobility at room and liquid-helium temperatures can be as high as 3×10^4 and 9×10^5 cm^2/(V s), respectively (see, e.g., [1–7]). The fact that the crystal-lattice parameters of InAs and AlSb are close to each other makes it possible to obtain smooth interfaces between the layers; as a result, the charge-carrier scattering by the roughness of the surface microprofile can be reduced to a minimum. The InAs/AlSb systems are promising for the development of both devices designed for operation in the midinfrared region of the spectrum and high-frequency transistors. A study of the cyclotron-resonance spectra is an effective method for determining both the degree of nonparabolicity of the conduction band and the spin-related splitting of the Landau levels in an InAs QW [8–11]. However, these studies, until now, were restricted to nominally undoped heterostructures with a two-dimensional (2D) electron concentration of no higher than 1.4×10^{12} cm^{-2}. In this paper, we report the results of studying the cyclotron resonance in AlSb/InAs/AlSb structures with QWs in which the 2D electron concentration was varied from 2.7×10^{11} to 8×10^{12} cm^{-2}. In previous publications, the cyclotron resonance was studied using the Fourier transform spectroscopy in magnetic fields that exceeded 20 kOe at frequencies higher than 1.5 THz. In this study, we used the backward-wave tubes (BWTs) as the sources of monochromatic radiation, which made it possible to study the cyclotron-resonance spectra in the frequency range from 160 to 700 GHz. In order to interpret the experimental data, we calculated the cyclotron electron masses in the context of the Kane model.

2. EXPERIMENTAL

The heterostructures under study were grown by molecular-beam epitaxy on the semi-insulating GaAs (100) substrates. Since the lattice constants of AlSb and InAs far exceed that of GaAs, the active part of the structure was grown on a composite buffer that consisted of a 200-nm-thick GaAs layer, a 100-nm-thick AlAs layer grown at 570°C, and a metamorphous buffer layer of AlSb or GaSb. The growth of the metamorphous layer started with the deposition of a 100-nm-thick AlSb layer at 570°C; on top of this layer, a 2.4-μm-thick layer of either AlSb grown at 570°C or GaSb grown at 510°C (sample 4, see table) was formed [3, 12]. For all samples, a ten-period smoothing GaSb(2.5 nm)/AlSb(2.5 nm) superlattice was grown on top of the buffer layer at 480–490°C. The active part of the structure consisted of a lower AlSb barrier with a thickness of 12 nm in undoped samples (samples 1–4) and a thickness of 40 nm in selectively doped samples (samples 5–8), an InAs QW with a nominal thickness of 15 nm, an upper barrier AlSb ($Al_{0.8}Ga_{0.2}Sb$ in sample 3) layer with a thickness of 30–40 nm, and a top coating GaSb layer that prevented the reaction of the AlSb with water vapors in the air. The active part of the structure was grown at a temperature of 480°C. A special sequence of interruptions in the supply of the materials (Al, Sb, In, and As) was used in the growth of the InAs QW; this sequence ensured that the In–Sb bonds were

Parameters of the undoped (1–4) and selectively doped (5–8) samples used in this study

Sample	n_s^{Hall}, 10^{12} cm^{-2}	$n_s^{1\text{SdH}}$, 10^{12} cm^{-2}	$n_s^{2\text{SdH}}$, 10^{12} cm^{-2}	$n_s^{3\text{SdH}}$, 10^{12} cm^{-2}	n_s^{PC}, 10^{12} cm^{-2}	μ, 10^5 cm^2 V^{-1} s^{-1}	μ_{CR}, 10^5 cm^2 V^{-1} s^{-1}	m_c/m_0
1	–	–	–	–	0.27	–	0.45	0.029–0.031
2	0.65	0.64	–	–	0.63	3.9	0.6–1.6	0.032–0.036
3	0.68	0.66	–	–	0.67	2.5	0.4–1.6	0.033–0.037
4	0.95	0.83	–	–	0.82	4.4	0.5–1.6	0.034–0.036
5	2.4	1.8	0.6	–	–	1.0	0.4	0.042–0.045
6	3.2	2.2	1.0	–	–	0.63	0.4	0.042–0.044
7	4.3	2.8	1.5	–	–	0.53	0.4	0.044–0.048
8	8.3	4.3	3.4	0.6	–	0.4	0.2	0.054–0.060

formed at both heteroboundaries of the AlSb/InAs/AlSb system, which made it possible to attain a high mobility of 2D electrons (in contrast to the mobility at the boundaries with the Al–As bonds) [13]. In samples 5–8, we performed the δ doping with Te (using a Ga_2Te_3 crucible evaporator) of the upper and lower AlSb barriers at a distance of 15 nm from the InAs QW.

In order to characterize the 2D electron gas, we studied the Hall and Shubnikov–de Haas effects in rectangular samples with an area of 15×4 mm^2 and ohmic contacts (with the geometry of the Hall bar) formed on the samples' surfaces. In studies of the cyclotron resonance, we used square samples with an area of 5×5 mm^2 and with two strip ohmic contacts. The samples were mounted in a cryomagnetic insert placed in a storage liquid-helium STG-40 Dewar flask. We used the OV-30 and OV-74 backward-wave tubes as the radiation sources; these tubes covered frequency ranges of 160–340 and 490–710 GHz, respectively. The measurements were performed at $T = 4.2$ K, using a constant radiation frequency of BWTs and the sweeping of the magnetic field that was directed perpendicularly to the samples' surface and parallel to the propagation of the BWT radiation. The radiation was modulated using a chopper (the modulation frequency $f \approx 200$ Hz). The radiation transmitted through the structure was detected using an *n*-InSb photodetector. We used a conventional scheme of lock-in amplification: The signal from the output of the lock-in amplifier was digitized using an analog-to-digital converter and was recorded as a function of the magnetic field. In order to suppress the interference effects, the substrates were wedged with an angle of 2°. For some of the samples, we measured the oscillations of the submillimeter photoconductivity in order to determine the concentration of 2D electron gas (these oscillations are similar to the Shubnikov–de Haas oscillations).

3. CALCULATION OF CYCLOTRON ELECTRON MASSES IN THE InAs/AlSb HETEROSTRUCTURES

We used the Kane Hamiltonian operator when calculating the electron spectrum. In this Hamiltonian operator, the terms proportional to the square of the wave vector and the terms that appeared owing to the absence of an inversion center in the crystal were disregarded [14]. The use of the basis suggested by Aleshkin *et al.* [15] makes it possible to represent the Hamiltonian operator in the block form as

$$H = \begin{pmatrix} H_+ & 0 \\ 0 & H_- \end{pmatrix}.$$

The wave function can be represented as

$$\psi = \begin{pmatrix} \psi_+ \\ \psi_- \end{pmatrix},$$

where $\psi_\pm$ satisfy the equations

$$H_\pm \psi_\pm = E\psi_\pm. \quad (1)$$

The electron spectrum is doubly degenerate; i.e., the same energies correspond to the $H_\pm$ operators. By solving Eq. 1, we determine the dispersion dependences of the energy of an electron in the *n*th subband ε_n on the wave vector *k*: $\varepsilon_n(k)$. Typical dispersion dependences for electrons in an InAs/AlSb QW are shown in Fig. 1.

The cyclotron masses at the Fermi level were determined from the obtained dependences $\varepsilon_n(k)$ using the formula

$$m_c = \hbar^2 k \left(\frac{d\varepsilon}{dk}\right)^{-1}. \quad (2)$$

The results of the calculations of the energy for three lower dimensional-quantization subbands in relation to the squared wave vector in an AlSb/InAs heterostructure with a QW thickness of 205 Å are shown in Fig. 1. The lattice parameter of the structure in the growth

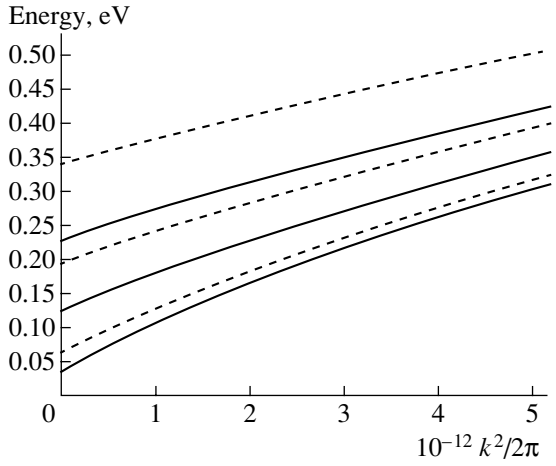

Fig. 1. The results of calculations of the energy for the three lower dimensional-quantization subbands in relation to the squared wave vector in an AlSb/InAs heterostructure with quantum-well widths of 205 Å (solid line) and 150 Å (dashed line).

plane is equal to the AlSb lattice parameter. The zero energy corresponds to the bottom of the InAs conduction band (with the dimensional-quantization energy disregarded). It is noteworthy that, if temperature is equal to zero and if only the first subband is filled, the wave vector at the Fermi level (k_F) is specified by the relation $n_s = k_F^2/2\pi$, where n_s is the concentration of 2D electron gas.

In order to test the accuracy of the algorithm used when calculating the energies of electronic states in the InAs QW, we calculated the energies of intersubband transitions that had been observed experimentally in previous studies [16, 17]. The energies of the transitions from the first subband to the second subband for the InAs QWs with widths of 6.5, 7.7, and 8.6 nm were found to be equal to 0.327, 0.273, and 0.245 eV, respectively [16]. The results of our calculation for these QWs are 0.329, 0.276, and 0.245 eV and they are in good agreement with reported experimental data.

Larrabee *et al.* [17] measured the intersubband-transition energies for the QWs with widths of 10, 8.4, 7.5, 7.0, 6.5, 6, and 5 nm. The transition energies for the four QWs with the largest width were found to be equal to 0.211, 0.244, 0.272, and 0.296 eV at 10 K. The calculated transition energies for these QWs are equal to 0.208, 0.252, 0.284, and 0.305 eV. In these structures, one should take into account the depolarization shift occurring as a result of a high electron concentration. This shift gives rise to a displacement of the line by several millielectronvolts from the short-wavelength edge that corresponds to transitions with $k = 0$ (we considered the energies of exactly such transitions). For the structures under consideration, the calculation yields a value of the transition energy that is too large, and the discrepancy between the theory and experiment increases as the QW width decreases. In all probability, this behavior is related to errors in the determination of the QW width. It is worth noting that, for the experiment under consideration [17], the discrepancy is within 5%, which indicates that the agreement between the theory and experiment is quite satisfactory.

4. RESULTS AND DISCUSSION

The parameters of the samples studied are listed in the table in the order (from top to bottom) of increasing concentration of 2D electron gas. In addition to the total concentration n_s^{Hall} determined from the Hall effect measurements, the table lists the electron concentrations in the first, second, and third dimensional-quantization subbands as determined from the Fourier analysis of the Shubnikov–de Haas oscillations (n_s^{1SdH}, n_s^{2SdH}, and n_s^{3SdH}); the concentration determined from oscillations of the submillimeter photoconductivity (n_s^{PC}) is also listed. The highest mobility ($\mu \approx 4 \times 10^5$ cm^2/(V s)) was observed in undoped samples 2–4, where the typical charge-carrier concentration was in the range of $(6–9) \times 10^{11}$ cm^{-2}. In such structures, the mobility is limited by the long-range potential of remote ionized impurities. This potential is screened by the charge carriers [12]. In nominally undoped samples, electrons are supplied to the InAs QW by surface donors in the top GaSb layer [4] and deep donors in the bulk of the Al(Ga)Sb barrier layers [18–20]. In selectively doped samples 5–8, the charge-carrier mobility decreases gradually as the electron concentration increases as a result of the charge-carrier scattering by ionized donors in the δ-doped layers. As can be deduced from the table, the electron concentrations determined for samples 2–4 from the measurements of the Hall and Shubnikov–de Haas effects differ somewhat. This difference is probably caused by the existence of a conductivity channel that is parallel to the InAs QW rather than by the filling of the second dimensional-quantization subband. The spectral analysis of the Shubnikov–de Haas oscillation in selectively doped samples 5–6 shows that the filling of the second subband only sets in at $n_s \approx 1.2 \times 10^{12}$ cm^{-2} (see table).

Typical cyclotron-resonance spectra are shown in Figs. 2a and 2b. It is worth noting that the electron mobility as determined directly from the half-width of the cyclotron-resonance line $\Delta H_{1/2}$ ($\mu_{\mathrm{CR}} = e/m_c\gamma$, where $\gamma = (1/2)\omega\Delta H_{1/2}/H_{\mathrm{res}}$), is much lower than that obtained from the measurements of the Hall effect and electrical conductivity (see table). This circumstance is related to the cyclotron-absorption saturation caused by a high mobility and/or a high charge-carrier concentration in the samples under study. The values of the cyclotron electron masses $m_c = eH_{\mathrm{res}}/(2\pi cf)$ determined from the magnitude of the resonance magnetic field H_{res} are listed in the table. It can be seen that the effective mass

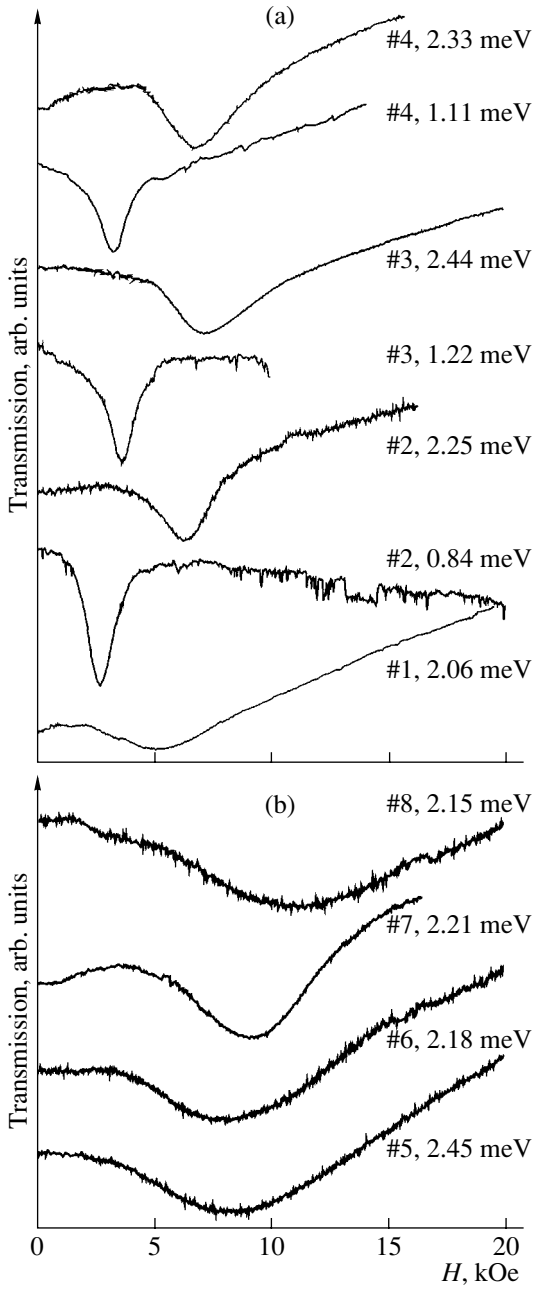

Fig. 2. Typical cyclotron-resonance spectra for undoped samples (a) 1–4 and selectively doped samples (b) 5–8 at various energies of photons. The sample numbers and the photon energies are indicated.

increases noticeably as the concentration (and, accordingly, the Fermi energy) increases. This increase in the effective mass is typical of semiconductors with a nonparabolic dispersion relation and has been studied in sufficient detail for nominally undoped InAs/AlSb heterostructures with QWs [11]. In order to interpret the results obtained, we calculated, in this study, the cyclotron masses at the Fermi level (2) in the context of the above-described simplified Kane model. The results of our calculations show that, as two or three of the dimensional-quantization bands are filled with electrons, the effective charge-carrier masses at the Fermi level differ insignificantly in different subbands and this difference in effective masses lies within experimental errors when determining the cyclotron masses (see table).

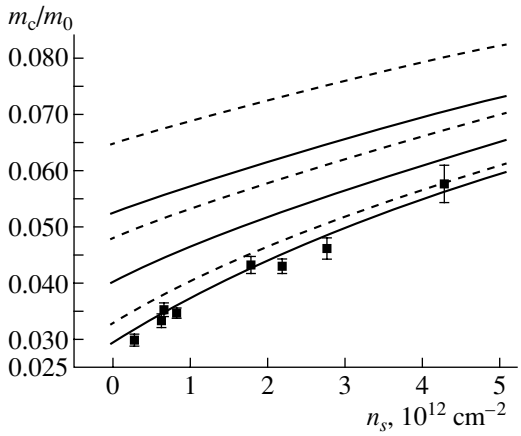

Fig. 3. Dependence of the cyclotron mass on the electron concentration: the theoretical calculation for the first three subbands in the InAs quantum wells with widths of 205 Å (solid lines) and 150 Å (dashed lines). Experimental data are represented by closed squares.

In Fig. 3, we show the measured values of the cyclotron electron masses in relation to the charge-carrier concentration in the first subband and also the calculated dependences of the cyclotron mass for the InAs QWs with widths of 205 and 150 Å. It can be seen that the calculation for the nominal (determined from the growth parameters) QW width of 150 Å yields a much worse agreement with the experiment than that for the QW width of 205 Å. Since the used model of the dispersion relation for electrons ensures good agreement between the theory and experiment in calculations of the energies of intersubband transitions, it is reasonable to assume that the discrepancy between the results of calculations and experimental data is caused by an insufficiently accurate calibration of the growth rates of the layers. In order to verify this assumption, one has to perform independent measurements of the thickness of the InAs layer in the studied structures.

ACKNOWLEDGMENTS

We are grateful to I.V. Erofeeva and A.N. Panin for their help with the preparation of measurements.

REFERENCES

1. G. Tuttle, H. Kroemer, and J. H. English, J. Appl. Phys. **65**, 5239 (1989).
2. H. Kroemer, C. Nguyen, and B. Brar, J. Vac. Sci. Technol. **10**, 1769 (1992).
3. C. Nguyen, B. Brar, C. R. Bolognesi, *et al.*, J. Electron. Mater. **22**, 255 (1993).

4. Ch. Gauer, J. Scriba, A. Wixforth, *et al.*, Semicond. Sci. Technol. **8**, S137 (1993).
5. B. R. Bennett, M. J. Yang, B. V. Shanabrook, *et al.*, Appl. Phys. Lett. **72**, 1193 (1998).
6. S. Brosig, K. Ensslin, B. Brar, *et al.*, Physica E (Amsterdam) **2**, 214 (1998).
7. M. J. Yang, K. A. Cheng, C. H. Yang, and J. C. Culbertson, Appl. Phys. Lett. **80**, 1201 (2002).
8. M. J. Yang, P. J. Lin-Chung, R. J. Wagner, *et al.*, Semicond. Sci. Technol. **8**, S129 (1993).
9. J. Scriba, A. Wixforth, J. P. Kotthaus, *et al.*, Semicond. Sci. Technol. **8**, S133 (1993).
10. M. J. Yang, P. J. Lin-Chung, B. V. Shanabrook, *et al.*, Phys. Rev. B **47**, 1691 (1993).
11. C. Gauer, J. Scriba, A. Wixforth, *et al.*, Semicond. Sci. Technol. **9**, 1580 (1994).
12. Yu. G. Sadofyev, A. Ramamoorthy, B. Naser, *et al.*, Appl. Phys. Lett. **81**, 1833 (2002).
13. G. Tuttle, H. Kroemer, and J. H. English, J. Appl. Phys. **67**, 3032 (1990).
14. G. Bastard, *Wave Mechanics Applied to Semiconductor Heterostructures* (Halsted, New York, 1988), pp. 31–61.
15. V. Ya. Aleshkin, A. V. Anshon, T. S. Babushkina, *et al.*, Fiz. Tekh. Poluprovodn. (St. Petersburg) **26**, 516 (1992) [Sov. Phys. Semicond. **26**, 291 (1992)].
16. I. Prevot, B. Vinter, F. H. Julien, *et al.*, Phys. Rev. B **64**, 195318 (2001).
17. D. C. Larrabee, G. A. Khodaparast, J. Kono, *et al.*, Appl. Phys. Lett. **83**, 3936 (2003).
18. A. Furukawa and S. Ideshita, J. Appl. Phys. **75**, 5012 (1994).
19. D. J. Chadi, Phys. Rev. B **47**, 13478 (1993).
20. J. Shen, J. D. Dow, S. Yu. Ren, *et al.*, J. Appl. Phys. **73**, 8313 (1993).

Translated by A. Spitsyn

Semiconductors, Vol. 39, No. 1, 2005, pp. 67–72. Translated from Fizika i Tekhnika Poluprovodnikov, Vol. 39, No. 1, 2005, pp. 76–81.

LOW-DIMENSIONAL SYSTEMS

Terahertz Luminescence of GaAs-Based Heterostructures with Quantum Wells under the Optical Excitation of Donors

N. A. Bekin*, R. Kh. Zhukavin*, K. A. Kovalevskiĭ*, S. G. Pavlov*, B. N. Zvonkov, E. A. Uskova**, and V. N. Shastin*^**

**Institute for Physics of Microstructures, Russian Academy of Sciences, Nizhni Novgorod, 603950 Russia*
^e-mail: shastin@ipm.sci-nnov.ru
***Nizhni Novgorod Physicotechnical Research Institute, Nizhni Novgorod State University, pr. Gagarina 23/5, Nizhni Novgorod, 603950 Russia*

Submitted June 1, 2004; accepted for publication June 14, 2004

Abstract—Spontaneous emission from selectively doped GaAs/InGaAs:Si and GaAs/InGaAsP:Si heterostructures is studied in the frequency range of ~3–3.5 THz for transitions between the states of the two-dimensional subband and donor center (Si) under the condition of excitation with a CO_2 laser at liquid-helium temperature. It is shown that the population inversion and amplification in an active layer of 100–300 cm^{-1} in multilayered structures with quantum wells (50 periods) and a concentration of doping centers $N_D \approx 10^{11}$ cm^{-2} can be attained under the excitation-flux density 10^{23} photons/(cm^2 s). © *2005 Pleiades Publishing, Inc.*

1. INTRODUCTION

The possibility of using quantum-dimensional heterostructures to attain the effect of stimulated radiation under an intraband optical excitation was, for the first time, shown in [1]. Lasing at the wavelength λ = 15.5 μm was observed for intersubband transitions in two-dimensional (2D) electron gas inside the GaAs quantum wells (QWs) of GaAs/AlGaAs structures using a four-level scheme of excitation by the radiation of a CO_2 laser (λ = 9.7 μm). In this case, the lower level of the operating transition was rapidly depleted by the emission of optical phonons for 0.5×10^{-12} s. However, for the upper level, the relaxation via optical phonons was somewhat suppressed (time 0.7×10^{-12} s) by the fact that the states of 2D electrons involved in the nonradiative transition were separated both in the coordinate space and in the space of wave vectors. Unfortunately, this line of research was not continued and was just an episode in the background of research into quantum-cascade lasers (see, for example, [2]) with current excitation. These lasers actively use the same principle of active medium formation, but under the conditions of the so-called vertical electron transport. This experimental study is the first step in an examination of the possibility of forming an inverse population and obtaining the effects of amplification for impurity–band transitions in the QW heterostructures. Therefore, we used optical excitation, since this approach considerably simplified the design of the required heterostructures.

It is noteworthy that the effects of stimulated radiation for the intracenter transitions of shallow-level donors that were optically excited had already been observed in a bulk semiconductor, specifically silicon [3]. However, the extension of similar studies to selectively-doped quantum-confined heterostructures seems to be important since resonant tunneling allows one to accomplish the current excitation of inverted electron distributions both for intracenter and at impurity-band optical transitions. In this case, due to the quantitative characteristics found in the spectra of states with shallow impurity levels and, which is of no small importance, with infinitesimal lattice absorption, the Si/SiGe heterostructures are of the most interest. It is clear that the occurrence of band offsets, the built-in strain, a high concentration of doping centers, and other features of artificial media for lowering dimensionality introduce complications. These complications do not allow one to blindly reproduce the effects already realized for bulk material. However, these features can offer advantages associated with a possible purposeful modification to the charge-carrier state. Taking into account the factor of technological availability and a striving to simplify the objects under study, we chose the selectively Si-doped GaAs/InGaAs and InGaAsP/GaAs multilayered QW heterostructures with one or two subbands of dimensional quantization. In the latter case, a shallow QW was incorporated into the barrier region. We adjusted the spectrum of states so that the intersubband radiative transitions were of little importance. In this case, the optical transitions between the 2D continuum and the ground state of the Coulomb center gave rise to a photoinduced emission in the terahertz frequency range. When interpreting the data, we attached much importance to comparing the results obtained for various structures, which differ in the concentration of doping centers and in their spatial distribution between QWs and barriers.

1063-7826/05/3901-0067$26.00 © 2005 Pleiades Publishing, Inc.

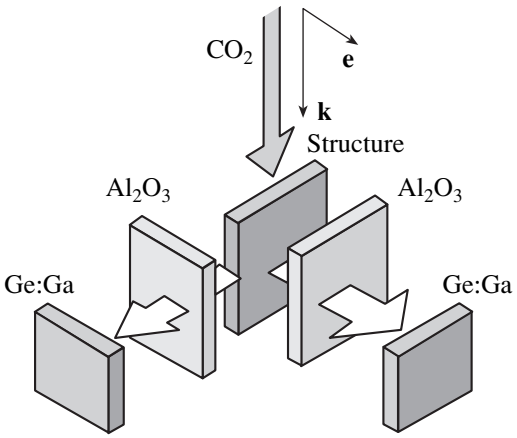

Fig. 1. Optical layout for measuring the spontaneous emission. **k** is the propagation vector of the electromagnetic wave, and **e** is the polarization vector.

2. EXPERIMENTAL

Figure 1 shows the optical layout of the measurements. We used a conventional sealed-off CO_2 laser with a longitudinal discharge as the pumping source. The laser operated in the active Q-switched mode and provided a peak power as high as 2 kW in a pulse with a duration of 300 ns. When measuring the current–voltage (*I–V*) characteristics and photocurrent, we used a synchronized pulsed voltage source with a pulse duration of 10 μs, which allowed us to avoid any undesirable overheating of the samples under study. The data were recorded using a digital oscillograph and were averaged over 1024 representations. The radiation was observed from the end of structures that were $0.5 \times 0.7 \times 0.04$ cm^3 in size and cooled with liquid helium. Optical excitation was accomplished using the emission of a CO_2 laser with a wavelength of 10.6 μm, which propagated in the growth-layer plane in a direction towards a narrow (0.5 cm) face. The characteristic absorption length of the pumping radiation for 50-period GaAs/InGaAs structures is estimated at 0.4 cm at a doping level of 2×10^{11} cm^{-2} per period. To detect the terahertz radiation, we used a Ge:Ga photodetector cooled with liquid helium and protected from the scattered pumping radiation with a sapphire filter. To increase the sensitivity, we coupled the photodetector output to an amplifier with an amplification band of 1 MHz.

The samples under study (see Tables 1, 2) were grown on a semi-insulating GaAs substrate 0.04 cm thick using the process of MOC-hydride epitaxy (vapor-phase epitaxy from metal-organic compounds).

The measured electron mobility for all GaAs/InGaAs structures was close to 4×10^3 cm^2/(V s) at room temperature and somewhat increased, to ~$(6–8) \times 10^3$ cm^2/(V s), at liquid-helium temperature.

The results of measurements of the dark current and photocurrent for structures 3122 and 3123 in relation to the voltage applied in the plane of the structures are shown in Figs. 2 and 3, respectively; in these structures, either only QWs or only barriers were doped. Similar results were also obtained for all the other samples listed in Table 1. From dark *I–V* characteristics, we may conclude that electron mobility increases only slightly as the applied field increases. The concentration of free (delocalized) electrons was high, even at liquid-helium temperature, for structures of all types, although this concentration was evidently lower when only QWs were doped. The *I–V* characteristics show that the breakdown regions of the delocalized states of the donors are rather diffuse. It is noteworthy that, in an approximation of the isolated Coulomb center, the binding energy of donors for the doped central parts of QWs was close to 10 meV, while for doped barriers in the structures (Table 1) this energy was no higher than 3–4 meV. At ~4.2 K, this value is quite sufficient to freeze the conductivity, whose presence of is associated with strong concentration-related broadening of bound states and their partial overlap with the 2D continuum (delocalization). The photocurrent measurement data in relation to the voltage applied confirm this point of view.

Table 1. Parameters of the $In_xGa_{1-x}As/GaAs$ heterostructures

Structure no.	Width, nm/In content, *x*			n_s, 10^{11} cm^{-2}	Impurity location		
	deep quantum well	barrier	shallow quantum well		deep quantum well	barrier	shallow quantum well
3120	7/0.17	4/0	14/0.05	2.2	–	–	Select.
3121	7/0.17	4/0	14/0.05	4.7	δ	–	Select.
3122	7/0.17	4/0	14/0.05	2.5	δ	–	–
3123	7/0.17	22/0	–	2.4	–	Select.	–
3124	7/0.17	22/0	–	5.1	δ	Select.	–
4167	7/0.17	22/0	–	1.3	–	Select.	–
4169	7/0.17	4/0	14/0.05	1.5	–	–	Select.

Note: Select. denotes selective doping.

Figures 2 and 3 also show the results of photocurrent measurements. The photocurrent is caused by the electron excitation from localized donor states to the 2D subband of dimensional quantization. We estimated the cross section of photoionization at ~10^{-14} cm^2 (see below). Other parameters, which specify the photocurrent, are the mobility of 2D electrons, the cross section of their capture at the charged Coulomb center, and the rate of impact ionization of localized states. The results of measurements show that, in fields exceeding the breakdown field of the donor centers, the photocurrent decreases. A rigorous quantitative analysis of populations is rather complex and requires the use of numerical simulation methods, which are beyond the scope of this report. However, a comparison of the data obtained for the samples with a different type and various levels of doping allows us to reach certain conclusions. For example, from the peak width of the photocurrent curve and its dependence on the parameters of the structures, we can conclude that the bound states of donors form a broad band of localized states and that the width of this band increases as the concentration of doping centers increases. In this case, the concentration of localized states increases disproportionately to the concentration of introduced donors and does not exceed 10^{11} cm^{-2}, even if the QWs are doped. This behavior is caused by the broadening of the energy spectrum of the bound states of neutral donor centers and their partial delocalization by an inhomogeneous field of neighboring charged donors and acceptors. In addition, the measurements of the current allow us to conclude that the residual doping level in the structures under study is high (~10^{16} cm^{-3}). This circumstance leads to the rise in dark conductivity and to an additional photocurrent, which is especially noticeable at a relatively low (~10^{10} cm^{-2}) concentration of purposefully introduced centers.

An important feature of the photocurrent is its leveling off at the excitation intensity $I > 0.4$ kW/cm^2 (Fig. 4). This phenomenon was observed for all GaAs/InGaAs structures when a low field was applied but vanished for characteristic breakdown fields and above. This result indicates that the rate of trapping of 2D electrons at the Coulomb charged centers, without heating the charge carriers with an external electric field, is no higher than $\nu \approx 10^8$ s^{-1}. This rate is mainly determined by the emission of optical (rather than acoustic) phonons by energetic electrons from the tail, which appears due to electron–electron collisions, of the distribution function. The above estimate is obtained under the assumption that the cross section of the photoionization of donors in the GaAs/InGaAs structures is close to 10^{-14} cm^2. In the fields exceeding the breakdown field, the collisions of heated electrons play a decisive role in the ionization of donors. This factor increases the ionization rate of the centers, and the pumping-intensity dependence of photocurrent becomes linear. At the same time, the rate of recombination with the emission of optical phonons should also increase. The mentioned factors allow us to understand the main features of the identified dependences of the photocurrent. For the GaAs/InGaAsP structures, where

Table 2. Parameters of the $In_{0.07}Ga_{0.93}As_{0.86}P_{0.14}$/GaAs heterostructures

Structure no.	Width, nm		n_s, 10^{11} cm^{-2}	Impurity location	
	quantum well	barrier		quantum well	barrier
4157	7	20	0.21	–	–
4159	7	20	0.7	δ	–
4160	7	20	0.44	δ	–
4161	7	20	1.1	–	Selective doping

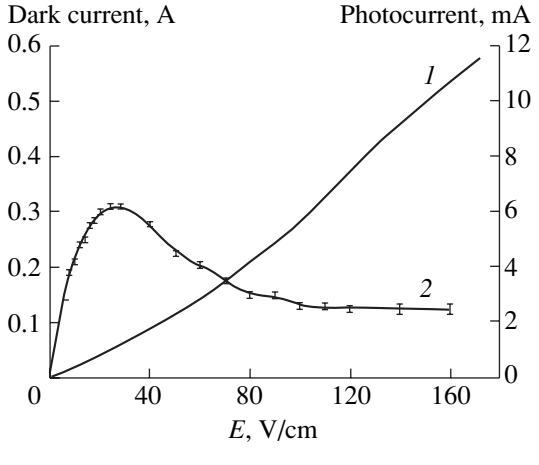

Fig. 2. Dependences of (*1*) dark current and (*2*) photocurrent on the applied electric field E for the highest pump intensity effected by the radiation of a CO_2 laser for structure 3122.

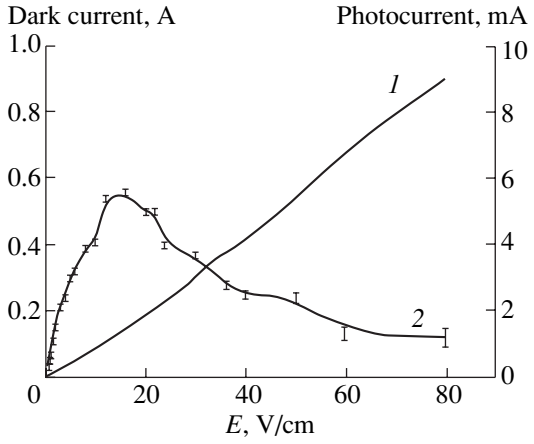

Fig. 3. (*1*) Dark current and (*2*) photocurrent in relation to the applied electric field E for the highest pump intensity effected by the radiation of a CO_2 laser for structure 3123.

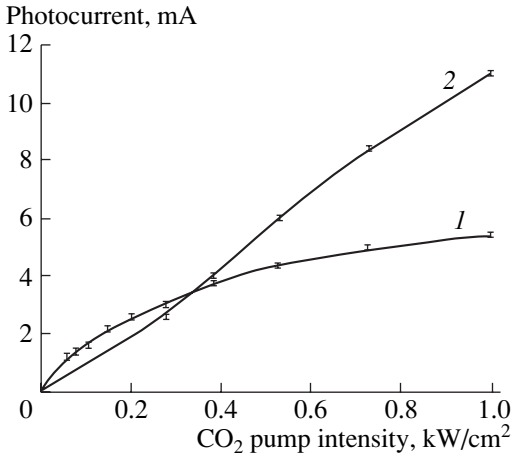

Fig. 4. Photocurrent as a function of the pump intensity produced by the radiation of a CO_2 laser for structure 3123 at an applied electric field of (*1*) 4 and (*2*) 20 V/cm.

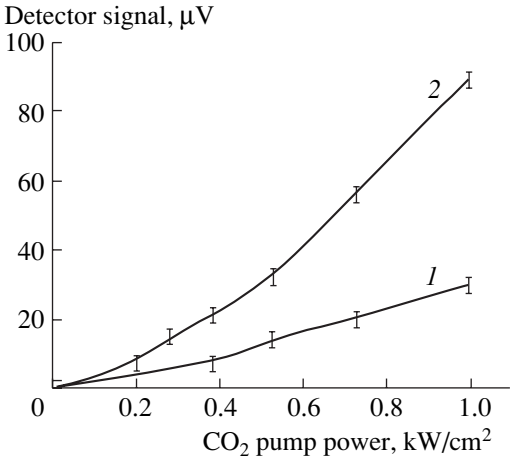

Fig. 5. The intensity of spontaneous radiation as a function of the pump intensity produced by the radiation of a CO_2 laser for structure 3123 with the detection (*1*) from the structure plane and (*2*) from the structure end.

the conduction band offset was ~10 meV, the voltage dependences of the photocurrent were almost linear. This behavior can be attributed to a decreased cross section of photoexcitation, which is lower by a factor of approximately 2 in this case. The photocurrent measurement data are important and used in full measure to interpret the data on the emission of heterostructures.

Spontaneous emission in the terahertz frequency range was observed for all the structures listed in Table 1. The emission intensity was proportional to the concentration of doping centers, with small deviations, within the measurement of error, for the samples with a different doping distribution over the layers of the heterostructure. The radiation intensity per donor was highest for the structures with doped QWs and barriers, and lowest for the structures that only had the barriers doped. Figures 5 and 6 show the typical photopumping-power dependences for the intensity of terahertz radiation. It is noteworthy that these dependences are superlinear. This behavior was found to be most pronounced for samples 3122 and 3123, and was practically unobserved within the accuracy of the measurements for the samples with the doping level ~10^{10} cm^{-2} or when the terahertz emission was detected from the structure plane. Using filters made of KRS-5 and fused quartz that were cooled by liquid helium, we found that the energy range of emitted photons was 12–14 meV.

We believe that the observed spontaneous emission is associated with optical transitions of 2D electrons from the lower subband of dimensional quantization of the QW to the localized states of ionized donors. The superlinear pumping-power dependence of the spontaneous-emission intensity is indicative of the gain for these transitions with the gain factor $\alpha_{eff} \approx 0.5$ cm^{-1} at a pumping radiation intensity $P \approx 1$ kW/cm^2. In our estimations, we assumed that $I = I_0 \exp(\alpha_{eff} d_{eff})$, where d_{eff} is the effective optical thickness and I_0 is the effective

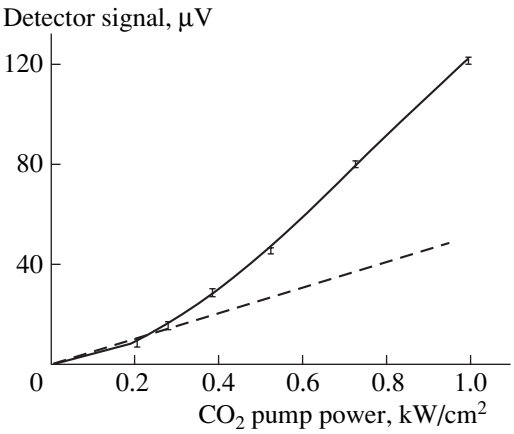

Fig. 6. The intensity of spontaneous radiation as a function of the pumping power produced by the radiation of a CO_2 laser for structure 3122 with the detection from the structure end (the solid line) and the extrapolation of the linear dependence (dashed line).

intensity of the spontaneous emission. We do not know the parameter d_{eff} exactly, but assumed that it was equal to the sample length (~1 cm). That this parameter could be larger by a factor of 2–3 due to the effects of internal reflection of outgoing radiation is not excluded. Another feature of the electrodynamics of the structures emerges in connection with a thick (0.04 cm) GaAs semi-insulating substrate. We can disregard the absorption of terahertz radiation in this substrate since the corresponding absorption coefficient is no larger than 0.5 cm^{-1} in the mentioned frequency range at liquid-helium temperature [4]. However, the overlap factor of the active medium and the waveguide formed by the substrate is small and amounts to a mere ~2×10^{-3}, which substantially decreases the value of the observed gain. In this case, the recalculated gain of the active

layer is rather high, $\alpha \approx 250$ cm^{-1} (pumping $P \approx 1$ kW/cm^2). This value exceeds the published data on this parameter for a quantum-cascade laser operating at almost the same frequencies [5].

Thus, optical excitation of neutral Si donors in the selectively doped InGaAs/GaAs and InGaAsP/GaAs structures under study leads to a pronounced gain for optical transitions of electrons from the 2D continuum to the localized states of positively charged donor centers. It is noteworthy that we failed to reveal any polarization effects with respect to the pump radiation. This fact requires additional verification but could be associated with depolarization of the pump radiation in the optical channel.

In order to analyze the experimental data, we calculated the localized and 2D electron states for the structures under consideration. For this purpose, we used the approximation of the isolated Coulomb center. It was already mentioned above that this is a rather rough approach for the structures under study. However, the simplified model (see below) allowed us to reveal necessary reference points for the values of energy levels and cross sections of optical transitions for localized, quasi-localized (resonant), and free 2D states in quantum wells.

3. THEORY

In our calculations, we used an expansion in terms of the wave functions of the electrons in the QW that were undisturbed by the impurity potential [6, 7]. In this case, since the distance between subbands in QWs, in the structures under study, considerably exceeds the binding energy of a donor, we disregarded the contribution of the three-dimensional (3D) continuum to the wave functions of localized states of donors. This approximation also remains admissible for a QW with a single subband if the energy spacing between the subband bottom and the boundary of the 3D continuum exceeds the binding energy of the donor.

When calculating the absorption cross section of the infrared (IR) radiation, we used the following simplifications: First, we disregarded the modification of the states of the 3D continuum by the Coulomb potential in calculations of the photoionization cross section of QWs. Second, the broadening of absorption lines was taken into account by replacing the Dirac function, which is responsible for the energy conservation for optical transitions, with the Lorentz function $\pi^{-1}\Gamma/[(E_f - E_i - \hbar\omega)^2 + \Gamma^2]$ when using the Fermi golden rule. Here, E_i and E_f are the energies of the initial and final electron states, $\hbar\omega$ is the photon energy, and Γ is the broadening parameter. The parameter Γ, with respect to the discussed experiment, approximately represents the inhomogeneous line broadening. To reveal the degree to which the choice of Γ affects the absorption cross section of IR radiation in different spectral ranges, we carried out calculations for two values of Γ, namely, 1 and 3 meV, with the donor located at the QW center (Fig. 7). In addition, Fig. 7 shows the absorption cross section calculated by averaging the location of the donors [8], which are distributed along the growth axis of the heterostructure according to the Gaussian law. The specified method takes into account only inhomogeneous broadening of absorption lines, which emerges due to the dependence of the impurity spectrum on its location in the quantum-confinement layer.

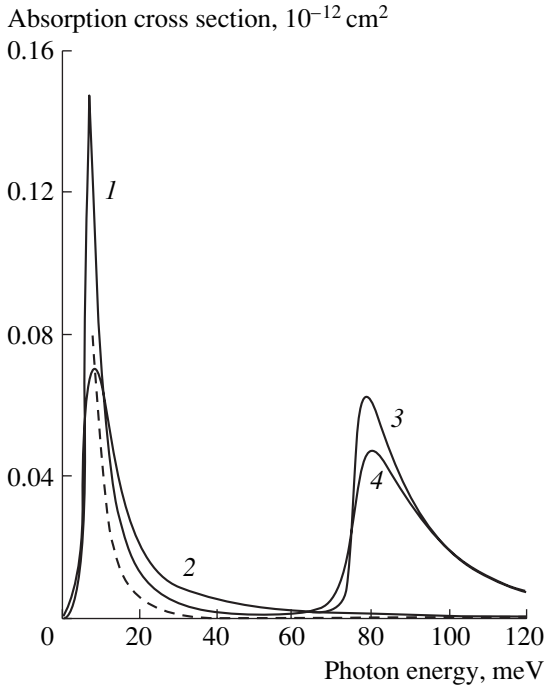

Fig. 7. The optical-absorption cross section for transitions from the ground donor state to the 2D and 3D states for the electromagnetic wave (dashed line, *1*, *2*) circularly polarized in the plane of the layers and (*3*, *4*) linearly polarized normally to the growth layers for the $In_{0.17}Ga_{0.83}As/GaAs$ structure with the doped $In_{0.17}Ga_{0.83}As$ quantum well 7 nm wide. The dashed line corresponds to the cross section of photoexcitation to the 2D donor states distributed (according to the Gaussian law) symmetrically relative to the layer middle with a variance of 2 nm. For comparison, the cross section of the photoionization of the donor located at the quantum well center is shown for the homogeneous broadening of its ground state (*1*, *3*) $\Gamma = 1$ meV and (*2*, *4*) $\Gamma = 3$ meV.

In the calculations carried out, we did not directly take into account an important mechanism of line broadening, the mutual effect of impurity centers. Therefore, the results of the calculations of absorption cross sections are especially estimative. This is particularly true when related to the frequency range, in which the emission was observed. Figure 7 shows that the absorption cross section depends heavily on the used parameter Γ in this range. The calculation of the cross section of optical transitions performed in terms of the dependence of the ionization energy of the center on its location in the QW (dashed line in Fig. 7) yielded closer but somewhat lower values. It is noteworthy that the

absorption cross section in the range 10–20 meV depends only slightly on the width of the selectively doped layer for sufficiently abrupt impurity distributions with a spread no larger than 2 nm along the growth axis of the heterostructure.

In the range 60–120 meV, the absorption cross section depends on the parameter Γ only near the photoionization threshold of the QW. For the samples studied, the energy of the pump photon ($\hbar\omega$ = 117 meV) noticeably exceeds the mentioned threshold. Therefore, the calculated cross sections of the photoionization of QWs produced by the emission of the CO_2 laser are satisfactorily accurate.

It is very important that the cross section of the intraband absorption of the IR radiation should have a sharply pronounced polarization dependence. The absorption cross section of the radiation with the polarization vector normal to the heterointerfaces is relatively large for photon energies, which approximately correspond to the distance between the subbands or the photoionization of the QW. In terms of this circumstance, in the experiments carried out, the radiation of the CO_2 laser was introduced into the heterostructure end to ensure the efficiency of the optical excitation.

For frequencies lower than the frequencies of intersubband transitions (in our case, this is the range of the photoinduced emission), the effects of optical transitions, in contrast, should be highly pronounced when the electromagnetic wave in the QW plane is polarized. Here, the specific features of the 2D structures manifest themselves, which implies that the spatial confinement in the QW profoundly affects the wave functions of electron states. As a result, the dipole moments corresponding to optical transitions between the localized states and to the impurity-band transition are aligned almost exclusively in the plane of the quantum-confinement layers.

4. CONCLUSIONS

The reported experimental data indicate that it is possible to form an inverted electron-distribution function and related gain for impurity-band transitions of the Si donor centers in the selectively doped quantum-confinement GaAs/InGaAs and InGaAsP/GaAs QW structures, when under intraband optical excitation using the radiation of the CO_2 laser. To attain the effects of the stimulated emission, a cavity based on the reflection from structure cleaved surfaces may be used. However, it is then necessary to increase the overlap factor of the active medium with the waveguide mode by shifting the latter closer to the heterostructure. This can be attained using a heavily doped GaAs layer specially grown for this purpose [9–11]. In conclusion, we would like to mention the situation where the optical excitation of the inverse electron distribution for the transitions from the 2D states of quantum wells to the localized states of impurity centers can be replaced by electric-current pumping under the conditions of resonant tunneling. We refer to the multilayered structures with the δ-doped barrier layers, in which the resonance states of the Coulomb centers are located between two weakly coupled QWs. In corresponding layouts, it is possible to avoid a complex system of variable-thickness QWs that appreciably complicates the design of existing quantum-cascade lasers based on intersubband transitions. As a result, one can attain a higher efficiency of induced radiation processes due to a larger gain cross section for operating transitions and due to a decrease in the detrimental factor of electron–electron collisions.

ACKNOWLEDGMENTS

This study was supported by the Russian Foundation for Basic Research (RFBR) (project nos. 02-02-16790 and 03-02-16775); the Joint Program of the Russian Foundation for Basic Research and the German Research Society (project no. 03-02-04010); and the Council on Grants of the President of the Russian Federation (grant no. MK-2442.2003.02).

REFERENCES

1. O. Gauhier-Lafaye, P. Boucaud, F. H. Julien, *et al.*, Appl. Phys. Lett. **71**, 3619 (1997).
2. J. Faist, F. Capasso, S. Sirtori, *et al.*, Nature **387**, 777 (1997).
3. V. N. Shastin, E. E. Orlova, R. Kh. Zhukavin, *et al.*, in *Towards the First Silicon Laser*, Ed. by L. Pavesi, S. Gaponenko, and L. Dal Negro (Kluwer Academic, Dordercht, 2003), p. 341.
4. C. J. Johnson, G. H. Sherman, and R. Weil, Appl. Opt. **8**, 1667 (1969).
5. R. Köhler, A. Tredicucci, F. Beltram, *et al.*, Appl. Phys. Lett. **82**, 1518 (2003).
6. N. A. Bekin, L. V. Krasilnikova, S. G. Pavlov, and V. N. Shastin, Phys. Status Solidi C **0** (2), 661 (2003).
7. N. A. Bekin, in *Proceedings of Meeting on Nanophotonics* (Nizhni Novgorod, 2004), p. 55.
8. R. L. Greene and K. K. Bajaj, Phys. Rev. B **34**, 951 (1986).
9. M. Rochat, M. Beck, J. Faist, and U. Oesterle, Appl. Phys. Lett. **78**, 1967 (2001).
10. J. Ulrich, R. Zobl, N. Finger, *et al.*, Physica B (Amsterdam) **272**, 216 (1999).
11. C. Sirtori, A. A. Tredicucci, F. Capasso, *et al.*, Opt. Lett. **23**, 463 (1998).

Translated by N. Korovin

Semiconductors, Vol. 39, No. 1, 2005, pp. 73–76. Translated from Fizika i Tekhnika Poluprovodnikov, Vol. 39, No. 1, 2005, pp. 82–86.

LOW-DIMENSIONAL SYSTEMS

Efficient Near IR Photoluminescence from Gallium Nitride Layers Doped with Arsenic

A. V. Andrianov*^, S. V. Novikov*, I. S. Zhuravlev*, T. Li, R. Xia**, S. Bull**, I. Harrison**, E. C. Larkins**, and C. T. Foxon****

**Ioffe Physicotechnical Institute, Russian Academy of Sciences, St. Petersburg, 194021 Russia*
^e-mail: alex.andrianov@mail.ioffe.ru
***School of Physics and Astronomy, School of Electrical and Electronic Engineering, University of Nottingham NG7 2RD, UK*

Submitted June 1, 2004; accepted for publication June 16, 2004

Abstract—Photoluminescence in the 1.2–1.4 eV spectral range from GaN:As layers grown on (0001) Al_2O_3 substrates was observed and studied. The photoluminescence is attributed to radiative recombination in GaAs nanocrystallites, self-organized in the GaN matrix during growth. The photoluminescence intensity attains a maximum at a growth temperature of ~780°C, which is explained by the competition between several temperature-dependent processes that affect the formation of GaAs nanocrystallites. Sharp emission lines were observed at the high-energy edge of the photoluminescence band. These lines are caused by an emission of bound excitons in the GaAs nanocrystallites and by phonon replicas of the bound-exciton emission. The energies of the corresponding optical phonons are typical of GaAs. The photoluminescence-excitation spectra exhibit features related to resonantly excited free and bound excitons as well as to excitons formed simultaneously with the emission of optical phonons. © *2005 Pleiades Publishing, Inc.*

Recently, considerable interest has arisen in the materials of the GaAsN system [1]. This interest is caused by a combination of the unique physical properties of these materials and by their potential to be the basis for a new generation of light-emitting devices for the telecommunication wavelength range (1.3–1.55 μm) [1, 2]. It should be noted that, previously, GaAs doped with nitrogen was intensively studied (see, e.g., [3, 4]), whereas GaN doped with arsenic has attracted interest only recently. In [5, 6], it was shown that GaN:As grown by molecular-beam epitaxy (MBE) exhibits intense photoluminescence (PL) in the blue spectral range (2.6 eV), which arises due to optical transitions that involve doubly charged ions (As^{++}). In [7, 8], observation of IR PL in this material (in the range 1.2–1.4 eV) was also reported. The IR PL in GaN:As grown by MBE is caused by radiative recombination in GaAs nanocrystallites formed in the GaN matrix during growth. The GaAs nanocrystallites embedded in a wide-gap GaN host matrix may prove to be of interest for applications in photonics, provided that one is able to control their formation. In this paper, we report the results of our investigations into the mechanisms of the radiative recombination responsible for IR PL in GaN:As. In addition, we report our results on the effect of the growth conditions of GaN:As layers on IR PL.

In our research, GaN:As layers grown by plasma MBE on sapphire substrates with the orientation (0001) were used. The thickness of the gallium nitride layers amounted to 1.0–2.5 μm. The MBE conditions were described in detail in [5]. The growth of the epitaxial layers was monitored by reflection high-energy electron diffraction, and the layers obtained were characterized by atomic-force microscopy and X-ray diffraction analysis. According to the X-ray measurements, the samples consisted of GaN layers that were oriented in the (0001) plane and contained GaAs crystallites oriented in the (111) plane. The intensity of the X-ray peak of the GaAs shows that, in the material obtained at the substrate temperature $T_{gr} \approx 800$°C, the volume fraction of the GaAs crystallites amounts to ~0.03%. An analysis of the shape of the X-ray diffraction curves using the Scherrer relations [9] made it possible to estimate the typical dimensions of the GaAs crystallites. The average dimension of the crystallites in the growth direction is ~22 nm and for those in the plane of the substrate, ~200 nm. This observation allows us to conclude that the GaN matrix does contain GaAs nanocrystallites.

Both steady-state and time-resolved types of PL were measured in the temperature range T = 6–300 K. As photoexcitation sources, we used (i) a cw Ar^+ laser emitting at 304 nm in the UV range, as well as at 488 and 514.5 nm in the visible range; (ii) a cw titanium–sapphire laser emitting in the range 700–850 nm; and (iii) a pulsed nitrogen laser with a radiation wavelength of 337 nm, pulse duration of 6 ns, and pulse-repetition frequency of 500 Hz. The spectra were recorded using a grating monochromator with a reciprocal linear dispersion of 16 Å/mm.

Figure 1 shows typical spectra of IR PL from GaN:As layers excited with light where the energy of the photons is greater than the band gap (E_g) of GaN

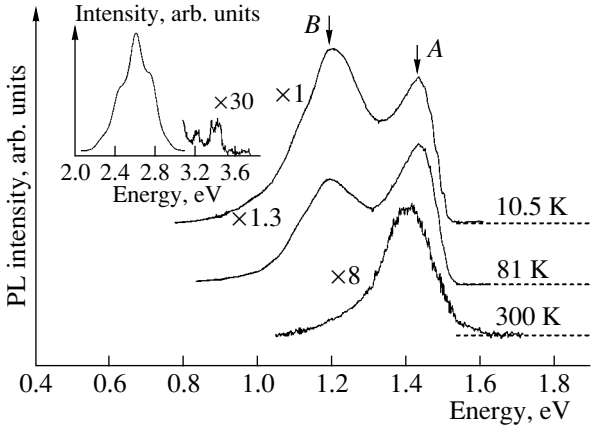

Fig. 1. Typical spectra of the IR PL of GaN:As in the temperature range 10.5–300 K. The spectra are excited by the radiation, at 304 nm, of the Ar^+ laser with an intensity of $J_{ex} \sim 1$ W/cm^2. The PL spectra are corrected for the spectral characteristic of the measuring system. The dashed lines show the zero levels of the corresponding PL signals. The inset shows the PL spectra in the visible and UV spectral regions.

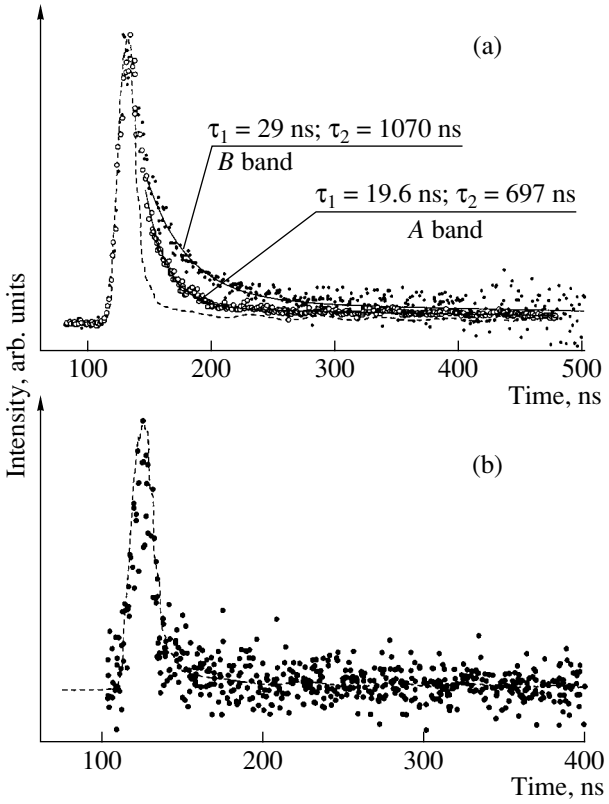

Fig. 2. Decay curves of the IR PL from GaN:As. The PL is excited by the N_2 laser with an intensity $J_{ex} \sim 10^3$ W/cm^2. (a) T = 78 K; the PL intensity of the *A* and *B* emission bands is measured. (b) T = 300 K; the PL intensity at 1.4 eV is measured. The experimental points are shown by dots and the solid lines represent the approximation of the PL decay for the *A* and *B* bands by the sum of two exponential functions with the corresponding decay times τ_1 and τ_2. The shape of the laser pulse is shown by the dashed line.

(radiation at 304 nm from the Ar^+ laser). It can be seen from Fig. 1 that, at 300 K, an emission band with a peak at ~1.4 eV, whose width is ~0.15 eV, is observed in the spectrum. The IR PL is caused by radiative recombination in the GaAs nanocrystallites, whose presence in the GaN:As layers is confirmed by the X-ray data. It is interesting that when the epitaxial layers are excited at room temperature by light with a photon energy smaller than the E_g of GaN (e.g., by the radiation at 488 or 514.5 nm from the Ar^+ laser), IR PL is virtually unobservable.

The IR PL excited by UV radiation was found to be rather intense: the IR PL intensity at 300 K amounted to ~6–7% of the intensity of the highly intense blue PL (see the inset in Fig. 1) studied in [5, 6]. The high efficiency of IR PL observed at a small volume fraction of GaAs nanocrystallites indicates that nonequilibrium electron–hole pairs generated by UV excitation in the GaN matrix are efficiently captured by GaAs nanocrystallites. A large difference between the band gaps of GaN and GaAs (~2 eV) undeniably plays an important role in this process. Therefore, the behavior of GaAs nanocrystallites in GaN:As during recombination processes is similar to that of buried heterostructures or quantum dots in a wide-gap matrix.

As can be seen from Fig. 1, as the temperature decreases, the intensity of the PL increases and the PL peak shifts, somewhat, to higher energies. Simultaneously, a new emission band peaked at ~1.20 eV appears in the spectrum and becomes dominant at $T <$ 150 K. In Fig. 1, the two bands observed in the spectrum at low temperatures are denoted as *A* (~1.43 eV at 10.5 K) and *B* (~1.20 eV at 10.5 K), respectively. An analysis of the temperature dependences of the spectral positions and the intensities of the *A* and *B* bands (see [8]) makes it possible to attribute the origin of both of them to the recombination of donor–acceptor pairs. Each recombination event involves either a shallow donor and a deep acceptor associated with the Ga vacancies (the *B* band) or a shallow acceptor and a deep donor related to the As vacancies (the *A* band). Similar donor–acceptor recombination channels involving shallow and deep centers introduced by the Ga and As vacancies were observed in bulk GaAs [10, 11] and, apparently, these channels occur in GaAs nanocrystallites formed in the GaN matrix.

Figure 2 shows typical decay curves for IR PL from GaN:As layers excited by the radiation of a pulsed nitrogen laser. It is important to note that, at a low temperature (78 K), there is a slow (on the microsecond scale) component in the decay kinetics of the *A* and *B* bands. Strictly speaking, this kinetics is not exponential; however, to estimate the characteristic time scale of the decay, we can satisfactorily represent the decay curve as a sum of two exponential functions (see Fig. 2a). The slow decay of the *A* and *B* PL bands favors

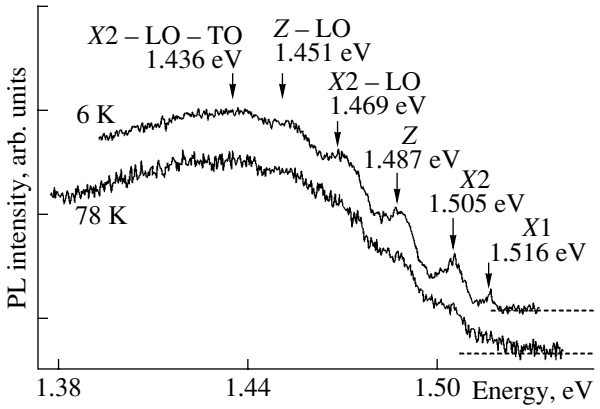

Fig. 3. The high-energy edge of the *A* PL band excited by the radiation, at 304 nm, of the Ar^+ laser with an intensity $J_{ex} \sim 1$ W/cm^2 at $T = 6$ K.

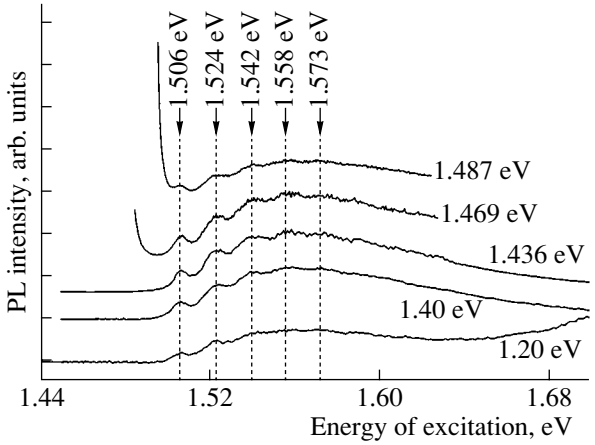

Fig. 4. Low-temperature spectra of the excitation of the IR PL in GaN:As. The PL detection energies are indicated on the curves.

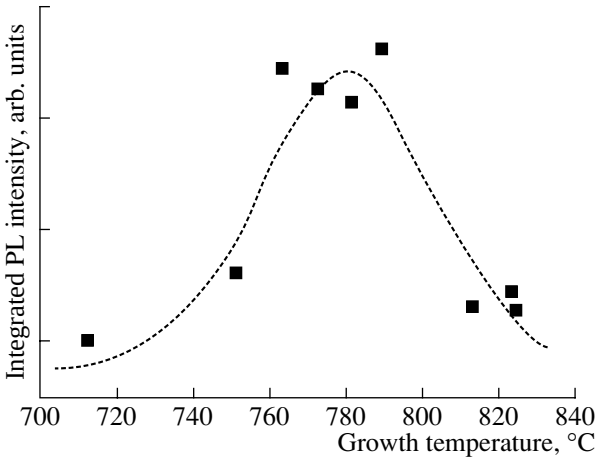

Fig. 5. Dependence of the integrated intensity of IR PL (0.9–1.5 eV) on the substrate temperature during MBE. The dependence was measured at $T = 78$ K. The dotted line is drawn to guide the eye.

the donor–acceptor recombination mechanism. At $T = 300$ K, PL decays rapidly (see Fig. 2b), which corresponds to the recombination of free holes with the electrons bound to complexes of As vacancies. This recombination becomes dominant in this temperature range.

At low temperatures, a series of narrow emission lines (whose widths vary from 5 to 18 meV) is observed at the high-energy edge of the *A* PL band against the smooth background of this band. This series vanishes at $T > 80$ K (see Fig. 3). After subtracting the smooth background, the energy positions of these lines (shown by the arrows in Fig. 3) were determined by approximating the lines with Gaussian curves. We can see the lines peaked at 1.516, 1.505, 1.487, 1.469, 1.451, and 1.436 eV. The lines at 1.516 and 1.505 eV, denoted in Fig. 3 as *X*1 and *X*2, respectively, arise due to the recombination of excitons bound to nitrogen atoms, which are the main impurity in these GaAs nanocrystallites.

It should be noted that a series of narrow lines caused by the emission from bound excitons and their phonon replicas was observed by a number of researchers [3, 12, 13] in bulk GaAs:N at a nitrogen content within ~$(10^{17}$–$10^{18})$ cm^{-3}. The shift of the *X*1 and *X*2 lines to higher energies by ~(8–9) meV, in comparison with the positions of the lines of the bound excitons characteristic of bulk materials, can be associated with quantum-dimensional effects as well as with the strain in GaAs nanocrystallites. The PL lines at 1.469 and 1.436 eV (see Fig. 3) are phonon replicas of the *X*1 line with the energies of the optical phonons (LO, TO), typical of GaAs [14]. The line *Z* at 1.487 eV can result from the recombination of excitons bound to NN pairs in GaAs nanocrystallites, and the peak at 1.451 eV is an LO-phonon replica of the *Z* line.

At low temperatures, we can also observe IR PL from GaN:As excited by the titanium–sapphire laser. Although the PL signal was low, the high sensitivity of the equipment made it possible to measure the spectra of PL excitation (see Fig. 4). In the spectra of excitation of both the *A* and *B* PL bands, a series of lines peaked at the energies 1.506, 1.524, 1.542, 1.558, and 1.573 eV is observed. The peaks at 1.506 and 1.524 eV arise due to the resonance photoexcitation, in GaAs nanocrystallites, of bound (*X*2) and free excitons, respectively. The features at 1.542, 1.558, and 1.578 eV result from the excitation of bound and free excitons and the simultaneous emission of optical phonons with energies typical of GaAs. The similar indirect excitation of excitons occurring simultaneously with the emission of optical phonons was studied in detail in [15] using the example of II–VI semiconductors.

Figure 5 shows the integrated intensity of the IR PL of GaN:As (in the range 0.9–1.5 eV) as a function of the substrate temperature in the course of MBE. It can be seen from Fig. 5 that, at $T_{gr} \approx 780$°C, the intensity of the IR PL is at its highest. The occurrence of this intensity

maximum is attributed to the joint effect of several temperature-dependent processes that affect the probability of forming GaAs nanocrystallites in the GaN matrix: the re-evaporation of As and Ga atoms from the surface of a crystal at high temperatures and, secondly, the formation of a $GaN_{1-x}As_x$ alloy at low temperatures of growth.

The investigation of the dependence of the integrated intensity of IR PL (I_{PL}) on the intensity of photoexcitation (J_{ex}) showed that, for both bands, this dependence has the characteristic form $I_{PL} \propto I_{ex}^{2/3}$. Such a dependence on the pumping intensity can be explained by the fact that the lifetime of nonequilibrium charge carriers in the GaAs nanocrystallites is governed, to a great extent, by the Auger recombination, whereas the PL signal is determined by a bimolecular (e.g., donor–acceptor) radiative recombination. It is worth noting that, as was shown theoretically and experimentally in [16, 17], the Auger recombination becomes the main channel of nonradiative recombination in nanostructures. This is due to a loosening of the restrictions related to the law of momentum conservation for the Auger processes in nanostructures.

Therefore, intense IR PL observed in the range 0.9–1.5 eV in GaN:As layers grown by MBE on sapphire is associated with the radiative recombination in GaAs nanocrystallites self-organized in the GaN matrix in the course of MBE. The intensity of the IR PL attains a maximum at a growth temperature of ~780°C, which is determined by the joint effect of several temperature-dependent processes that affect the probability of forming GaAs nanocrystallites. The low-temperature spectra of PL contain two main broad emission bands peaked at 1.20 and 1.43 eV, which occur due to the recombination involving shallow centers and deep centers. The latter are caused by vacancy complexes of Ga and As in GaAs nanocrystallites. The low-temperature PL spectra also include a series of narrow emission lines, which arise due to the radiative recombination of the excitons bound to nitrogen atoms, as well as their phonon replicas. The spectra of the PL excitation contain a series of peaks, which correspond to the resonance excitation of free and bound excitons, as well as the excitation of excitons simultaneously with the emission of optical phonons. The energies of the optical phonons involved in these processes are characteristic of GaAs.

REFERENCES

1. J. W. Ager III and W. Walukiewicz, Semicond. Sci. Technol. **17**, 741 (2002).
2. I. A. Buyanova, W. M. Chen, and B. Monemar, MRS Internet J. Nitride Semicond. Res. **6**, 2 (2001).
3. R. Schwabe, W. Seifert, F. Bugge, *et al.*, Solid State Commun. **55**, 167 (1985).
4. S. Sakai, Y. Ueta, and Y. Terauchi, Jpn. J. Appl. Phys., Part 1 **32**, 4413 (1993).
5. A. J. Winser, S. V. Novikov, C. S. Davis, *et al.*, Appl. Phys. Lett. **77**, 2506 (2000).
6. B. Gill, A. Morel, T. Taliercio, *et al.*, Appl. Phys. Lett. **79**, 69 (2001).
7. A. V. Andrianov, S. V. Novikov, R. Xia, *et al.*, in *Proceedings of 26th International Conference on Physics of Semiconductors* (Edinburgh, Scotland, UK, 2002), D19.
8. A. V. Andrianov, S. V. Novikov, T. Li, *et al.*, Phys. Status Solidi B **238**, 204 (2003).
9. T. H. De Keijser, E. J. Mittemeijer, and H. C. F. Rozendaal, J. Appl. Crystallogr. **16**, 309 (1983).
10. E. W. Williams, Phys. Rev. **168**, 922 (1968).
11. R. L. Willardson and A. C. Beer, in *Semiconductors and Semimetals* (Academic, New York, 1972), Vol. 8.
12. T. Makimoto and N. Kobayashi, Appl. Phys. Lett. **67**, 688 (1995).
13. T. Shima, Y. Mikita, S. Kimura, *et al.*, Nucl. Instrum. Methods Phys. Res. B **127–128**, 437 (1997).
14. J. S. Blakemore, J. Appl. Phys. **53**, R123 (1982).
15. E. Gross, S. Permogorov, V. Travnikov, and A. Selkin, J. Phys. Chem. Solids **31**, 2595 (1970).
16. V. A. Kharchenko and M. Rosen, J. Lumin. **70**, 158 (1996).
17. M. Ghanassi, M. C. Schanne-Klein, F. Hache, *et al.*, Appl. Phys. Lett. **62**, 78 (1993).

Translated by V. Rogovoĭ

Semiconductors, Vol. 39, No. 1, 2005, pp. 77–81. Translated from Fizika i Tekhnika Poluprovodnikov, Vol. 39, No. 1, 2005, pp. 87–91.

LOW-DIMENSIONAL SYSTEMS

Properties of Structures Based on Laser-Plasma Mn-Doped GaAs and Grown by MOC-Hydride Epitaxy

Yu. V. Vasil'eva*, Yu. A. Danilov*, Ant. A. Ershov*, B. N. Zvonkov*, E. A. Uskova*, A. B. Davydov, B. A. Aronzon**, S. V. Gudenko**, V. V. Ryl'kov**, A. B. Granovsky***, E. A. Gan'shina***, N. S. Perov***, and A. N. Vinogradov*****

**Nizhni Novgorod Physicotechnical Research Institute of Nizhni Novgorod State University, pr. Gagarina 23/3, Nizhni Novgorod, 603950 Russia*

***Russian Research Centre Kurchatov Institute, pl. Kurchatova 1, Moscow, 123182 Russia*

****Faculty of Physics, Moscow State University, Vorob'evy gory, Moscow, 119899 Russia*

Submitted June 1, 2004; accepted for publication June 16, 2004

Abstract—A method of doping GaAs with Mn using the laser evaporation of a metal target during MOC-hydride epitaxy is developed. The method is used to form both homogeneously doped GaAs:Mn layers and two-dimensional structures, including a δ-doped GaAs:Mn layer and a $In_xGa_{1-x}As$ quantum well separated by a GaAs spacer with a thickness of d = 3–6 nm. It is shown that, at room temperature, the formed structures have magnetic and magnetooptical properties most probably caused by the presence of MnAs clusters. In the low-temperature region (~30 K), the anomalous Hall effect is observed. This effect is attributed to the exchange interaction between Mn ions via 2D-channel holes. © *2005 Pleiades Publishing, Inc.*

1. INTRODUCTION

Manganese-doped GaAs is used as the main material of semiconductor spintronics, since it can possess ferromagnetism under certain fabrication conditions [1]. The most developed method of growing GaAs:Mn layers is molecular-beam epitaxy (MBE). This circumstance is associated with the fact that a supersaturated solid solution of Mn in GaAs can be formed in low-temperature MBE (~250°C) [1]. These solid solutions $Ga_{1-x}Mn_xAs$ ($x \approx 0.05$) have ferromagnetic properties at low temperatures (the Curie temperature $T_C \approx 110$ K [2]). It is noteworthy that T_C can be increased to 170 K in GaAs-based structures with a layer δ-doped with Mn, due to the formation of a two-dimensional (2D) hole conductivity channel near the δ-doped layer [3]. At $x > 0.05$ in $Ga_{1-x}Mn_xAs$ and/or after subsequent thermal treatment ($T >$ 550°C), the solid solution segregates and the MnAs clusters are formed [4].

It is of interest to examine the possibility of forming of the Mn-doped GaAs layers, and 2D structures based on them, by MOC-hydride epitaxy, as well as to study their properties. We have doped the MOC-hydride grown GaAs epitaxial layers with various impurities in earlier research. For this purpose, we evaporated the impurity using the emission of a Nd:YAG laser operating in the Q-switched mode [5]. In this study, we used the same method of impurity introduction for doping with Mn.

2. EXPERIMENTAL

Epitaxial structures were grown in a horizontal quartz reactor in an atmosphere of H_2 purified by its diffusion through a Pd membrane. The precursors used were trimethylgallium, trimethylindium, and arsine. For laser sputtering, we used the targets made of Mn, of a special-purity grade, and undoped GaAs. Generally, the substrates were semi-insulating GaAs (100) wafers.

It was found that the rate of deposition of the laser-sputtered substance on the substrate depends heavily on the gas pressure in the reactor. The required pressure in the reactor was established using a valve that controlled the pumping rate for a constant hydrogen flow of 2.7 l/min. The deposition rate of Mn was about 0.03 nm/s at a pressure of 50 Torr and about 0.015–0.02 nm/s at a pressure of 150 Torr. Sputtering of Mn at atmospheric pressure for 1 h did not produce any noticeable coating on the quartz substrate. A basic disadvantage of laser sputtering is the high velocity of evaporated particles, which may lead to the formation of defects in the growing structure. Therefore, to reduce the velocity of particles arriving at the substrate, we chose a reactor pressure of 150 Torr for laser sputtering. The layers of low-temperature GaAs were deposited using laser sputtering of the GaAs wafer. To compensate for As loss during sputtering, the process was carried out in an arsine atmosphere. We assumed that arsine decomposes in laser plasma and atomic As arrives at the substrate. To obtain the low-temperature GaMnAs alloys, we used a target composed of GaAs and Mn. The laser beam was moved from one target to another with a period of 8 s. The composition of the alloy could be specified by varying the ratio of irradiation times for each target.

1063-7826/05/3901-0077$26.00 © 2005 Pleiades Publishing, Inc.

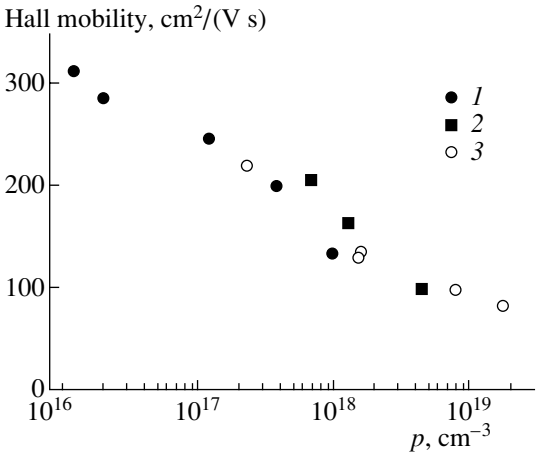

Fig. 1. The dependence of the Hall mobility on the hole concentration in the uniformly doped *p*-GaAs layers. The experimental points correspond to samples of (*1*) type 1 and (*2*) type 2 with the Mn-doped layers, and (*3*) type 3 (see the text).

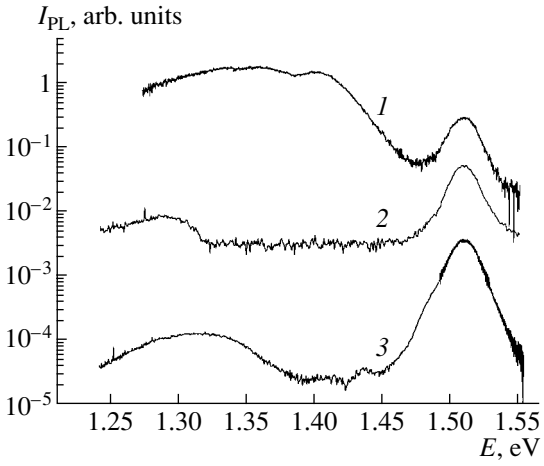

Fig. 2. Photoluminescence spectra for (*1*) the sample with the uniformly Mn-doped GaAs layer (type 1), (*2*) the structure with a layer δ-doped with Mn and the quantum well, and (*3*) the quantum-well structure. For clarity, the curves are shifted along the intensity axis.

The photoluminescence (PL) spectra of the structures were measured at 77 K under excitation by an He–Ne laser with a power of 40 mW.

The magnetic properties of the structures were studied by measuring the magnetization at room temperature, using a vibrational magnetometer–anisometer with a sensitivity of 10^{-8} erg/G [6], and by recording the magnetic Kerr effect. Magnetooptical studies were carried out in two variants: (i) using the magnetooptical Kerr magnetometer at a fixed optical wavelength (0.63 μm) in a temperature range from 40 to 300 K and (ii) at room temperature using a spectral magnetooptical system in the energy range 0.5 to 4.0 eV in the geometry of the equatorial Kerr effect with a light incidence angle of 60°.

3. RESULTS AND DISCUSSION

Figure 1 shows the dependence of the Hall mobility on the hole concentration measured at room temperature for the GaAs:Mn layers. These data are obtained for samples of three types: (i) a GaAs:Mn layer 0.6 μm thick, grown at 620°C under atmospheric pressure in the reactor; (ii) a GaAs:Mn layers 0.2 μm thick, grown at 300°C under a reduced pressure in the reactor, where GaAs and Mn were deposited by laser sputtering with a ratio of sputtering times GaAs/Mn from 5 to 1; and (iii) epitaxial *p*-GaAs layers doped with conventionally used shallow-level Zn or C acceptor impurities. The experimental points for the layers grown in various modes lie close to the same curve. This allows us to conclude that the structural quality of the laser-sputtered layers is rather high. The highest attained concentration of electrically active acceptor manganese $N_{Mn} = 4.5 \times 10^{18}$ cm^{-3} is close to that of the layers grown by liquid phase epitaxy [7].

Figure 2 (curve *1*) shows the PL spectrum of the sample with a layer doped homogeneously with Mn [sample of type (i)]. In addition to the fundamental PL band at 1.507 eV, the spectrum includes two bands with energies of 1.403 and ~1.36 eV. The former of these bands is typical of Mn-doped GaAs layers [8]. This band is believed to be related to carrier transitions from the conduction band to the Mn acceptor level. However, the origin is not clear for the very broad second band. We found that the depth of the Mn acceptor level is 0.104 eV, which agrees well with earlier reported data [9].

For the subsequent measurements, we used structures containing a layer δ-doped with Mn and an $In_xGa_{1-x}As$ ($x \approx 0.2$) quantum well (QW) ~12 nm wide located under the δ-doped layer. This layer and the QW are separated by a GaAs spacer layer. The buffer layer, the QW, and the spacer were grown at 620°C, while the δ-doped layer and the top GaAs layer were deposited at 300°C. Thus, we fabricated structures 3979, 3988, and 3980, which differed from each other in relation to the Mn deposition time during the formation of the δ-doped layer (20, 10, and 5 min for structures 3979, 3988, and 3980, respectively). The effective hole concentration in the structures due to Mn-doping was $(1–1.4) \times 10^{12}$ cm^{-2}. The spacer thickness d was 3 nm for structure 3979, 4 nm for structure 3988, and 6 nm for structure 3980. Figure 2 (curve *2*) shows the PL spectrum of the structure with d = 3 nm. The PL spectrum for a similar Mn-undoped QW-structure is peaked at a photon energy of 1.315 eV (Fig. 2, curve *3*). When the thickness of the spacer between the Mn layer and the QW equals d = 6 nm, the location of the PL peak from the QW corresponds to its location for the Mn-undoped structures. However, curve *2* in Fig. 2 shows that, as the spacer thickness decreases to 3 nm, this peak shifts, by 26 meV, to lower photon energies. This fact may be attributed either to Mn diffusion into the QW bulk and

the formation of an acceptor level above its top or to radiative recombination involving the Mn level that is tunneling-close to the QW.

Figure 3 shows the magnetization measurements for the mentioned structures, in relation to the applied magnetic field, at room temperature using a magnetometer. The hysteresis loop indicates that there is a ferromagnetic phase in the samples. The coercive force H_c varies from 27 to 65 mT. The dependences level off in the magnetic field at ~0.25–0.3 T. The curves shown in Fig. 3 indicate that an increase in the amount of deposited Mn leads to an increase in the saturation magnetization.

The magnitude and shape of the magnetic field-effect, as well as the spectral dependences of the magnetooptical equatorial Kerr effect, varied when the production conditions of the layer δ-doped with Mn were changed. In the first measurement version of the equatorial Kerr effect, at a fixed wavelength of light and a measurement temperature of 40–300 K, the observed magnetization curves were generally consistent with the dependences shown in Fig. 3. In this case, no magnetic phase transitions were revealed in the temperature range under study. In the second measurement version of the effect, by a dynamic procedure, we measured the parameter of the equatorial (transverse) Kerr effect denoted as the TKE, i.e., the relative variation in the intensity of the *p*-polarized light in relation to the sample magnetization. The dispersion spectral curves of the Kerr effect for the structures under study (inset in Fig. 3) revealed considerable variations in the TKE in a range of photon energies of 1 to 2 eV. Particularly, for structure 3979 (curve *1*), negative values of the TKE $\approx -2 \times 10^{-3}$ were observed in the range 0.5–1.0 eV. Then, as the photon energy E increased, the TKE abruptly increased to $\sim +7.5 \times 10^{-3}$ at ~1.5 eV. The change in the TKE sign was observed in a narrow spectral range of 1.5–1.7 eV. The lowest magnitude of the TKE, $\approx -4.5 \times 10^{-3}$, was found for $E \approx 1.75$ eV. Then the TKE magnitude increased again and went up to, but not over, 10^{-3} in the range 2.0–4.0 eV. Similar variations in the TKE spectra were also observed for structures 3988 and 3980 (inset in Fig. 3, curves *2* and *3*). In this case, the span of the TKE variations decreases as the amount of Mn deposited in the δ-doped layer decreases. Similar behavior of the spectra of the equatorial Kerr effect has previously been observed for GaAs samples with MnAs clusters [10]. Such a similarity suggests that the MnAs phase is present in the studied Mn-doped structures. The formation of the MnAs phase can be caused by the Mn segregation from the solid solution in GaAs due to the fact that when the solubility limit for Mn ($\sim 8 \times 10^{19}$ cm^{-3} [11]) is exceeded, a compound of Mn and As is formed at the growth temperature of the coating GaAs layer.

For the structures with a layer δ-doped with Mn and a InGaAs QW, we measured the conductivity and the Hall effect in magnetic fields as high as 3 T in the temperature range 30–300 K. The temperature dependences of the conductivity and the Hall effect are indicative of an activation process. At temperatures below 30 K, the resistance of the structures attains several GΩ, which makes the measurements unreliable. The conductivity's activation energy of 12 meV for sample 3980 (d = 6 nm) is approximately constant. This magnitude corresponds to the activation energy of carrier excitation from the acceptor Mn levels, which are located in GaAs, to the first QW subband. This indicates, therefore, that conductivity is realized over QWs, by holes located in them, rather than over the layer δ-doped with Mn. This fact can be understood from a consideration of the energy-band diagram for the structures under study (Fig. 4). As follows from the above PL measurements, the ionization energy of Mn relative to the valence-band top in GaAs $E_a^{\mathrm{Mn}} - E_v = 104$ meV. The calculation of energies in the structure with a strained

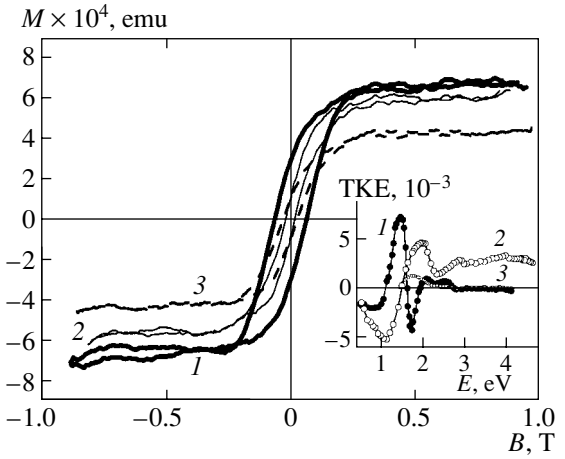

Fig. 3. Magnetization curves for the structures with a layer δ-doped with Mn and the QW: (*1*) structure 3979, (*2*) 3988, and (*3*) 3980. The spectral curves of the Kerr effect for the same structures are shown in the inset.

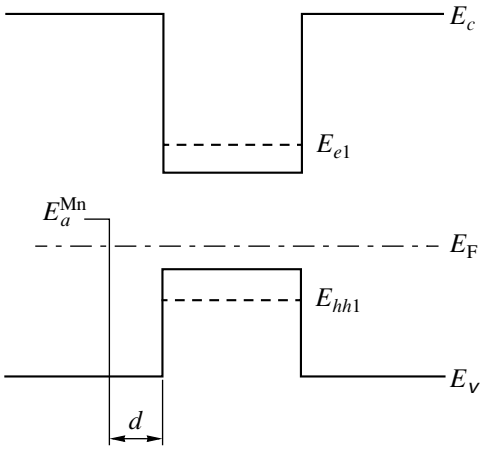

Fig. 4. An energy-band diagram of the quantum-well structure with a layer δ-doped with Mn.

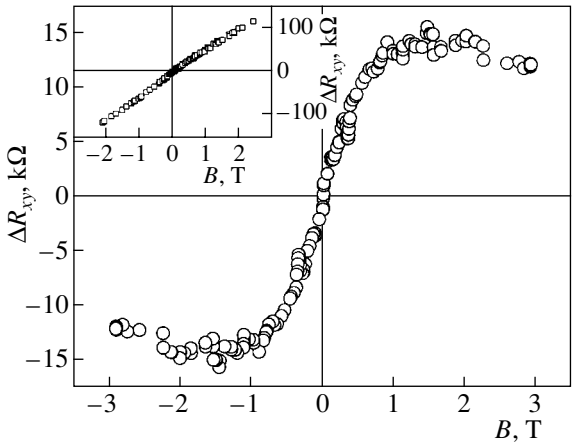

Fig. 5. The anomalous component of the Hall effect ΔR_{xy} for sample 3980 at T = 30 K. The magnetic-field dependence of the total Hall resistance R_{xy}, which involves the normal and anomalous components, is shown in inset.

12-nm-wide $In_xGa_{1-x}As$ QW in GaAs at $x \approx 0.2$ is made consistent with the location of the PL peak (Fig. 2, curve *3*) at 1.315 eV. This value corresponds to that of $E_{e1} - E_{hh1}$. According to the calculation, the valence-band offset at the QW boundary equals $E_v^{QW} - E_v$ = 86 meV while the dimensional-quantization level of holes $E_v^{QW} - E_{hh1}$ in the QW is spaced 5 meV from the QW top. Let us take into account that the Fermi level E_F in a structure at low temperatures is located below the level of the isolated acceptors by $\Delta = E_a^{Mn} - E_F$, which is determined by the Coulomb energy. In addition, according to [12], $\Delta \approx 10$ meV in the case of a weak compensation of the acceptors at their concentration $N_{Mn} \approx 10^{18}$ cm^{-3}. As a result, we obtain the activation energy of conductivity: $E_F - E_{hh1} = (E_a^{Mn} - E_v) - \Delta - (E_v^{QW} - E_v) + (E_v^{QW} - E_{hh1}) = 13$ meV, which is in good agreement with the experimental value. For sample 3979 with d = 3 nm, the activation energy is noticeably higher (22 meV) and decreases to 15 meV as the temperature decreases. This behavior corresponds to a situation where the Mn centers, which effectively determine the charge transport in this sample, are close to the QW boundary so that the wave functions of acceptor states can propagate deeper into the QW. Based on the above-mentioned facts, we may conclude that it is the Mn acceptors in GaAs which determine the QW conductivity in these structures.

In contrast to the above-given data for magnetic measurements, the influence of the ferromagnetic phase on the Hall effect was not observed at room temperature. The voltage across the Hall contacts varies linearly with the magnetic field over the entire range of its variation. As the temperature decreases to T = 30 K, the dependence of the Hall voltage on the magnetic field B generally remains linear. However, for sample 3980, by subtracting the straight line corresponding to the usual Hall effect from the experimental data, we managed to extract a signal that depended nonlinearly on B. Figure 5 shows the odd-numbered component of this signal with respect to the magnetic field. This component corresponds to the anomalous Hall effect. It is known [13] that, for magnetic materials, the total Hall resistance R_{xy} consists of two components:

$$R_{xy} = R_0 B + R_s \mu_0 M,$$

where R_0 is the coefficient of the normal Hall effect, which is caused by the effect of the Lorentz force; B is the magnetic induction; M is the magnetization; μ_0 is the magnetic permeability of free space; and R_s is the coefficient of the anomalous Hall effect associated with anisotropic scattering of spin-polarized charge carriers under the conditions of their spin–orbit interaction.

The dependence shown in Fig. 5 is similar to the dependence of the anomalous Hall effect for Mn-doped structures based on GaSb and GaAs [14, 15]. For these structures, the contribution of the anomalous Hall effect prevails over that of the normal component. However, it is noteworthy that the authors of [14, 15] studied the objects in which the Mn concentration substantially exceeded the critical value N_c that corresponds to a metal–insulator transition. In our case, the situation is different. The anomalous Hall effect manifests itself in a situation where the variation in the carrier concentration in relation to the temperature has an activation (dielectric) character. It is also noteworthy that the sign of the normal Hall effect (positive) and the sign of the anomalous Hall effect coincide similarly with the case of heavily Mn-doped GaAs samples [15].

4. CONCLUSION

The experimental results of studying the magnetic and electrical properties of produced structures can be explained by assuming that the Mn-doped layer is a hybrid structure which consists of a $Ga_{1-x}Mn_xAs$ solid solution and MnAs clusters. The presence of the MnAs clusters gives rise to the ferromagnetism, which is observed up to room temperature. However, the contribution of the MnAs clusters to the anomalous Hall effect, which is observed at low measurement temperatures (~30 K), should not be substantial due to the fact that the QW carriers (2D channel) do not flow into clusters, and that the magnetic exchange between carriers in QW and Mn atoms in clusters is weak. The metal clusters' lack of influence on the carrier transport in the layer may similarly be attributed to the formation of Schottky barriers around these clusters [16]. It is evident that only the Mn ions, which are incorporated into the GaMnAs solid solution and are distributed almost uniformly in it, can noticeably exchange with the QW carriers, leading to their spin polarization and, consequently, to the anomalous Hall effect.

Thus, we showed that it is basically possible to use MOC-hydride epitaxy to form structures based on Mn-doped GaAs that possess the electrical and magnetic properties characteristic of this material.

ACKNOWLEDGMENTS

We thank Yu.N. Drozdov for his help in the calculation of the energy band diagram of the QW structures.

This study was supported by a Program of the Russian Academy of Sciences "Spin-Dependent Effects in Solids and Spintronics" and by the Russian Foundation for Basic Research, project no. 04-02-16158 and 03-02-16777.

REFERENCES

1. H. Ohno, A. Shen, F. Matsukura, *et al.*, Appl. Phys. Lett. **69**, 363 (1996).
2. H. Ohno and F. Matsukura, Solid State Commun. **117**, 179 (2001).
3. A. M. Nazmul, S. Sugahara, and M. Tanaka, Phys. Rev. B **67**, 241308 (2003).
4. H. Shimizu, M. Miyamura, and M. Tanaka, J. Vac. Sci. Technol. B **18**, 2063 (2000).
5. B. N. Zvonkov, V. V. Podol'skiĭ, V. P. Lesnikov, *et al.*, Vysokochist. Veshchestva, No. 4, 114 (1993).
6. N. Perov and A. Radkovskaya, in *Proceedings of 1 and 2 Dimensional Magnetic Measurements and Testing, Bad-Gastain, Austria, 2000* (Vienna Magnetic Group Report, 2001), p. 104.
7. K. S. Zhuravlev, T. S. Shamirzaev, and N. A. Yakusheva, Fiz. Tekh. Poluprovodn. (St. Petersburg) **32**, 791 (1998) [Semiconductors **32**, 704 (1998)].
8. M. Ilegems, R. Dingle, and L. W. Rupp, J. Appl. Phys. **46**, 3059 (1975).
9. D. A. Woodbury and J. S. Blakemore, Bull. Am. Phys. Soc. **18**, 381 (1973).
10. H. Akinaga, M. Mizuguchi, T. Manado, *et al.*, J. Magn. Magn. Mater. **242–245**, 470 (2002).
11. S. K. Kuznetsova, Izv. Akad. Nauk SSSR, Neorg. Mater. **11**, 950 (1975).
12. B. I. Shklovskiĭ and A. L. Éfros, *Electronic Properties of Doped Semiconductors* (Nauka, Moscow, 1979; Springer, New York, 1984).
13. H. Munekata, Mater. Sci. Eng. B **31**, 151 (1995).
14. X. Chen, M. Na, M. Cheon, *et al.*, Appl. Phys. Lett. **81**, 511 (2002).
15. K. W. Edmonds, R. P. Campion, K.-Y. Wang, *et al.*, J. Appl. Phys. **93**, 6787 (2003).
16. N. Otsuka, Y. Tesaki, T. Yamada, *et al.*, J. Appl. Phys. **88**, 6016 (2000).

Translated by N. Korovin

Semiconductors, Vol. 39, No. 1, 2005, pp. 8–10. Translated from Fizika i Tekhnika Poluprovodnikov, Vol. 39, No. 1, 2005, pp. 13–16.

ELECTRONIC AND OPTICAL PROPERTIES OF SEMICONDUCTORS

Effect of the Conditions of Metal–Organic Chemical-Vapor Epitaxy on the Properties of GaInAsN Epitaxial Films

V. M. Danil'tsev^, D. M. Gaponova, M. N. Drozdov, Yu. N. Drozdov, A. V. Murel', D. A. Pryakhin, O. I. Khrykin, and V. I. Shashkin

Institute for Physics of Microstructures, Russian Academy of Sciences, Nizhni Novgorod, 603950 Russia

^e-mail: danil@ipm.sci-nnov.ru

Submitted June 1, 2004; accepted for publication June 16, 2004

Abstract—Epitaxial layers of GaInNAs quaternary alloys were grown by metal–organic chemical-vapor epitaxy. The structure of the layers was studied using X-ray diffraction and secondary-ion mass spectrometry, and their optical properties were investigated by photoluminescence and photocurrent measurements. GaInNAs layers lattice-matched to GaAs were grown. At lattice mismatches smaller than 10^{-4}, the layers show strong photoluminescence; at larger mismatches, the photoluminescence is quenched. © *2005 Pleiades Publishing, Inc.*

1. INTRODUCTION

III–V semiconductor compounds with low nitrogen content are promising candidates for near-infrared devices. It is well known that the introduction of a small amount of nitrogen significantly decreases the band gap of a number of III–NAs compounds [1]. It was predicted theoretically that emitters and detectors can be designed on the basis of InGaAsN epitaxial layers that are lattice-matched to GaAs for fiber-optical communication lines in the smallest dispersion and best transparency range (1.3–1.55 μm) of optical fibers [2].

However, the fabrication of such layers meets a number of problems. A large difference in the covalent radii of N and As atoms leads to the decomposition of solid solutions at N contents higher than 4%. The content of nitrogen and indium compounds in a chemical-vapor reactor affects the incorporation of nitrogen into epitaxial layers. Substitution of more than 2% of the arsenic for nitrogen leads to a significant decrease in the semiconductor compound quality. Another problem is measuring small amounts of nitrogen in a quaternary solid solution. Indeed, X-ray diffraction (XRD) analysis only provides data on the total lattice strain, and secondary-ion mass spectrometry (SIMS) has a low sensitivity to nitrogen (which is electronegative when a surface is sputtered with oxygen). It is also obvious that exact matching between the layer and substrate lattices cannot be obtained due to errors in setting the contents of components and the difference in the thermal expansion coefficients.

In this paper, we report the results on the epitaxial growth of layers of the $In_xGa_{1-x}N_yAs_{1-y}$ quaternary compound on GaAs substrates, including lattice-matched layers, and the investigation of the growth features and properties of the layers obtained.

2. EXPERIMENTAL

InGaAsN epitaxial layers were grown by metal–organic chemical-vapor epitaxy (MOVPE), in an EPIQUIP system with a horizontal quartz reactor, and induction heating of the substrate at low pressure in the growth zone (75 Torr). The growth temperature was varied in the range 500–650°C. Trimethylindium, trimethylgallium, arsine, and 1,1-dimethylhydrazine were used as sources of In, Ga, As, and N, respectively. Hydrogen was used as a carrier gas. $In_xGa_{1-x}N_yAs_{1-y}$ layers with thicknesses of up to 1000 nm were grown at rates in the range 10–60 nm/min.

The layers were analyzed by XRD, SIMS depth profiling, photoluminescence (PL), optical transmission, and atomic force microscopy (AFM). To estimate the composition of quaternary compounds, we used a previously developed method for determining N and In contents [3]. This method is based on independent XRD and SIMS measurements with a preliminary calibration against three-component samples.

3. INVESTIGATION OF THE $In_xGa_{1-x}N_yAs_{1-y}$ GROWTH

The MOVPE of quaternary compounds was optimized on the basis of data on the epitaxial growth of a GaN_xAs_{1-x} ternary compound using 1,1-dimethylhydrazine as an N source. Let us list some specific features of this process:

(1) The degree of nitrogen incorporation into a growing layer increases when the 1,1-dimethylhydrazine content is increased in the flux of the gas mixture.

(2) With a decrease in the growth temperature from 600 to 550°C, all other epitaxy conditions remaining constant, the degree of N incorporation increases by a factor of two. A probable reason is that, following a decrease in the epitaxy temperature, the desorption of

N from the surface of a growing layer also decreases, while the number of unoccupied positions of the V-group element (As) rises, caused by an exponential decrease in the decomposition rate of arsine as the temperature decreases.

(3) When the trimethylgallium content in the flux of a gas mixture is increased (in order to increase the growth rate), all other conditions remaining constant, the N content in GaN_xAs_{1-x} layers increases, which was also noted in [4].

(4) At high epitaxial growth rates (60 nm/min) and low temperatures (500°C), GaN_xAs_{1-x} layers with an N content of $x \approx 6\%$ and $E_g \approx 0.9$ eV can be obtained. However, the structural quality of such layers is very poor. In addition, with an increase in the N content in GaAsN layers of more than 4%, the band gap hardly decreases. It should also be noted that, at relatively low growth rates (no more than 40 nm/min) and growth temperatures in the range 530–570°C, solid solutions are homogeneous with respect to their composition and have no inclusions of other phases. In this case, with an increase in the 1,1-dimethylhydrazine content in the gas mixture under certain growth conditions (temperature and pressure), self-regulation occurs (the saturation mode) with respect to the incorporation of nitrogen into the epitaxial layer, and an increase in the 1,1-dimethylhydrazine content above a certain value does not change the composition of the film grown.

When growing the $In_xGa_{1-x}N_yAs_{1-y}$ layers, it was found that the main features of the nitrogen incorporation were the same as for GaN_xAs_{1-x}. Figure 1 shows the experimental dependences of the N content y on the growth temperature T_g for two values of the In content x.

It should be noted that, when indium is introduced at low 1,1-dimethylhydrazine contents in the gas phase ($y < 1.5\%$), the 1,1-dimethylhydrazine and trimethylindium fluxes mutually affect the incorporation of In and N into the epitaxial layer. This fact was also noted in [5]. It was found that, when InGaAsN is grown under the same conditions as GaAsN, the addition of In reduces the N content in the epitaxial film by several times. In the saturation mode, the effect of indium on the nitrogen incorporation into the film is much smaller (see table and Fig. 1; $T_g = 550$°C). The results of our four growth experiments, in which the temperature and fluxes of components remained constant, are listed in the table. Due to the complete cutting off of the fluxes of individual components in the growth of samples E821, E823, and E824, different ternary compounds were obtained. As follows from the table, all other epitaxy conditions remaining constant, the degree of nitrogen incorporation into InGaAsN is the same as in the case of InAsN and only slightly lower for GaAsN.

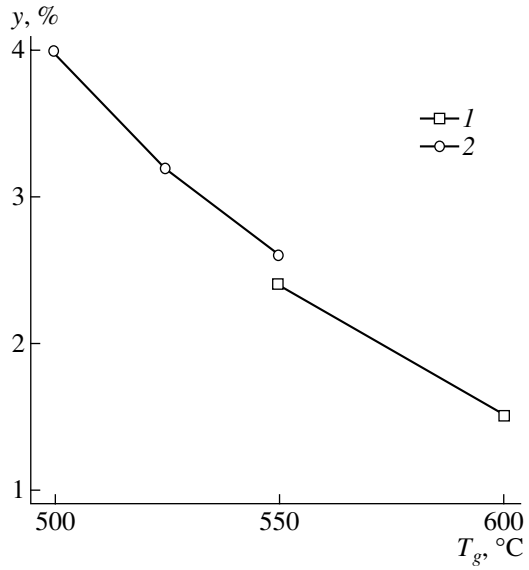

Fig. 1. Nitrogen content in an $In_xGa_{1-x}N_yAs_{1-y}$ layer as a function of the growth temperature T_g for the In content x = (*1*) 25 and (*2*) 15%.

4. GROWTH OF $In_xGa_{1-x}N_yAs_{1-y}$ LAYERS LATTICE-MATCHED TO GaAs

On the basis of the revealed growth behavior, experiments were performed in the temperature range 550–600°C at a growth rate of 30 nm/min. The growth-temperature range was chosen from the following considerations: At $T > 600$°C, the incorporation of nitrogen into GaAs is significantly reduced, and, at $T < 550$°C, the quality of GaAs layers is somewhat deteriorated due to the increasing contamination of the growing layer with carbon. The increase in the carbon contamination is related to the reduced desorption of hydrocarbons from the GaAs(100) surface upon decomposition of trimethylgallium at low temperatures. In addition, under these conditions of epitaxial growth, there is no layering of quaternary solid solutions into several layers of different compositions.

As was noted in Section 1, it is impossible to grow a solid solution layer that is exactly lattice-matched to GaAs, since the composition of a solid solution is set with a finite error. In addition, the difference in the thermal expansion coefficients makes matching possible either in the growth-temperature range (in which the defect formation is suppressed) or at room temperature

Data on the layers obtained in the series of growth experiments with constant fluxes

Sample no.	Compound	Composition
E821	GaAsN	3.8% N
E822	InGaAsN	3.4% N, 17% In
E823	InAsN	3.4% N
E824	InGaAs	17% In

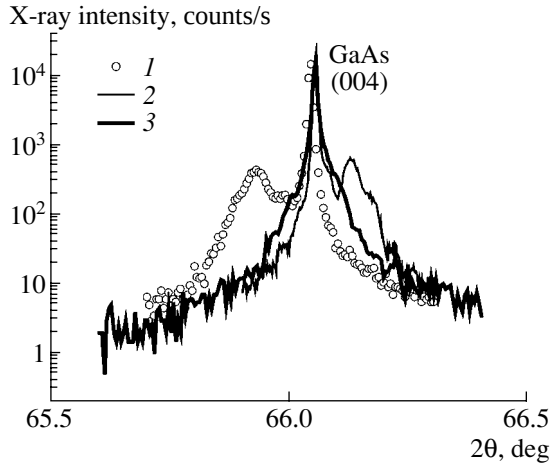

Fig. 2. X-ray diffraction spectra of three regions in sample E831: (*1*) a region with an excess of indium, (*2*) a region with an excess of nitrogen, and (*3*) a region lattice-matched to the GaAs substrate.

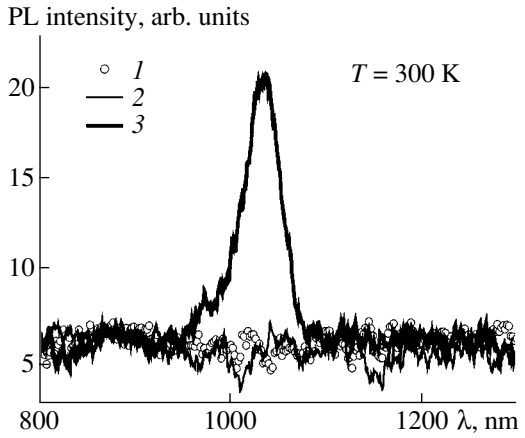

Fig. 3. PL spectra (300 K) of three regions in sample E831: (*1*) a region with an excess of indium, (*2*) a region with an excess of nitrogen, and (*3*) a region lattice-matched to the GaAs substrate.

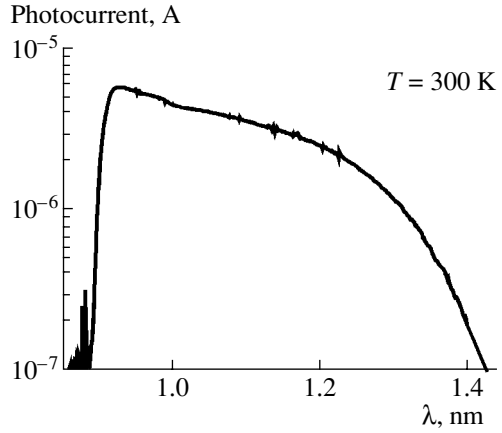

Fig. 4. The photocurrent through an In-enriched InGaAsN layer lattice-mismatched to the GaAs substrate.

(where, elastic strains are suppressed in the system). From a practical point of view, the matching accuracy should exclude misfit dislocations at a specified film thickness. The thicker the layer, the stricter the requirements for accuracy. To obtain a set of layers in the range of exact matching and in the vicinity of this range, we used a composition gradient method. A long GaAs wafer was placed in the reactor along the direction of the flux of reagents, and the substrate holder was not rotated. Due to the different rates of depletion of the gas mixture with different components, a composition gradient was formed along the wafer. By varying the growth conditions, we managed to obtain three regions with different compositions on one wafer: a region with an excess of indium at one of the ends, a region with an excess of nitrogen at the other end, and an exactly lattice-matched region in the middle. Figure 2 shows the X-ray diffraction spectra of these three regions in sample E831. It can be seen that, in region *3*, the peak of the layer coincides with the peak of the GaAs(004) substrate. The lattice mismatch is about 10^{-4}. Figure 3 shows the PL spectrum of this region at 300 K. The wavelength of the PL peak is about 1000 nm. In the regions that were not lattice-matched to the substrate, almost no luminescence was observed. According to the photocurrent measurements (Fig. 4) of the band gap width of InGaAsN samples that were not lattice-matched to GaAs, the band width was smaller than 0.9 eV.

5. CONCLUSIONS

Specific features of the epitaxial growth of $In_xGa_{1-x}N_yAs_{1-y}$ layers on GaAs substrates in a low-pressure MOVPE reactor were investigated.

Layers that are lattice-matched to GaAs are obtained. It is found that, at a mismatch of 10^{-4}, the layers grown show strong PL, whereas a deviation from the matching conditions leads to the quenching of the PL line.

ACKNOWLEDGMENTS

This study was supported by the Russian Foundation for Basic Research, project nos. 03-02-17404 and 04-02-17046, and the program "Physics of Solid-State Nanostructures."

REFERENCES

1. J. W. Ager III and W. Walukiewicz, Semicond. Sci. Technol. **17**, 741 (2002).
2. III–Vs Review **13** (6), 25 (2000).
3. A. V. Murel', V. M. Danil'tsev, M. N. Drozdov, *et al.*, Izv. Ross. Akad. Nauk, Ser. Fiz. **68**, 87 (2004).
4. Kurtz Sarah, R. Ready, G. D. Barber, *et al.*, J. Cryst. Growth **234**, 318 (2002).
5. D. G. Friedman, J. F. Geisz, S. R. Kurtz, *et al.*, J. Cryst. Growth **195**, 438 (1998).

Translated by Yu. Sin'kov

Semiconductors, Vol. 39, No. 1, 2005, pp. 82–85. Translated from Fizika i Tekhnika Poluprovodnikov, Vol. 39, No. 1, 2005, pp. 92–95.

LOW-DIMENSIONAL SYSTEMS

A Study of the Properties of the Structures with Al Nanoclusters Incorporated into the GaAs Matrix

N. V. Vostokov*^, S. A. Gusev*, V. M. Danil'tsev*, M. N. Drozdov*, Yu. N. Drozdov*, A. I. Korytin, A. V. Murel*, and V. I. Shashkin***

**Institute for the Physics of Microstructures, Russian Academy of Sciences, Niznhi Novgorod, 603950 Russia*
^e-mail: vostokov@ipm.sci-nnov.ru
***Institute of Applied Physics, Russian Academy of Sciences, Nizhni Novgorod, 603000 Russia*
Submitted June 1, 2004; accepted for publication June 16, 2004

Abstract—It is shown that organometallic vapor-phase epitaxy can be used to form an artificial medium that constitutes a matrix of single-crystal GaAs with incorporated Al nanoparticles. Electrical and optical properties of this medium are studied. © *2005 Pleiades Publishing, Inc.*

1. INTRODUCTION

Interest in semiconductor materials with metallic nanosized inclusions is caused by the wide potential of these materials with respect to applications in optoelectronics. One of the examples of these materials is epitaxial GaAs grown at a decreased temperature and contains As nanoclusters [1, 2]. A short lifetime of photogenerated charge carriers, low electrical conductivity, high mobility of electrons, and high breakdown field make it possible to use GaAs grown at comparatively low temperatures for generation and detection of terahertz radiation [3, 4]. In this paper, we discuss the possibility of forming a semiconductor medium with incorporated metallic nanoclusters using the organometallic vapor-phase epitaxy (MOVPE).

The aim of this study was to fabricate a multilayered three-dimensional medium that incorporated the contacts between metallic nanoparticles and semiconductor; to this end, we used the repeated formation of Al nanoclusters at the GaAs surface and the in situ overgrowth of these nanoclusters with the GaAs layer. We also studied the electrical and optical properties of the medium under consideration.

2. EXPERIMENTAL

Epitaxial GaAs layers were grown by MOVPE on GaAs (100) substrates in a horizontal reactor at a comparatively low pressure. $Ga(CH_3)_3$ (trimethylgallium), AsH_3 (arsine), $AlH_3(CH_3)_2(C_2H_5)$ (dimethylethylaminalan) were used as the Ga, As, and Al sources. Hydrogen was used as the carrier gas. The Al layers were formed in situ in a single growth process. A GaAs buffer layer with a thickness of no less than 100 nm was grown before deposition of the Al layers. The GaAs layer was grown at 550–600°C and Al layers were grown at 500–550°C. The admission of arsine was interrupted during Al deposition (this interruption was effected at least 30 s before the admission of dimethylethylaminalan into the reactor).

In order to analyze the structures obtained, we used a Solver-P4 atomic force microscope (AFM) produced by NT-MDT (Zelenograd), a Shipovnik secondary-ion mass spectrometer (SIMS) produced by the Ryazan Research Technological Institute, a DRON-4 X-ray diffractometer, a JEM 2000 EX-II scanning electron microscope (SEM), a Spitfire femtosecond titanium–sapphire laser system produced by Spectra-Physics Lasers Inc. (USA), and a bench for the optical and transport measurements. Ohmic contacts were formed by alloying Au–Ge in order to carry out transport measurements. The photocurrent spectra were obtained using structures with Schottky barriers. The latter were formed by depositing the Al contacts onto the surface using evaporation and photolithography. When measuring the photocurrent spectra, we exposed the rear side of the structure to monochromatized light of a halogen lamp with the wavelength scan from 900 to 1300 nm. In order to study the dynamics of ultrafast relaxation of photogenerated charge carriers, we employed the subpicosecond reflection absorption spectroscopy using the excitation and probe pulses. A laser system generated the pulses with the duration of 45 fs, energy of 2 mJ, the repetition frequency of 1 kHz, and wavelength of 795 nm. The energy-flux density in the excitation pulses was 1 mJ/cm^2 at the sample surface. The highest relative degree of induced modulation of the reflection coefficient ($\Delta R/R$) was $(1–2) \times 10^{-3}$ at normal incidence of light.

3. RESULTS

Layer-by-layer growth of Al on GaAs occurs at the early stages. In Fig. 1, we show the AFM images of the structures with a small amount of aluminum deposited on the substrates with various misorientation angles.

1063-7826/05/3901-0082$26.00 © 2005 Pleiades Publishing, Inc.

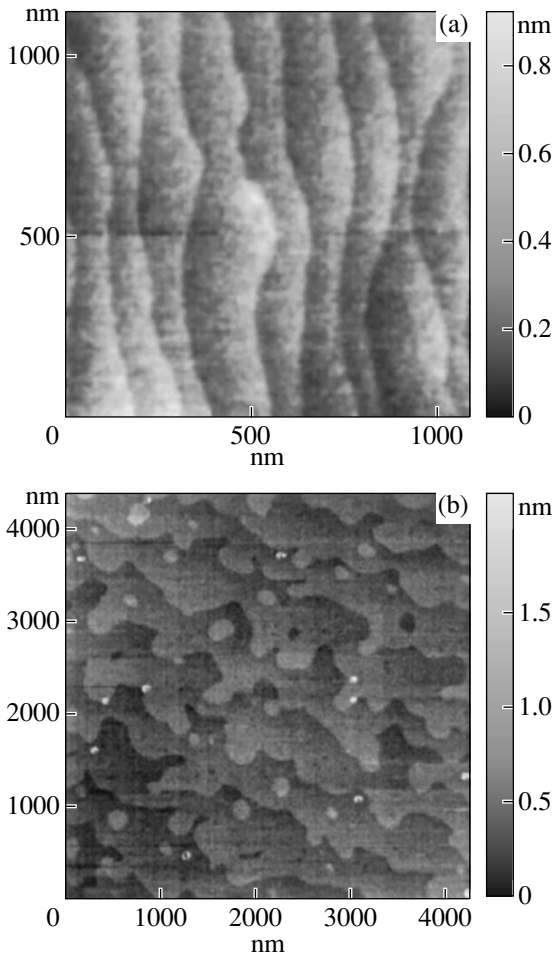

Fig. 1. AFM images of the structure surface after deposition of a small amount of Al on GaAs with (a) a large and (b) a small misorientation angle of the surface.

Layer-by-layer growth combined with the step formation occurs on the highly misoriented substrate (Fig. 1a). In the case of a substrate with a low degree of misorientation, the surface-diffusion length of Al atoms at a temperature of 500°C is found to be smaller the growth-step width. In this case, layer-by-layer growth combined with island formation is observed; the atoms form monolayer nuclei at the terrace plane and have no time to reach the edge (Fig. 1b). The presence of aluminum at the surface of the structures is confirmed by SIMS layer-by-layer analysis. The Al content is highest at the surface and decreases by more than three orders of magnitude in the bulk of the samples.

If the thickness of the aluminum layer exceeds a critical value equal to several monolayers, aluminum nanoclusters with cross-sectional sizes of 10–100 nm are formed [5, 6]. This situation is characteristic of the Stranski–Krastanov mechanism; however, we cannot produce a direct evidence that aluminum layer grows according to this mechanism.

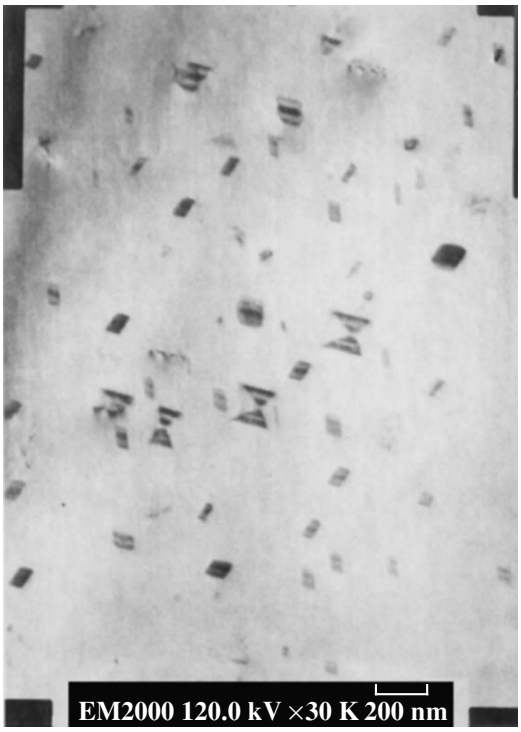

Fig. 2. SEM image of a thin GaAs layer with incorporated aluminum nanoclusters; the image was obtained in the transmission mode.

Epitaxial growth of GaAs on top of the Al layer occurs according to the Volmer–Weber mechanism. The growth begins with the formation of nuclei; the latter join each other at a later stage. Planarization of the surface of the GaAs layer occurs when the layer thickness is as large as ~100 nm [5, 6].

The presence of Al nanoclusters in the GaAs matrix can be inferred from Fig. 2 where a SEM image of a thin (<100 nm) GaAs layer with incorporated nanoclusters is shown; the image was obtained in the transmission mode. It can be seen from Fig. 2 that the nanoclusters are shaped as pyramids with rectangular or triangular bases, which is consistent with the current views about Al growth on GaAs under conditions of MOVPE [7].

In order to study the quality of the layer that overgrows the layer with aluminum nanoclusters, we grew a GaAs/InGaAs/GaAs heterostructure. The spectrum of X-ray diffraction for this structure includes a peak related to the single-crystal $In_{0.12}Ga_{0.88}As$ layer. The coherence length of the layer (48 nm, according to the data of X-ray diffraction) coincides with the layer thickness, which indicates that the concentration of structural defect is low. The photocurrent spectrum of a structure with the $In_{0.12}Ga_{0.88}As$ layer exhibits a higher photocurrent intensity at the wavelengths that correspond to band-to-band optical transitions in the $In_{0.12}Ga_{0.88}As$ layer, which indicates that this layer has a high optical quality.

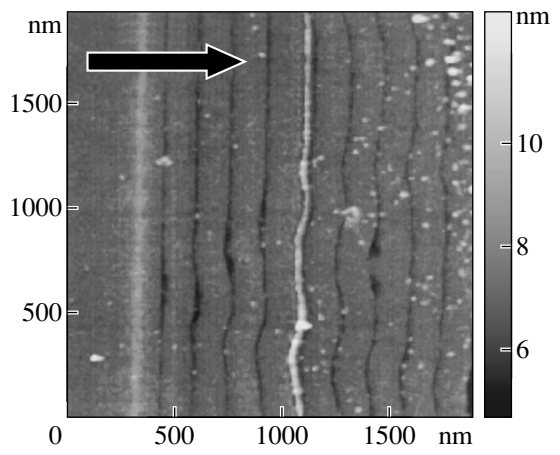

Fig. 3. The AFM image of the cleaved surface of the structure with nine Al layers after the structure was etched in a KOH solution. The arrow indicates the growth direction.

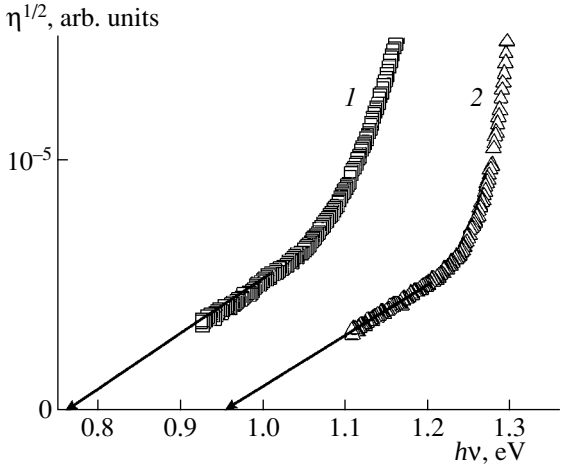

Fig. 4. Dependences of the square root of the photoresponse per photon $\eta^{1/2}$ on the photon energy $h\nu$; these dependences were obtained for (*1*) a structure with nine layers that incorporated Al nanoclusters and (*2*) a structure with epitaxial GaAs layer.

In order to measure the optical and transport characteristics, we grew the structure that contained nine layers with aluminum nanoclusters; each of these layers was overgrown with a GaAs layer with the thickness of ~100 nm. In Fig. 3, we show the AFM image of the cleaved surface of one of the structures exposed preliminarily to 10-min etching in a 0.5% KOH solution at room temperature. Selective removal of Al with GaAs and AlAs intact occurs as a result of this method of etching [8]. When examining Fig. 3, we can see the grooves that are extended over the layers with Al nanoclusters and result from etching off of these layers; this observation can indicate that there is a certain continuous layer that contains Al. Thickened sites at the grooves are related to etching off of aluminum nanoclusters.

Longitudinal current–voltage (*I–V*) characteristics were measured for the structures that included nine layers and were grown on semi-insulating substrates. The structures grown on n^+-type substrates were used in measurements of transverse *I–V* characteristics. The *I–V* characteristics measured along the length of the layers using ohmic contacts formed on the structures were linear. The *I–V* characteristics measured across the layers using ohmic contacts showed that the voltage dependence of current was exponential for either polarity. Such behavior can be caused by an overlap of GaAs depletion regions around Al nanoclusters in the layers.

The photocurrent spectra were measured in the transverse geometry using the structures with nine layers grown on the n^+-type substrate. In Fig. 4, we show the dependences of the square root of the photoresponse per photon ($\eta^{1/2}$) on the photon energy $h\nu$. The dependences were measured for one of the structures with nine layers that included the Al nanoclusters (curve *1*); for comparison, the corresponding dependence for the reference structure composed of 2-μm-thick GaAs epitaxial layer is also shown (curve *2*). Apparently, the linear portions in the dependences are related (i) to the excitation of electrons and their exit from Al nanoclusters to GaAs in the case of the structure with nine layers and (ii) to the exit of electrons from the Al macrocontact formed on the sample surface in the case of the reference structure. Extrapolating these straight lines to the photon-energy axis, we obtain the heights of the Schottky barriers. The barrier height is equal to 0.95 eV in the case of the reference structure. Apparently, such a large barrier height is caused by the presence of an intermediate layer at the Al–GaAs boundary; this layer appears during formation of the aluminum contact to the sample. The extrapolation yields the barrier height of 0.76 eV for the structure with nanoclusters. It was shown by Shashkin *et al.* [7] that the height of the Schottky barrier in the GaAs–Al contacts formed in situ by MOVPE increases as the formation temperature increases and can be as large as 0.95 eV at temperatures of 300–350°C. This increase in the barrier height is related to the appearance of an intermediate AlAs layer at high growth temperatures. In the case under consideration, the small height of the Schottky barrier at the interface between GaAs and an Al nanocluster can be caused by the small sizes of Al particles [9, 10].

In order to study photoinduced ultrafast processes in the structures with Al nanoclusters, we measured (with subpicosecond time resolution) the evolution of the coefficient of reflection from the structures as this coefficient was modulated by a high-power optical pulse. The results of measurements for the structure with nine layers are shown in Fig. 5. The probe optical pulse and the high-power excitation pulse had the linear polarization of light. The evolution of the reflection coefficient was measured for two directions of polarization of the excitation-pulse light: perpendicularly (curve *1*) and parallel (curve *2*) to the direction of polarization of the

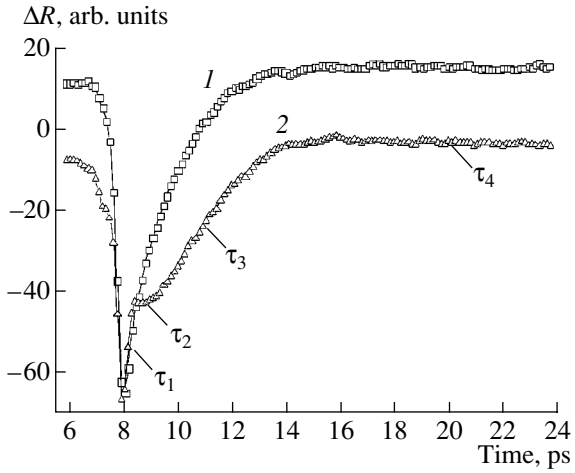

Fig. 5. Evolution of the coefficient of reflection from a structure incorporating nine layers when this coefficient was modulated by a high-power optical pulse; the direction of polarization of the excitation-pulse light was (*1*) perpendicular and (*2*) parallel to the direction of polarization of the probe-pulse light.

probe-pulse light. The high-power excitation pulse transfers electrons from the valence band to the conduction band. On completion of the pulse, the relaxation of the charge carriers to the equilibrium state sets in; this relaxation affects the dielectric constant of the medium and, thus, the reflection coefficient. An analysis of the curves makes it possible to distinguish four characteristic time constants each of which corresponds to a specific relaxation process: $\tau_1 < 1$ ps, $\tau_2 \approx 1$ ps, $\tau_3 \approx 3$ ps, and τ_4, whose value varies from tens to hundreds of picoseconds. Apparently, τ_1 and τ_2 correspond to the processes of thermalization of the electron–hole plasma in the semiconductor. The relaxation process with the time constant τ_2 changes its sign, depending on the polarization of the excitation-pulse light. The issue concerning why this sign reversal is observed and what are the specific processes with characteristic time constants τ_1 and τ_2 that occur during thermalization requires additional studies. The fast process with the time constant τ_3 makes the major contribution to the relaxation of the reflection coefficient to the equilibrium value; in our opinion, this process involves the nonradiative recombination of photogenerated charge carriers at the metal nanoclusters in the situation where the concentration of photogenerated charge carriers is high and the energy bands are flat in the space-charge region around the nanoclusters. In this case, there arises a diffusion current of electrons and holes to the nanocluster where the recombination occurs [11]. Later on, the concentration of photogenerated charge carriers decreases and an electric field arises in the space-charge regions; this field separates the remaining photogenerated charge carriers that recombine in the characteristic time τ_4.

4. CONCLUSIONS

Thus, we showed that it is possible to form a medium that constitutes single-crystal GaAs with incorporated Al nanoparticles. Our studies indicate that the concentration of structural defects in the semiconductor matrix is low and the optical quality of this matrix is high.

We studied the electrical and optical properties of the structures with nanoparticles. We experimentally observed the photoresponse related to the excitation of electrons and their transfer from Al nanoclusters to GaAs. The measurements of relaxation times for the relaxation of the coefficient of reflection from the structures with nanoparticles indicate that the lifetime of photoexcited charge carriers is short (several picoseconds).

ACKNOWLEDGMENTS

We thank Z.F. Krasil'nik and V.Ya. Aleshkin for their helpful participation in discussions; we are also grateful to I.Yu. Shuleshova and E.A. Vopilkin for their help with preparation of the samples.

This study was supported by the program Problems in Radiophysics of the Presidium of the Russian Academy of Sciences and by the Ministry of Industry, Science, and Technology of the Russian Federation (contract no. 40.072.1.1.1173).

REFERENCES

1. A. C. Warren, J. M. Woodall, J. L. Freeout, *et al.*, Appl. Phys. Lett. **57**, 1331 (1990).
2. Kian-Giap Gan, Jin-Wei Shi, Yen-Hung Chen, *et al.*, Appl. Phys. Lett. **80**, 4054 (2002).
3. S. Gregory, C. Baker, W. R. Tribe, *et al.*, Appl. Phys. Lett. **83**, 4199 (2003).
4. C. Baker, S. Gregory, W. R. Tribe, *et al.*, Appl. Phys. Lett. **83**, 4113 (2003).
5. V. Shashkin, V. Daniltsev, M. Drozdov, *et al.*, in *Booklet of Extended Abstracts of 10th European Workshop on Metalorganic Vapour Phase Epitaxy* (Lecce, Italy, 2003), p. 79.
6. N. V. Vostokov, V. M. Danil'tsev, M. N. Drozdov, *et al.*, Izv. Ross. Akad. Nauk, Ser. Fiz. **68** (1), 55 (2004).
7. V. Shashkin, S. Rushworth, V. Daniltsev, *et al.*, J. Electron. Mater. **30**, 980 (2001).
8. V. M. Danil'tsev, M. N. Drozdov, Yu. N. Drozdov, *et al.*, Phys. Low-Dimens. Semicond. Struct., Nos. 3–4, 321 (2001).
9. N. V. Vostokov and V. I. Shashkin, in *Abstracts of VI Russian Conference on the Physics of Semiconductors* (St. Petersburg, 2003), p. 257.
10. N. V. Vostokov and V. I. Shashkin, Fiz. Tekh. Poluprovodn. (St. Petersburg) **38**, 1084 (2004) [Semiconductors **38**, 1047 (2004)].
11. M. Achermann, U. Siegner, L.-E. Wetnersson, and U. Keller, Appl. Phys. Lett. **77**, 3370 (2000).

Translated by A. Spitsyn

Semiconductors, Vol. 39, No. 1, 2005, pp. 86–88. Translated from Fizika i Tekhnika Poluprovodnikov, Vol. 39, No. 1, 2005, pp. 96–99.

LOW-DIMENSIONAL SYSTEMS

InGaAs/GaAs Quantum Dot Heterostructures for 3–5 μm IR Detectors

A. V. Antonov, D. M. Gaponova, V. M. Danil'tsev, M. N. Drozdov, L. D. Moldavskaya^, A. V. Murel', V. S. Tulovchikov, and V. I. Shashkin

Institute for Physics of Microstructures, Russian Academy of Sciences, Nizhni Novgorod, 603950 Russia

^e-mail: lmd@ipm.sci-nnov.ru

Submitted June 1, 2004; accepted for publication June 16, 2004

Abstract—Specific features in the formation of InAs quantum dots (QD) by MOCVD were studied in relation to the growing time or equivalent thickness of the InAs layer. TEM and photoluminescence studies have shown that, as the growing time of QDs in a GaAs matrix becomes longer, both the size and shape of the QDs are modified; namely, the aspect ratio increases. Selectively doped multilayer InGaAs/GaAs QD structures were fabricated, and photoconductivity in the IR range was studied for lateral and vertical electron transport. Under a normal incidence of light, intraband photoconductivity in the mid-IR range, 2.5–5 μm, was observed at temperatures of up to 110 K. © *2005 Pleiades Publishing, Inc.*

1. INTRODUCTION

At present, considerable attention is focused on the application of InGaAs/GaAs quantum dot (QD) heterostructures as photodetectors for the mid-IR and far-IR spectral range [1, 2]. Owing to zero-dimension quantum confinement, QD IR detectors are sensitive to the light of arbitrary polarization under normal incidence, as distinct from quantum well (QW) structures. Furthermore, the electron scattering by phonons can be reduced in QD structures. This strongly increases the lifetime of photoexcited electrons, which is one of the principal parameters defining the sensitivity of IR detectors, and thereby opens the way to operation at higher temperatures. The central problem in the implementation of the potentiality of a QD detector is the necessity of precisely controlling the band structure in QD arrays. Multiple publications have been devoted to IR detectors for the 8–14 μm range, but there are far fewer reports on detectors for the spectral window in the mid-IR range, 3–5 μm [3–7]. Additional attention has been drawn to the design of wide-band detectors for this range. The principal requirement imposed upon these detectors is a red shift of the spectral lines of interband transitions in QDs to 1.3–1.5 μm, which can raise the transition energy of the intraband absorption in the conduction band to 400–450 meV. These QDs are usually produced by MBE, with the formed QDs being overgrown with an InGaAs layer. In this study, photodetectors for the 3–5 μm range were produced by MOCVD. The band structure of QD arrays was studied using the methods of photoluminescence (PL) and interband photoconductivity. Several spectral lines of lateral and vertical photoconductivity were observed in the mid-IR range.

2. EXPERIMENT

Multilayer InGaAs/GaAs QD heterostructures were grown on (100) GaAs substrates by MOCVD under reduced pressure in an EPIQUIP VP-502RRP installation. The structures for the photoconductivity measurements in the lateral configuration of the electron transport were grown on insulating substrates, and those for vertical configuration, on conducting n^+-GaAs substrates. The structures consisted of 10 layers of InAs QDs separated by 90-nm-thick GaAs barrier layers. They were selectively doped with Si δ-layers located at a distance of 2.5 nm in front of each QD layer. InAs QDs were grown at the reduced temperature of 480°C; after that, the reactor was blown through, and the QDs were overgrown with a thin GaAs layer at the same temperature. The reactor was again blown through, the temperature was raised to 600°C, and GaAs barrier layers were grown. The critical parameter in the procedure was the growing time of QDs, or the equivalent thickness of the InAs layer. The lateral photoconductivity was measured in samples of 5×3 mm^2 in size, with ohmic contacts formed on the surface by burning-in indium. Square mesa-structures of 300×300 μm^2 in size were fabricated by photolithography in order to perform photoconductivity studies on the vertical direction of the electron transport. Ohmic AuGeNi contacts were deposited onto the mesa-structure surfaces, in the shape of strips of 100 μm in width, along the perimeter of the square. The input window for light was 100×100 μm^2 in size, its area was smaller by a factor of 1000 than that in the measurements of the lateral photoconductivity.

Photoluminescence was measured at the temperature $T = 77$ K, with excitation by a laser with a 514 nm wavelength and a cooled Ge detector. The lateral pho-

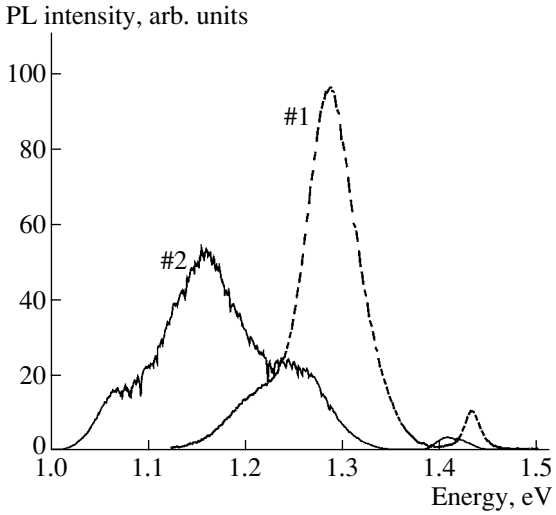

Fig. 1. PL spectra of two structures differing in relation to the time of InAs deposition during QD growth: structure no. 1, 10 s and no. 2, 8 s.

toconductivity was measured using a BOMEM Fourier spectrometer and the vertical photoconductivity with an IKS-21 spectrometer. TEM data were obtained on a JEM2000EXII electron microscope.

Figure 1 shows the PL spectra of two QD structures differing in relation to the time of InAs deposition during QD growth: 10 s for structure no. 1 and 8 s for structure no. 2. The spectrum of structure no. 1 exhibits two PL peaks: at 1.21 eV, related to the transitions between the ground states in a QD, and at 1.29 eV, for transitions between the excited states. Earlier, we observed several spectral lines in the lateral photoconductivity in the mid- and far-IR ranges in a similar structure [8]. In structure no. 2, the PL lines of the ground and first excited transitions (1.07 and 1.16 eV) are red-shifted, and an additional line, 1.25 eV, related to transitions between higher excited states, is observed. It is necessary to note that, along with the shift of the line related to transitions between the QD ground states, the spacing between the ground and first excited transitions increases as well. According to [9, 10] this is indicative of a modification of not only the size, but also the shape of the QD: in structure no. 2, the aspect ratio k, i.e., the ratio between the vertical and lateral size, is larger. This conclusion is supported by the TEM data: $k \approx 0.15$ in structure no. 1 and $k \approx 0.3$ in structure no. 2.

Figure 2 shows the experimental data on the lateral IR photoconductivity in structure no. 2 at 77 K. Several spectral lines of intraband photoconductivity are observed at 0.26, 0.35, and 0.49 eV. An additional feature is the presence of lines of interband photoconductivity at 0.92 and 1.18 eV. These lines are considerably more pronounced when another source of light and another beam splitter, both intended for the near-IR range, are used in the Fourier spectrometer, as can be seen in Fig. 3 (a characteristic dip at 0.88 eV in curves *2* and *3* in Fig. 3 can be attributed to the specific features of the quartz lamp used). It is noteworthy that the

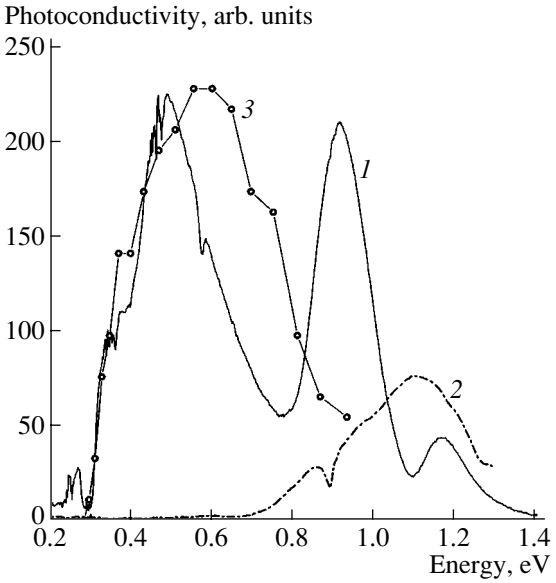

Fig. 2. Photoconductivity spectra for structure no. 2: (*1*) lateral at 77 K, (*2*) lateral at 300 K, and (*3*) vertical at 77 K.

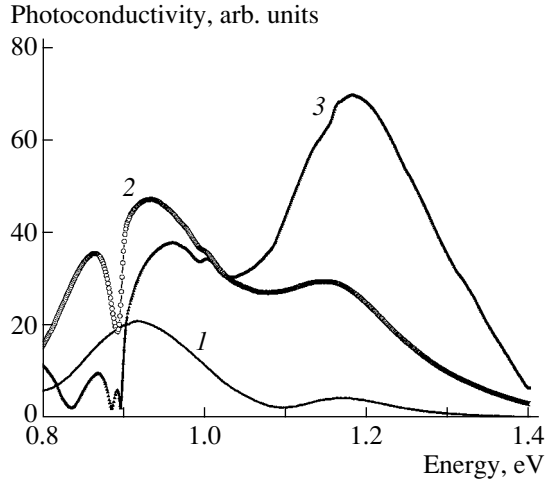

Fig. 3. Photoconductivity spectra of structure no. 2, recorded at 77 K using different beam splitters and sources of light in the Fourier spectrometer: (*1*) KBr splitter, globar; (*2*) KBr splitter, quartz lamp; and (*3*) quartz splitter, quartz lamp.

1.18 eV line in the PL spectra in Figs. 2 and 3 coincides with the PL line in Fig. 1, which is related to the transition between the excited states in QDs. These states lie deep enough below the edge of the conduction band of GaAs and the wetting layer for the probability of thermal emission or tunneling of photoexcited carriers from QDs to be low. As a rule, spectral lines of interband photoconductivity are not observed in this situation. However, in [11] we have noted the specific features of the lateral photoconductivity in QD structures that were attributed to a change in the scattering Coulomb fields creating charged QDs during the photoexcitation of carriers. This provides a new mechanism of photocon-

ductivity in QD structures that is not "carrier-density-related." The presence of lines of interband photoconductivity in Figs. 2 and 3 additionally confirms the existence of this mechanism.

Furthermore, the photoconductivity spectrum in the near-IR range exhibits a line at 0.92 eV that is absent in the PL spectrum in Fig. 1. We believe that this fact is indicative of a bimodal distribution of QDs with radiative (type 1) and nonradiative (type 2) transitions in structure no. 2. The possibility of forming bimodal distributions of QD by MOCVD was discussed in [12–14]. The width of the PL line is 0.095 eV, whereas the photoconductivity lines are wider, 0.2 eV, which indicates that the nonuniform broadening of QD levels produces a stronger effect on the spectrum of interband photoconductivity. The mentioned transitions in the near-IR photoconductivity spectrum account for the observed spectrum of mid-IR intraband photoconductivity: the lines at 0.26 and 0.35 eV are related to type 1 QDs, and the line at 0.49 eV, to type 2 QDs. The widths of the spectral lines of intraband photoconductivity are between 0.15–0.18 eV. The photoconductivity in the mid-IR range was observed at temperatures of up to T = 110 K, with the maximum intensity at 62 K. The interband photoconductivity in the near-IR range is observed up to room temperature (Fig. 2, curve *2*).

The spectral dependence of vertical photoconductivity at +0.5 V bias is shown in Fig. 2 (curve *3*). Changing the sign of the bias has only a slight effect on the results of the measurements. At the low-wavelength edge, the vertical photoconductivity virtually coincides with the lateral one. The line at 0.26 eV cannot be observed, presumably because of the poorer signal-to-noise ratio from having a considerably smaller photodetector area. At the same time, the lines of vertical photoconductivity in the short-wavelength range demonstrate a blue shift by ~70 meV in respect to the lateral photoconductivity. In our opinion, the specific features of the vertical photoconductivity can be attributed to a significant difference in the magnitudes of the applied electric fields; namely, the lateral effect is measured in the electric field below 10 V/cm, whereas the vertical one in much higher field, ~5 kV/cm. The broadening of the vertical photoconductivity line in InGaAs/GaAs QD structures at an increased bias has been observed before (e.g., twofold broadening was reported in [5]), but in that case the red shift of the line edge was larger. The dependence of the spectrum of vertical photoconductivity on the applied bias and the possibility of its modulation by the bias is currently being studied. Furthermore, the specific features in the vertical photoconductivity can be related to the difference between the spectral characteristics of the instrument functions of the two different setups used in measuring the lateral and vertical photoconductivity.

3. CONCLUSION

Selectively doped multilayer InGaAs/GaAs QD heterostructures were grown by MOCVD. The variation of the conditions of QD growing results in the red shift of the PL lines with a simultaneous increase of the energy spacing between the ground and first excited levels. Combined with the TEM data, the results of our PL study demonstrate that not only the size of QDs, but also their shape changes in this case; i.e., the aspect ratio increases. At temperatures of up to 300 K, the structures demonstrate lateral photoconductivity in the near-IR range (0.8–1.2 eV, 1–1.5 μm), related to the interband transitions within QDs. At temperatures below 110 K, several lines of lateral intraband photoconductivity in the mid-IR range (0.25–0.49 eV, 2.5–5 μm) were observed under a normal incidence of light. The maximum photoconductivity in this range was obtained at 62 K. Vertical photoconductivity in the mid-IR range (0.36 and 0.55 eV lines) was observed in mesa structures with an input window of 100×100 μm^2, which is comparable to the size of the elements in matrix photodetectors.

ACKNOWLEDGMENTS

The study was supported by the Russian Foundation for Basic Research (project nos. 03-02-16780, 03-02-17404, and 04-02-17180) and several programs of the Ministry of Industry, Science, and Technology of the Russian Federation.

REFERENCES

1. J. Phillips, J. Appl. Phys. **91**, 4590 (2002).
2. H. C. Li, J.-Y. Duboz, R. Dudek, *et al.*, Physica E (Amsterdam) **17**, 631 (2003).
3. S.-F. Tang, S.-Y. Lin and S.-C. Lee, Appl. Phys. Lett. **78**, 2428 (2001).
4. A. D. Stiff, S. Krishna, P. Bhattacharya, and S. Kennerly, Appl. Phys. Lett. **79**, 421 (2001).
5. A. D. Stiff, S. Krishna, P. Bhattacharya, and S. Kennerly, IEEE J. Quantum Electron. **37**, 1412 (2001).
6. S.-Y. Lin, Y.-J. Tsai, and S.-C. Lee, Appl. Phys. Lett. **83**, 752 (2003).
7. B. Aslan, H. C. Liu, M. Korkusinski, *et al.*, Appl. Phys. Lett. **82**, 630 (2003).
8. L. D. Moldavskaya, V. I. Shashkin, M. N. Drozdov, *et al.*, Physica E (Amsterdam) **17**, 634 (2003).
9. J. S. Kim, J. H. Lee, S. U. Hong, *et al.*, J. Appl. Phys. **94**, 6603 (2003).
10. U. H. Lee, Y. D. Jang, H. Lee, *et al.*, Physica E (Amsterdam) **17**, 129 (2003).
11. V. I. Shashkin, V. M. Danil'tsev, M. N. Drozdov, *et al.*, in *Abstracts of VI Russian Conference on the Physics of Semiconductors* (Fiz.–Tekh. Inst., St. Petersburg, 2003), p. 403.
12. G. Saint-Girons, G. Patriarche, A. Mereuta, and I. Sagnes, J. Appl. Phys. **91**, 3859 (2002).
13. G. Saint-Girons and I. Sagnes, J. Appl. Phys. **91**, 10115 (2002).
14. L. D. Moldavskaya, V. I. Shashkin, M. N. Drozdov, *et al.*, Acta Phys. Pol. A **103**, 579 (2003).

Translated by D. Mashovets

Semiconductors, Vol. 39, No. 1, 2005, pp. 89–94. Translated from Fizika i Tekhnika Poluprovodnikov, Vol. 39, No. 1, 2005, pp. 100–105.

LOW-DIMENSIONAL SYSTEMS

Study of the Photoelectric Properties of Ge Quantum Dots in a ZnSe Matrix on GaAs

I. G. Neizvestny, S. P. Suprun^, and V. N. Shumsky

Institute of Semiconductor Physics, Siberian Division, Russian Academy of Sciences, pr. Akademika Lavrent'eva 13, Novosibirsk, 630090 Russia

^e-mail: suprun@thermo.isp.nsc.ru

Submitted June 1, 2004; accepted for publication June 16, 2004

Abstract—The current–voltage (*I–V*) and spectral characteristics of a photocurrent are studied at $T = 4.2$ and 300 K for an unstrained GaAs/ZnSe/QD-Ge/ZnSe/Al structure with tunneling-transparent ZnSe layers and Ge quantum dots (QDs). Features such as the Coulomb staircase were observed in *I–V* characteristics at room temperature and in the absence of illumination. An energy-band diagram of the structure is constructed based on an analysis of the experimental data. In the GaAs/ZnSe/QD-Ge/ZnSe/*p*-Ge transistor structure with a *p*-Ge channel and Ge-QD floating gate, the total current of the channel both increased and decreased under exposure to light with various spectra. These variations in channel current are associated with the capture of a positive and negative charge at QDs during different optical transitions. The charge accumulation changes the state of a channel at the heterointerface from depletion to inversion and either decreases or increases the total current. © *2005 Pleiades Publishing, Inc.*

1. INTRODUCTION

The spectra of electronic states in semiconductor quantum dots (QDs) is of interest because of new QD properties that were unobservable in systems with a higher dimensionality [1] as well as the prospect of using these properties to develop new QD-based devices. At present, in view of the development of nanotechnology, some researchers are discussing the possibility of developing memory cells based on single-electron field-effect transistors, in which one bit of information corresponds to an electron trapped at the QD located between the main gate and the channel. Such a memory cell operating at room temperature has previously been discussed [2].

It is known that QD arrays can be obtained in double heterosystems with a considerable lattice mismatch. In our studies, we attempted to identify the conditions needed for three-dimensional growth at the initial stage of epitaxy for a heterosystem with nearly matched lattice parameters; for example, the lattice mismatch for semiconductors such as GaAs, ZnSe, and Ge is less than 0.2%. However, the GaAs/Ge pair exhibits a strong chemical interaction between its components. We showed that the introduction of an intermediate ZnSe layer between GaAs and Ge provides radically different conditions at the initial stage of epitaxy. In this case, the GaAs wafer is the substrate for the growth of a continuous ZnSe epitaxial film, on which the Ge-QD array is formed. We have previously studied and described the mechanism for the formation of a QD array in a Ge–ZnSe system [3, 4]. It is noteworthy that, despite a considerable difference in the band gaps (about 2 eV) for ZnSe and Ge, there are no elastic stresses in the system.

The purpose of this study was to examine the electronic properties of a Ge QD in a ZnSe host material for structures obtained by molecular-beam epitaxy (MBE).

2. FABRICATION AND STUDY OF THE GaAs/ZnSe/QD-Ge/ZnSe/Al STRUCTURES WITH TUNNELING-TRANSPARENT ZnSe LAYERS AND Ge QUANTUM DOTS

2.1. Fabrication

We used *n*-GaAs(001) wafers doped to a level of 10^{18} cm^{-3} as substrates. The structure consisted of a QD array between two ZnSe layers ~10 nm thick grown on the GaAs substrate. The sequence of sample preparation was reported previously in [5]. A contact window to the layers in the electron resist was about ~150 nm in diameter, which was monitored using an atomic-force microscope (AFM).

2.2. Current–Voltage Characteristic

The current–voltage (*I–V*) characteristics of the structures were recorded using an automated computer-controlled system of low-current measurement. A voltage with a specified step was supplied to the sample according to the program, the current was measured in equal time intervals (more than 100 measurements), and the average current was fixed. The *I–V* characteristics were measured at 300 K. We failed to measure the characteristics of the samples in a cryostat because of low currents and large spurious signals. However, measurements of large-area test structures showed that the

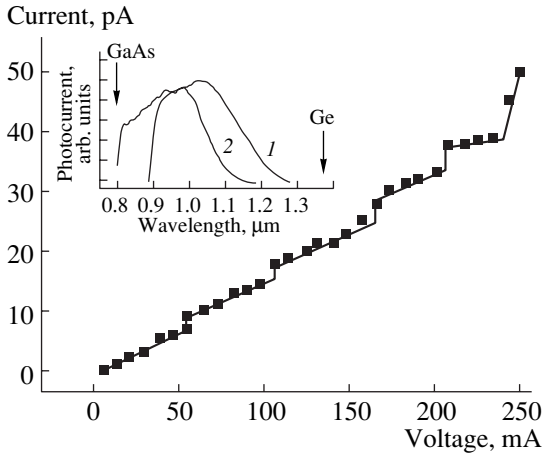

Fig. 1. *I–V* characteristic of a structure with a contact of 150 nm in diameter at $T = 300$ K. The points correspond to the experimental data, and the solid line is an approximation of the *I–V* characteristic. The spectral dependence of the photosignal at zero bias under the illumination of the GaAs side is shown in the inset: T = (*1*) = 300 and (*2*) 4.2 K. Arrows show the GaAs band-gap edge and the onset of direct transitions in bulk Ge at 4.2 K.

current only decreases by a factor of 30–40 as the temperature is decreased from 300 to 4.2 K, which is indicative of predominance of tunneling.

Features shaped like small steps are present in the *I–V* characteristic of the structure at a reverse-bias voltage of no higher than 250 mV. In these steps, the current increases with the voltage rather than remaining constant (Fig. 1). The average current through the structure is determined not only by the tunneling of charge carriers through the QD but also by the current tunneling through the ZnSe film in the spacings between Ge clusters. The estimations show that this current is restricted by the space charge. Therefore, a linear voltage dependence of the current should be, and in fact is, observed in low electric fields ($E \approx 10^5$ V/cm), being most pronounced at low voltages. The main feature of the *I–V* characteristic is that current variations such as the Coulomb staircase emerge at a voltage of about 50 mV. These variations are not exactly periodic with respect to the voltage. The irregularity in the repetition of the Coulomb staircase steps is characteristic of vertical QDs with a small number of trapped electrons and is caused by the strong interaction between these electrons. In addition, this irregularity can be associated with a high temperature and somewhat different QD sizes. Thus, the emergence of the current and the features of the *I–V* characteristics are observed at low voltages; i.e., when the difference between the Fermi levels in Al and GaAs is small. These phenomena indicate that at least the first quantum level of the QD-trapped electron is below the Fermi level of metal in the equilibrium state when there is no external bias.

2.3. Spectral Dependences of Photovoltage

Spectral characteristics were measured, using a periodic signal with a frequency of ~10^2 Hz, under illumination of the substrate side. The photoresponse spectrum of the structure at $T = 300$ and 4.2 K without external bias is shown in the inset in Fig. 1. The presence of photovoltage indicates that a built-in electric field, which is caused by the contact potential difference, exists in the structure. The saturation of the open-circuit photovoltage was as high as 0.12 V.

The long-wavelength spectral edge is located at approximately 1.3 μm when at room temperature and at 1.15 μm at liquid-helium temperature. Such an edge location does not correspond to the absorption edge of bulk Ge. However, the edge shift agrees well with the variation in the Ge band gap in a temperature range from 300 to 4.2 K.

The features observed in the spectral characteristic measured at 4.2 K can be associated with the discrete character of the spectrum. In the high-energy region, the spectrum edge abruptly drops due to the absorption in the substrate.

Let us consider the location of the region of photoactive absorption in the structure, which induces the photovoltage. The photovoltage can only be induced by the excitation of electron–hole pairs, with their subsequent separation being due to the built-in electric field. It is evident that neither GaAs nor ZnSe could be the regions where electron–hole pairs are generated since the band-gaps of these compounds are wider than 1.5 eV at $T = 4.2$ K, while the impurity absorption cannot cause the photovoltage. The absorption in the QD array can lead to the formation of localized electrons and holes; however, a mechanism should exist to separate them spatially.

A built-in electric field exists in the structure under study. This field is induced owing to the contact potential difference between Al and GaAs. The magnitude of this field equals approximately $(3–5) \times 10^5$ V/cm. Since the ZnSe layers are tunneling-transparent for electrons, the electron of the photoexcited electron–hole pair can tunnel in this field from the QD into the GaAs. Subsequently, two possibilities can, in principle, be realized: The nonequilibrium hole from the QD can tunnel into the Al, or the electron from the Al can enter the QD. In each case, the photocurrent will flow in the external circuit, while the photovoltage will emerge in the structure in an open-circuit mode.

2.4. Energy-Band Diagram of the Structure

The experimental data, namely, known QD sizes, *I–V* characteristics, and the spectral dependence of photovoltage, along with the available published data on the energy-band offset for the heteropairs involved in the structure, allow us to construct an energy-band diagram of the GaAs/ZnSe/QD-Ge/ZnSe/As structure.

We calculated the energy-band diagram using the values of the valence-band offset, which was 1.3 eV between GaAs and ZnSe and 1.0 eV between ZnSe. The available published data give a rather wide range of values for the energy-band offset between the materials involved in the structure. This circumstance is associated with a difference in the conditions of fabrication, namely, in the substrate preparation, the growth temperature, the surface stoichiometry and substrate orientation, and in some other factors [6, 7]. For the existing spread of data, the energy-band offset for the calculation was chosen according to the following conditions:

(i) The location of the first quantum electron level in the L valley should be below the Fermi level when the system is in equilibrium. The Fermi level position was determined from the difference between the work functions for Al and GaAs (0.8 eV).

(ii) The experimentally measured optical transition with the lowest energy should correspond to the electron transition from the quantum level in the QD valence band to the free electron level nearest to the Fermi level.

The lowest energy of the radiation, whose absorption induces the photovoltage, can be written as

$$E_{\min} \approx E_{111hh} + E_{g\mathrm{Ge}} + (E_f - E_{c\mathrm{Ge}}),$$

where E_{111hh} is the first quantum level of heavy holes; $E_{g\mathrm{Ge}}$ is the Ge band gap; and $E_f - E_{c\mathrm{Ge}}$ is the difference between the Fermi level and the conduction-band bottom for germanium, which determines the optical transition with the lowest photon energy. At $T = 4.2$ K, the lowest experimental photon energy that induces the photovoltage is approximately 1.1 eV. The electrons are transferred to an unoccupied quantum level located above the Fermi level. This circumstance explains the fact that the absorption edge is shifted to shorter wavelengths than we would expect based on the known QD sizes.

The self-capacitance of a disc-shaped QD of 12.5 nm in diameter is $C = 8\varepsilon_0\varepsilon r = 3.8 \times 10^{-18}$ F, which yields a characteristic energy of about 40 meV. The scanning tunneling microscopy data for the QD sizes, shape, and distribution of height and diameter, in relation to the average thickness of the deposited Ge layer [3, 5], allowed us to estimate the energy spectrum of the electron and hole QD levels. In the calculation, we approximated a cluster by a parallelepiped of $3 \times 15 \times 15$ nm in size taking into account the effective mass of the corresponding hole subband with the Coulomb interaction disregarded under the Bastard boundary conditions. In the calculation, we used the effective carrier masses in ZnSe and various Ge valleys as well as the Ge and ZnSe band gaps at about 0 K.

Based on the given energy band diagram in Fig. 2, the levels located below the Fermi level exist in an equilibrium-state QD. Therefore, electron tunneling from the Al contact should occur when the potential corresponding to the self-capacitance of the QD is applied; i.e., at $V = 40$–50 mV. In this case, the occurrence of a low potential in GaAs should not substantially restrict the tunneling since the electron concentration in GaAs is high ($n = 10^{18}$ cm^{-3}) and the space-charge region at the GaAs/ZnSe heterointerface is no thicker than a few nanometers. As the voltage increases, the current is restricted only by the QD charging, since the energy difference between neighboring electron levels is given by

$$\Delta E = E_{1i+1j+1} - E_{1i+1j} = E_{1i+1j+1} - E_{1ij+1} < 2 \text{ meV},$$

where the first subscript for the energy corresponds to the QD height while the second and the third subscripts correspond to the QD base.

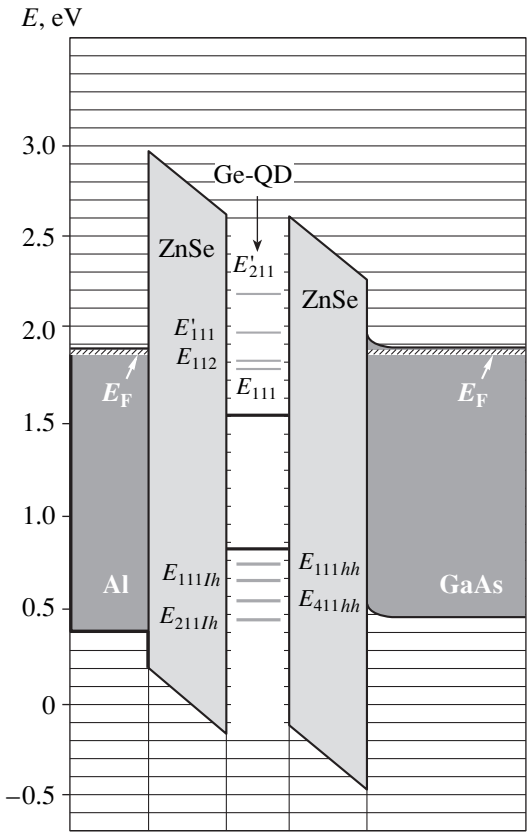

Fig. 2. An energy-band diagram of the GaAs/ZnSe/Ge-QD/ZnSe/Al structure under equilibrium. The diagram shows the energy levels for the subband of heavy holes (subscript *hh*) and light holes (subscript *hl*), and the electrons for the L valley and Γ valley (with the prime).

3. TRANSISTOR STRUCTURE GaAs/ZnSe/QD-Ge/ZnSe/*p*-Ge

3.1. Fabrication

It is clear from a consideration of the energy-band diagram in Fig. 2 that, owing to the electron tunneling into GaAs, the charge can be accumulated under illumination in the QD layer of a structure with one tunnel-

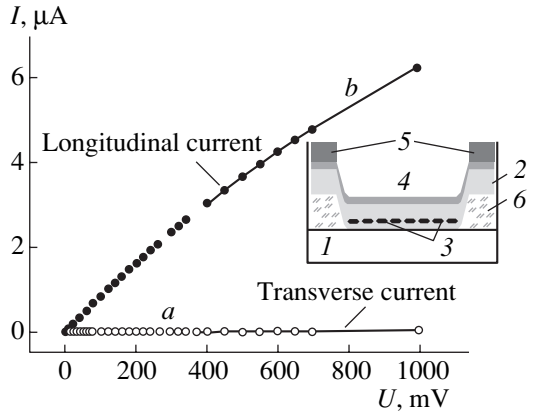

Fig. 3. The *I–V* characteristic for (*a*) the transverse current and (*b*) the longitudinal current of the structure at $T = 300$ K. The cross section of the GaAs/ZnSe/QD-Ge/ZnSe/*p*-Ge structure is shown in the inset: (*1*) GaAs, (*2*) ZnSe, (*3*) QD-Ge, (*4*) *p*-Ge channel, (*5*) Al contact, and (*6*) SiO.

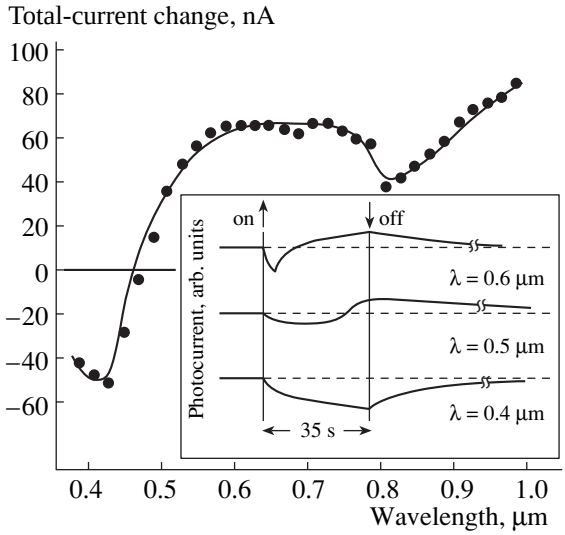

Fig. 4. The spectral dependence of the variation in the total channel current. The time dependence of the channel current for switching on and switching off the illumination for various wavelengths at $T = 300$ K is shown in the inset.

ing-impermeable layer. If we use the QD layer as the floating gate of the field-effect transistor, where a thin epitaxial Ge layer serves as the channel, we can study the process of charge accumulation in the Ge-QD structure. In this case, the accumulation of even a very small charge should induce a measurable variation in the channel current.

The sequence of operations followed to form the structure was reported previously in [8]. The ZnSe (~15 nm)–QD-Ge–ZnSe (150 nm)–*p*-Ge (40 nm) layers were grown in a single process (see the inset in Fig. 3).

The current of the Ge channel was measured at $T =$ 300 and 77 K. The transverse current across the structure was much lower than the longitudinal channel current. Therefore, the former could not introduce any error in measurements, while the channel current tended to level off at both temperatures (Fig. 3). Under an exposure of the channel-side of the structure to white light, the total current decreased.

3.2. Characteristics of the Channel Current under Illumination

To study the behavior of the structure under illumination in detail, we measured the constant-signal spectral dependences of the channel current. The measurements were carried out for a source–drain voltage of 20–150 mV that had a zero gate voltage. The spectral dependence of variations in the total current in the Ge channel at a sweeping voltage of 50 mV is shown in the inset in Fig. 4. Exposure to light with a wavelength lower than 0.5 μm leads to a decrease in the current, while at longer wavelengths the current increases.

The relaxation curves of the variation in the channel current under illumination, which were measured at room temperature for the wavelengths 0.6, 0.5, and 0.4 μm, are shown in the inset in Fig. 4. After switching-on the light, the channel current decreased in all three cases. During a certain time interval, the change in the current at $\lambda = 0.6$ and 0.5 μm then became positive, and the current leveled off. However, at $\lambda =$ 0.4 μm, the variation in the channel current remained negative, and the current leveled off at a negative value. It is noteworthy that the variation in the channel current always remained negative as the radiation intensity of the argon laser ($\lambda = 0.46$ μm) varied from 3 to 100 mW; i.e., the variation in the total channel current is determined by the energy rather than the intensity of the excitation radiation.

A possible mechanism of the decrease in the channel current under illumination and the slow current relaxation after switching off the illumination can be analyzed by considering the energy-band diagram of the transistor structure in Fig. 5. The calculation for the situation where there was neither external voltage nor illumination yielded the following results: the fraction of the built-in potential applied to Ge, the QD charge density, and the electron concentration at charged QDs was $V_{\mathrm{Ge}} = 0.033$ V, $\sigma_{KT} = -6.1 \times 10^{-8}$ C cm^{-2}, and $N_{eKT} = 3.8 \times 10^{11}$ cm^{-2}, respectively.

Since transverse leakage currents through the structure are small, the channel current can only be varied due to the spatial electron and hole localization. Let us consider the possible optical transitions in the structure (Fig. 5), starting with low photon energies: The energy band diagram shows that transitions I from the conduction band levels located above the Fermi level to the levels of the quasi-continuous spectrum can proceed at $h\nu \geq 0.1$ eV. Experimentally, the photocurrent is observed at $h\nu \cong 1.25$ eV. For the transitions from the

first level in the valence band to the levels from which the electrons can tunnel either into GaAs or to the levels of the quasi-continuous spectrum (transition II in Fig. 5), the lowest photon energy equals approximately 2.0–2.1 eV. Finally, for the electron transition from the quasi-continuous spectrum of the valence band to unoccupied electron QD levels (transition III in Fig. 5), the lowest energy is higher than 2.3 eV.

During transition I, the electron in the built-in electric field drifts into GaAs, while the hole is localized at the QD. The same situation is observed for transition II. However, during transition III, the electron is localized in the QD, while the hole drifts into Ge or is trapped in the holes in ZnSe. The QD charging via holes (transitions I and II in Fig. 5) should lead to a strengthening of the transverse field and electron inflow to the Ge/ZnSe heterointerface and to a depletion of the holes. As the positive charge accumulates at the QD, the depletion transforms into an inversion, which causes an increase in the total channel conductivity and in the current. The dynamics of the variation in the channel conductivity versus the time of the charge accumulation accounts well for the relaxation curves of the variation in the current when switching-on the radiation with wavelengths of 0.6 and 0.5 μm. By starting with a photon energy of 2.3 eV, at the least, transitions II and III can occur; i.e., the QD recharging is possible for both holes and electrons. In this case, the steady-state channel current is controlled by the established equilibrium between the generation and recombination of carriers of both signs and by their separation. In addition, during transition III, the escape of holes into the channel and the reduction of the transverse field there prevent the attainment of the inversion state. Therefore, when such an excitation is realized experimentally at $\lambda < 0.5$ μm, the channel is depleted. This leads to a negative variation in the current, in contrast with $\lambda > 0.5$ μm, when only transitions I and II are realized by the accumulation of a positive charge at the QD.

The relaxation curves allow us to estimate the characteristic times taken to attain a steady state or another such state when the generation is balanced by the recombination of electron–hole pairs, while carrier flows from the Ge-QD layer to both sides (in both directions) are equal. These times are tens of seconds long at $T = 300$ K and increase to several hours as the temperature decreases to 77 K.

We estimated the charge, which should be accumulated in the QD, to attain the inversion point in the quasi-neutral volume of the Ge channel. For this point, the concentration of nonequilibrium carriers, specifically electrons, equals the hole concentration. The estimation shows that $\sigma_{KT} = (4.2–4.7) \times 10^{-7}$ C cm^{-2}, which corresponds to the hole density at charged QDs $N_{pKT} = (2.6–2.9) \times 10^{12}$ cm^{-2}. The time variations in the photocurrent at wavelengths of incident light of 0.5 and 0.6 μm are associated with the gradual accumulation of holes in the QD and should depend on the illumination intensity. However, the steady state, which is characterized by a decrease in the photocurrent under optical excitation with a wavelength of 0.4 μm, is associated with the emergence of another transition type. This state is determined by the ratio of ionization cross sections for transitions II and III.

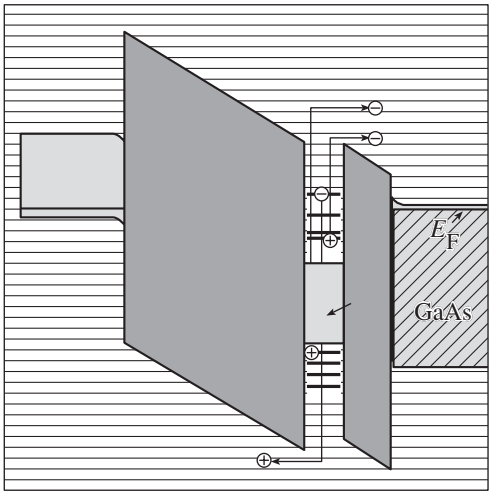

Fig. 5. An equilibrium energy-band diagram of the GaAs/ZnSe/QD-Ge/ZnSe/*p*-Ge structure. The arrows indicate the possible optical transitions with the subsequent electron (hole) withdrawal and localization of the second charge carrier. The diagram shows only overbarrier transitions, although tunneling into GaAs also can occur.

4. CONCLUSION

This study of the *I–V* and photoelectric characteristics of the n^+-GaAs/ZnSe/QD-Ge/ZnSe/Al and n^+-GaAs/ZnSe/QD-Ge/ZnSe/*p*-Ge structures showed that it is possible to observe single-electron processes in tunneling-thin Ge-QD ZnSe layers. It is shown that the charge accumulation at QDs in the n^+-GaAs/ZnSe/QD-Ge/ZnSe/*p*-Ge transistor structure is affected by exposure to light with various spectra. This effect leads to various changes in the total channel current. Based on the experimental data, we constructed energy-band diagrams of the structures and consistently considered the features of both *I–V* and spectral characteristics.

ACKNOWLEDGMENTS

This study was supported by the Russian Foundation for Basic Research, project no. 02-02-17800; and by the Projects “Surface Atomic Structures” and “Low-Dimensional Quantum Structures.”

REFERENCES

1. F. A. Reboredo and Alex Zunger, Phys. Rev. B **62**, R2275 (2000).
2. L. Guo, E. Leobundung, and S. Y. Chou, Science **275**, 649 (1997).
3. I. G. Neizvestnyĭ, S. P. Suprun, A. B. Talochkin, *et al.*, Fiz. Tekh. Poluprovodn. (St. Petersburg) **35**, 1135 (2001) [Semiconductors **35**, 1088 (2001)].
4. I. G. Neizvestny, S. P. Suprun, V. N. Shumsky, *et al.*, Nanotechnology **12**, 437 (2001).
5. I. Yu. Borodin, I. A. Litvinova, I. G. Neizvestnyĭ, *et al.*, Pis'ma Zh. Éksp. Teor. Fiz. **78**, 184 (2003) [JETP Lett. **78**, 152 (2003)].
6. H. Kroemer, Surf. Sci. **132**, 543 (1983).
7. G. Bratina, R. Nicolini, L. Sorba, *et al.*, J. Cryst. Growth **127**, 387 (1993).
8. I. A. Litvinova, I. G. Neizvestnyĭ, A. V. Prozorov, *et al.*, Pis'ma Zh. Éksp. Teor. Fiz. **78**, 1289 (2003) [JETP Lett. **78**, 768 (2003)].

Translated by N. Korovin

Semiconductors, Vol. 39, No. 1, 2005, pp. 95–99. Translated from Fizika i Tekhnika Poluprovodnikov, Vol. 39, No. 1, 2005, pp. 106–111.

LOW-DIMENSIONAL SYSTEMS

Unusual Persistent Photoconductivity in the InAs/AlSb Quantum Well

Yu. G. Sadofyev^, A. Ramamoorthy, J. P. Bird, S. R. Johnson, and Y.-H. Zhang

Department of Electrical Engineering and Center for Solid State Electronics Research, Arizona State University, Tempe, AZ 85287-5706, USA

^e-mail: sadofyev@hotmail.com

Submitted June 1, 2004; accepted for publication June 16, 2004

Abstract—Unusual features of persistent photoconductivity are reported for the InAs/AlSb quantum-well (QW) structure with a backgate. A negative persistent photoconductivity made it possible to decrease the electron concentration by an order of magnitude from 6×10^{11} cm^{-2}. This is the largest variation in the electron concentration for this effect. In addition to a pronounced negative persistent photoconductivity, the relaxation of the structural resistance was bistable under exposure of the structure to visible light. These phenomena are attributed to the effect of a thin Ge film deposited on the structure surface prior to photolithography. This film forms a region in the GaSb layer in which the holes are accumulated from the sequence of the Ge/GaSb/AlSb layers located above the QW. IR radiation initiates beats of Shubnikov–de Haas oscillations in the region of weak magnetic fields. These beats are believed to be caused by spin splitting in a zero magnetic field due to the asymmetry of a potential profile of the QW. This asymmetry is induced by prolonged illumination of the structure. © *2005 Pleiades Publishing, Inc.*

Quantum wells (QWs) in the InAs/AlSb system represent an attractive object for fabrication of mid-IR devices and ultrahigh-speed transistors. Good lattice-matching of InAs and AlSb makes in possible to prepare smooth interfaces between layers and thus to ensure that scattering by surface roughness is weak. In combination with a small electron effective mass in InAs and a high (~1.35 eV) potential barrier for electrons at the InAs/AlSb interface, this circumstance makes it possible to attain electron mobilities at a level of 3×10^4 and 9×10^5 cm^2/(V s) at 300 and 4.2 K, respectively [1]. A large *g*-factor for electrons in InAs single crystals (–15) also makes it possible to use the spin-induced degree of freedom for the development of spintronics devices.

It is known that undoped InAs/AlSb QWs have a rather high two-dimensional (2D) electron concentration (~1×10^{12} cm^{-2}). The specific features of the structure under consideration is the bipolarity of persistent photoconductivity at low temperatures [2, 3]. The positive persistent photoconductivity (PPPC) is observed for the IR spectral region. An increase in the electron concentration in InAs is attributed to the ionization of deep donors that are located in barrier layers and supply electrons to QWs. For a long time after illumination, the new value of the 2D electron concentration remains virtually unchanged.

Photons with an energy exceeding the AlSb indirect band gap, which equals 1.69 eV, can generate electron–hole pairs in the AlSb barriers. The built-in electric field of the heterostructure is favorable for hole transfer to the QW. The subsequent recombination of 2D electrons of the QW with nonequilibrium holes decreases the 2D electron concentration. This circumstance leads to a negative persistent photoconductivity (NPPC). The generation of electron–hole pairs is also possible in the coating GaSb layer, which is usually used to prevent contact of chemically unstable AlSb with moisture in the air. The threshold energy for hole transfer from GaSb to the QW is determined by the sum of the GaSb band gap (0.81 eV) and the valence-band offset at the GaSb/AlSb interface (~0.35 eV) [3]. Recharging of the deep donor and acceptor levels located close to the ground quantized subband for electrons can also induce the NPPC [4]. The information on spectral dependences of usual persistent photoconductivity in the InAs/AlSb structures were reported in more detail previously [5].

In this study, we will consider some features of bipolar persistent photoconductivity, which are unusual for structures of this type. We observed these features for the InAs/AlSb QW structure grown on the n^+-GaAs(100) substrate. The purpose of the experiment was to use the n^+-GaAs substrate as a backgate that allowed us to control the electron concentration in the QW without preventing photons to propagate into the active part of the structure.

A combined buffer region that included an AlAs layer (0.5 μm), an AlSb layer (2.5 μm), and an AlSb (2.5 nm)/GaSb (1.5 nm) superlattice (25 periods) was grown on the substrate by molecular-beam epitaxy (MBE). This combination of the layers was chosen in order to decrease the surface roughness and density of extended structural defects caused by a substantial lat-

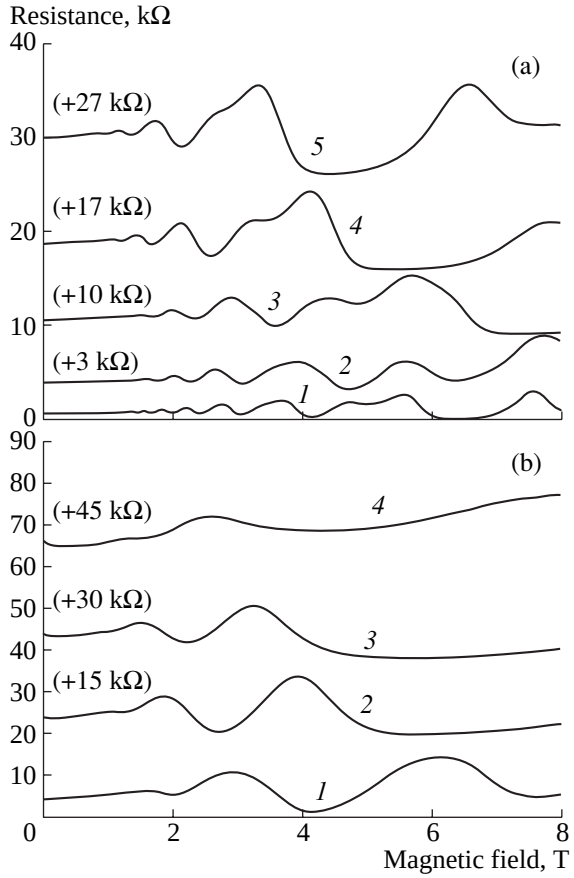

Fig. 1. Effect of pulsed illumination with (a) red and (b) blue light-emitting diodes on the magnetoresistance of the InAs/AlSb quantum well at 4.2 K and zero voltage at the backgate. (a): (*1*) The initial curve; (*2–5*) the current of the red light-emitting diode is 0.5, 1.3, 30, and 100 μA, respectively. (b): (*1–4*) the current of the blue light-emitting diode is 0.1, 0.15, 5, and 50 μA, respectively. The values of the shift of the curves along the vertical axis are given in parentheses.

tice mismatch between InAs and GaAs. The AlAs layer induces the potential barrier for hole transport, which makes it possible to reduce the leakage current of the backgate. The active part of the structure includes a bottom 25-nm-thick AlSb barrier, a 15-nm-thick InAs QW, a top 40-nm-thick AlSb barrier, and a 6-nm-thick coating GaSb layer. The AuGe/Ni/Au metal composition was deposited after epitaxy on the rear side of the substrate to form a nonrectifying contact. Double Hall bars were formed for subsequent measurements of magnetoresistance and the Hall effect at the front side of the structure using photolithography and mesa etching. In the geometry used for the measurement of the transverse magnetoresistance ρ_{xx}, the ratio of the sample length between potential probes l to its width w was 5 at $w = 70$ μm. The lateral sides and the mesa periphery were coated with silicon nitride film grown at 50°C by vapor-phase chemical deposition in the radio-frequency discharge plasma. Nonalloyed ohmic contacts to contact areas of the Hall bar were formed by thermal deposition of the Cr/Au metal combination directly on the surface of the QW layer after selective etching of top layers.

Developers used in photolithography actively etch GaSb and AlSb. Therefore, prior to photoresist deposition, an amorphous Ge film 10 nm thick was deposited on the structure surface using vacuum thermal evaporation. This film effectively prevented etching of bottom layers by the developer. At liquid-helium temperature used to investigate the transport properties of the sample, the electrical resistance of the Ge layer is much higher than the resistance of the QW and no manifestations of shunting of the active part of the structure are observed. The Ge film was removed from the photoresist-unprotected regions of the structure using a nonselective etchant based on phosphoric acid used to form the mesa. The difference in etching rates of AlSb and GaSb allowed us to use the superlattice as a stable mesa floor.

The contact areas of the Hall bar were connected using ultrasonic bonding with the leads of a standard crystal holder of the integrated circuit. Light-emitting diodes (LEDs), which emitted in the red, blue, and IR (wavelength $\lambda = 0.97$ μm) spectral regions, were mounted near the fabricated device. The transport properties of the 2D electron gas in the QW were studied in magnetic fields from 0 to 8 T. The intensity of illumination of the structure was controlled using a precision supply source, which provided setting of the specified current through the LED. The bias voltage at a backgate was selected so that the leakage current across the structure was no larger than 10 nA. This gate current introduced no errors into the results of measurements.

After cooling the structure to 4.2 K, the electron mobility in the QW was equal to $\mu = 1.1 \times 10^5$ cm^2/(V s) with a sheet concentration of $n_s = 6 \times 10^{11}$ cm^{-2}. The depth of modulation of the layer concentration due to the field effect at the nonzero gate voltage amounted to ~25% of the initial value. The negative potential (V_G) applied to the backgate leads to the depletion of the QW in electrons. The opposite effect occurred under change in the gate potential sign. The short-term (several tens of seconds) irradiation of the structure with photons from the visible region of the spectrum led to an increase in the electric resistance of the sample and a decrease in the 2D electron concentration. Figure 1 illustrates variations in the magnetoresistance of the sample as a result of illumination of the structure at various intensity with red and blue LEDs. The curves were measured ~30 min after illumination, when relaxation did not already noticeably change the structure properties during measurement. The sheet electron concentration n_s can be determined from the period of the Shubnikov–de Haas oscillations in the inverse magnetic field.

It follows from Fig. 1a that irradiation with red-region photons, which correspond to an indirect band gap of the AlSb barrier layers, ensures a decrease in the sheet electron concentration of the InAs QW due to the

NPPC by a factor of 3 compared to the initial value. Further increase in the illumination intensity (the LED current) does not enhance the NPPC for this photon energy.

The NPPC effect is substantially enhanced under irradiation of the structure with blue-region photons (Fig. 1b), whose energy considerably exceeds the direct AlSb band gap (E_G^Γ = 2.35 eV [6]). This enhancement is caused by a sharp distinction between the absorption factors and efficiencies of generation of electron–hole pairs for photons with energies corresponding to indirect or direct band gaps of the barrier material. The highest magnitude of NPPC is attained for a blue-emission LED current of about 50 μA. In this case, the n_s is 6×10^{10} cm^{-2}, which is by an order of magnitude lower than the initial sheet electron concentration. As far as we know, this is the largest electron-concentration variation related to the NPPC in such QWs. For the InAs/AlSb QWs, the typical value of the coefficient of a decrease in the layer electron concentration due to the NPPC is close to two [2], while the highest of previously attained values is five [7].

The data shown in Fig. 1 are obtained at zero gate bias. Upon application the external bias, the effect of the gate potential sign on the electron concentration in the QW was similar to that prior to illumination of the structure.

The unusual character of relaxation of the sample resistance in zero magnetic field after switching off the LED is of special interest. Figure 2 shows that, during illumination, the resistance attains a certain value characteristic of the used intensity of light and is much higher than the initial resistance. After switching off the LED, the sample resistance continues to increase rather than relaxing to the initial value. In this case, we may state that there exists a certain new quasi-steady state, which is generated by illumination of the structure. As a result, a powerful "attractor" of electrons from the QW is formed. A long-term (~10 h) relaxation measurement allowed us to find that the slow resistance relaxation; i.e., the difference between R_{sat} established due to the relaxation and the current value of resistance R, $R_{sat} - R$, has a single time constant close to 7700 s. This process could not be attributed to the recharging of surface states at a particular boundary of the structure. Surface states are characteristic of a broad density distribution in energy, which inevitably causes the emergence of a set of relaxation times. The observed effect is reversible. The structure returns to the initial state after heating to room temperature and repeated cooling. It is noteworthy that no such slow and unusual relaxation was found in our structures without the Ge layer on top of the coating GaSb layer.

It is known that, at the GaSb/GaAs contact, the bottom of the conduction band E_C for GaSb is located by 0.1 eV above the corresponding energy level for GaAs (the energy-band diagram of the second type) [6]. The heterojunction between the Ge and GaAs single-crystal

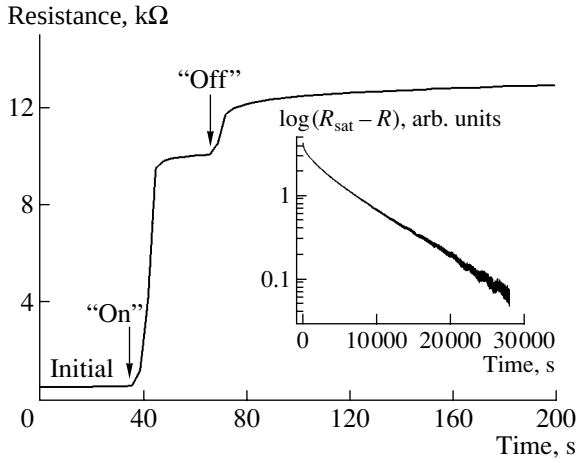

Fig. 2. Effect of radiation of a blue light-emitting diode on the structure resistance in the zero magnetic field. The slow portion of resistance relaxation to the metastable saturated value R_{sat} with a single time constant is shown in the inset.

layers has the structure of energy bands of the first type, and E_C for Ge is shifted by 0.07–0.4 eV downward relative to E_C for GaAs [8]. Single-crystal Ge and GaSb have virtually coinciding band gaps at liquid-helium temperature (~0.8 eV). For amorphous Ge, the band gap is somewhat wider than that for single-crystal Ge. However, we may assume that the sequence of the Ge/GaSb/AlSb layers located above the InAs QW forms the QW for holes in the GaSb layer. The holes accumulated in GaSb under illumination of the sample can afterwards overcome the AlSb potential barrier, drift to the InAs QW, and recombine with the 2D electron gas. Such recombination of spatially separated carriers can be the cause of enhancement of the NPPC effect and slow relaxation with a single time constant.

The interface between Ge and GaSb is imperfect since the Ge layer was deposited outside the MBE facility. Consequently, the 2D hole gas cannot have high mobility. Therefore, this gas cannot give rise to additional series of Shubnikov–de Haas oscillations in the range of magnetic fields used. The charge exchange between InAs and GaSb under an external electric field applied to the structure can also lead to the observed effect of the potential sign at the backgate on the 2D electron concentration in the InAs QW.

The short-term (pulsed) illumination of the structure using the IR LED leads to positive persistent photoconductivity. An increase in the electron concentration in the InAs QW amounts to 10% of the initial value, which is typical of structures of this type. In this case, the Shubnikov–de Haas oscillations are not much different from the initial curve, which is shown in Fig. 3 (the lowest curve). However, long-term illumination or continuous illumination of the structure during measurements of magnetoresistance leads to beats of Shubnikov–de Haas oscillations in the region of low magnetic fields (0.4–1.1 T). Once they have emerged, beats

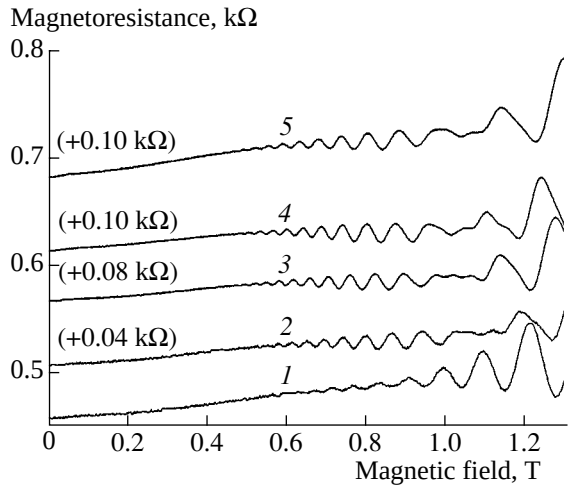

Fig. 3. Magnetoresistance of the structure under the radiation of an IR light-emitting diode (wavelength $\lambda = 0.97$ μm) and zero backgate voltage. (*1*) The initial curve; (*2–4*) continuous illumination of the structure for the currents of the light-emitting diode 0.1, 0.5, and 2.5 μA, respectively; (*5*) dark magnetoresistance after long-term illumination. The values of the shift of the curves along the vertical axis are given in parentheses.

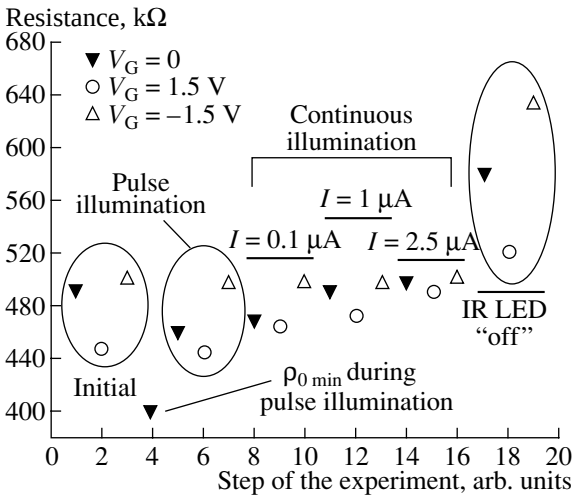

Fig. 4. Variation in the resistance of the InAs/AlSb structure in the zero magnetic field in a series of sequential measurements of the Shubnikov–de Haas oscillations under various illumination intensities provided by an IR light-emitting diode and at several V_G voltages applied to the inverse gate. The values of V_G and current I through the IR light-emitting diode are given.

are retained both under application of external electric field to the structure and under variation in the illumination intensity within a wide range. We observed beats in sequential measurements of magnetoresistance for values of the IR LED direct current of 0.1, 0.5, and 2.5 μA. For each value of the current, we measured three magnetoresistance curves, which corresponded to the zero, positive, and negative potential at the backgate. Beats were also observed after switching off the LED during the measurement of magnetoresistance curves for different gate potentials. We may state with confidence that beats of the Shubnikov–de Haas oscillations induced by IR radiation are retained for 10 h after illumination. We carried out no further detailed studies.

Beats of Shubnikov–de Haas oscillations can be caused by both nonuniformity of properties of the structure and asymmetry of the potential profile of the QW, which is sufficient to observe spin splitting in zero magnetic field (the Rashba effect) [9]. The emergence of beats of the Shubnikov–de Haas oscillations under application of external electric field to quantum-dimensional structures with the configuration of layers close to that studied by us is considered to be indicative of the Rashba effect [10–12].

We know only a single previous study where the emergence of beats of the Shubnikov–de Haas oscillations was observed under the effect of the IR radiation on the InAs/AlSb QW [13]. The following features of the effect were reported [13]: (i) beats of Shubnikov–de Haas oscillations depend heavily on the sample shape and emerge only in "long" Hall bars with an l/w ratio larger or equal to 10 ($w = 100$ μm); (ii) beats are observed for no longer than 1 h after illumination of the sample or vanish during measurement; and (iii) the effect is observed only for certain wavelengths and illumination intensities. Based on the above-listed features, it was concluded that Shubnikov–de Haas oscillations induced by IR radiation are associated with nonuniform distribution of 2D electron concentration in the QW, which is caused by a nonuniform distribution of illumination intensity over the structure area.

In our experiment, beats of Shubnikov–de Haas oscillations emerged in a "short" sample and in a wide range of variation in the illumination intensity. The effect is stable for a long time after illumination as well as under application of weak external electric field (~10^4 V/cm) of different polarity.

Figure 4 shows the dynamics of variation in the sample resistance in the zero magnetic field (ρ_0) in a series of experiments concerned with measuring the Shubnikov–de Haas effect and performed sequentially for one day under various illumination conditions at various backgate voltages. It follows from Fig. 4 that the degree of influence of the field effect on the sample resistance (the electron concentration in the InAs QW) varies under the effect of LED IR radiation. The field-effect magnitude can be determined from the ratio between the sample resistances for the negative and positive potentials at the backgate under specified conditions of illumination of the sample. This ratio decreases almost to unity as the illumination intensity increases due to screening of the external electric field by the charge of nonequilibrium carriers generated by radiation. The magnitude of the field effect after switching off the LED is much larger than that prior to illumination of the sample. This observation indicates

that the space charge and the built-in electric field, which screen the QW from the gate electric field, vary in structure. In addition, due to the long-term illumination of the sample, the Shubnikov–de Haas oscillations shift to weaker magnetic fields, which indicates that the efficiency of scattering at spatially distributed defects decreases.

The totality of the above-mentioned features of the effect allows us to assume that the phenomenon observed is associated with spin splitting in the electric field built in the structure and induced by the IR radiation, rather than with nonuniformity of properties over the sample area. Conclusive confirmation of this assumption can be obtained by carrying out the measurements in "inclined" magnetic fields, which allow one to separate spin splitting from the Shubnikov–de Haas oscillations at the Landau levels with different indices.

It is noteworthy that the final dark resistance of the structure in the absence of external electric and magnetic fields (Fig. 4) is larger than the initial resistance. Thus, despite the impossibility of generating electron–hole pairs in the AlSb barrier layers and of transferring the optically excited holes from the coating GaSb layer to the InAs QW, it can be stated in confidence that we observed a negative persistent photoconductivity (or a decrease in the density of the 2D electron gas in the QW). We believe that this phenomenon is caused by competition of two processes: (i) an increase in the electron concentration in the InAs QW due to the activation of deep donors (located in the AlSb barriers) by IR radiation and (ii) the generation of electron–hole pairs in GaSb by IR radiation with the subsequent accumulation of holes in the GaSb layer and their recombination with electrons localized in the InAs QW. As a result, we have a decrease in the 2D electron concentration in the sample relative to the initial level.

In conclusion, it is noteworthy that we observed an unprecedentedly large variation in the 2D electron concentration due to the NPPC in the InAs/AlSb QW under irradiation with photons from the red and blue spectral regions as well as an unusual type of slow relaxation of the sample resistance. Both effects are associated with the formation of an additional quantum well for holes in the coating GaSb layer confined by the Ge and AlSb barriers. Under the long-term effect of IR photons on the structures, we observed beats of Shubnikov–de Haas oscillations. It is our opinion that this effect can represent the manifestation of spin splitting in the built-in electric field induced by IR irradiation of InAs/AlSb QWs.

REFERENCES

1. C. Nguyen, B. Brar, C. R. Bolognesi, *et al.*, J. Electron. Mater. **22**, 255 (1993).
2. G. Tuttle, H. Kroemer, and J. H. English, J. Appl. Phys. **65**, 5239 (1989).
3. Ch. Gauer, J. Scriba, A. Wixforth, *et al.*, Semicond. Sci. Technol. **8**, S137 (1993).
4. S. Ideshita, A. Furukava, Y. Mochizuki, and M. Mizuta, Appl. Phys. Lett. **60**, 2549 (1992).
5. V. Ya. Aleshkin, V. I. Gavrilenko, D. M. Gaponova, *et al.*, Fiz. Tekh. Poluprovodn. (St. Petersburg) **39**, 30 (2005) [Semiconductors **39**, 22 (2005)].
6. I. Vurgaftman, J. R. Meyer, and L. R. Ram-Mohan, J. Appl. Phys. **89**, 5815 (2001).
7. P. F. Hopkins, A. J. Rimberg, R. M. Westervelt, *et al.*, Appl. Phys. Lett. **58**, 1428 (1991).
8. R. S. Bauer and H. W. Sang, Jr., Surf. Sci. **132**, 479 (1983).
9. Yu. A. Bychkov and E. I. Rashba, JETP Lett. **39**, 78 (1984).
10. J. Luo, H. Munekata, F. F. Fang, and P. J. Stiles, Phys. Rev. B **41**, 7685 (1990).
11. J. P. Heida, B. J. van Wees, J. J. Kuipers, *et al.*, Phys. Rev. B **57**, 11911 (1998).
12. D. Grundler, Phys. Rev. Lett. **84**, 6074 (2000).
13. S. Brosig, K. Ensslin, R. J. Warburton, *et al.*, Phys. Rev. B **60**, 13989 (1999).

Translated by N. Korovin